Full Length Article

Revealing natural fluorescence in transparent insect wings by linear and nonlinear optical techniques

Sébastien R. Mouchet [a,b,1,*], Charlotte Verstraete [c,1], Bojana Bokic [d], Dimitrije Mara [c,e,f], Louis Dellieu [b], Albert G. Orr [g], Olivier Deparis [b], Rik Van Deun [e], Thierry Verbiest [c], Pete Vukusic [a,**], Branko Kolaric [d,h]

[a] School of Physics, University of Exeter, Stocker Road, Exeter, EX4 4QL United Kingdom
[b] Department of Physics & Namur Institute of Structured Matter (NISM), University of Namur, Rue de Bruxelles 61, 5000 Namur, Belgium
[c] Molecular Imaging and Photonics, Department of Chemistry, KU Leuven, Celestijnenlaan 200D, 3001 Heverlee, Belgium
[d] Center for Photonics, Institute of Physics, University of Belgrade, Pregrevica 118, 11080 Belgrade, Serbia
[e] L³ – Luminescent Lanthanide Lab, Department of Chemistry, Ghent University, Krijgslaan 281-S3, 9000 Ghent, Belgium
[f] Institute of General and Physical Chemistry, Studentski trg 12/V, 11158 Belgrade, Serbia
[g] Environmental Futures Centre, Griffith University, Nathan, QLD 4111, Australia
[h] Micro- and Nanophotonic Materials Group, University of Mons, Place du Parc 20, 7000 Mons, Belgium

ABSTRACT

For most natural organisms, the physical, chemical and biological aspects of fluorescence emission are poorly understood. For example, to the best of our knowledge, fluorescence from the transparent wings of any of the 3000 known species of cicadas has never been reported in the literature. These wings are known to exhibit anti-reflective properties arising from quasi-periodic arrays of nipples. Our study, using linear and nonlinear optical techniques, including spectrofluorimetry, two-photon fluorescence spectroscopy and Second Harmonic Generation (SHG), reveals the fluorescence properties in the wings the grey and the common cicadas (*Cicada orni* and *Lyristes (Tibicen) plebejus*, respectively), as well as the broad-bordered bee hawk-moth (*Hemaris fuciformis*). The study suggests that fluorescence would be more widespread in transparent insect wings than what was previously believed. Comparing this result to the fluorescence emission from the wings of the Bornean damselfly (*Vestalis amabilis*), we inferred that this emission probably arises from resilin, a protein reported to enhance wing flexibility. Moreover, the nonlinear optical investigation of the insects' wings provided further insight into wing structure, indicating that multiphoton techniques add valuable information for the analysis of insect integuments. The strong SHG signal detected from the wing veins implies that these veins are materially organised in a non-centrosymmetric and hence non-random fashion.

1. Introduction

Fluorescence emission takes place in the integument of several natural organisms including species from the animal classes Insecta, Aves, Amphibia, Reptilia and Mammalia as well as the plant kingdom [1–21]. This emission of light has been shown to play a role in visual communication of some organisms, facilitating species recognition, mate selection, prey detection, camouflage and agonistic behaviour [7,11]. Fluorescence results from the presence of fluorophores, such as papiliochrome II, biopterin, psittacofulvin, or green fluorescent protein (GFP) within the biological integuments. Following the absorption of incident light (typically in the UV or the shorter-wavelength part of the visible range), these molecules emit light at a longer wavelength (usually in the visible), resulting from transitions between their electron states. In spite of the crucial role that it is believed to play in nature, fluorescence in natural organisms remains under-investigated from optical, chemical and biological perspectives. One example is the transparent wings of certain insects of the order Hemiptera. For example, in

---

* Corresponding author. School of Physics, University of Exeter, Stocker Road, Exeter EX4 4QL, United Kingdom.
** Corresponding author. School of Physics, University of Exeter, Stocker Road, Exeter EX4 4QL, United Kingdom.
  E-mail addresses: s.mouchet@exeter.ac.uk (S.R. Mouchet), P.Vukusic@exeter.ac.uk (P. Vukusic).
[1] Co-shared first authorship.

both males and females of many cicadas, both pairs of wings are known for their anti-reflective properties [21–26] arising from electromagnetic impedance matching between the air and the wing material covered by quasi-periodic arrays of hexagonally close-packed protrusions, often referred to as nipples (Fig. 1a and b). Similar structures also cover parts of the integument in other organisms such as the wings of several moths and butterflies (Order Lepidoptera), dragonflies and damselflies (Order Odonata) (Fig. 1c–f) [21,25,27–35] and the corneas of some insect eyes [36,37]. In all these examples, the basic building material of the insect tissues is chitin, a polysaccharide, overlaid by a thin epicuticle of wax. In cicadas, transmittance spectra of their wings have been measured to reach more than 90% and to peak at up to 98% over the range from 500 to 2500 nm [22,23]. These anti-reflective properties are thought to be involved as part of the insects' strategy for crypsis and the nano-structured protrusions have been mimicked for the development of anti-reflective coatings for a full range of applications such as solar cells,

screens, anti-glare glasses, light-sensitive detectors, telescopes and camera lenses [21,38–40]. In addition to this optical property, the transparent wings of insects are known to be hydrophobic [23–25, 41–44] and some exhibit anti-bacterial properties [44–48]. In the case of cicadas, the surface morphology was found to influence jointly the hydrophobic and anti-reflective properties (Fig. 1) [24,25]. The protrusions on the wing surface can be modelled as truncated cones covered by hemispheres. The cone shape affects the transparency and the hemispheres enhance the wing's hydrophobicity. Despite these properties, which are relevant in many scientific fields ranging from physics and material science to chemistry and biology, to the best of our knowledge fluorescence emission has so far not been reported, to the best of our knowledge, in any of the 3000 described species of the superfamily Cicadoidea. The phenomenon has however been investigated in several butterfly and moth species, in which the coloured wing scales are known to embed fluorophores such as papiliochrome II [3,6,49–52].
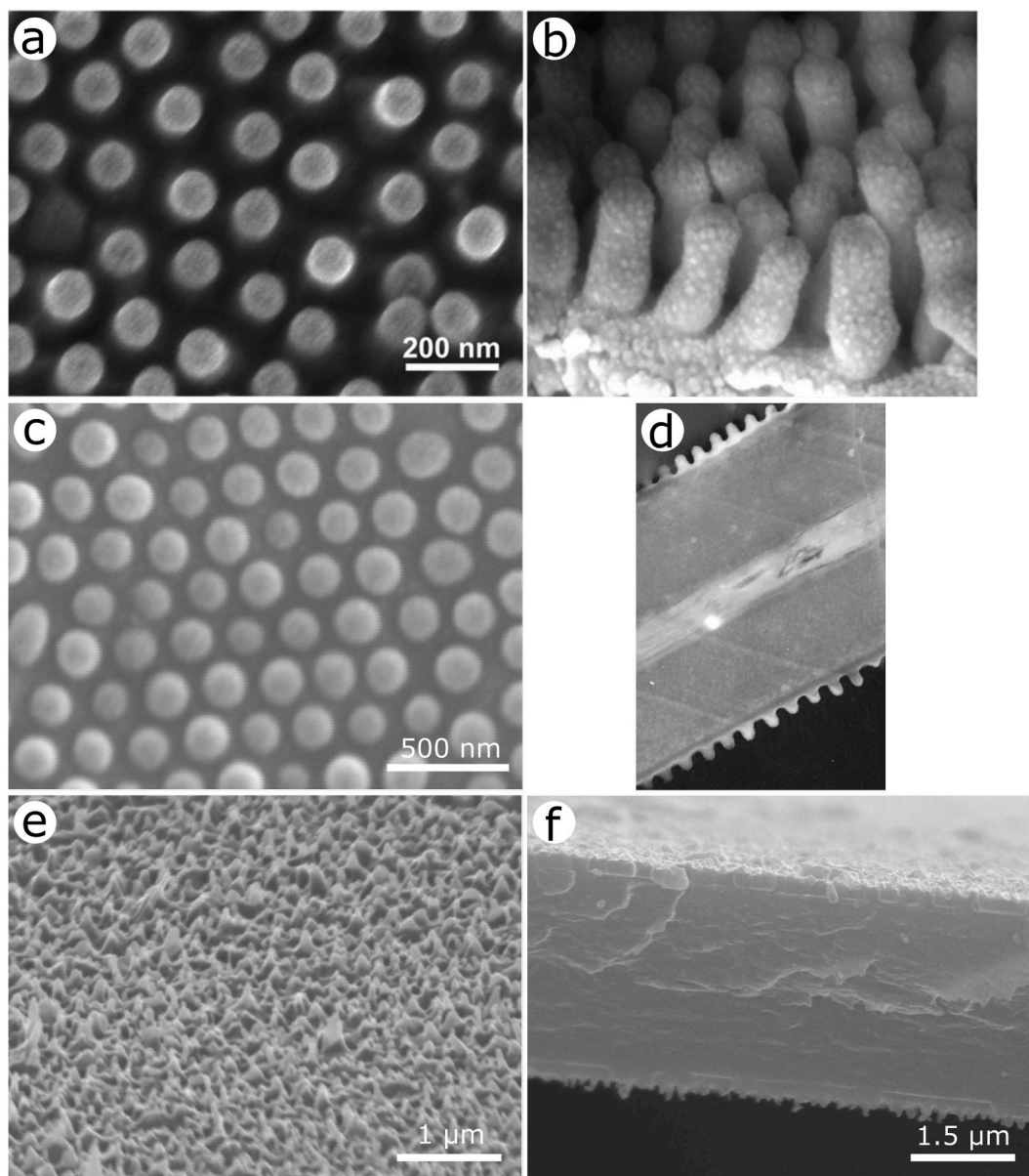

Fig. 1. The transparent parts of the wings of insects including the grey cicada Cicada*orni*(a,b), the broad-bordered bee hawk-moth*Hemaris fuciformis*(c,d) and the dragonfly blue hawker*Aeshna cyanea*(e,f) are covered by arrays of protrusions. These protrusions are sometimes displayed along a quasi-periodic hexagonally close-packed array such as on the wings of *C. orni* (a,b) and *H. fuciformis* (c) or a disordered pattern such as in the case of *A. cyanea* (e), as observed here by scanning electron microscopy (a-c,e-f) and transmission electron microscopy (d) with top views (a,c), oblique views (b,e) and views of cross-sections (d,f). Figures (a,b) and (d) were reproduced (a,b) from Ref. [24] with permission from AIP publishing and (d) from Ref. [30] with permission from Springer Nature.

Photonic structures present in these scales sometimes mediate the associated light emission [53–55]. Fluorescence has also been described in the vein joints and the membrane of the transparent wings of damselflies and dragonflies [56–59]. This emission was attributed to the presence of autofluorescent proteins such as resilin. Resilin proteins emit blue light (at about 400 nm) under incident UV light and were reported to decrease in concentration toward the distal regions of the wings (on both sides) [56,57]. They give rise to low stiffness and high strain in biological tissues, allowing passive wing deformations [60,61]. We note that resilin fluorescence may often be incidental with little or no semiotic function. However, in the case of males of the red-winged damselfly *Mnesarete pudica* (Hagen in Selys, 1853), fluorescence emission from resilin-containing wings was demonstrated to have a role in signalling (e.g., in courtship and territorial behaviour) in combination with pigments and UV reflection, by modulating the visual appearance of the insect according to sex and age [62].

In this article, we characterised the fluorescence emission from the transparent wings of two species of cicadas, the grey cicada *Cicada orni* (Linnaeus, 1758) (Fig. 2a) and the common cicada *Lyristes (Tibicen) plebejus* (Scopoli, 1763), using both linear and nonlinear optical methods. We compared their properties with the fluorescence emission from two other insects exhibiting transparent wings, namely, *Hemaris fuciformis* (Linnaeus, 1758) commonly known as the broad-bordered bee hawk-moth (Fig. 2b) and the Bornean damselfly *Vestalis amabilis* (Lieftinck, 1965) (Fig. 2c). These fluorescent properties were optically characterised by one- and multi-photon microscopy and spectrometry. The one-photon fluorescence techniques allowed us to explain the previously measured high absorption in the range 300–400 nm [24] and to infer the biological role of the fluorophores in the visual perception of insects. Multi-photon techniques enabled us to highlight the symmetry properties of the material within the wings.

2. Materials and methods

2.1. Sample collection

Adult specimens of *C. orni* and *L. plebejus* were collected in Fournès in the Gard Department (France) on the June 22, 2014 (by S.R. Mouchet and L. Dellieu), and *V. amabilis* was collected in swamp forest in Belait Division (Brunei Darussalam) in 1994 (by A.G. Orr). Adult specimens of *H. fuciformis* were bought from licensed vendors. *V. amabilis* was immersed for 24 h in acetone and air-dried. Other specimens were air-dried. No further sample preparation was necessary for the microscopy and spectrofluorimetry observations. All analyses were performed on the insects' wings.

2.2. Optical and fluorescence microscopy

The sample wings were analysed using two different configurations of the microscope: a reflection mode (illumination with visible light and observation in the visible range) and a fluorescence mode (illumination with ultraviolet light and observation in the visible range). Optical microscopy analysis was performed using an Olympus BX61 (Tokyo, Japan) microscope, an Olympus XC50 camera and an Olympus BX-UCB visible light source (in reflection mode) or a Lumen Dynamics X-cite Series 120 PCQ (Mississauga, Ontario, Canada) UV-lamp (in fluorescence mode).

2.3. Spectrofluorimetry

One-photon fluorescence (1 PF) emission spectra were recorded using a 450 W xenon lamp as steady state excitation source. The incident light formed a 45° angle with the normal direction to the sample surface and emitted light was detected at a 45° angle on the other side of the normal direction. The sample was excited at different excitation wavelengths: 320 nm, 340 nm, 360 nm, 380 nm, 400 nm, 420 nm, and 440 nm. Time-resolved measurements of fluoresence emission were performed using a microF920H xenon Flashlamp light source operating at a frequency of 100 Hz with a pulse width of 4 μs and excitation wavelengths equal to 340 nm and 360 nm. These time-resolved measurements were performed at the wavelengths of the maximum of emission peak intensity. They were fitted to double exponential functions. These best fits allowed us to assess the decay time of the fluorescence emission.

2.4. Multiphoton microscopy

Multiphoton microscopy experiments were carried out with an Olympus BX61 WI-FV1200-M (Münster, Germany) system. The laser was a Spectra-Physics (Santa Clara, CA, USA) InSight DS+ laser (82-MHz repetition rate, 120-fs pulse width, *p*-polarised) at 800 nm, 900 nm, 1000 nm, and 1100 nm fundamental wavelengths. The incident laser power was controlled by an achromatic half-wave plate and a *s*-oriented polariser directly after the laser. The laser beam was focused on the sample via either a 15× LMV objective (NA 0.3) or a 50× SLMPlan N objective (NA 0.35). The resulting signal was detected non-descanned in backwards reflection via a Hamamatsu R3896 photomultiplier tube. Different detection optics were used, depending on the excitation wavelength, in order to separate the two-photon fluorescence (2 PF) and the Second Harmonic Generation (SHG) signal. At 1000 nm, a 525 LPXR dichroic mirror was used to remove the SHG from the 2 PF, and an additional 500/10 bandpass filter cleared the SHG signal further. Similar filters were used for the other three fundamental wavelengths. The signal at each pixel was depicted in the micrographs as different intensities in false green (SHG) or false red (2 PF) colours. A routine providing an extended depth field allowed us to obtain in-focus micrographs from multiple images recorded at different depths in steps of 4 μm. Samples were observed over several minutes of time, in order to assess the photostability.

2.5. Electron microscopy

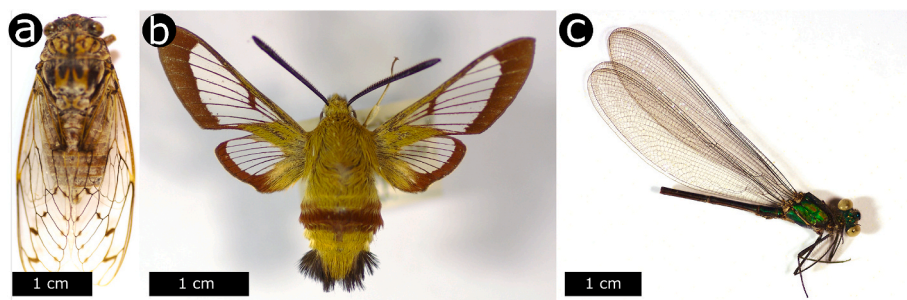Apart from two scanning electron microscopy (SEM) images taken

Fig. 2. The wings of the grey cicada *C. orni* (a), the broad-bordered bee hawk-moth *H. fuciformis* (b) and the damselfly *V. amabilis* (c) exhibit transparent wings.

from the literature [24], SEM observations were performed with a FEI (Hillsboro, OR) Nova 600 NanoLab Dual-Beam FIB/SEM microscope on small transparent regions of the wing membranes of *H. fuciformis* and *A. cyanea*. These samples were mounted onto SEM stubs with electrically conducting epoxy resin and sputter-coated with ca. 8 nm of gold palladium.

Transmission electron microscopy (TEM) imaging was carried on with cross-sections of transparent regions of *H. fuciformis*'s wings using a JEOL (Tokyo, Japan) 100S TEM instrument. The figure was previously published in Ref. [30]. The samples were fixed in 3% glutaraldehyde at 21°C for 2 h and consequently rinsed in sodium cacodylate buffer before being fixed in 1% osmic acid in buffer for 1 h. The samples were then block-stained in 2% aqueous uranyl acetate for 1 h, dehydrated through

an acetone series (ending in 100% acetone) and embedded in Spurr resin [63]. After microtoming, cross-sections were stained with lead citrate.

3. Results and discussion

Both *C. orni* and *L. plebejus* cicada species have brown-grey bodies and transparent wings (Fig. 2) with very low light reflection [21–26]. The bodies and wings are approximately 25 mm and 30–35 mm long, respectively. Like most insects including moths and damselflies, the wings of cicadas are divided by veins (Fig. 3a–d) appearing as darker structures forming the structurally flexible frame supporting of the wing membranes, while the transparent parts are membranes that form the main aerodynamic surface of the wing [60,64].
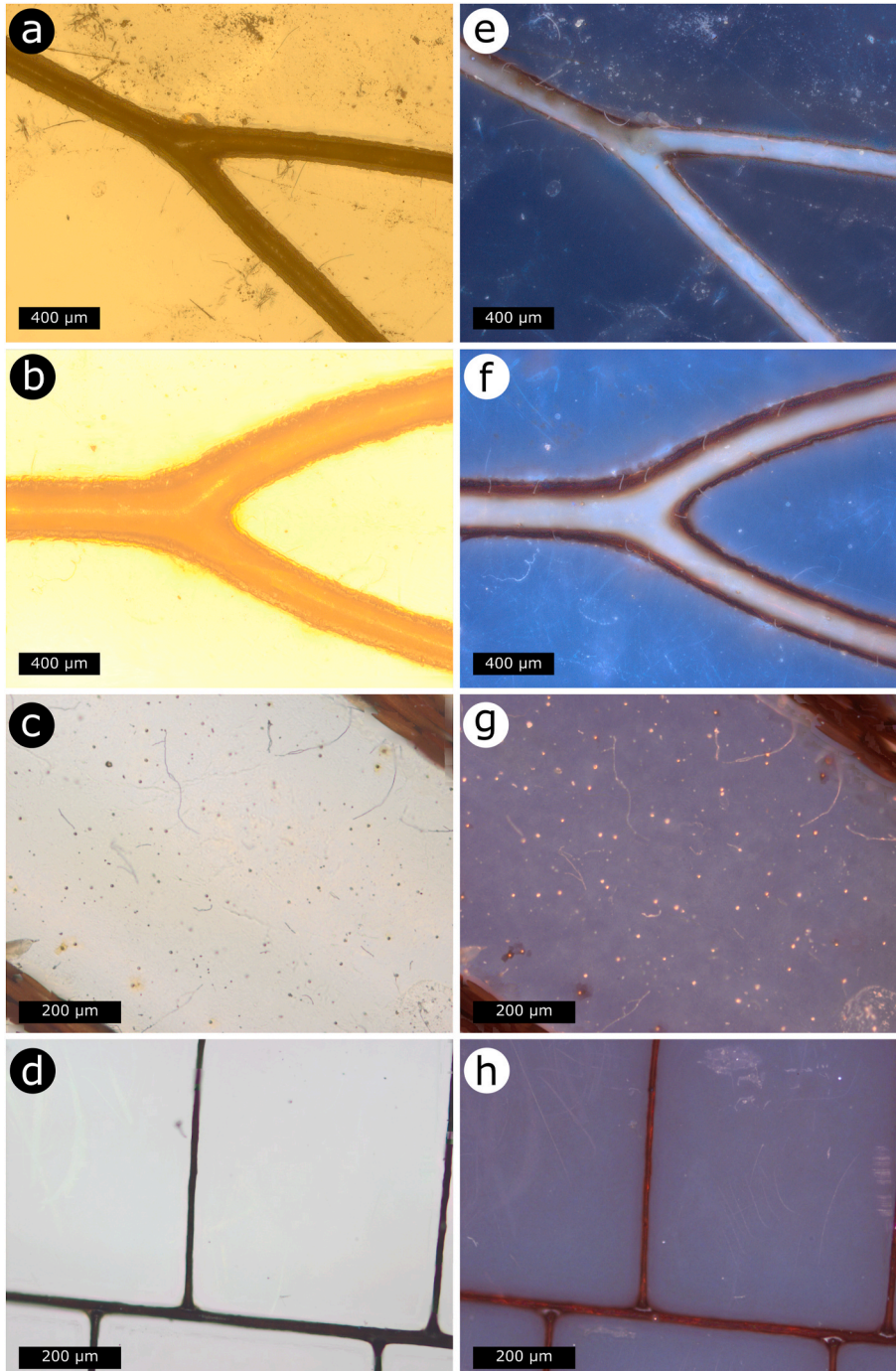

Fig. 3. The membranes and the veins of the transparent wings of the grey cicada (*C. orni*), the common cicada (*L. plebejus*), the broad-bordered bee hawk-moth (*H. fuciformis*) and *V. amabilis* damselfly emit light by fluorescence under UV irradiation. The transparent wings of *C. orni* (a), *L. plebejus* (b), *H. fuciformis* (c) and *V. amabilis* (d) are divided by brown veins. Both their transparent membranes and the veins of the wings emit visible light under UV incident light (e–h). The 1 PF signal from the veins of the cicada species (e,f) is especially intense.

Fluorescent microscopy observations indicate that both the transparent membrane and the veins of the wings fluoresce (Fig. 3). The latter are clearly brighter in the two investigated cicada species (Fig. 3e and f), indicating that they might contain many more fluorescent molecules than the membrane. Chitin is known to give rise to autofluorescence, with a very low quantum yield [65]. In addition, autofluorescent proteins such as resilin are known to be at the origin of blue hue fluorescence emission from damselfly and dragonfly species [56–58,62]. Hence both chitin and resilin are likely to play a role in the fluorescence emission observed from investigated cicada and moth species (Fig. 3e–g). It was previously reported that the extinction coefficient κ -namely, the imaginary part of the complex refractive index- of the wing material of *C. orni* exhibits a double peak in the UV range 200–300 nm, reaching ca. $\kappa = 2.5 \times 10^{-2}$ and $\kappa = 1.5 \times 10^{-2}$, with a non-negligible component in the range 300–400 nm [24]. Similarly, Azofeifa et al. measured peaks at 280 nm and 325 nm in the extinction coefficient for chitin samples from the exoskeleton of fresh Pacific white shrimps *Litopenaeus* (formerly *Penaeus*) *vannamei* (Boone, 1931) [66].

Our results show that light absorption in the wings of insects such as cicadas within the range 300–400 nm gives rise to fluorescence emission. In all four investigated insect wings, fluorescence emission single peaks were measured upon excitation with wavelengths ranging from 320 nm to 440 nm (Fig. 4). For instance, the measured emission spectra display peaks at about 410–420 nm with a 360-nm excitation wavelength. In addition, a 340-nm excitation wavelength appears to give rise to the most intense emission. The presence of a single peak in the emission spectra suggests that there is likely only a single type of fluorophore within the insect wings. The presence of mixtures of several fluorophores is less likely as this would imply emission spectra with multiple peaks. The measured emission peaks for all four insect wings are similar to the fluorescence emission measured by Chuang et al. from the wings of the damselfly *Ischnura senegalensis* (Rambur, 1842) [59]. Despite the fact that our observations are significantly different from the fluorescence response from the male neotropical damselfly *M. pudica* (i. e., emission at ca. 650 nm upon excitation at 405 nm) [62], the wings of

which are known to contain resilin, the emission peaks that we measured are in agreement with the emission band of resilin located at ca. 415 nm [58,67].

In addition, the emission peak widths and positions strongly depend on the excitation wavelength (Fig. 4). The peak position shifts from ca. 380 nm to ca. 490 nm as the excitation wavelength is increased from 320 nm to 440 nm. This dependence is similar to the previously reported one for males of the beetle *Hoplia coerulea* (Drury, 1773) [14]. It suggests that the fluorophores could exhibit complex dynamics with several excited states. In complex organic fluorophores, several excited states are likely related to exciton resonances (i.e., energy transfers between different donor and acceptor groups within the same molecule) [14,68, 69].

In order to understand better the radiative response in the linear regime, we performed time-resolved measurement of the emitted fluorescence intensity (Fig. 5).

In all cases (Table 1), the best fits to double exponential functions gave rise to a long decay time (of ca. 7–8 ns) and a short decay time (of ca. 1.1–1.3 ns), whatever the excitation and detection wavelengths were. This also suggests that only one type of fluorophores is present in the wings of each insect. The long decay time is related to the radiative decay of the fluorophores, whereas the short one is related to non-radiative decay [70]. If we assume that measured fluorescent signals originate from the same molecule (namely, resilin), the discrepancy observed in the emission spectra and decay time among the investigated samples could be attributed to differences in the chemical environment among the various species.

In addition, both *C. orni* and *L. plebejus* were probed at fundamental wavelengths ranging from 800 nm to 1100 nm, and showed significant SHG and 2 PF signal response over all this wavelength range (see Fig. 6 at a 1000-nm wavelength). At any of these selected fundamental wavelengths, the veins clearly appear in both SHG and 2 PF observations. The difference in signals between the veins and the membrane (in 1 PF, 2 PF, and SHG) is likely due to the significant difference in composition [56,57,64]: the veins of cicadas would show a much higher
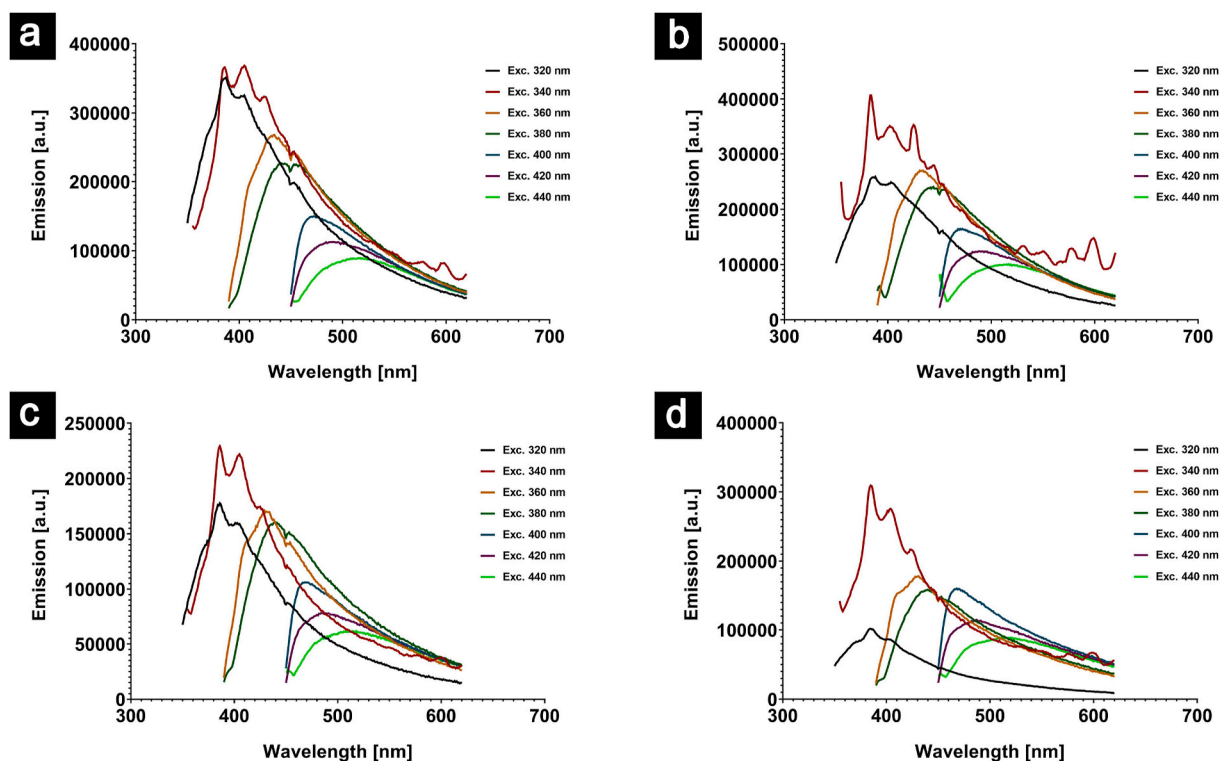

Fig. 4. **Fluorescence emission from the transparent wings of a)** *C. orni,* **b)** *L. plebejus,* **c)** *H. fuciformis,* **d)** *V. amabilis*. The emission peak widths, intensities and positions strongly depend on the excitation wavelength and are in agreement with the narrow emission band of resilin reported in the literature [67].
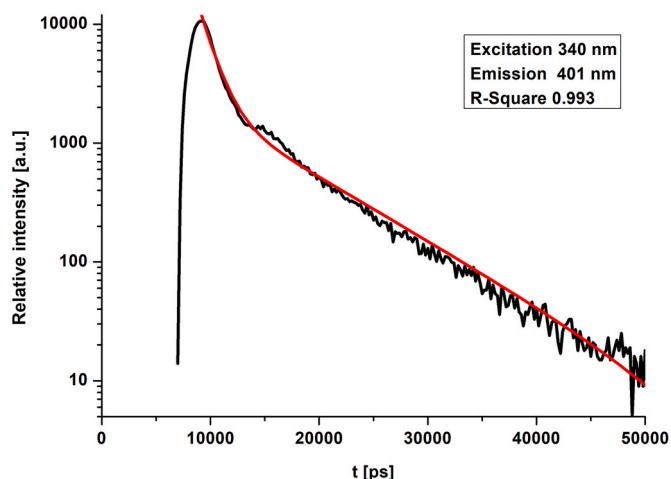
Fig. 5. Time-resolved measurement of the emission intensity of the fluorophores embedded in the wings of *H. fuciformis* (black curve). The measurements were performed with an excitation wavelength at 340 nm and an emission wavelength at 401 nm. The best fit to the decay is a double exponential function (red curve).

Table 1
Decay times of the fluorophores embedded within the transparent wings of *C. orni*, *L. plebejus*, *H. fuciformis* and *V. amabilis*. Measurements were performed at excitation wavelengths equal to 340 nm and 360 nm, and emission wavelengths lying within the emission peaks.

Species	Excitation Wavelength [nm]	Emission Wavelength [nm]	Decay time [ps]
Cicada orni	340	385	$t_1 = 1271.23$
			$t_2 = 8933.32$
	340	403	$t_1 = 1309.57$
			$t_2 = 9272.42$
	360	388	$t_1 = 1192.96$
			$t_2 = 8508.55$
	360	406	$t_1 = 1237.31$
			$t_2 = 8831.80$
Lyristes (Tibicen) plebejus	340	384	$t_1 = 1372.48$
			$t_2 = 8288.30$
	340	402	$t_1 = 1184.63$
			$t_2 = 7688.22$
	360	387	$t_1 = 1107.87$
			$t_2 = 7708.26$
	360	406	$t_1 = 1328.55$
			$t_2 = 8299.55$
Hemaris fuciformis	340	384	$t_1 = 1322.55$
			$t_2 = 8249.07$
	340	401	$t_1 = 1278.86$
			$t_2 = 8149.58$
	340	425	$t_1 = 1313.99$
			$t_2 = 8491.21$
	360	406	$t_1 = 1298.20$
			$t_2 = 7997.02$
	360	424	$t_1 = 1284.24$
			$t_2 = 8262.70$
	360	451	$t_1 = 1245.23$
			$t_2 = 8126.60$
Vestalis amabilis	340	384	$t_1 = 1235.50$
			$t_2 = 7578.67$
	340	402	$t_1 = 1374.48$
			$t_2 = 8060.57$
	340	425	$t_1 = 1338.49$
			$t_2 = 8220.30$
	360	387	$t_1 = 1326.02$
			$t_2 = 8226.46$
	360	406	$t_1 = 1203.75$
			$t_2 = 7596.25$
	360	450	$t_1 = 1119.60$
			$t_2 = 7841.73$

concentration in chitin and the fluorescent compounds. The former is known to give rise to an SHG signal [71]. Additionally, the veins are much thicker than the membrane, leading to an increased amount of material. Optical second-order behaviours such as SHG are known to take place exclusively in non-centrosymmetric media [72]. The detected SHG signal implies that the veins are materially organised in a non-centrosymmetric (and hence non-random) way.

From a visual point of view, the biological significance of fluorescence emission in the transparent wings of insects depends on the total number of photons emitted or scattered from the wings and transmitted through the wings from their backgrounds. Many cicadas are known to be mainly active during the hottest hours of summer days, when sunlight is very intense (but may also be active at twilight and at night). Although the measured fluorescence emission ranges match the range of both scotopic and photopic photoreceptors of many insects [73–76], it is hard to conclude that the measured 1 PF signal plays any role in cicadas' behaviour since the quantum yield of natural fluorophores are generally low [4,5,12], especially that of chitin [65], and the ratio of UV light in both sun- and moonlight is very limited with respect to that of visible light (for instance, ca. 6% of sunlight at sea level lies in the UV range, whereas about 50% is visible) [77]. The role of this fluorescence emission may possibly be a by-product of another biological function such as photoprotection due to the increased absorption of UV by the fluorophores (for example, when the wings are at rest over the insect's body in the case of cicadas) and incidental property of resilin that enhances wing flexibility.

4. Conclusion

Transparent wings of two cicada species, namely *C. orni*, *L. plebejus*, as well as the broad-bordered bee hawk-moth *H. fuciformis*, were demonstrated to emit light under incident UV light by fluorescence decay. All of them showed similar 1 PF properties, as their wings were excited in the 320–440 nm range and emitted in the range 380–490 nm. They were compared to the transparent wings of the damselfly *V. amabilis*, which showed similar fluorescent behaviours. Damselflies fluorescence emission is reported to arise from substances such as resilin embedded in their tissues. Additionally, the wings of both cicada species and more specifically their veins showed strong SHG and 2 PF signals, which are possibly due to the higher concentration of resilin or chitin in the veins with respect to the membrane that makes up most of the wing. The nonlinear optical characterisation of the cicadas' wings gives us more insight into the wing structure, indicating that multiphoton techniques add valuable information while characterising biological samples.
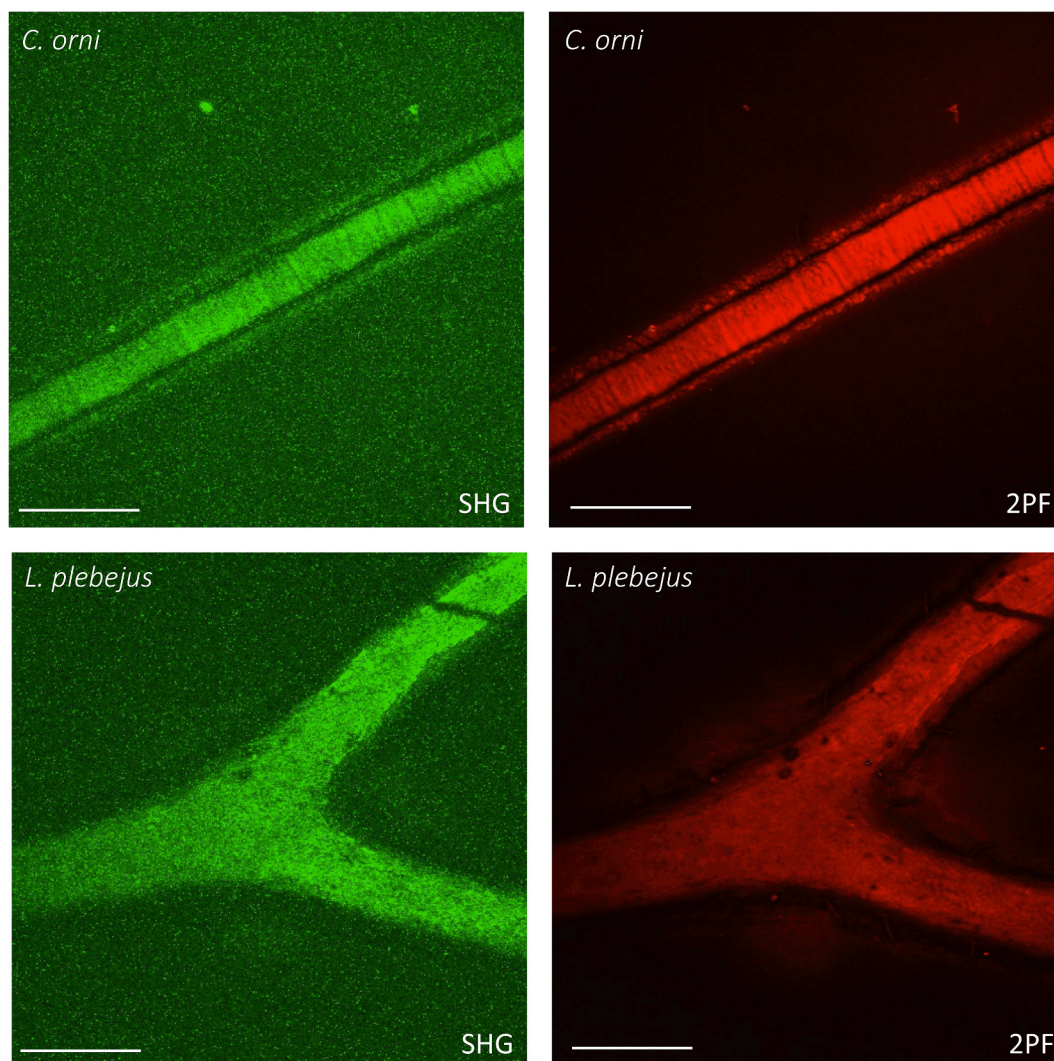
Fig. 6. Strong SHG and 2 PF signals are observed from the veins of the wings. Multiphoton micrographs of *C. orni* (top) and *L. plebejus* (bottom) at a fundamental wavelength of 1000 nm. Left: SHG response. Right: 2 PF response. Laser power: 200 mW (*C. orni*) and 80 mW (*L. plebejus*). Scale bars: 200 μm.

Declaration of competing interest

The authors declare that they have no known competing financial interests or personal relationships that could have appeared to influence the work reported in this paper.

Data availability

Data will be made available on request.

Acknowledgments

References

[1] M. Pavan, M. Vachon, Sur l'existence d'une substance fluorescente dans les téguments des scorpions (Arachnides), C. R. Acad. Sci. 239 (1954) 1700–1702.

[2] K. Tani, F. Watari, M. Uo, M. Morita, Fluorescent properties of porcelain-restored teeth and their discrimination, Mater. Trans. 45 (2004) 1010–1014.

[3] P. Vukusic, I. Hooper, Directionally controlled fluorescence emission in butterflies, Science 310 (2005) 1151.

[4] A. Iriel, M.G. Lagorio, Is the flower fluorescence relevant in biocommunication? Naturwissenschaften 97 (10) (2010) 915–924.

[5] A. Iriel, M.G. Lagorio, Implications of reflectance and fluorescence of *Rhododendron indicum* flowers in biosignaling, Photochem. Photobiol. Sci. 9 (2010) 342–348.

[6] V.L. Welch, E. Van Hooijdonk, N. Intrater, J.-P. Vigneron, Fluorescence in insects, Proc. SPIE 8480 (2012), 848004.

[7] M.G. Lagorio, G.B. Cordon, A. Iriel, Reviewing the relevance of fluorescence in biological systems, Photochem. Photobiol. Sci. 14 (2015) 1538–1559.

[8] D.F. Gruber, J.P. Gaffney, S. Mehr, R. DeSalle, J.S. Sparks, J. Platisa, V. A. Pieribone, Adaptive evolution of eel fluorescent proteins from fatty acid binding proteins produces bright fluorescence in the marine environment, PLoS One 10 (11) (2015) e0140972.

[9] D.F. Gruber, E.R. Loew, D.D. Deheyn, D. Akkaynak, J.P. Gaffney, W.L. Smith, M. P. Davis, J.H. Stern, V.A. Pieribone, J.S. Sparks, Biofluorescence in catsharks (Scyliorhinidae): fundamental description and relevance for elasmobranch visual ecology, Sci. Rep. 6 (24751) (2016) 1–16.

[10] S.R. Mouchet, M. Lobet, B. Kolaric, A.M. Kaczmarek, R. Van Deun, P. Vukusic, O. Deparis, E. Van Hooijdonk, Controlled fluorescence in a beetle's photonic structure and its sensitivity to environmentally induced changes, Proc. R. Soc. Lond. B Biol. Sci. 283 (1845) (2016).

[11] J. Marshall, S. Johnsen, Fluorescence as a means of colour signal enhancement, Philos. Trans. R. Soc. Lond. B Biol. Sci. 372 (1724) (2017).

[12] C. Taboada, A.E. Brunetti, F.N. Pedron, F. Carnevale Neto, D.A. Estrin, S.E. Bari, L. B. Chemes, N. Peporine Lopes, M.G. Lagorio, J. Faivovich, Naturally occurring fluorescence in frogs, Proc. Natl. Acad. Sci. USA 114 (14) (2017) 3672–3677.

[13] P. Deschepper, B. Jonckheere, J. Matthys, A light in the dark: the discovery of another fluorescent frog in the Costa Rican rainforests, Wilderness Environ. Med. 29 (3) (2018) 421–422.

[14] S.R. Mouchet, A.M. Kaczmarek, D. Mara, R. Van Deun, P. Vukusic, Colour and fluorescence emission of *Euchroea auripigmenta* beetle, Proc. SPIE 10965 (2019) 72–82.

[15] M. Ladouce, T. Barakat, B.-L. Su, O. Deparis, S.R. Mouchet, Scattering of ultraviolet light by avian eggshells, Faraday Discuss. 223 (2020) 63–80.

[16] M. Ladouce, T. Barakat, B.-L. Su, O. Deparis, S.R. Mouchet, UV scattering by pores in avian eggshells, Proc. SPIE 11481 (2020) 101–109.

[17] M. Mohd Top, C.L. Puan, M.-F. Chuang, S.N. Othman, A. Borzée, First record of ultraviolet fluorescence in the bent-toed gecko *Cyrtodactylus quadrivirgatus* taylor, 1962 (Gekkonidae: Sauria), Herpetol. Notes 13 (2020) 211–212.

[18] A.C. Croce, Light and autofluorescence, multitasking features in living organisms, Photochemistry 1 (2) (2021) 67–124.

[19] L. Reinhold, Mammals with fluorescent fur: observations from the wet tropics, North Queensl. Nat. 51 (2021) 1–8.

[20] S.L.D. Toussaint, J. Ponstein, M. Thoury, R. Métivier, D.C. Kalthoff, B. Habermeyer, R. Guilard, S. Bock, P. Mortensen, S. Sandberg, P. Gueriau, E. Amson, Fur glowing under ultraviolet: *in situ* analysis of porphyrin accumulation in the skin appendages of mammals, Integr. Zool. 0 (2021) 1–12.

[21] S.R. Mouchet, O. Deparis, Natural Photonics and Bioinspiration, Artech House, 2021.

[22] P.R. Stoddart, P.J. Cadusch, T.M. Boyce, R.M. Erasmus, J.D. Comins, Optical properties of chitin: surface-enhanced Raman scattering substrates based on antireflection structures on cicada wings, Nanotechnology 17 (3) (2006) 680.

[23] M. Sun, A. Liang, Y. Zheng, G.S. Watson, J.A. Watson, A study of the anti-reflection efficiency of natural nano-arrays of varying sizes, Bioinspiration Biomimetics 6 (2) (2011), 026003.

[24] L. Dellieu, M. Sarrazin, P. Simonis, O. Deparis, J.-P. Vigneron, A two-in-one superhydrophobic and anti-reflective nanodevice in the grey cicada *Cicada orni* (Hemiptera), J. Appl. Phys. 116 (2) (2014), 024701.

[25] O. Deparis, S.R. Mouchet, L. Dellieu, J.-F. Colomer, M. Sarrazin, Nanostructured surfaces: bioinspiration for transparency, coloration and wettability, Mater. Today Proc. 1S (2014) 122–129.

[26] C. Verstraete, S.R. Mouchet, T. Verbiest, B. Kolaric, Linear and nonlinear optical effects in biophotonic structures using classical and nonclassical light, J. Biophot. (2019), e201800262.

[27] A. Yoshida, M. Motoyama, A. Kosaku, K. Miyamoto, Nanoprotuberance array in the transparent wing of a hawkmoth, *Cephonodes hylas*, Zool. Sci. 13 (4) (1996) 525–526.

[28] A. Yoshida, M. Motoyama, A. Kosaku, K. Miyamoto, Antireflective nanoprotuberance array in the transparent wing of a hawkmoth, *Cephonodes hylas*, Zool. Sci. 14 (5) (1997) 737–741.

[29] A. Yoshida, Antireflection of the butterfly and moth wings through microstructure, Forma 17 (2) (2002) 75–89.

[30] P. Vukusic, J.R. Sambles, Photonic structures in biology, Nature 424 (6950) (2003) 852–855.

[31] I.R. Hooper, P. Vukusic, R.J. Wootton, Detailed optical study of the transparent wing membranes of the dragonfly *Aeshna cyanea*, Opt Express 14 (11) (2006) 4891–4897.

[32] O. Deparis, N. Khuzayim, A. Parker, J.-P. Vigneron, Assessment of the antireflection property of moth wings by three-dimensional transfer-matrix optical simulations, Phys. Rev. E 79 (2009), 041910.

[33] D.G. Stavenga, Thin film and multilayer optics cause structural colors of many insects and birds, Mater. Today Proc. 1S (2014) 109–121.

[34] R. Siddique, G. Gomard, H. Hölscher, The role of random nanostructures for the omnidirectional anti-reflection properties of the glasswing butterfly, Nat. Commun. 6 (2015) 6909.

[35] S.R. Mouchet, C. Verstraete, D. Mara, S.V. Cleuvenbergen, E.D. Finlayson, R. Van Deun, O. Deparis, T. Verbiest, B. Maes, P. Vukusic, B. Kolaric, Nonlinear optical spectroscopy and two-photon excited fluorescence spectroscopy reveal the excited states of fluorophores embedded in a beetle's elytra, Interface Focus 9 (1) (2019), 20180242.

[36] C.G. Bernhard, The insect corneal nipple array. a biological, broad-band impedance transformer that acts as an antireflection coating, Acta Physiol. Scand. 63 (243) (1965) 1–79.

[37] D.G. Stavenga, S. Foletti, G. Palasantzas, K. Arikawa, Light on the moth-eye corneal nipple array of butterflies, Proc. R. Soc. Lond. B Biol. Sci. 273 (1587) (2006) 661–667.

[38] G. Xie, G. Zhang, F. Lin, J. Zhang, Z. Liu, S. Mu, The fabrication of subwavelength anti-reflective nanostructures using a bio-template, Nanotechnology 19 (9) (2008), 095605.

[39] Z. Han, Z. Wang, X. Feng, B. Li, Z. Mu, J. Zhang, S. Niun, L. Ren, Antireflective surface inspired from biology: a review, Biosurf. Biotribol. 2 (2016) 137–150.

[40] I. Zada, W. Zhang, P. Sun, M. Imtiaz, W. Abbas, D. Zhang, Multifunctional, angle dependent antireflection, and hydrophilic properties of SiO$_2$ inspired by nano-scale structures of cicada wings, Appl. Phys. Lett. 111 (15) (2017), 153701.

[41] G. Zhang, J. Zhang, G. Xie, Z. Liu, H. Shao, Cicada wings: a stamp from nature for nanoimprint lithography, Small 2 (12) (2006) 1440–1443.

[42] M. Sun, G.S. Watson, Y. Zheng, J.A. Watson, A. Liang, Wetting properties on nanostructured surfaces of cicada wings, J. Exp. Biol. 212 (19) (2009) 3148–3155.

[43] K.M. Wisdom, J.A. Watson, X. Qu, F. Liu, G.S. Watson, C.-H. Chen, Self-cleaning of superhydrophobic surfaces by self-propelled jumping condensate, Proc. Natl. Acad. Sci. USA 110 (20) (2013) 7992–7997.

[44] J. Román-Kustas, J.B. Hoffman, J.H. Reed, A.E. Gonsalves, J. Oh, L. Li, S. Hong, K. D. Jo, C.E. Dana, N. Miljkovic, D.M. Cropek, M. Alleyne, Molecular and topographical organization: influence on cicada wing wettability and bactericidal properties, Adv. Mater. Interfac. 7 (10) (2020), 2000112.

[45] E.P. Ivanova, J. Hasan, H.K. Webb, V.K. Truong, G.S. Watson, J.A. Watson, V. A. Baulin, S. Pogodin, J.Y. Wang, M.J. Tobin, C. Löbbe, R.J. Crawford, Natural bactericidal surfaces: mechanical rupture of *Pseudomonas aeruginosa* cells by cicada wings, Small 8 (16) (2012) 2489–2494.

[46] E.P. Ivanova, J. Hasan, H.K. Webb, G. Gervinskas, S. Juodkazis, V.K. Truong, A. H. Wu, R.N. Lamb, V.A. Baulin, G.S. Watson, J.A. Watson, D.E. Mainwaring, R. J. Crawford, Bactericidal activity of black silicon, Nat. Commun. 4 (2013) 2838.

[47] T. Diu, N. Faruqui, T. Sjöström, B. Lamarre, H.F. Jenkinson, B. Su, M.G. Ryadnov, Cicada-inspired cell-instructive nanopatterned arrays, Sci. Rep. 4 (2014) 7122.

[48] S.M. Kelleher, O. Habimana, J. Lawler, B. O'Reilly, S. Daniels, E. Casey, A. Cowley, Cicada wing surface topography: an investigation into the bactericidal properties of nanostructural features, ACS Appl. Mater. Interfaces 8 (24) (2016) 14966–14974.

[49] E. Cockayne, I. The distribution of fluorescent pigments in Lepidoptera, Trans. R. Entomol. Soc. Lond. 72 (1–2) (1924) 1–19.

[50] K. Kumazawa, S. Tanaka, K. Negita, H. Tabata, Fluorescence from wing of *Morpho sulkowskyi* butterfly, Jpn. J. Appl. Phys. 33 (1;4A) (1994) 2119–2122.

[51] T.M. Trzeciak, B.D. Wilts, D.G. Stavenga, P. Vukusic, Variable multilayer reflection together with long-pass filtering pigment determines the wing coloration of papilionid butterflies of the *nireus* group, Opt. Express 20 (8) (2012) 8877–8890.

[52] B.D. Wilts, T.M. Trzeciak, P. Vukusic, D.G. Stavenga, Papiliochrome II pigment reduces the angle dependency of structural wing colouration in *nireus* group papilionids, J. Exp. Biol. 215 (5) (2012) 796–805.

[53] J.-P. Vigneron, K. Kertész, Z. Vértesy, M. Rassart, V. Lousse, Z. Bálint, L.P. Biró, Correlated diffraction and fluorescence in the backscattering iridescence of the male butterfly *Troides magellanus* (Papilionidae), Phys. Rev. E 78 (2008), 021903.

[54] E. Van Hooijdonk, C. Barthou, J.-P. Vigneron, S. Berthier, Detailed experimental analysis of the structural fluorescence in the butterfly *Morpho sulkowskyi* (Nymphalidae), J. Nanophotonics 5 (1) (2011), 053525.

[55] E. Van Hooijdonk, C. Barthou, J.-P. Vigneron, S. Berthier, Angular dependence of structural fluorescent emission from the scales of the male butterfly *Troïdes magellanus* (Papilionidae), J. Opt. Soc. Am. B 29 (5) (2012) 1104–1111.

[56] S.N. Gorb, Serial elastic elements in the damselfly wing: mobile vein joints contain resilin, Naturwissenschaften 86 (11) (1999) 552–555.

[57] E. Appel, S.N. Gorb, Resilin-bearing wing vein joints in the dragonfly *Epiophlebia superstes*, Bioinspiration Biomimetics 6 (4) (2011), 046006.

[58] E. Appel, L. Heepe, C.-P. Lin, S.N. Gorb, Ultrastructure of dragonfly wing veins: composite structure of fibrous material supplemented by resilin, J. Anat. 227 (4) (2015) 561–582.

[59] C.-J. Chuang, C.-D. Liu, R.A. Patil, C.-C. Wu, Y.-C. Chang, C.-W. Peng, T.-K. Chao, J.-W. Liou, Y. Liou, Y.-R. Ma, Impact of cuticle photoluminescence on the color morphism of a male damselfly *Ischnura senegalensis* (Rambur, 1842), Sci. Rep. 6 (2016), 38051.

[60] C.M. Elvin, A.G. Carr, M.G. Huson, J.M. Maxwell, R.D. Pearson, T. Vuocolo, N. E. Liyou, D.C.C. Wong, D.J. Merritt, N.E. Dixon, Synthesis and properties of crosslinked recombinant pro-resilin, Nature 437 (2005) 999–1002.

[61] M. Burrows, S.R. Shaw, G.P. Sutton, Resilin and chitinous cuticle form a composite structure for energy storage in jumping by froghopper insects, BMC Biol. 6 (41) (2008) 1–16.

[62] R. Guillermo-Ferreira, E.M. Therézio, M.H. Gehlen, P.C. Bispo, A. Marletta, The role of wing pigmentation, UV and fluorescence as signals in a neotropical damselfly, J. Insect Behav. 27 (1) (2014) 67–80.

[63] A.R. Spurr, A low-viscosity epoxy resin embedding medium for electron microscopy, J. Ultra. Res. 26 (1) (1969) 31–43.

[64] J.D. Gullion, T. Gullion, Solid-state NMR study of the cicada wing, J. Phys. Chem. B 121 (32) (2017) 7646–7651.

[65] T.A.P. Hai, R. Sugimoto, Fluorescence control of chitin and chitosan fabricated via surface functionalization using direct oxidative polymerization, RSC Adv. 8 (2018) 7005–7013.

[66] D.E. Azofeifa, H.J. Arguedas, W.E. Vargas, Optical properties of chitin and chitosan biopolymers with application to structural color analysis, Opt. Mater. 35 (2012) 175–183.

[67] S.O. Andersen, Characterization of a new type of cross-linkage in resilin, a rubber-like protein, Biochim. Biophys. Acta 69 (1963) 249–262.

[68] J. Lakowicz, Principles of Fluorescence Spectroscopy, Kluwer Academic/Plenum Publishers, New York, NY, 1999.

[69] C. Ramanan, C. Hoon Kim, T.J. Marks, M.R. Wasielewski, Excitation energy transfer within covalent tetrahedral perylenediimide tetramers and their intermolecular aggregates, J. Phys. Chem. C 118 (2014) 16941–16950.

[70] B. Kolaric, R.A.L. Vallée, Dynamics and stability of DNA mechano-nanostructures: energy-transfer investigations, J. Phys. Chem. C 114 (3) (2010) 1430–1435.

[71] M.D. Rabasović, D.V. Pantelić, B.M. Jelenković, S.B. Ćurčić, M.S. Rabasović, M. D. Vrbica, V.M. Lazović, B.P. Ćurčić, A.J. Krmpot, Nonlinear microscopy of chitin and chitinous structures: a case study of two cave-dwelling insects, J. Biomed. Opt. 20 (1) (2015), 016010.

[72] T. Verbiest, K. Clays, V. Rodriguez, Second-order Nonlinear Optical Characterization Techniques: an Introduction, CRC press, 2009.

[73] D. Peitsch, A. Fietz, H. Hertel, J. de Souza, D.F. Ventura, R. Menzel, The spectral input systems of hymenopteran insects and their receptor-based colour vision, J. Comp. Physiol. 170 (1) (1992) 23–40.

[74] D.G. Stavenga, Colour in the eyes of insects, J. Comp. Physiol. 188 (5) (2002) 337–348.

[75] D.G. Stavenga, Surface colors of insects: wings and eyes, in: Functional Surfaces in Biology: Little Structures with Big Effects, 1, Springer Netherlands, Dordrecht, 2009, pp. 285–306.

[76] K. Lunau, Visual ecology of flies with particular reference to colour vision and colour preferences, J. Comp. Physiol. 200 (6) (2014) 497–512.

[77] J. Moan, Visible light and UV radiation, in: A. Brune, R. Hellborg, B. Persson, R. Pääkkönen (Eds.), Radiation at Home, Outdoors and in the Workplace, Oslo), Scandinavian Science Publisher, 2001, pp. 69–85.

Perspective

Bioinspired NEMS—Prospective of Collaboration with Nature

Marina Simovic-Pavlovic [1,2,*], **Bojana Bokic** [1] , **Darko Vasiljevic** [1] and **Branko Kolaric** [1,3,*]

1. Photonics Center, Institute of Physics, University of Belgrade, Pregrevica 118, 11000 Belgrade, Serbia; bojana@ipb.ac.rs (B.B.); darko@ipb.ac.rs (D.V.)
2. Faculty of Mechanical Engineering, University of Belgrade, Kraljice Marije 16, 11000 Belgrade, Serbia
3. Micro- and Nanophotonic Material Group, Department of Physics, University of Mons, Place du Parc 20, 7000 Mons, Belgium
* Correspondence: simovicmarina99@gmail.com (M.S.-P.); branko.kolaric@umons.ac.be (B.K.); Tel.: +381-604273777 (M.S.-P.)

Abstract: The fields of micro- and nanomechanics are strongly interconnected with the development of micro-electro-mechanical (MEMS) and nano-electro-mechanical (NEMS) devices, their fabrication and applications. This article highlights the biomimetic concept of designing new nanodevices for advanced materials and sensing applications.

Keywords: NEMS; bio photonics; biomimetics; bioinspiration; nanotechnology

1. Introduction

Nowadays, technology of any kind is faced with the constant need to minimalize gauges as an imperative for lowering the energy consumption and reduction in materials utilization. The most contributing aspect in this technological revolution is science. By emulating nature's patterns, science seeks sustainable solutions for everyday human challenges. It is vital to harness biomimetic concepts to develop advanced bio-inspired devices for various applications. This article describes the potentials of biomimetic concepts for the design of future nanodevices, especially NEMS, which could have a plethora of potential applications. A practical representation of the order of magnitude of nano devices is given in Figure 1.

After a short introduction, we discuss the state-of-the-art bioinspired NEMS from a fundamental and design perspective, especially highlighting bio-oriented applications. We hope that this article will increase the awareness of the engineering community for biomimetics and highlight biomimetic-inspired concepts and solutions.
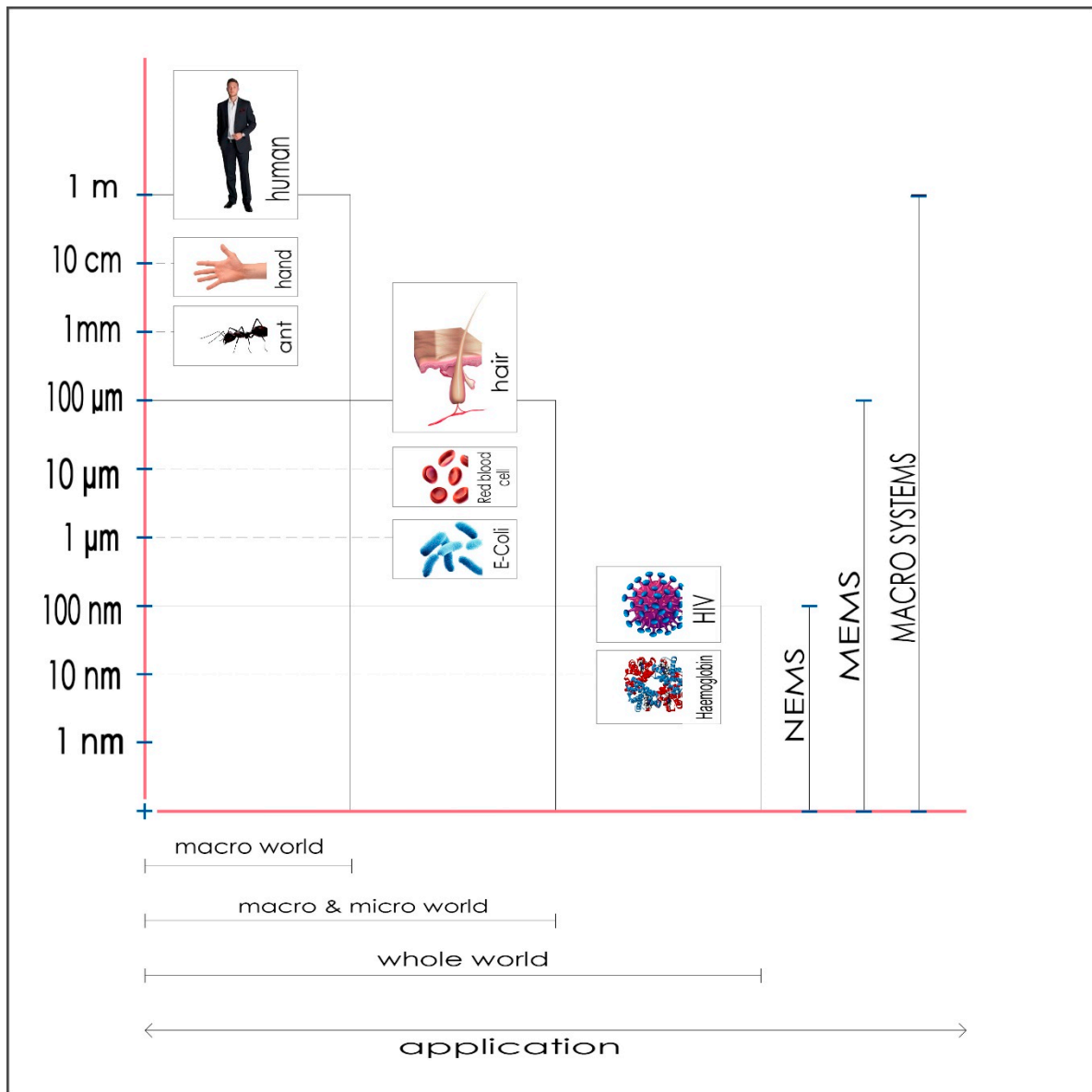
Figure 1. Different scales in nature.

2. The Emergence of Bioinspired NEMS

Bioinspired devices are nanodevices with structure and functions designed to mimic examples from the natural world. Biomimetics is based on mimicking biological principals and patterns as a recipe for creating new materials and structures and integrating them into functional devices. The functionality of these devices also relies on the combined power of optics and nanoengineering. Figure 2 shows the synergy between nanoengineering, optics and biomimetics, which creates the new field of bioinspired NEMS.
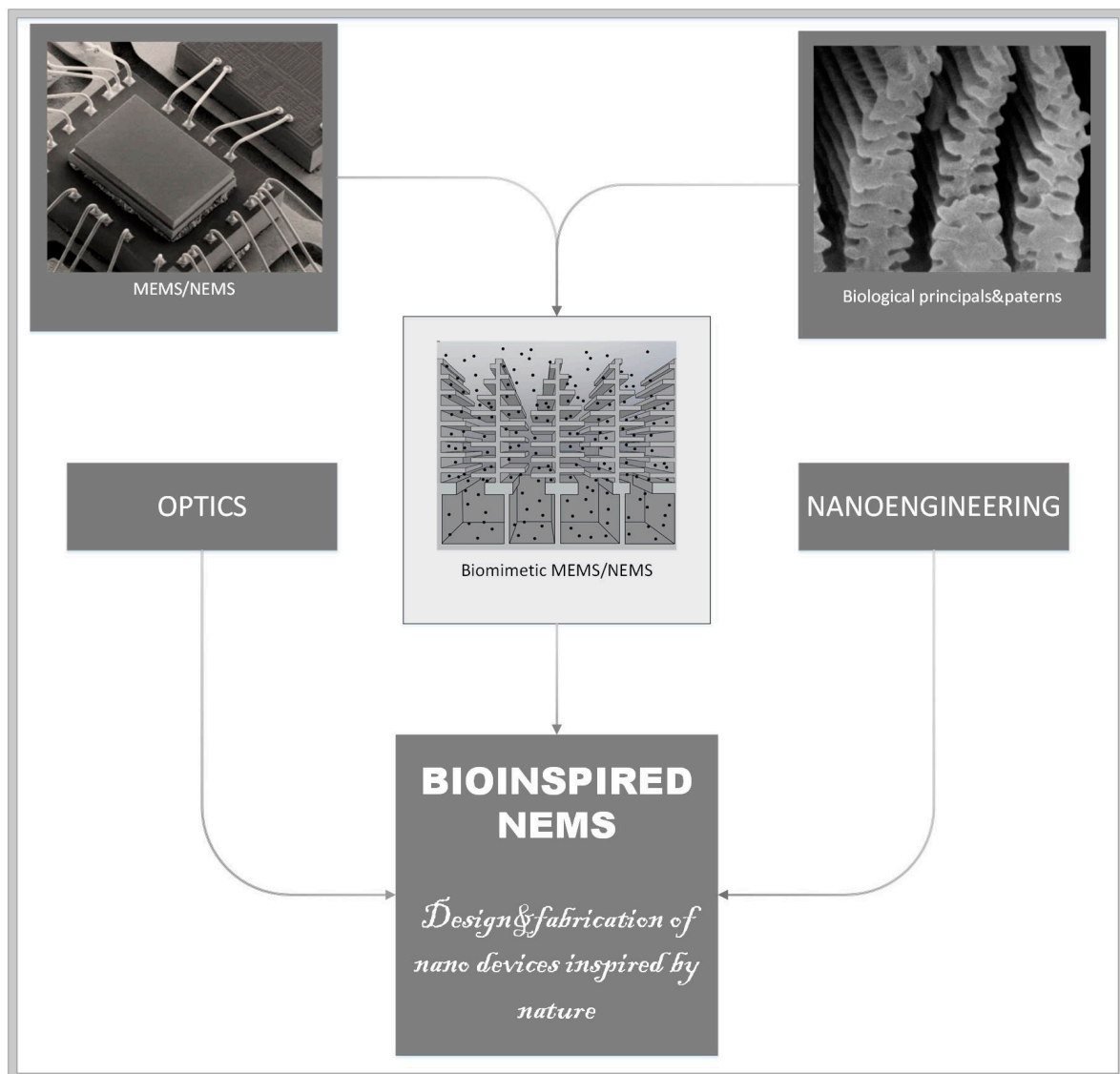
Figure 2. NEMS–Synergy of different technical approaches.

Devices inspired by nature can be classified into two categories: (1) devices that incorporate natural biological structures within their systems and (2) biomimetic (bioinspired) devices that mimic structures and functions from the natural world.

The primary aim of this paper is to attract the interest of the broad material science community towards the bioinspired NEMS concept, which could be used to open new horizons in physical and material research. The authors of this article are confident that soon, in order to reach a cellular economy-driven society, we must develop technology that will be able to harness perfect engineering solutions designed by billions of years of evolution. For this approach to succeed, we must understand the complexity of the biological functions and patterns and their interconnections.

Biomimetics, to begin with [1–3], has a great potential for solving human problems by imitating the natural environment or learning from it. For example, an extensive review of bioinspired triboelectric nanogenerators includes a comparative analysis of structures and materials that draw inspiration from nature [4]. Additionally, a comprehensive review of nanomembranes and their application can be found in MDPI papers [5].

3. Fabrication of Bioinspired NEMS

Most of techniques for the fabrication of bioinspired NEMS use the lithographic method (Figure 3), which proved very suitable for processing nanoelements [6].
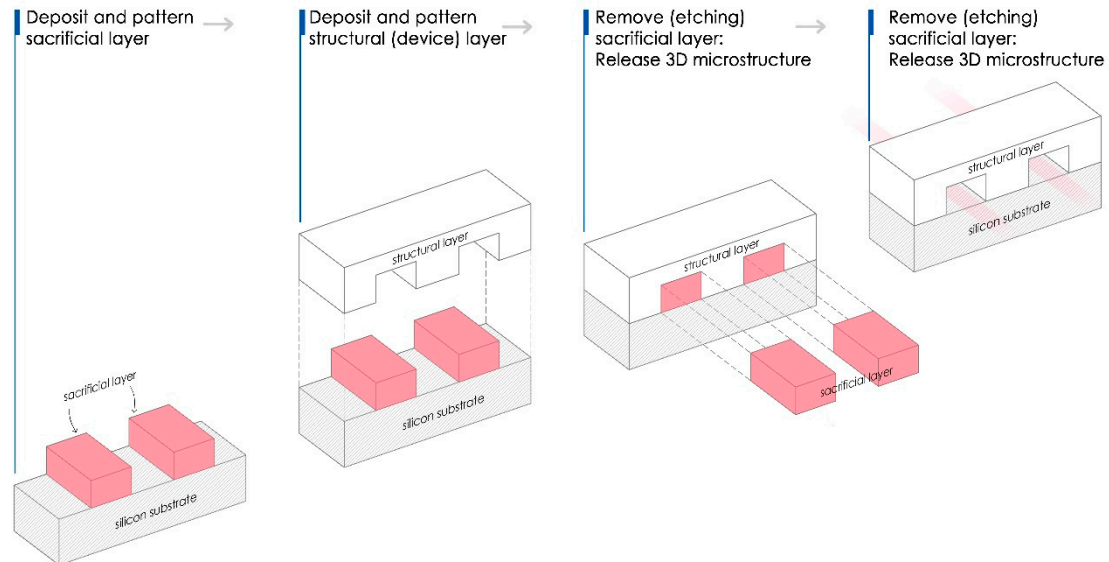

Figure 3. Simplified scheme of a lithography process.

Fabrication of Bioinspired Nano-Structures

Recently, the additive engineering, i.e., 3D printing [7], is used for NEMS fabrication [8].

The future of bioNEMS technology is strongly connected with the development of new fabrication techniques (3D printing, self-assembly, etc.) and opens up many possibilities for potential applications in various fields, such as photonics, biomedicine, nanoelectronics, and sensing.

Micro molding is one of the most widely used techniques. The fabrication of replicas that perfectly match biostructure geometry is an enormous challenge for NEMS fabrication. The most straightforward technique used for replication consists of two-step process.

The development of a negative mold from a biopattern is the first step, and the second is making the positive replica. Kumar et al. [9] presents a precise micro-replication technique, as shown in Figure 4, to transfer surface microstructures of plant leaves onto a highly transparent, soft polymer material to design smooth surfaces with specific nano-corrugation. Structuring surfaces is beneficial for designing materials with controllable properties such as wetting, heat transfer, fluid flow, optical effects, etc.
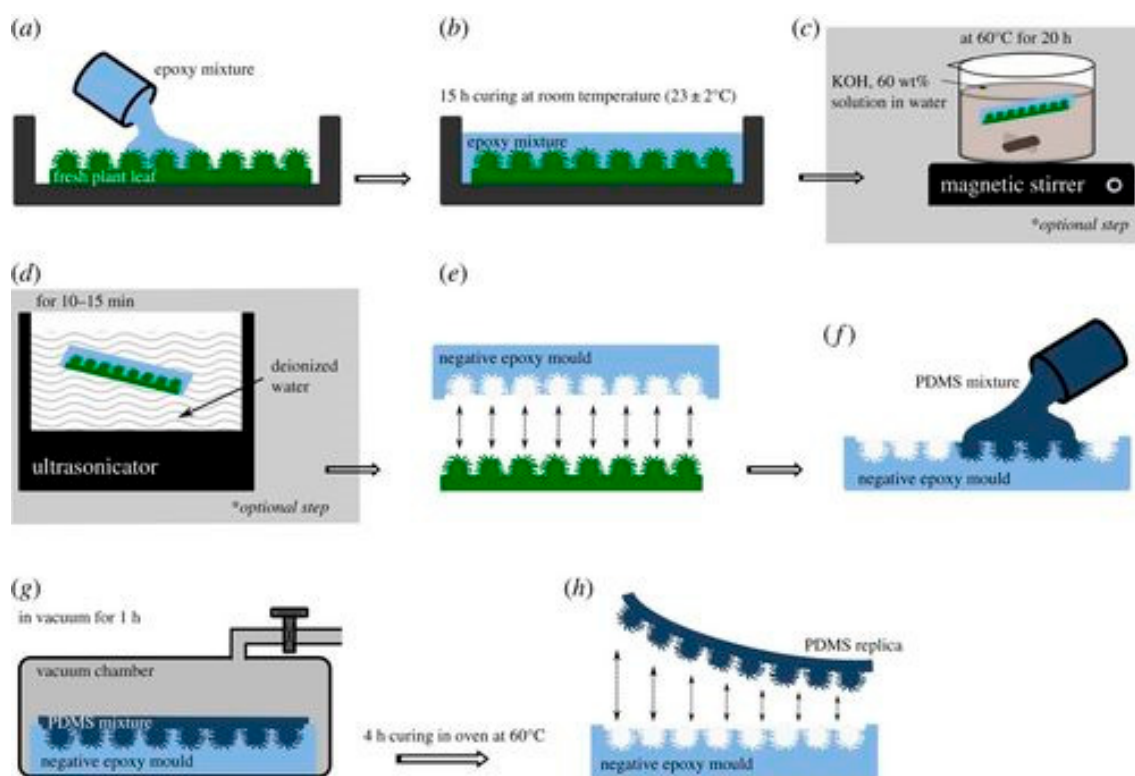
Figure 4. Schematic sketch of the two-step replication process: (**a**) Fresh plant leaf glued on a plastic Petri dish, filled up with epoxy resin. (**b**) Curing of epoxy mixture for 15 h to produce negative epoxy mould. (**c**) Epoxy sample (which adhered with leaf surface) is kept for chemical treatment in potassium hydroxide solution on magnetic stirrer (at $60 \pm 3\ ^{\circ}$C for 20 h). (**d**) Chemically treated sample washed in deionized water using an ultrasonicator. (**e**) Negative epoxy mould separated from the leaf surface. (**f**) Negative epoxy mould filled up with PDMS mixture. (**g**) Degassed in vacuum chamber to remove air trapped at the interface. (**h**) PDMS-positive replica peeled off from the epoxy mould. Reproduced with permission [9].

The unification of biostructures and nanosystems requires simple but reliable tools and techniques. The limited knowledge regarding materials leave us with just a few types of micro- and nanodevices. Modern technologies such as nanopatterning provide an excellent potential to obtain a new class of customized energetic materials for MEMS/NEMS application [10]. These materials allow advances in the processing of microscopic systems that are energy-demanding and may be even more important for bioinspired NEMS. An even more fascinating proposal is based on the utilization of so-called Pavlovian materials [11]. These materials are specially adapted to respond to certain stimuli, and they are proposed for application in integrated devices. As far as materials science is concerned, the inevitable dominance of bioinspired materials in technological applications will happen soon [12].

Recently, Shanker et al. designed melanin nanoparticles for new printable inks with a high boiling point to manage stable jetting and a high-printing efficiency [13]. The advantages of inkjet printing are mainly the reduction in processing times and materials requirement. An even more interesting example of nanofabrication is presented through the method of roll-to-plate (R2P) ultraviolet nanoimprint lithography (UV-NIL). This method uses the combined power of Nickel mold and transparent polycarbonate substrates [14]. The operation simplicity, high efficiency and low-cost fabrication make this antireflection technique promising. The imprint of nanostructures is also described elsewhere [15].

4. Bioinspired NEMS—The State of the Art

Here, we present a few exciting applications based on mimics of natural structures.

4.1. Hair-like Structures

Structures that resemble the hair are widespread in the living world. In biology, organisms often use these body parts to communicate with the environment [16]. Regarding the relatively simple shape of the hair, functional devices that mimic hair structures are constructed with the capability to mold mechanical responses as a function of the slightest changes in their environment. Inspired by the clavate hair-based sensory system used by crickets to sense gravitational acceleration and obtain information on their orientation, a one-axis-biomimetic accelerometer was developed and fabricated using different micro-machining processes [17,18]. Clavate hair is a receptor that is most sensitive to positional changes, while in practical terms, it can be seen as a pendulum subjected to external influences or accelerations from the environment. Staring at the halters of flies that serve to maintain balance based on Coriolis forces, a biomimetic gyroscope was made with the help of MEMS technology [19]. These are tiny organs by which flies sense the rotation of the body, practically opposing the orientation of wings during flight. The oblong extensions that are an integral part of most hair cells receive an external impulse and generate displacement to neurons as a mechanical response. The remarkable abilities of the fish and many sophisticated functions of their organs have led to the development of micro-biomimetic sensors made of artificial materials that resemble hair cells in shape and dimensions [20]. Practically, and in the physiological sense, sensory units are distributed throughout the body of the fish. These units receive flow rate information and convert it to electrical signals that pass through the innervated fibers directly to the brain for further processing. In the end, there are plenty of attractive models from nature to mimic, that could be used for the design of new functional devices.

4.2. BioMEMS: Medical Perspective

A significant subset of MEMS/NEMS devices is biomedical MEMS/NEMS or bioMEMS /bioNEMS. BioMEMS/BioNEMS refers to devices developed for biomedical and medical applications [21]. The potential for the applications of MEMS/NEMS in medicine is practically unlimited [22–24]. Scuor et al. [22] described a new appliance as MEMS-based in-plane biaxial cell stretcher used to study the influences of biaxial stresses on an individual living cell. By exploiting stretchable tools of the described device, the authors [22] recorded a displacement of several micrometers. Using this MEMS approach, it is possible at the same time to actuate and sense at a length scale comparable with single cells. In combination with biological microscopy techniques such as fluorescence, it is possible to visualize the effect of the stress. Parallel with Scuor research, Wang et al. [23] described the new micro-fabrication method for designing micro and nanosize artificial biocompatible capillaries.

Additionally, Tsuda et al. [24] observed a large multi-nuclear, single-cellular organism with no nervous system. The objective of his research was to make an integrated local sensor system that relies on intercellular information exchange. In search of an alternative to control and monitor the functioning of autonomous robots, Tsuda developed a system that works for an extended period without a power supply. This bio-hybrid creation is based on circuitry from amoeboid plasmodia of the slime mold, Physarum polycephalum. The circuits are connected to a hexapod robot that drives the system and exchanges information with the environment.

Soft robotics is an example of a field that has great potential for applications in medicine. Recently Kim et al. [25] developed an artificial micro-muscle fiber crafted from coiled shape–memory alloy (NiTi) springs.

4.3. The Last Decade—an Age of Great Promise

Ten years ago, an exciting moment occurred in materials science. The ability of all complex biological organisms to self-repair minor damages [26] was described, as well as the prospect of mimicking this feature in nanodevices.

"We continually learn things and borrow ideas from nature, but we design devices beyond nature" [27]. This beautiful, harmonious quote as well as the whole book by Di

Zhang [27] represents a useful and exciting introduction to biomimetics. During this period, one gets the impression that thinking begins with a look at biomimetics; biomimetics finally gains its true meaning and becomes officially recognized.

Bioinspired NEMS can play a crucial role in curing or preventing disease. There are currently many NEMS applications in biology and biomedicine, and thus many articles in this field [28,29].

An example of such an application is a silicon micro-channel, used to provide an improved blood plasma separation from whole blood by acoustophoresis. Karthick et al. [30] harnessed the theory of acoustophoresis of dense suspension to understand the acoustic focusing of cells within blood capillaries. Such works are not only inspiring but also have promising applications.

A new lab-on-a-chip (LOC) technology is a kind of bioinspired nano system, recently described elsewhere [31–33]. It is a device that integrates one or several laboratory functions on a single integrated circuit. LOC can be defined as a subset of complex MEMS/NEMS devices. LOC is designed as a sensor capable of detecting different chemicals in bodily fluids and providing information about the current health condition. Currently, many MEMS are customized and programmed within LOC devices for various sensing applications. However, the ultimate goal is to detect any health issue without using expensive techniques and to stop the disease before it progresses. The potential uses of LOC in medicine and health application are unlimited. Recently, the *New York Post* highlighted LOC technology for non-specialists [33].

An exceptional example is a prototype of a 3D-printed artificial lung [34]. In brief, lungs are a mechanical sensor that reacts to the external effects, which is analogous to microsystems. Potkay [34] foresaw this product for short- and long-term respiratory support. In the beginning, it was used as a temporary measure while waiting for transplantation or another healing process, but it could become a permanent solution in the future. Although it does not look like an original organ overall, the structure is perfectly imitated. Thanks to the flexibility enabled by 3D printing, the variation in dimensions and shape is a huge advantage and a step towards new possibilities. Biomimicry is a constant inspiration to researchers and engineers, and now with new 3D technology, better production possibilities are affordable.

The successful replication of organ functions by natural materials, or biocompatible materials, represents the future of medical technology [35]. The possibility of replacing the lung is mind-blowing, with the potential to drastically change many patients' lives.

Aside from that, You et al. [28] studied a self-organization of sessile bacteria within a controlled and closed environment. The ability of bacteria to sense the environment and its gradients and to adjust their movements to them, in combination with the hydrodynamic properties, has a significant impact on the bacterial colonization and management of nutrient resources [29] and could have a substantial impact on understanding complex ecological interactions.

Finally, the MEMS/NEMS applications reach the realm of pharmacy. The main challenge in pharmaceutical analytics is to find a fast and accurate test for sensing in the nano domain at a single-molecule or -particle level. Recently the PMTA method (Particle Mechanical Thermal Analyses) [36] was developed and uses a single particle as a resonator to determine changes in their mechanical properties. The PMTA opens the possibility of the characterization of materials at the single-particle level, which is crucial for developing future nano medicine devices. This achievement represents a remarkable advancement in pharmaceutical science. In recent years, various nanosystems targeting the drug delivery of different anticancer drugs were proposed and based on biomimetic approaches [37].

5. Biomimetics Meets Photonics and Nanomechanics

Recently, Pris et al. [38] and Zhang et al. [39] showed an interesting usage of biostructures. In their papers, the unique example of the management of thermal radiation by biophotonic structures of a *Morpho* butterfly is described. Additionally, the research described

by Grujic et al. [40], pointed out the exciting mechanisms of thermophoresis/photophoresis within biophotonic structures, which could be harnessed for thermal radiation detection. Grujic et al. shows that, in the case of the *Morpho* butterfly, nature exploited natural photonic structures and their optical properties to develop IR detectors much more advanced than currently fabricated ones. Grujic et al.'s [40] experiment revealed a complex functional relationship between biological patterns and their functions. By imitating butterfly wing scales by polymer or composite materials, the thermophoretic effect can be further amplified for different sensing applications and the large-scale production of sensing devices. Polymers are particularly promising materials for infrared sensing applications because of their high IR absorption due to their organic bonds' vibrational resonance modes and their high thermal expansion coefficient compared to metals and semiconductors [41]. Figure 5 shows a portion of a circular section of a sample, the microscopic image, and a holographic image of the investigated butterfly's wing, accompanied with holographic reconstruction.
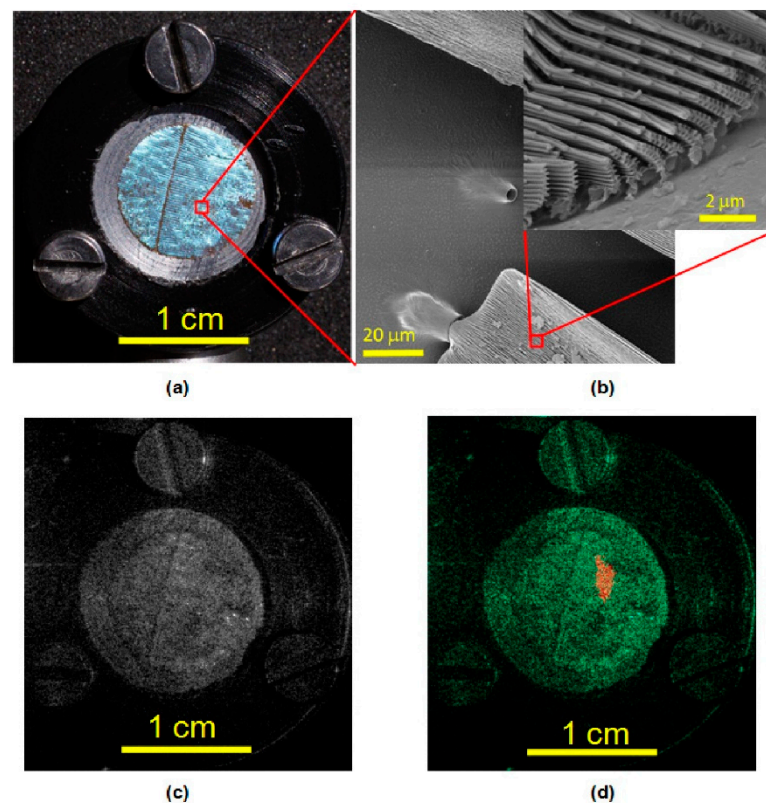

Figure 5. Circular section of a butterfly's wing: (**a**) A photograph, (**b**) a microscope image, (**c**) a hologram reconstruction and (**d**) a holographic image. Reproduced with permission [40].

In the end, to advance in nanoscience and biomimetics, it is imperative to understand the physics of the studied systems. When the microscale is reached, for example, when the distance between two structures or surfaces corresponds to the molecule-free path, thermal forces can occur [42]. Due to the temperature gradient, the surrounding gas causes the formation of a force that creates mechanical displacement at the microscale level. This phenomenon is called thermophoresis. These forces are mechanical forces that scale almost linearly with pressure and temperature. In their paper, Passian et al. [43] described the study of the pressure dependence of Knudsen forces by exploiting MEMS devices.

Moreover, when downscaling from the MEMS to NEMS level, forces between system elements cannot be described by using a classical physics framework. The quantum effect must be considered and controlled, which is one of the most challenging tasks for the development and applications of future NEMS. Figure 6 shows the cartoon image of "strangeness" of quantum mechanics [44].
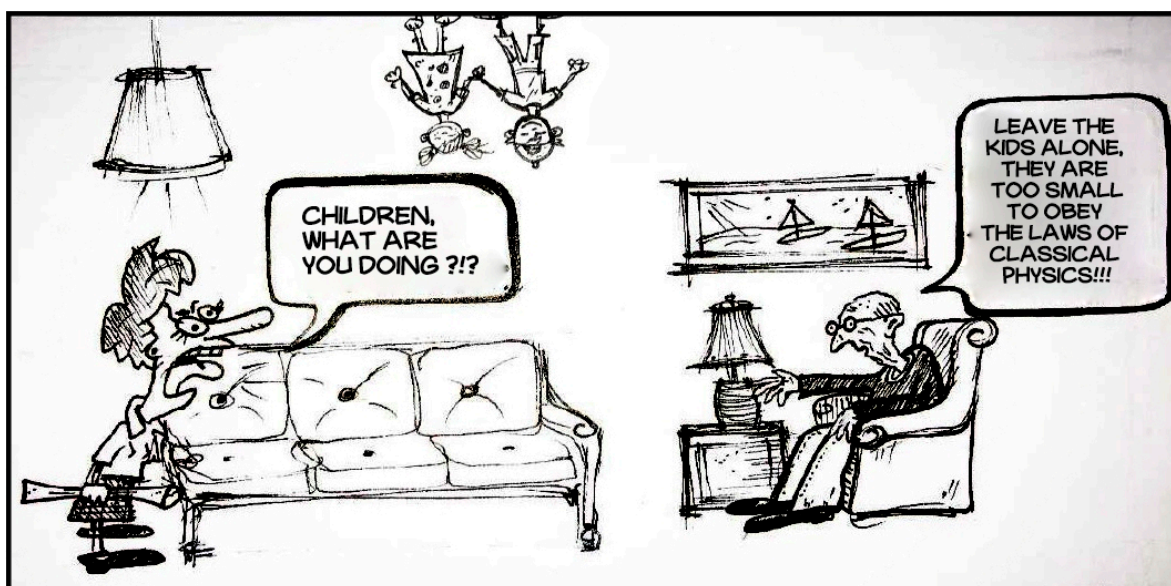
Figure 6. Cartoon sketch of the limitations of classical physics and "strangeness" of quantum mechanics.

6. Conclusions

The possibility of harnessing biomimetics for the design of advanced NEMS devices is highlighted in this account. The topic discussed here is interesting from a fundamental perspective, with practically unlimited applications in the areas of photonics, sensing, and biomedicine. Even though, at the moment, bioinspired NEMS is still in its infant stage of development, the primary aim of this article is to attract the interest of the broad material and photonics science community for the biomimetic concept, which could open new horizons in material research.

References

1. Driessen-Mol, A. Biomimetics: A Molecular Perspective. *Green Processing Synth.* **2013**, *2*, 527. [CrossRef]
2. Zheng, X.; Kamot, A.M.; Cao, M.; Kottapalli, A.G.P. Creating underwater vision through wavy whiskers: A review of the flow-sensing mechanisms and biomimetic potential of seal whiskers. *J. R. Soc. Interface* **2021**, *18*, 20210629. [CrossRef]
3. Stenvinkel, P.; Painer, J.; Johnson, R.J.; Natterson-Horowitz, B. Biomimetics—Nature's roadmap to insights and solutions for burden of lifestyle diseases. *Rev. Simp.* **2020**, *287*, 238–251. [CrossRef]
4. Li, W.; Pei, Y.; Zhang, C.; Kottapalli, A.G.P. Bioinspired designs and biomimetic applications of triboelectric nanogenerators. *Nano Energy* **2021**, *84*, 105865. [CrossRef]

5.　Jakšić, Z.; Jakšić, O. Biomimetic nanomembranes: An overview. *Biomimetics* **2020**, *5*, 24. [CrossRef] [PubMed]

6.　Liu, L.; Sun, L.; Qi, L.; Guo, R.; Li, K.; Yin, Z.; Wu, D.; Zou, H. A low-cost fabrication method of nanostructures by ultraviolet proximity exposing lithography. *AIP Adv.* **2020**, *10*, 045221. [CrossRef]

7.　Duda, T.; Raghavan, L.V. 3D Metal Printing Technology. *IFAC-PapersOnLine* **2016**, *49*, 103–110. [CrossRef]

8.　Chen, Y.P.; Yang, M.D. Micro-Scale Manufacture of 3D Printing. *Appl. Mech. Mater.* **2014**, *670*, 936–941. [CrossRef]

9.　Kumar, C.; Le Houerou, V.; Speck, T.; Bohn, H.F. Straightforward and precise approach to replicate complex hierarchical structures from plant surfaces onto soft matter polymer. *R. Soc. Open Sci.* **2018**, *5*, 172132. [CrossRef]

10.　Rossi, C.; Zhang, K.; Esteve, D.; Alphonse, P.; Tailhades, P.; Vahlas, C. Nanoenergetic materials for MEMS: A review. *J. Microelectromech. Syst.* **2007**, *16*, 919–931. [CrossRef]

11.　Zhang, H.; Zeng, H.; Priimagi, A.; Ikkala, O. Pavlovian materials—Functional biomimetics inspired by classical conditioning. *Adv. Mater.* **2020**, *32*, 1906619. [CrossRef] [PubMed]

12.　Wang, Y.; Naleway, S.E.; Wang, B. Biological and bioinspired materials: Structure leading to functional and mechanical performance. *Bioact. Mater.* **2020**, *5*, 745–757. [CrossRef] [PubMed]

13.　Shanker, R.; Sardar, S.; Chen, S.; Gamage, S.; Rossi, S.; Jonsson, M.P. Noniridescent biomimetic photonic microdoms by inkjet printing. *Nano Lett.* **2020**, *20*, 7243–7250. [CrossRef]

14.　Sun, J.; Wang, X.; Wu, J.; Jiang, C.; Shen, J.; Cooper, M.A.; Wu, D. Biomimetic moth-eye nanofabrication: Enhanced antireflection with superior self-cleaning characteristic. *Sci. Rep.* **2018**, *8*, 1–10. [CrossRef]

15.　Chou, S.Y.; Krauss, P.R.; Renstrom, P.J. Imprint of sub-25 nm vias and trenches in polymers. *Appl. Phys. Lett.* **1995**, *67*, 3114–3116. [CrossRef]

16.　Seale, M.; Cummins, C.; Viola, I.M.; Mastropaolo, E.; Nakayama, N. Design principles of hair-like structures as biological machines. *J. R. Soc. Interface* **2018**, *15*, 20180206. [CrossRef]

17.　Droogendijk, H.; De Boer, M.J.; Sanders, R.G.P.; Krijnen, G.J.M. A biomimetic accelerometer inspired by the cricket's calvate hair. *J. R. Soc. Interface* **2014**, *11*, 20140438. [CrossRef]

18.　Sakaguchi, D.S.; Murphy, R.K. The equilibrium detecting system of the cricket: Physiology and morphology of an identified interneuron. *J. Comp. Physiol.* **1983**, *150*, 141–152. [CrossRef]

19.　Droogendijk, H.; Brookhuis, R.A.; De Boer, M.J.; Sanders, R.G.P.; Krijnen, G.J.M. Towards a biomimetic gyroscope inspired by the fly's haltere using microelectromechanical systems technology. *J. R. Soc. Interface* **2014**, *11*, 20140573. [CrossRef]

20.　Asadnia, M.; Kottapalli, A.G.P.; Miao, J.; Warkiani, M.E.; Triantafyllou, M.S. Artificial fish skin of self-powered microelectromechanical systems hair cells for sensing hydrodynamic flow phenomena. *J. R. Soc. Interface* **2015**, *12*, 20150322. [CrossRef]

21.　Folch, A. *Introduction to bioMEMS*; CRC Press: Boca Raton, FL, USA, 2016.

22.　Scuor, N.; Gallina, P.; Panchawagh, H.V.; Mahajan, R.L.; Sbaizero, O.; Sergo, V. Design of a novel MEMS platform for the biaxial stimulation of living cells. *Biomed. Microdevices* **2006**, *8*, 239–246. [CrossRef]

23.　Wang, G.J.; Chen, C.L.; Hsu, S.H.; Chiang, Y.L. Bio-MEMS fabricated artificial capillaries for tissue engineering. *Microsyst. Technol.* **2005**, *12*, 120–127. [CrossRef]

24.　Tsuda, S.; Zauner, K.P.; Gunji, Y.P. Robot control with biological cells. *Biosystems* **2007**, *87*, 215–223. [CrossRef]

25.　Kim, S.; Hawkes, E.; Choy, K.; Joldaz, M.; Foleyz, J.; Wood, R. Micro Artificial Muscle Fiber Using NiTi Spring for Soft Robotics. In Proceedings of the International Conference on Intelligent Robots and Systems, St. Louis, MO, USA, 10–15 October 2009; pp. 2228–2234.

26.　Nosonovsky, M.; Rohatgi, P.K. *Biomimetics in Materials Science: Self-Healing, Self-Lubricating, and Self-Cleaning Materials*; Springer Science & Business Media: Berlin/Heidelberg, Germany, 2011; Volume 152.

27.　Zhang, D. *Morphology Genetic Materials Templated from Nature Species*; Springer Science & Business Media: Berlin/Heidelberg, Germany, 2014.

28.　You, Z.; Pearce, D.J.G.; Sengupta, A.; Giomi, L. Geometry and mechanics of microdomains in growing bacterial colonies. *Phys. Rev. X* **2018**, *8*, 031065. [CrossRef]

29.　Desai, N.; Ardekani, A.M. Combined influence of hydrodynamics and chemotaxis in the distribution of microorganisms around spherical nutrient sources. *Phys. Rev. E* **2018**, *98*, 012419. [CrossRef] [PubMed]

30.　Karthick, S.; Sen, A.K. Improved understanding of acoustophoresis and development of an acoustofluidic device for blood plasma separation. *Phys. Rev. Appl.* **2018**, *10*, 034–037. [CrossRef]

31.　Zhang, J.M.; Ji, Q.; Liu, Y.; Huang, J.; Duan, H. An integrated micro-milli fluidic processing system. *Lab Chip* **2018**, *18*, 3393–3404. [CrossRef]

32.　Shuler, M.L. Advances in Organ-, body-, and Disease-on-a-chip Systems. *Lab Chip* **2019**, *19*, 9–10. [CrossRef] [PubMed]

33.　Tousignant, L. This Miracle Medical Chip Could One Day Heal almost Anything. *New York Post*, 8 August 2017.

34.　Richman, M. *Breathing Easier*; U.S. Department of Veterans Affairs: Washington, DC, USA, 2018.

35.　Tan, G.Z.; Zhou, Y. Electrospinning of biomimetic fibrous scaffolds for tissue engineering: A review. *Int. J. Polym. Mater. Polym. Biomater.* **2020**, *69*, 947–960. [CrossRef]

36.　Okeyo, P.O.; Larsen, P.E.; Kissi, E.O.; Ajalloueian, F.; Rades, T.; Rantanen, J.; Boisen, A. Single particles as resonators for thermomechanical analysis. *Nat. Commun.* **2020**, *11*, 1–11. [CrossRef]

37. Li, A.; Zhao, Y.; Li, Y.; Jiang, L.; Gu, Y.; Liu, J. Cell-derived biomimetic nanocarriers for targeted cancer therapy: Cell membranes and extracellular vesicles. *Drug Deliv.* **2021**, *28*, 1237–1255. [CrossRef] [PubMed]

38. Pris, A.D.; Utturkar, Y.; Surman, C.; Morris, W.G.; Vert, A.; Zalyubovskiy, S.J.; Deng, T.; Ghiradella, H.T.; Potyrailo, R.A. Towards high-speed imaging of infrared photons with bio-inspired nanoarchitecture. *Nat. Photonics* **2012**, *6*, 195–200. [CrossRef]

39. Zhang, F.; Shen, Q.; Shi, X.; Li, S.; Wang, W.; Luo, Z.; He, G.; Zhang, P.; Tao, P.; Song, C.; et al. Infrared detection based on localized modification of Morpho butterfly wings. *Adv. Matter.* **2015**, *27*, 1077–1082. [CrossRef]

40. Grujic, D.; Vasiljevic, D.; Pantelic, D.; Tomic, L.J.; Stamenkovic, Z.; Jelenkovic, B. Infrared camera on the butterfly's wing. *Opt. Express* **2018**, *26*, 14143–14158. [CrossRef] [PubMed]

41. Mueller, M.T. Biomimetic, Polymer-Based Microcantilever Infrared Sensors. Ph.D. Dissertation, University of California, Berkeley, CA, USA, 2007.

42. Passian, A.; Wig, A.; Meriaudeau, F.; Ferrell, T.L.; Thundat, T. Knudsen forces on microcantilevers. *J. Appl. Phys.* **2002**, *92*, 6326–6333. [CrossRef]

43. Passian, A.; Warmack, R.J.; Ferrel, T.L.; Thundat, T. Thermal transpiration at the microscale: A Crookes cantilever. *Phys. Rev. Lett.* **2003**, *90*, 124503. [CrossRef] [PubMed]

44. Verstraete, C.; Mouchet, S.R.; Verbiest, T.; Kolarić, B. Linear and nonlinear optical effects in biophotonic structures using classical and nonclassical light. *J. Biophotonics* **2019**, *12*, e201800262. [CrossRef]

jove

Uncovering Hidden Dynamics of Natural Photonic Structures using Holographic Imaging

Marina Simovic-Pavlovic[1,2], **Maja C. Pagnacco**[3], **Dusan Grujic**[1], **Bojana Bokic**[1], **Darko Vasiljevic**[1], **Sébastien Mouchet**[4,5], **Thierry Verbiest**[6], **Branko Kolaric**[1,7]

[1] Institute of Physics, Photonics Center, University of Belgrade [2] Faculty of Mechanical Engineering, University of Belgrade [3] Institute of Chemistry, Technology and Metallurgy, University of Belgrade [4] School of Physics, University of Exeter [5] Department of Physics & Namur Institute of Structured Matter (NISM), University of Namur [6] Chemistry Department, Laboratory of Molecular Imaging and Photonics, KULeuven [7] Université de Mons

Corresponding Authors

Maja C. Pagnacco
maja.pagnacco@nanosys.ihtm.bg.ac.rs
Branko Kolaric
branko.kolaric@umons.ac.be

Abstract

In this method, the potential of optics and holography to uncover hidden details of a natural system's dynamical response at the nanoscale is exploited. In the first part, the optical and holographic studies of natural photonic structures are presented as well as conditions for the appearance of the photophoretic effect, namely, the displacement or deformation of a nanostructure due to a light-induced thermal gradient, at the nanoscale. This effect is revealed by real-time digital holographic interferometry monitoring the deformation of scales covering the wings of insects induced by temperature. The link between geometry and nanocorrugation that leads to the emergence of the photophoretic effect is experimentally demonstrated and confirmed. In the second part, it is shown how holography can be potentially used to uncover hidden details in the chemical system with nonlinear dynamics, such as the phase transition phenomenon that occurs in complex oscillatory Briggs-Rauscher (BR) reaction. The presented potential of holography at the nanoscale could open enormous possibilities for controlling and molding the photophoretic effect and pattern formation for various applications such as particle trapping and levitation, including the movement of unburnt hydrocarbons in the atmosphere and separation of different aerosols, decomposition of microplastics and fractionation of particles in general, and assessment of temperature and thermal conductivity of micron-size fuel particles.

Introduction

To fully understand and notice all the unique phenomena in the nanoworld, it is crucial to employ techniques that are capable of revealing all details regarding structures and dynamics at the nanoscale. On this account, the unique combination of linear and nonlinear methods, combined with the power of holography to reveal the system's dynamics at the nanoscale are presented.

The described holographic technique can be viewed as the triple rec method (rec is the abbreviation for recording), since at a given time the signal is simultaneously recorded by a photographic camera, a thermal camera, and an interferometer. Linear and nonlinear optical spectroscopy and holography are well-known techniques, the fundamental principles of which are extensively described in the literature[1,2].

To cut a long story short, holographic interferometry allows the comparison of wavefronts recorded at different moments in time to characterize the dynamics of the system. It was previously used to measure vibrational dynamics[3,4]. The power of holography as the simplest interferometry method is based on its ability to detect the smallest displacement within the system. First, we exploited holography to observe and reveal the photophoretic effect[5] (i.e., the displacement of deformation of a nanostructure due to a light-induced thermal gradient), in different biological structures. For a true presentation of the method, representative samples were selected from a number of tested biological specimens[6]. Wings of the Queen of Spain fritillary butterfly, *Issoria lathonia* (Linnaeus, 1758; *I. lathonia*), were used in the framework of this study.

After having successfully demonstrated the occurrence of photophoresis at the nanoscale in biological tissues, a similar protocol was applied to monitor the spontaneous symmetry breaking process[7] caused by a phase transition in an oscillatory chemical reaction. In this part, the phase transition from a low concentration of iodide and iodine (called state I) to a high concentration of iodide and iodine with solid iodine formation (defined as state II) that occurs in a chemically nonlinear BR reaction was studied[8,9]. Here, we reported for the first time a holographic approach that allows studying

such a phase transition and spontaneous symmetry breaking dynamics at the nanoscale occurring in condensed systems.

Protocol

1. Precharacterization

1. Perform a full precharacterization of the sample.

    1. Perform all experiments on dry specimens purchased from a commercial source. Store the samples in the laboratory, in a dry and dark place, at room temperature.

    2. Prior to holographic measurements, perform a complete sample characterization by scanning electronic microscope (SEM), linear optical spectroscopy, and nonlinear optical microscopy (NOM)[10] (**Figure 1**).

    3. In addition to the optical properties of samples measured by linear techniques, gather supplementary information with higher intensity laser beams that allow characterization of their nonlinear optical properties.

    4. Use the corresponding nonlinear optical susceptibilities to quantify the nonlinear optical response and form the basis of nonlinear optical techniques such as nondestructive multiphoton excitation fluorescence and second harmonic generation (SHG), which are used to characterize various biological samples.

    5. For the nonlinear chemical phenomena occurring in the oscillating BR reaction, carry out the study of interferometric monitoring of the *in situ* phase transition from state I to state II with the following concentrations of reactants: $[CH_2(COOH)_2]_0$ =

0.0789 mol dm^{-3}, [MnSO$_4$]$_0$ = 0.0075 mol dm^{-3}, [HClO$_4$]$_0$ = 0.03 mol dm^{-3}, [KIO$_3$]$_0$ = 0.0752 mol dm^{-3}, and [H$_2$O$_2$]$_0$ = 1.269 mol dm^{-3} (0 after the bracket stands for the initial concentration at the beginning of the process). Make the total volume used for the BR reaction equal to 2.5 mL.

2. Prepare the sample for the experiment.

    1. Use wings of the Queen of Spain fritillary butterfly, *I. lathonia,* for this experiment. Place the wing on a hard surface and make a section with a 10 mm diameter cutter. Place the sample in the sample box, which can be any container with a lid.
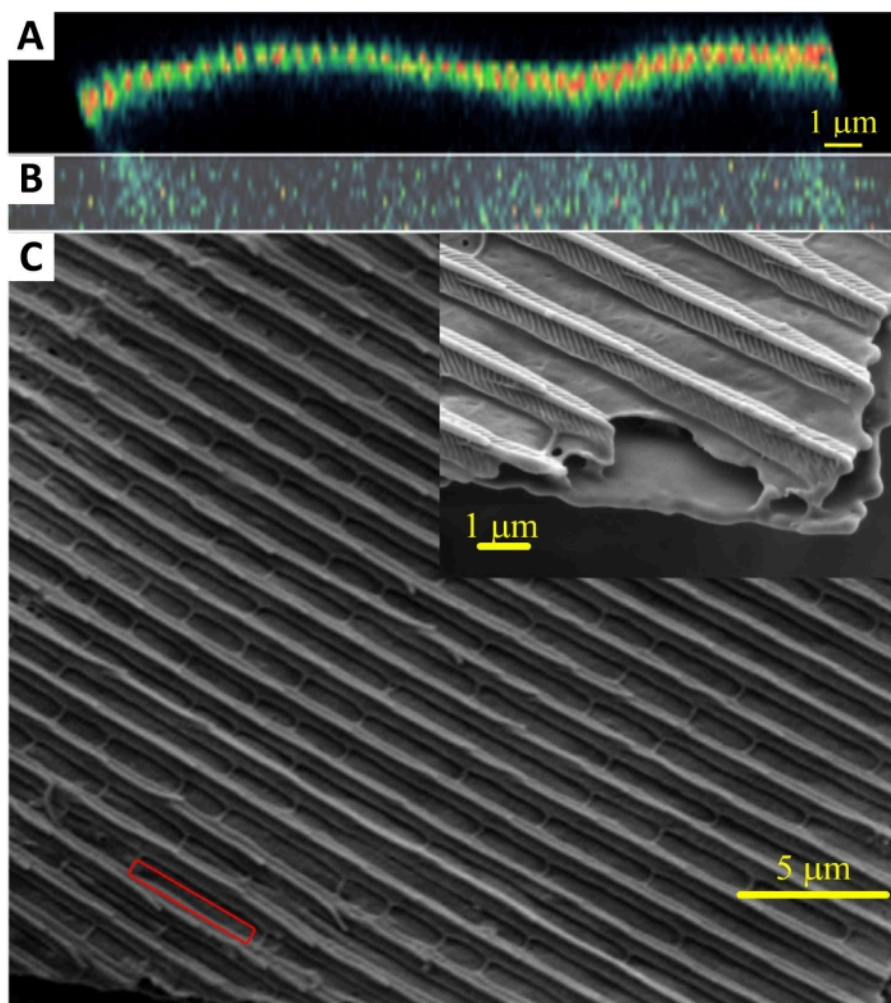
Figure 1: Wavy cross-section of butterfly wing scale. The cross-section was recorded on a nonlinear optical scanning microscope (**A,B**). A SEM observation (**C**) of a wing of the Queen of Spain fritillary butterfly, *I. lathonia*, was also done. This figure has been modified from[14].

2. Experimental setup

1. Holographic setup

   NOTE: The holographic interferometry measurements were performed with a tailor-made optical setup (**Figure 2**).

   1. Adjust the laboratory temperature to be 23 °C ± 0.2 °C. Turn the laser on. Use a laser (details given in the **Table of Materials**) with an excitation wavelength of 532 nm for these holographic observations.

   2. Check the alignment of the optical elements (**Figure 2**). First, check that setup is made according to the scheme in **Figure 2**.

   3. Align the laser beam perfectly with the concave mirror M. Check and adjust the position of the optical beam expander (L).

   4. Determine the beam part that impinges on sample S and ensure that it forms a reflex beam O. Check if the rest of the beam is collected on a spherical mirror CM, to be used to generate the reference beam R. Check if the detector C is placed within the interference zone of the two specified beams.

      NOTE: A complementary metal oxide semiconductor (CMOS) sensor is used as detector.

   5. Set up the cameras according to the instructions for the camera used. Set up an optical/photographic camera for the holographic experiment as shown in **Figure 2** (C is the camera; details given in the **Table of Materials**). Set up a second optical/photographic camera to view visible changes in BR reaction and a thermal camera with a thermal resolution of 50 mK and a focal length of 13 mm above the optical table.

      NOTE: The camera used in the holographic experiment does not use an objective lens; the light directly impinges on the chip.

2. Prepare the sample into holographic setup.

   1. Prepare the wing sample as in step 1.2.1. Place the prepared sample on a round metal support with a diameter of 15 mm. The support has three existing holes for the screws to which the metal ring holding the sample is attached.

   2. Attach the ring to the support. Place the attached sample in the part of the sample mount located on the optical table.

   3. Prepare the sample for chemical reaction monitoring. On the optical table, in the intended place, place a support with a flat adhesive surface on which the cuvette/vessel will be placed.

   4. Prepare the reagent used to initialize the reaction as in step 1.1.5. Fill the reactants into the cuvette, and mix in cuvette in the following order of volumes and concentrations: 0.7 mL of 0.2817 mol dm^{-3} CH$_2$(COOH)$_2$; 0.5 mL of 0.0375 mol dm^{-3} MnSO$_4$; 0.5 mL of 0.15 mol dm^{-3} HClO$_4$; 0.5 mL of 0.376 mol dm^{-3} KIO$_3$; and 0.3 mL of 10.575 mol dm^{-3} H$_2$O$_2$.

   5. Ensure that the total volume in the cuvette is 2.5 mL, and place it on the support in the setup.

6. Set up additional instruments if needed. For monitoring the photophoretic effect, use an additional laser (details given in **Table of Materials**) for local heating.
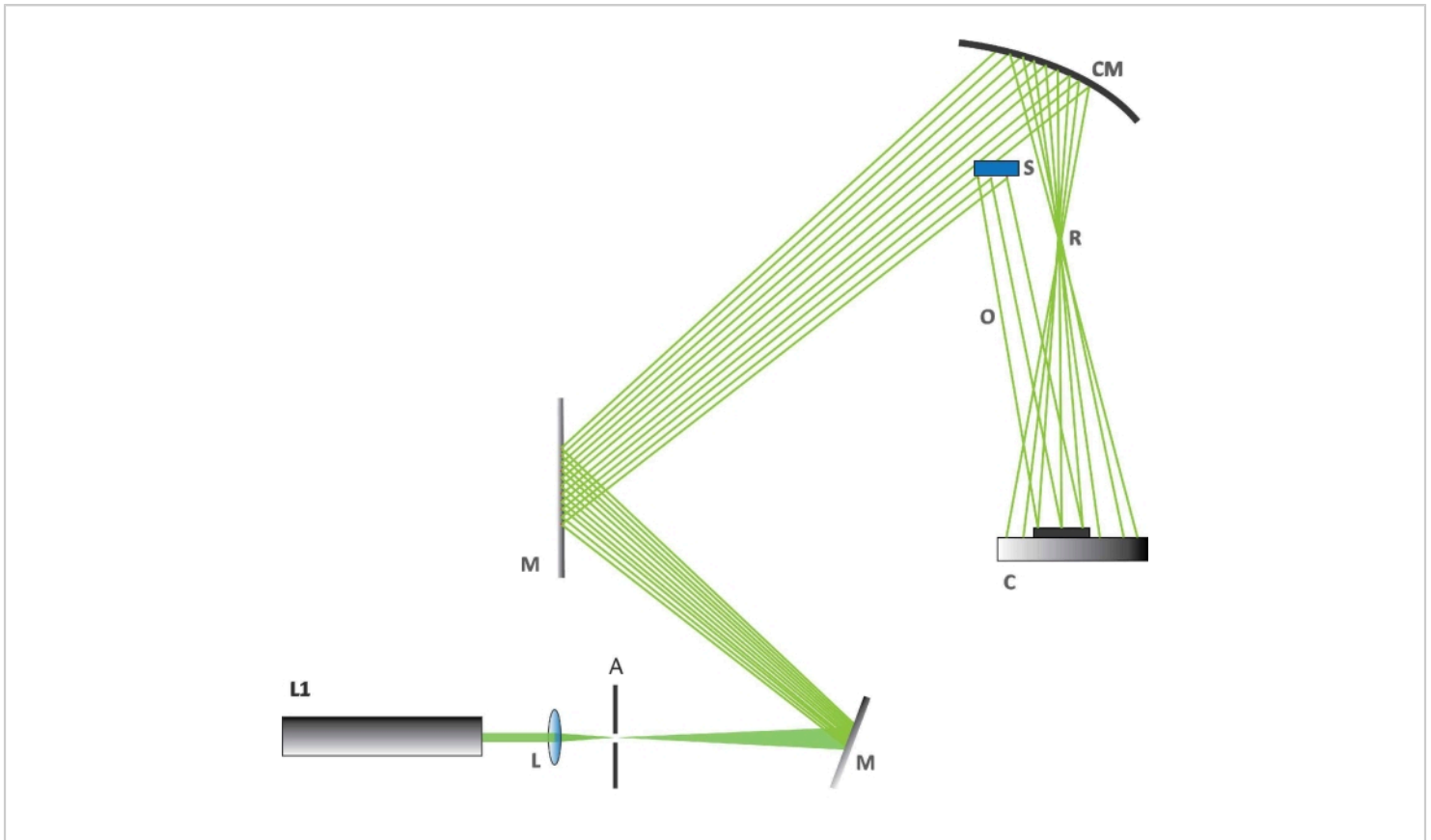

Figure 2: The holographic setup. The figure shows how the various components are arranged for the holographic experiment. Abbreviations: L1 = laser at 532 nm, L = biconvex lens, A = aperture, M = a flat mirror used to deflect the laser beam, CM = concave mirror, C = CMOS camera, S = butterfly wing section, R = reference beam, O = object beam. Please click here to view a larger version of this figure.

3. Setup of the software used

NOTE: Home-built C++ software based on Fresnel approximation[11] is used to analyze data from holographic experiments. The software developed for the presented study can be found at .[12] The details of software cannot be published at the moment; however, additional information will be provided on request. Fresnel approximation is extremely useful in digital holography since it focuses on different surfaces and zooms in on the area of the first diffraction order, which contains complete information about the recorded scene.

1. Turn on the computer and run the software.

   NOTE: The step for running the software depends on the software itself. There is no commercial software for this purpose.

4. Perform the experiment

1. Switch off the external lights. Carry out the whole experiment in a dark room.

2. Synchronize the cameras by using a chosen interval. For this experiment, start the holographic camera after 60 s, and the two other cameras immediately after it, using either a software or manually.

3. Press the recording buttons and define in the software when the recording starts.

4. Induce dynamical changes in the system of interest. The method of initiation depends on the type of sample; in the case of photophoretic effect, externally heat the sample by using the available lasers: 450 nm, 532 nm, 660 nm, 980 nm. In the case of the BR reaction, start the reaction by mixing the chemical reactants. Observe the holographic experiment.

5. Set the photographic and thermal camera to follow the whole experiment and determine the moment of the end of the holographic recording from the optical and thermal measurements.

6. Pronounce the end of the process. The end of the recording is preprogrammed, according to the estimated duration of the process. For the BR reaction, use solidification as the end of the reaction. In the case of the photophoretic effect, there is no such specific moment. In any case, this step emphasizes the importance of triple recording.

5. Acquisition of results[12]

1. Save the results. Precisely sort the files as a function of time for reconstructing holograms and deeper data analysis.

NOTE: In this step, the data is transferred from the camera used for holography to the computer (hard disk) in folders named after the shooting dates. Use copy/paste and rename buttons.

2. Check the probe hologram for appropriate settings. In this way, the best settings are selected on the first hologram by looking at it, and then used for the reconstruction of all holograms.

   1. Choose one hologram by clicking on one of them from the folder you previously made (step 5.1) and make a reconstruction by clicking on the **Reconstruct** button.

   2. Change the settings to achieve the best image and make the reconstruction again. Options for adjusting parameters such as sampling, offset, and Fresnel distance will appear on the screen (software menu). Repeat these steps until the best settings are defined.

   3. Perform the reconstructions. Choose all the holograms by clicking the **Open File** button and choosing all files. Apply the desired parameters for numerical reconstruction of holograms; they remain unchanged after the step 5.2.1, so do not perform any action this time.

   4. Carry out the reconstructions using the **Reconstruct** button, and the interferograms by inserting the file names in the start with/end with field and then by clicking the button **Batch**. The interferograms appear in the previously made folder (in step 5.1).

   NOTE: After recording a series of holograms in time, the first hologram represents an unperturbed state, while the action of an external force causes subsequent holograms. It is necessary to

reconstruct the holograms using shifted Fresnel transform[13].

5. Obtain the interferograms by subtraction (in terms of complex numbers) of a particular hologram in time with the first hologram obtained.

   NOTE: This protocol allows observing the effect of the force on the object. The change in the interference pattern as a function of time is a consequence of deformation or displacement that occurs within the system during the measurement. These changes are used to monitor the system's dynamics at the nanoscale.

6. Analyses of the results

1. Perform a visual analysis as the first quality control step of the process. In this step, look for visible changes in interference pattern and try to match the changes in the interference pattern with results obtained by optical and thermal measurements.

2. Perform a cross-examination of all recordings. In this second phase of the analysis, thoroughly analyze the images visually from both the optical and thermal cameras with the holographic reconstructions in order to reveal dynamics at the nanoscale. In this way, the reaction moment is seen simultaneously in holographic, thermal, and photographic images.

3. Make a graphical representation of results based on numerical/software analysis and present them in the form of graphs (1D, 2D, or 3D), charts, histograms etc. After a complete analysis of results, draw conclusions and anticipate further research based on this.

Representative Results

A photophoretic effect was induced and monitored in a first experiment on the wing of a *Morpho menelaus* butterfly[5]. The effect was initiated by the action of LED lasers of different wavelengths (450 nm, 532 nm, 660 nm, and 980 nm). Here, the wings from an *I. lathonia* butterfly[14] were used. After the recording procedure, the hologram image was reconstructed.
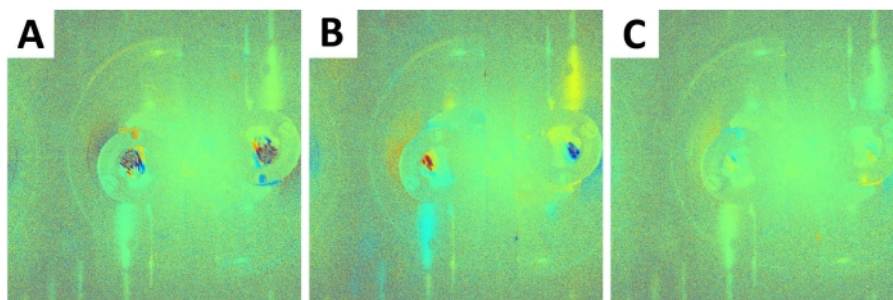

Figure 3: *I. lathonia* wings' holographic reconstructions. The reconstruction was done at 450 nm initiation (**A**), 532 nm initiation (**B**), and 980 nm initiation (**C**). The images show an obvious difference in the visual sense, where depending on the wavelength, the colored area appears in different sizes. Please click here to view a larger version of this figure.

The fringes observed in **Figure 3A-C** are the consequence of the interference. This figure clearly shows that changes occur only during the irradiation of the sample with a second laser (placed to hit the sample with a beam that does not interfere with the beam from the primary laser; put into operation at any time during the recording), and confirms that holographic interferometry can be used to monitor the deformation or displacement of the biological tissues.

Figure 3A-C shows how different wavelengths between 450 nm (**Figure 3A**), 532 nm (**Figure 3B**), and 980 nm (**Figure 3C**) affect the interferometric pattern by causing different morphological displacements within the tissues.

In the second experiment regarding the oscillatory BR reaction, this reaction started immediately after the addition of hydrogen peroxide, producing a large amount of oxygen (**Figure 4A**). As the transition from state I to state II (**Figure 4**) is essentially irreproducible for an individual kinetic run[8], the moment of transition is very difficult to monitor. Therefore, the presented results are the consequence of a large number of attempts. In the analysis of interferograms, a change in the fringe pattern was noticed at the exact moment when the reaction occurred (i.e., when transition from state I to state II occurred). **Figure 4E** shows a moment before the reaction occurred (left) and the exact moment (right). The wavelength used here is 573 nm. When calculating the displacement data from the amplitude image, the method of direct fringe counting was used. One fringe corresponds to a displacement of half the wavelength (i.e., 286.5 nm). If the displacement data is calculated from the phase, the following relation applies: $\Delta l / \lambda = \Delta \Phi / 2\pi$.
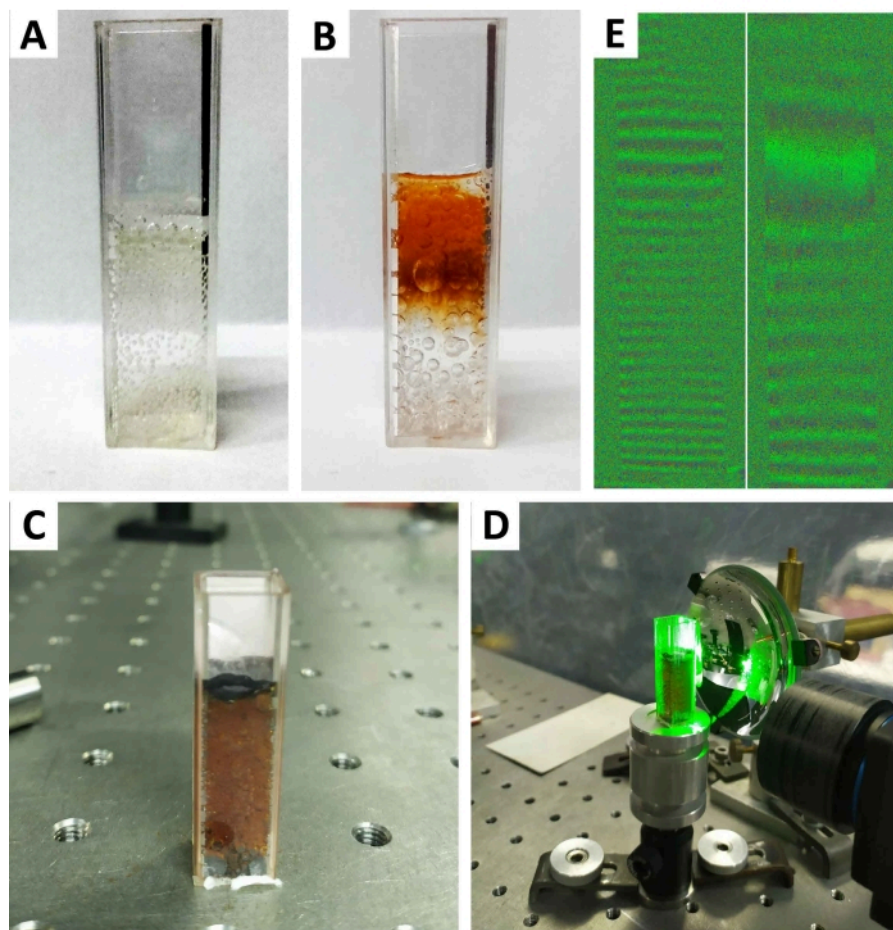
Figure 4: The transition from state I to state II in Briggs-Rauscher (BR) reaction. The different recordings for the transition from state I to state II in Briggs-Rauscher (BR) reaction. (**A**) The beginning of the BR reaction with bubbles corresponds to oxygen and carbon dioxide formation. (**B**) The state I to state II reaction course. (**C**) The end of state I to state II transition. (**D**) Cuvette in setup. (**E**) Interferogram of the moment before reaction (left) and the moment of reaction (right). Please click here to view a larger version of this figure.

Nonlinear chemical phenomena have been known for more than 100 years[15], but despite this, there are still doubts about their full mechanism and dynamics[16,17]. The results obtained open new possibilities for the investigation and monitoring of such complex chemical phenomena *in situ* by a holographic technique.

Discussion

In the presented biophotonic study, it is shown that a novel holographic method can be used to detect minimal morphological displacement or deformation caused by low-level thermal radiation.

The most critical step in holographic measurement with biological samples is the preparation step. The preparation

of the sample (cutting/gluing to match the size of the holder) depends on the sample's mechanical properties, and it is not possible to have a standard protocol for this step.

Regarding the BR study, it is vital to have a transparent reaction vessel and relatively clear optical path, since every obstacle during a chemical reaction, or physical transformation (like the release of oxygen, impurity) will affect interference pattern and therefore recorded results.

In general, the most significant limitation of the described method is the sample size that can be studied. The sample must have an appropriate dimension to be inserted within the optical setup.

Here we show that holographic interferometry (HI) should be considered as an essential complementary tool for the characterization of samples. For example, a classic optical/IR image captures information only regarding the intensity, while the information about the phase is totally lost[18]. Holographic interferometry provides all information regarding the intensity and phase, and additionally can be used to monitor their changes in real time.

The importance of exploiting this method in condensed matter science is to reveal *in situ* the slightest changes in system dynamics. For example, the BR reaction can reveal the first cause of the symmetry-breaking process. Is the symmetry-breaking process predetermined by physical constraints connected with nonlinear dynamics, or is the process truly random? On the other hand, in another way, can the minor differences in BR oscillatory period duration cause a significant deviation in transition appearance?

The presented results are the first step that will lead to a deeper understanding of dynamics at the nanoscale. Since the potential of holography in condensed science research has still not been fully recognized, the purpose of this article is to highlight the power of holography for future material science research and applications; for example, particle trapping and levitation such as movement of unburnt hydrocarbons in the atmosphere or separation of various aerosols[19], breaking down of microplastics in water and fractionation of particles in general[20], and characterisation of temperature and thermal conductivity properties of micron-size fuel particles[21].

Disclosures

The authors declare no conflict of interests.

Acknowledgments

Simović Pavlović at the University of Belgrade, Faculty of Mechanical Engineering.

References

1. Pietrzyk, D. J., Frank, C. W. Development of an analytical method. *Analytical Chemistry.* 10-19 (1979).

2. Ostrovsky, Y. I., Shchepinov, V. P., Yakovlev, V. V. *Holographic Interferometry in Experimental Mechanics.* Volume 60. Springer (2013).

3. Pedrini, G., Osten, W., Gusev, M. E. High-speed digital holographic interferometry for vibration measurement. *Applied Optics.* **45** (15), 3456-3462 (2006).

4. Pantelić, D. V., Grujić, D. Ž., Vasiljević, D. M. Single-beam, dual-view digital holographic interferometry for biomechanical strain measurements of biological objects. *Journal of Biomedical Optics.* **19** (12), 127005 (2014).

5. Grujić, D. et al. Infrared camera on butterfly's wing. *Optics Express.* **26** (11), 14143-14158 (2018).

6. Mouchet, S. R., Deparis, O. *Natural Photonics and Bioinspiration.* Artech House (2021).

7. Pagnacco, M. C. et al. Spontaneous symmetry breaking: the case of crazy clock and beyond. *Symmetry.* **14**, 413 (2022).

8. Pagnacco, M. C., Maksimovic, J. P., Potkonjak, N. I., Božić, B. Đ., Horvath, A. K. Transition from low to high iodide and iodine concentration states in the Briggs-Rauscher reaction: evidence on crazy clock behavior. *The Journal of Physical Chemistry A.* **122** (2), 482-491 (2018).

9. Pagnacco, M. C., Maksimović, J. P., Janković, B. Ž. Analysis of transition from low to high iodide and iodine state in the Briggs-Rauscher oscillatory reaction containing malonic acid using Kolmogorov-Johnson-Mehl-Avrami (KJMA) theory. *Reaction Kinetics, Mechanisms and Catalysts.* **123** (1), 61-80 (2018).

10. Mouchet, S. R. et al. Unveiling the non-linear optical response of Trichtenotoma childreni longhorn bestle. *Journal of Biophotonics.* **12** (9), e201800470 (2019).

11. Shimobaba, T. et al. Computational wave optics library for C++: CWO++ library. *Computer Physics Communications.* **183** (5), 1124-1138 (2012).

12. Grujic, D. Application of digital holography for detection of infrared radiation on biophotonic structures. Ph. D. Thesis, Faculty of Physics, University of Belgrade, (2022); Available online after the Novembar (2022).

13. Muffoletto, R. P., Tyler, J. M., Tohline, J. E. Shifted Fresnel diffraction for computational holography. *Optical Express.* **15** .(9), 5631-5640 (2007).

14. Pavlović, D. et al. Naturally safe: Cellular noise for document security. *Journal of Biophotonics.* **12** (12), e201900218 (2019).

15. Bray, W. C. A periodic reaction inhomogeneous solution and its relation to catalysis. *Journal of the American Chemical Society.* **43** (6), 1262-1267 (1921).

16. Nicolis, G. Self-organization in nonequilibrium systems. *Dissipative Structures to Order through Fluctuations.* 339-426 (1977).

17. Prigogine, I., Hiebert, E. N. From being to becoming: Time and complexity in the physical sciences. *Physics Today.* **35** (1), 69 (1982).

18. Nikolova, L., Ramanujam, P. S. *Polarization Holography.* Cambridge University Press (2009).

1 JoVE

19. Haisch, C., Kykal, C., Niessner, R. Photophoretic velocimetry for the characterization of aerosols. *Analytical Chemistry.* **80** (5), 1546-1551 (2008).

20. Kononenko, V. L., et al. Feasibility studies on photophoretic effects in field-flow fractionation of particles. *Journal of Liquid Chromatography & Related Technologies.* **20** (16-17), 2907-2929 (1997).

21. Zhang, X., Bar-Ziv, E. A novel approach to determine thermal conductivity of micron-sized fuel particles. *Combustion Science and Technology.* **130** (1-6), 79-95 (1997).

Article

Spontaneous Symmetry Breaking: The Case of Crazy Clock and Beyond

Maja C. Pagnacco [1,*], Jelena P. Maksimović [2], Marko Daković [2], Bojana Bokic [3], Sébastien R. Mouchet [4,5], Thierry Verbiest [6], Yves Caudano [7] and Branko Kolaric [3,8,*]

[1] Center for Catalysis and Chemical Engineering, Institute of Chemistry, Technology and Metallurgy, University of Belgrade, Njegoševa 12, 11000 Belgrade, Serbia

[2] Faculty of Physical Chemistry, University of Belgrade, Studentski Trg 12, 11158 Belgrade, Serbia; jelena.maksimovic@ffh.bg.ac.rs (J.P.M.); marko@ffh.bg.ac.rs (M.D.)

[3] Center for Photonics, Institute of Physics, University of Belgrade, Pregrevica 118, 11080 Belgrade, Serbia; bojana@ipb.ac.rs

[4] Department of Physics, Namur Institute of Structured Matter (NISM), University of Namur, Rue de Bruxelles 61, 5000 Namur, Belgium; sebastien.mouchet@unamur.be

[5] School of Physics, University of Exeter, Stocker Road, Exeter EX4 4QL, UK

[6] Department of Chemistry, Molecular Imaging and Photonics, KU Leuven, 3001 Heverlee, Belgium; thierry.verbiest@fys.kuleuven.be

[7] Department of Physics, Namur Institute of Structured Matter (NISM), Namur Institute for Complex Systems (naXys), University of Namur, Rue de Bruxelles 61, 5000 Namur, Belgium; yves.caudano@unamur.be

[8] Micro- and Nanophotonic Materials Group, University of Mons, Place du Parc 20, 7000 Mons, Belgium

* Correspondence: maja.pagnacco@nanosys.ihtm.bg.ac.rs (M.C.P.); branko.kolaric@umons.ac.be (B.K.)

Abstract: In this work, we describe the crazy-clock phenomenon involving the state I (low iodide and iodine concentration) to state II (high iodide and iodine concentration with new iodine phase) transition after a Briggs–Rauscher (BR) oscillatory process. While the BR crazy-clock phenomenon is known, this is the first time that crazy-clock behavior is linked and explained with the symmetry-breaking phenomenon, highlighting the entire process in a novel way. The presented phenomenon has been thoroughly investigated by running more than 60 experiments, and evaluated by using statistical cluster K-means analysis. The mixing rate, as well as the magnetic bar shape and dimensions, have a strong influence on the transition appearance. Although the transition for both mixing and no-mixing conditions are taking place completely randomly, by using statistical cluster analysis we obtain different numbers of clusters (showing the time-domains where the transition is more likely to occur). In the case of stirring, clusters are more compact and separated, revealed new hidden details regarding the chemical dynamics of nonlinear processes. The significance of the presented results is beyond oscillatory reaction kinetics since the described example belongs to the small class of chemical systems that shows intrinsic randomness in their response and it might be considered as a real example of a classical liquid random number generator.

Keywords: crazy clock; Briggs–Rauscher reaction; state I to state II transition; symmetry breaking; iodine; K-means analysis; random number generator

1. Introduction

The presence of symmetry around us inspired many scientists to search for beauty, harmony, order, and regularity in nature and her fundamental laws [1,2]. Additionally, phase transitions with and without spontaneously broken symmetries are widespread concepts through different areas of physics and physical chemistry. The applications of spontaneously broken symmetries cover a wide range of condensed matter science topics, such as superconductivity, super-fluidity, Bose–Einstein condensation, nucleation

physics, self-assembly processes, morphogenesis, and chemical kinetics. In this account, we describe spontaneous symmetry breaking in the case of the nonlinear Briggs–Rauscher reaction. We highlight the importance of symmetry breaking, in non-equilibrium and pattern formation processes, which is of vital meaning to the understanding of the morphogenesis process and for applications in several areas of biomimetics and nanoscience.

The Briggs–Rauscher (BR) [3] reaction is a hybrid oscillating reaction formed by coupling two chemical oscillators, Bray–Liebhafsky [4,5] and Belousov–Zhabotinskii [6]. Since its discovery in 1973, the Briggs–Rauscher oscillating reaction has been one of the most investigated oscillatory systems. It is probably due to its simplicity and exciting colour alternation caused by changes in reaction kinetics (when starch is used as an indicator) [7].

BR reaction typically occurs within mixtures of H_2O_2, H_2SO_4, and KIO_3. Additionally, Mn(II) ions are added as a metal catalyst and malonic acid (H_2MA) as an organic substrate. Substitutions of chemicals are possible; different acids, organic substrates, and ions, such as Ce(III) instead of Mn(II) catalyst, can be used to generate BR oscillations [7–10]. However, the oscillatory behavior is not the only one that attracted the attention of non-linear scientists in the Briggs–Rauscher reaction [11–15].

Indeed, as described elsewhere [16], after the well-controlled initial oscillatory behavior, the reaction becomes chaotic. Depending on the initial conditions, particularly on the ratio $[H_2MA]_0/[IO_3^-]_0$ [16,17], the reaction exhibits a sudden and unpredictable phase transition. This transition, from state I (low concentration of iodide and iodine) to state II (high concentration of iodide and iodine), happens randomly in practice, as the time spent by the system in the state I is irreproducible (see Figure 1). The transition is characterized by a "sharp and sudden" increase of iodine and iodide concentration, followed by the formation of solid iodine. The observed stochastic feature, called a crazy clock (due to the unpredictable time needed to provoke the transition), is linked to imperfect mixing that affects convection and diffusion dynamics. The imperfect mixing results in extremely complicated phenomena, which occur on multiple length and time scales [18]. Possible kinetical consequences are the appearance of bifurcation, chaos, intermittent behavior, and symmetry-breaking [18,19]. In the experiments of our previous paper [16], the mixing was stopped after an intensive homogenization (stirring at 900 rpm) of the Briggs–Rauscher solution in the oscillatory period. Herein, the experiments carried out with or without specific mixing were maintained all the time. Additionally, we apply the statistical cluster K-means analysis for the first time, by processing more than 60 experiments. Therefore, this paper further studies the mixing effects in connection to the crazy-clock phenomenon in the Briggs–Rauscher oscillatory reaction. It compares and processes statistically more than #60 experiments obtained under identical initial concentrations of all reactants. Although the BR crazy-clock phenomenon was previously detected [16], this behavior is linked for the first time to symmetry-breaking, highlighting the entire process in a novel way. Furthermore, the investigated crazy clock exhibits a truly random behavior that might be considered as an example of a classical, liquid random number generator. Additionally, the investigated system also belongs to the particular class of classical systems that shows intrinsic randomness in their response (as also observed in colloid particles placed on an oscillating surface) [20,21].
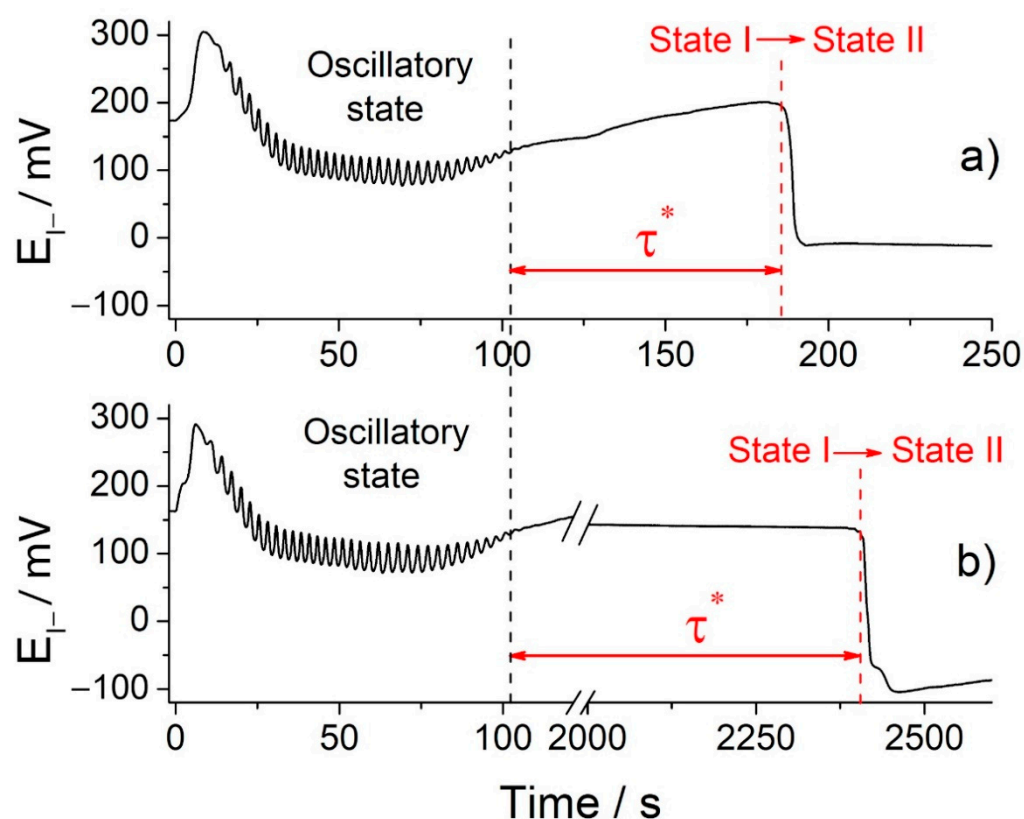
Figure 1. Two independent measurements (**a**,**b**) of iodide potential vs. time obtained for BR reaction under experimental conditions: $[H_2MA]_0 = 0.0789$ mol/dm^3, $[MnSO_4]_0 = 0.00752$ mol/dm^3, $[HClO_4]_0 = 0.03$ mol/dm^3, $[KIO_3]_0 = 0.0752$ mol/dm^3, $[H_2O_2]_0 = 1.176$ mol/dm^3, T = 37.0 °C. The experiments were performed without stirring and without protection from light. τ^* denotes the time from the end of the oscillatory mode to the occurrence of state I→state II transition.

2. Materials and Methods

2.1. Briggs–Rauscher Experimental Setup

Since the time of the transition between state I and II is unpredictable, great attention must be paid to the experimental procedure. Only analytically graded reagents without further purification were used for preparing the solutions. Malonic acid was obtained from Acrōs Organics (Geel, Belgium), manganese sulphate from Fluka (Buchs, Switzerland), perchloric acid, potassium iodate, and hydrogen peroxide from Merck (Darmstadt, Germany). The solutions were prepared in deionized water with specific resistance 18 MΩ/cm (Milli-Q, Millipore, Bedford, MA, USA).

All experiments were done in a container not protected from light. Reactions were monitored electrochemically (unless specified in the text). An I-ion-sensitive electrode (Metrohm 6.0502.160) was used as the working electrode and an Ag/AgCl electrode (Metrohm 6.0726.100), as the reference. During the experiments, the temperature of the reaction container was regulated by a circulating thermostat (JULABO GmbH, Seelbach, Germany) and maintained constant at 37 °C. The reaction mixture was stirred by magnetic stirrer (Ingenieurbüro, M. Zipperrer GmbH, Cat-ECM5, Staufen, Denmark).

Five independent series of measurements were carried (they differed in stirring bar size and shape, as well as mixing rate) with the identical solution composition $[H_2MA]_0 = 0.0789$ mol/dm^3, $[MnSO_4]_0 = 0.00752$ mol/dm^3, $[HClO_4]_0 = 0.03$ mol/dm^3, $[KIO_3]_0 = 0.0752$ mol/dm^3 and $[H_2O_2]_0 = 1.176$ mol/dm^3 in 25 mL volume:

(1) without mixing (number of conducted experiments #30);

(2) with mixing 100 rpm using cylindrical stirring bar 10 mm length, 4 mm diameter (BRAND magnetic stirring bar, PTFE-coated cylindrical), (number of conducted experiments #30)

(3) with mixing 300 rpm using cylindrical stirring bar 10 mm length, 4 mm diameter (BRAND magnetic stirring bar, PTFE-coated cylindrical), (in triplicate);

(4) with mixing 100 rpm using cylindrical stirring bar 20 mm length, 6 mm diameter (BRAND magnetic stirring bar, PTFE-coated cylindrical) (in triplicate);

(5) with mixing 100 rpm using triangular stirring bar 12 mm length, 6 mm diameter (BRAND magnetic stirring bar, PTFE-coated triangular) (in triplicate).

2.2. Statistical Processing and Cluster Analysis

The obtained experimental results were analyzed in the open-source statistic software "R" using "hclust" algorithm for the hierarchical cluster analysis (HCA) [22,23].

3. Results and Discussion

3.1. Effects of the Stirring Bar Shape and Dimensions on the State I→State II Transition

The BR oscillatory period is strongly reproducible, while the transition from state I to state II occurred practically randomly (Figure 1), as previously reported by our research group [16].

It is imperative to emphasize that in our measurements (Figure 1), unlike in other crazy-clock reactions found in the literature [18,19,24], large time fluctuations (the order of magnitude could be more than two hours) occur after a highly reproducible oscillatory period. Two independent measurements and consequently obtained BR oscillograms exhibit identical trends in oscillation amplitude and time between two neighboring oscillation maxima $\tau_{n-(n-1)} = t_n - t_{n-1}$, as it can be observed in Figures 1 and 2a,b. Conversion from higher to lower potential of iodine electrode (or from low to high iodide concentration) marks the transition from state I to state II (state I→ state II). Furthermore, the choice of the working electrode affects only the transition shape. However, the transition itself is very noticeable due to the intense color change of the system from colorless to yellow accompanied by solid iodine formation. This allows monitoring the state I→ state II transition with the naked eye.
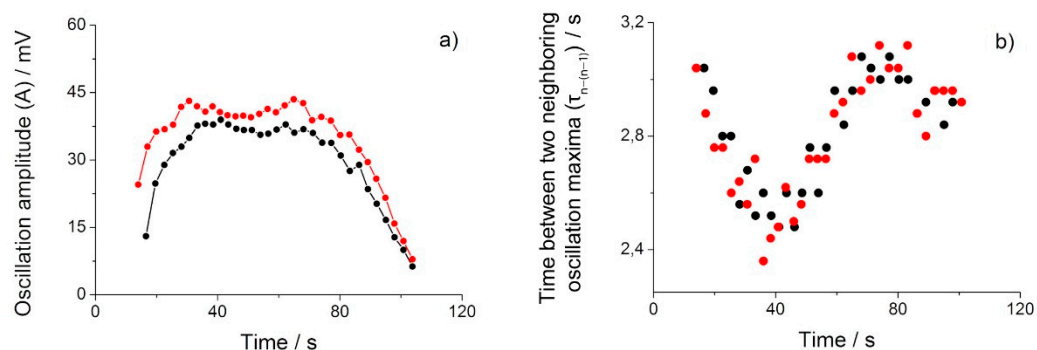

Figure 2. Briggs–Rauscher oscillation amplitude (**a**) and time between two neighboring oscillation maxima $\tau_{n-(n-1)} = t_n - t_{n-1}$ (**b**) in the two independent measurements presented at Figure 1. The resulting BR oscillograms have the same number of oscillations (N_{osc} = 33) and identical oscillation period, however the time of state I→state II transition differs more than 10 times (as shown at Figure 1).

The cause of this unexpected transition is still unknown. Previous work highlighted the significance of mixing conditions for the appearance of state I→ state II transition and crazy-clock behavior [13,16]. Therefore, we want to reveal in detail the effect of mixing on

the transition, by using stirring bars of different sizes and shapes and applying various mixing rates (Figure 3).
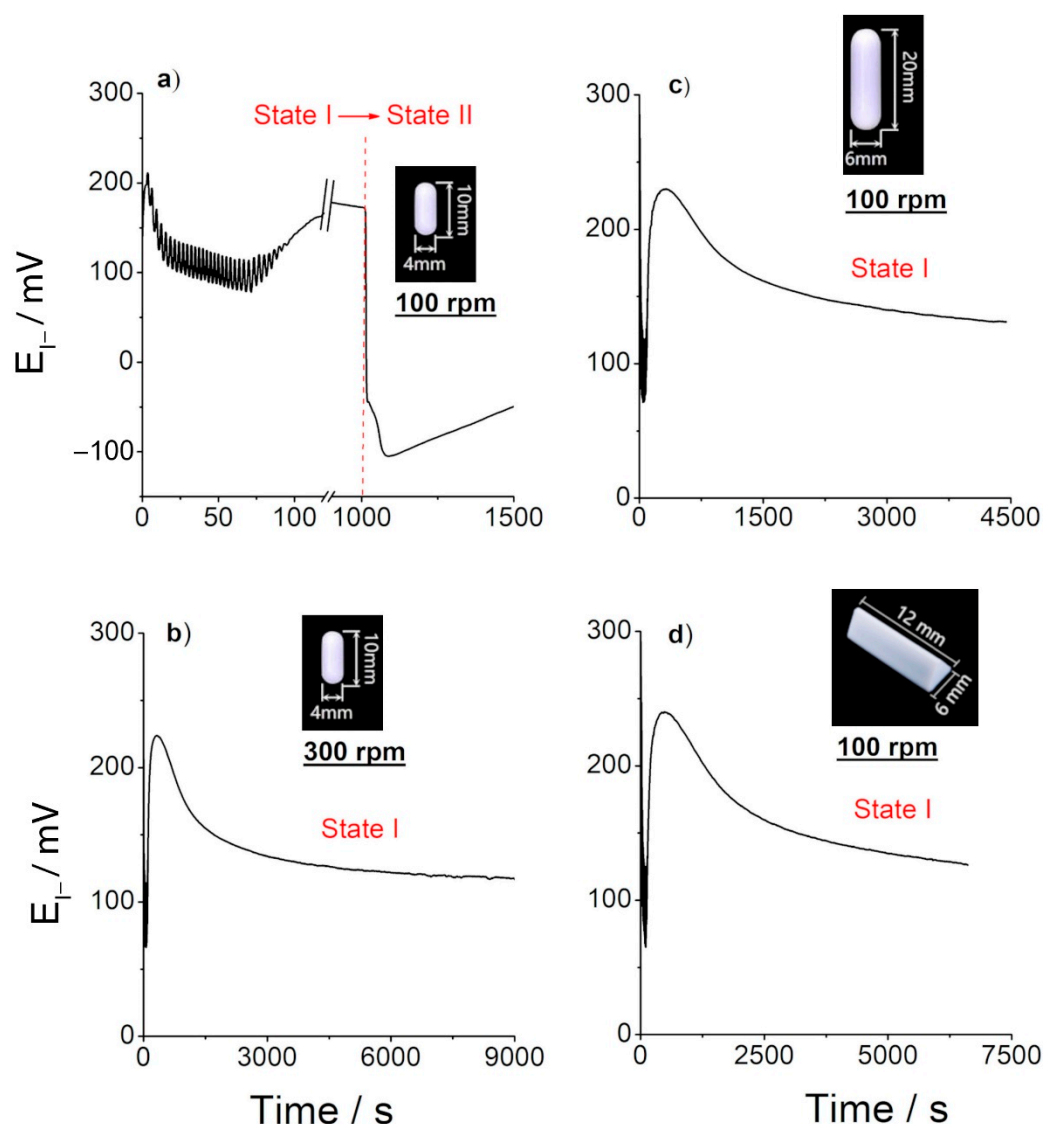

Figure 3. Typical measurements with iodide-sensing and reference electrodes with different mixing rates and different shapes of magnetic bar: (**a**) 100 rpm with magnetic stirring bar, PTFE-coated cylindrical, 10 mm length, 4 mm diameter (in inset), (**b**) 300 rpm with magnetic stirring bar, PTFE-coated cylindrical, 10 mm length, 4 mm diameter (in inset), (**c**) 100 rpm with magnetic stirring bar, PTFE-coated cylindrical, 20 mm length, 6 mm diameter (in inset), and (**d**) 100 rpm with magnetic stirring bar, PTFE-coated triangular, 12 mm length, 6 mm diameter (in inset). The reactant concentrations are identical as in Figure 1.

The transition from the state I to state II occurs only with a low stirring rate and a stirring bar of small dimensions (namely, 100 rpm and a magnetic stirring bar made of PTFE-coated cylindrical with a length of 10 mm and a diameter of 4 mm, Figure 3a). The results also underline the importance of the particular magnetic bar shape and mixing rate that was used (Figure 3a–d). Even with a low stirring rate (100 rpm), the transition does not occur with a bar exhibiting a triangular section (bar 12 mm length, 6 mm diameter) (Figure 3d). This result implies that the transition is strongly connected a particular diffusion conditions and vortex type behavior created by using specific stirring rods. Furthermore, we perform a detailed statistical analysis to reveal the connection between the state I→state II transition and the mixing rate (using the 10-mm long and 4-mm large

cylindrical stirring bar). A set of 60 experiments were performed without stirring and with stirring at a 100-rpm mixing rate (30 experiments, each). The results (τ_{osc} and τ^*) are tabulated (Tables S1 and S2) and presented in Supplementary Materials. The τ^* mean value with 95% confidence limit is for no-mixing $\tau^*_{no\ mix} = (12 \pm 4)$ min and for mixing conditions, $\tau^*_{mix} = (17 \pm 5)$ min.

3.2. Statistical Analysis of Experimental Results and Evidence of Clustering

Is there a connection between the time that the system spends in the oscillatory regime (τ_{osc}) and the time when the state I to state II transition occurs (τ^*)? Or, in other words, are the minor differences in oscillatory period duration responsible for a significant deviation in transition appearance? The detailed exploration of the relation between BR oscillatory time, τ_{osc}, and the time τ^* of the occurrence of the state I→state II transition (Figure 1), with and without stirring of the solutions, was performed by statistical cluster analysis (CA). Cluster analysis performs subdivision of datasets based on the relationships among their members (in our case datasets of τ_{osc} and τ^*). The application of CA allows the separation of data in clusters (namely, in groups) based on mutual distances, which reflect a degree of similarity among data [25]. The greater the similarity in the cluster, the higher the distance between the clusters, and hence the better the clustering. Our results combine a total of 60 experiments, obtained with no-mixing conditions (30 experiments) and with a mixing rate of 100 rpm (30 experiments). They were analyzed in the open-source statistic software "R" using "hclust" algorithm for the hierarchical cluster analysis (HCA) [22,23]. The HCA divided the ratios τ_{osc}/τ^* into three clusters for both mixing and no-mixing measurements (Figure 4a,b). It can be noticed that the number of members of a particular cluster slightly changes upon alteration of experimental conditions (Table 1).

It appears that the stirring effect causes an increase in the members of Cluster 1 and Cluster 3, as well as decreasing in members in Cluster 2. The increase of members in Cluster 3 suggested that stirring has prolonged time for the state I→state II transition taking place (Figure 4b.). It can be also seen from the τ^* mean value for no-mixing $\tau^*_{no\ mix} = (12 \pm 4)$ min and mixing conditions, $\tau^*_{mix} = (17 \pm 5)$ min. Furthermore, all clusters are more compact and separated, in the case of stirring (if compared with those obtained without stirring).

Table 1. Clusters and Cluster centroids.

Exp. Condition	Cluster	Number of Cluster Members	Cluster Centroids in Minute	
			τ_{osc}	τ^*
without stirring	1	15	1.686	3.036
	2	13	1.691	16.672
	3	2	/	/
with stirring	1	16	1.681	5.893
	2	10	1.658	26.536
	3	4	/	/

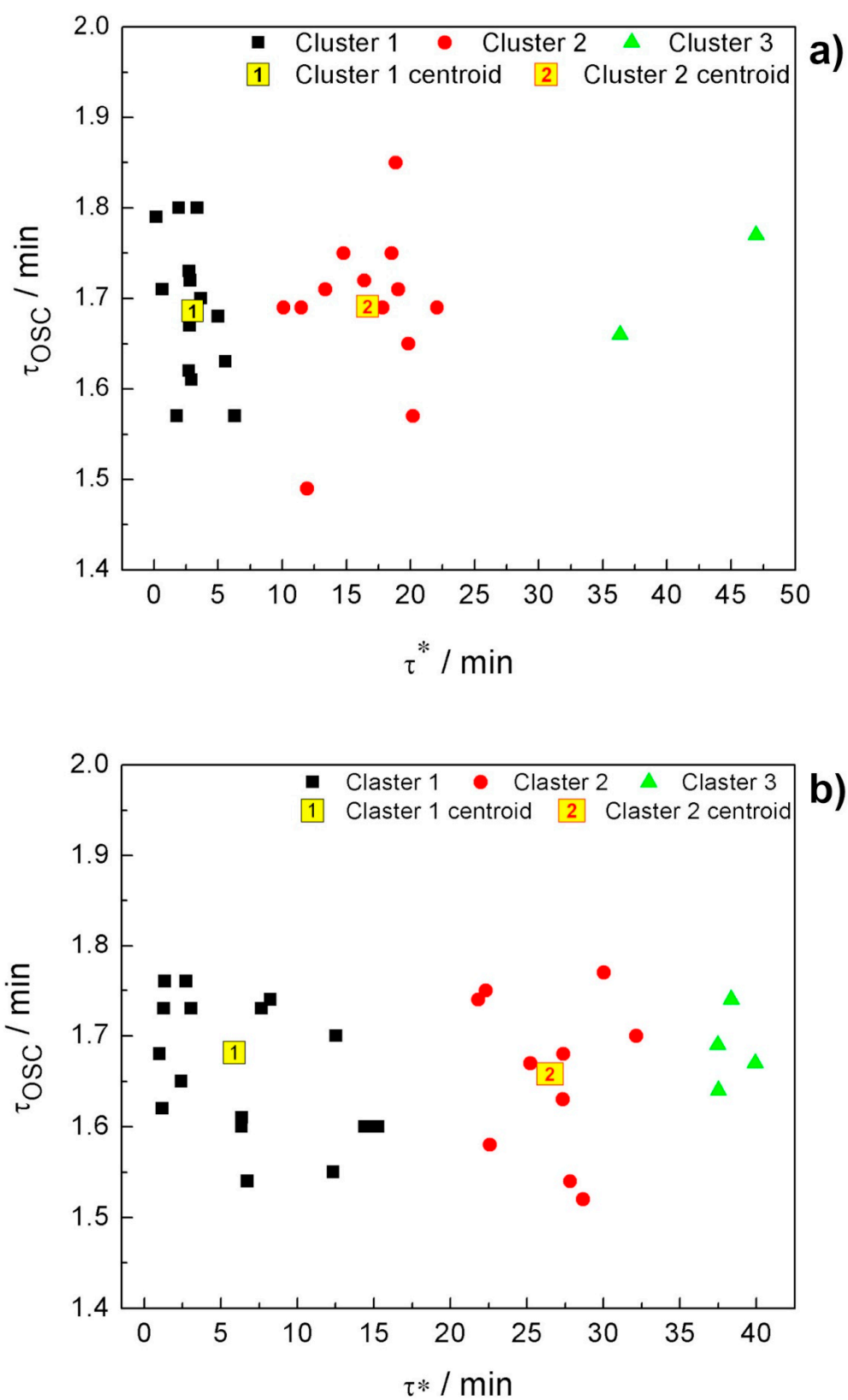**Figure 4.** Clusters obtained for thirty experiments run without stirring of the reaction mixture (**a**) and clusters obtained for thirty experiments run with stirring of reaction mixture in the vessel, stirring rate was 100 rpm (**b**). τ_{osc} is the BR oscillatory time, while τ^* denotes the time from the end of the oscillatory mode to the occurrence of state I→state II transition (see Figure 1).

The results presented in Table 1 clearly indicate that the investigated crazy-clock exhibits a truly random behavior. The shift (Figure 4a,b, Table 1) in the position of the cluster centroids towards higher τ^* values (i.e., a delaying time to transition to happen) can be observed for the case of applied stirring conditions. Due to a small number of members, the centroid of Cluster 3, in both cases, was not calculated. Furthermore, there is no significant change in the cluster's centroid position regarding τ_{osc} oscillatory coordinate for clusters. That leads to the conclusion that the transition from state I to state II is independent of oscillatory time duration or, in other words, that the minor differences in oscillatory period duration are not responsible for a significant deviation in transition appearance. Therefore, we calculated the optimal number of clusters by a one parameter (by parameter τ^*) K-means analysis, for no-mixing and mixing conditions (Figure 5a,b, respectively). The determination of optimal numbers of clusters was performed using gap method in fviz_nbclust alghoritm [26]. In brief, the gap statistic compares the total within intra-cluster variation for different values of k with their expected values under null reference distribution of the data. The estimate of the optimal clusters will be value that maximizes the gap statistic (i.e., that yields the largest gap statistic) [27].
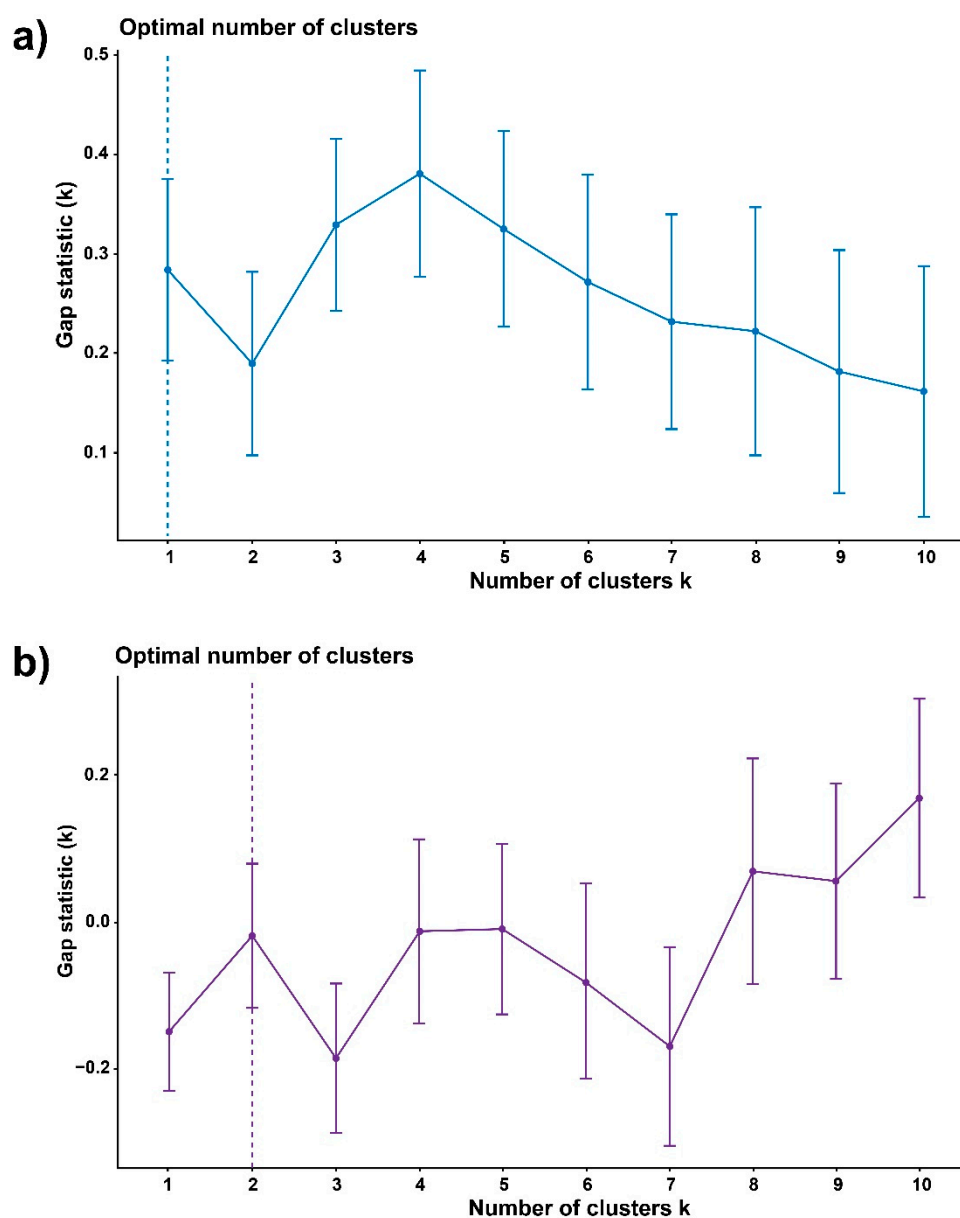
Figure 5. The optimal number of clusters for one parameter analysis by parameter τ^* (time when state I to state II transition occurs) for non-mixing conditions (**a**) and mixing conditions 100 rpm (**b**).

As it can be seen from the Figure 5 the optimal number of clusters obtained by using one parameter K-means analysis is changed. The BR system which is not stirred has one cluster (Figure 5a), while the stirring induces differentiation of two clusters (see Figures 5b and 6). The dimensions refer to the first two components. The fitviz_cluster function has been used to analyze the main components, after which the cluster is represented in the dimensions of the first two Principal Component Analysis (PCA) components. The clusters are well separated. This indicates that mixing introduced additional effects responsible for a significant cluster separation revealing the existence of time domains where the state I to state II transition is more likely to occur.
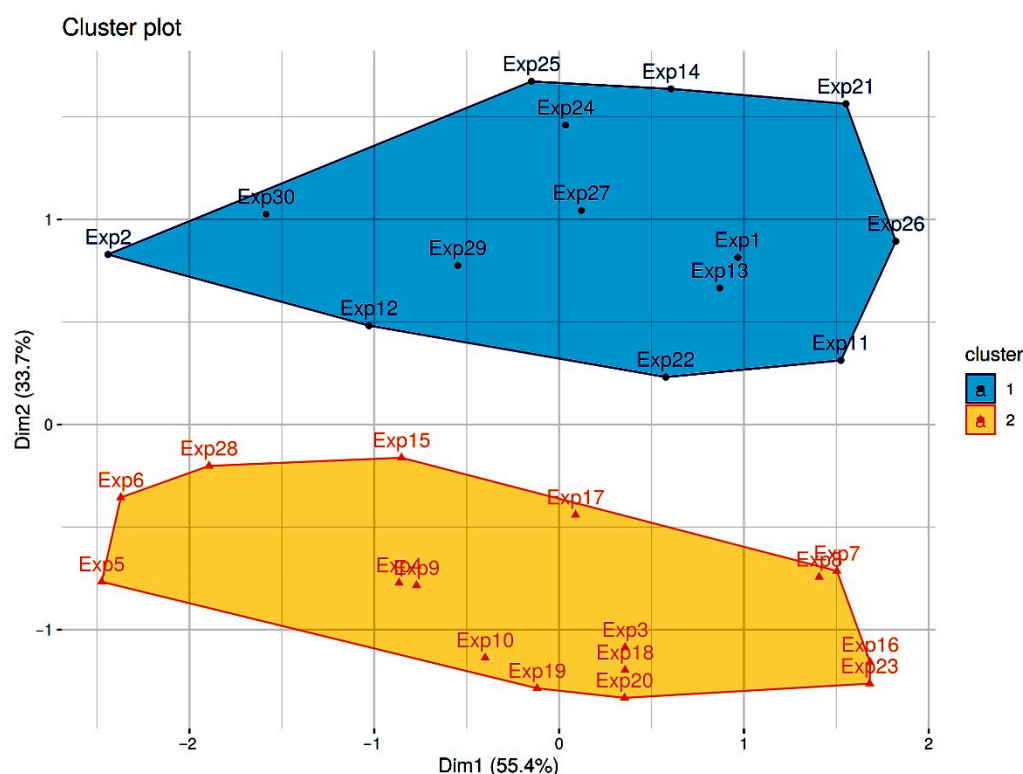

Figure 6. The evidence of two clusters for state I→state II transition obtained for mixing condition in BR system. Clusters are plotted in two dimensions (Dim1 and Dim2).

3.3. The State I→State II Phenomenon and Its Relation to (Spontaneous) Symmetry Breaking

The appearance of clusters indicates the existence of time domains where the state I to state II transition is more likely to occur. The stirring of the reaction mixture has a strong indirect influence on the state I→state II transition, delaying the crazy-clock behavior, shifting cluster centroids toward higher τ^* values, and increasing the cluster separation (i.e., time domain separation), as well. The existence of clusters could be connected to different nucleation and growth mechanisms of iodine crystals in the case of mixing [28], and further examination of solid iodine products would be the subject of future work.

However, if we assumed that state I (low iodide and iodine concentration) is the symmetric state, which under some conditions becomes absolutely unstable, then, reaching the state II (high iodide and iodine concentration, with a new I_2 solid phase) could be considered as spontaneous symmetry breaking [29], see Figure 7. Such an observation of state I to state II transition could also explain the persistence of the BR system "indefinitely" in the state I, as obtained for strong mixing condition (see Figure 3).
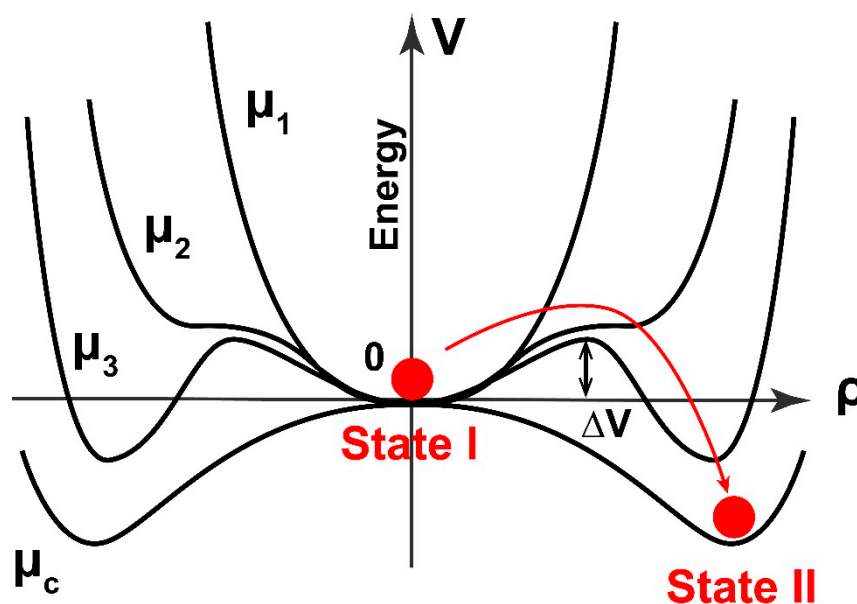
Figure 7. Possible symmetry breaking during the transition from the state I (low iodide and iodine concentration) to state II (high iodide and iodine, with segregation of solid iodine) in Briggs–Rauscher oscillatory reaction after an oscillatory period. Energetic consideration and symmetry breaking depending on control parameter, μ and ordering parameter, ϱ. ΔV corresponds to the energy threshold of the formation of solid iodine from chemical reactions that occur in the BR solution after oscillatory period.

Namely, in the case of the symmetry-breaking process, the system must overcome a sufficiently large energy barrier (as shown in Figure 7). Therefore, the system's state (state I, low iodide and iodine concentration) will remain unchanged until a sufficiently large perturbation throws it over the energy barrier, ΔV, which separates the states. We assume that ΔV corresponds to the energy threshold of the formation of solid iodine from chemical reactions that principally occur in the BR solution after the oscillatory period. It is well-known that the post-oscillatory period could be excitable [30,31], meaning that a nonlinear system can be shifted (perturbed) from one state to another. It is usually achieved by the addition of some stable intermediate or reactants, playing the role of an external perturbation, to the reaction mixture [32]. Since, in our case, there is no external perturbants/stimulus (all experiments are conducted under identical conditions, and the system remained under constant temperature), the BR system should find an internal stimulus to overcome the energy barrier. The mixing itself should not influence activation energies of chemical reactions responsible for state I to state II transition. In other words, the energy threshold (ΔV) should be identical for mixing and no-mixing condition. However, the system has behaved differently, and the state I to state II transition strongly depends on the mixing conditions. Therefore, some phenomena related to mixing are accountable for the obtained behavior. Figure 7 is a cartoon view that links thermodynamics (far from equilibrium) with kinetic processes driven by the gradient of diffusion/concentration. The changes in time of these local gradients are probably a source of fluctuations. When fluctuations reach a certain threshold (such as a critical number of interacted dissipative structures), a new order/phase spontaneously appears. Cluster analysis (Figures 4–6) allows us to group different dissipation architectures as a function of time.

The diffusion-driven instability combined with nonlinear chemical reactions (with autocatalytic steps and radical reactions) is a broad concept and it could be responsible for the "internal stimulus" necessary for passing the energy barrier. The diffusion-driven instability is intensified by gaseous oxygen and carbon dioxide/carbon monoxide, which are released in the BR solution during the oscillatory period [33]. Additionally, the pos-

sible energetic coupling between physical and chemical processes, such as the nucleation of gaseous phase (O_2 and/or CO_2), nucleation of solid iodine and particular chemical reactions, could also be considered as an "internal stimulus" necessary for overcoming the energy barrier and breaking symmetry [34–36].

This proposal is actually a reformulated original idea of Turing [37], where the interplay of chemical reactions and diffusion are responsible for pattern formation in living systems. As suggested by Prigogine, the spontaneous appearance of a spatial organization via diffusion-driven instability can be considered as a spontaneous symmetry-breaking transition [38]. In the presented work, we deal with a bulk solution and there is no visible spatial organization, but the spatial organization (spatiotemporal patterns) of the identical process (state I → state II transition in Briggs–Rauscher reaction) in a thin layer, is very recently found by Li and coworkers [15]. Therefore, this work indirectly links spontaneous symmetry breaking and crazy-clock behavior (stochastic nature) in the bulk. The stochastic nature of state I to state II transition and its relation to symmetry breaking (and pattern formation), introduced a new approach in the investigation of crazy-clock behavior. On the other hand, the investigation of chemical systems with stochastic nature and symmetry breaking could improve our understanding of more complex phenomena in living organisms, such as morphogenesis.

Additionally, this paper nominates state I → state II transition as an easily available chemical system for intrinsic random number generator and thus, expands the potential application of this crazy-clock reaction.

4. Conclusions

In this work, we further investigated the crazy-clock phenomenon (state I to state II transition) which occurs after a strongly reproducible Briggs–Rauscher oscillatory reaction. The mixing rate, as well as the magnetic bar shape and dimensions, have a strong influence on the transition appearance. In order to better understand the stochasticity of the mentioned process, we ran more than 60 experiments (30 experiments with mixing and 30 experiments with no-mixing conditions), and we applied the statistical cluster K-means analysis. Although the transition for both mixing and no-mixing conditions are taking place completely randomly, by using statistical cluster analysis, we obtained different number of clusters pointing to different time-domains where the transition is more likely to occur. Two-parameter analysis (by oscillatory time duration, τ_{osc} and by the moment when the transition occurs, τ^*) suggests that the state I → state II is independent of the oscillatory time duration. Therefore, we performed a one parameter analysis (by τ^*). In the case of no-mixing, we found one cluster, while the statistical analysis of the results for mixing conditions revealed two compact and well-separated clusters. The clustering method reveals new hidden details regarding the chemical dynamics of nonlinear processes. The state I to state II transition could be explained through a symmetry breaking approach, and the necessity of the BR system to overcome a sufficiently large energy barrier. This is the first link of the crazy-clock behavior to the symmetry breaking phenomenon. The investigation of chemical systems with stochastic nature and symmetry breaking could improve our understanding of more complex phenomena in living organisms and therefore the scope of the presented results goes beyond oscillatory reaction kinetics. Furthermore, the described example belongs to the small class of chemical systems that shows intrinsic randomness in their response and it might be considered as a real example of a classical liquid random number generator.

when 100 rpm mixing conditions is applied: [Malonic acid]$_0$ = 0.0789 M, [MnSO$_4$]$_0$ = 0.00752 M, [HClO$_4$]$_0$ = 0.03 M, [KIO$_3$]$_0$ = 0.0752 M, [H$_2$O$_2$]$_0$ = 1.176 M, T= 37.0 °C, reaction volume 25 mL.

Author Contributions: Conceptualization, M.C.P. and B.K.; methodology, M.C.P., J.P.M., Y.C., and B.K.; statistical K-means analysis M.D.; investigation, M.C.P. and J.P.M.; writing—original draft preparation, M.C.P. and B.K.; writing—review and editing, M.C.P., B.K., Y.C., S.R.M. and T.V.; visualization, J.P.M. and B.B. All authors have read and agreed to the published version of the manuscript.

Institutional Review Board Statement: Not applicable.

Informed Consent Statement: Not applicable.

Data Availability Statement: Data underlying the results presented in this paper are not publicly available at this time but may be obtained from the authors upon reasonable request. Please contact for this corresponding authors.

Conflicts of Interest: The authors declare no conflict of interest.

References

1. Gross, D.J. The role of symmetry in fundamental physics. *Proc. Natl. Acad. Sci. USA* **1996**, *93*, 14256–14259.
2. Smits, J.; Stoof, H.T.C.; Straten, P.V.D. Spontaneous symmetry breaking in a driven-dissipative system. *Phys. Rev. A* **2021**, *104*, 023318.
3. Briggs, T.S.; Rauscher, W.C. An oscillating iodine clock. *J. Chem. Educ.* **1973**, *50,* 496. https://doi.org/10.1021/ed050p496.
4. Bray, W.C. A periodic reaction in homogeneous solution and its relation to catalysis. *J. Am. Chem. Soc.* **1921**, *43*, 1262–1267. https://doi.org/10.1021/ja01439a007.
5. Bray, W.C.; Liebhafsky, H.A. Reaction involving hydrogen peroxide, iodine and iodate ion. *I. Introd. J. Am. Chem. Soc.* **1931**, *53*, 38–43.
6. Belousov, B.P. A periodic reaction and its mechanism, in collection of short papers on radiation medicine for 1958. *Medgiz* **1959**, 145–147.
7. Furrow, S.D. A modified recipe and variations for the briggs–rauscher oscillating reaction. *J. Chem. Educ.* **2012**, *89*, 1421–1424. https://doi.org/10.1021/ed200764r.
8. Furrow, S.D.; Noyes, R.M. The oscillatory Briggs-Rauscher reaction. 1. Examination of subsystems. *J. Am. Chem. Soc.* **1982**, *104*, 38–42. https://doi.org/10.1021/ja00365a009.
9. Noyes, R.M.; Furrow, S.D. The oscillatory Briggs-Rauscher reaction. 3. A skeleton mechanism for oscillations. *J. Am. Chem. Soc.* **1982**, *104*, 45–48. https://doi.org/10.1021/ja00365a011.
10. Schmitz, G.; Furrow, S. Kinetics of the iodate reduction by hydrogen peroxide and relation with the Briggs–Rauscher and Bray–Liebhafsky oscillating reactions. *Phys. Chem. Chem. Phys.* **2012**, *14*, 5711–5717. https://doi.org/10.1039/c2cp23805e.
11. Furrow, S.D.; Cervellati, R.; Greco, E. A study of the cerium-catalyzed briggs-rauscher oscillating reaction. *Z. Nat. B* **2012**, *67*, 89–97.
12. Vanag, V.K.; Alfimov, M.V. Light-induced nonequilibrium phase transition between quasistationary states of the Briggs-Rauscher reaction under batch conditions. *J. Phys. Chem.* **1993**, *97*, 1878–1883. https://doi.org/10.1021/j100111a027.
13. Vanag, V.K.; Alfimov, M.V. Effects of stirring on photoinduced phase transition in a batch-mode Briggs-Rauscher reaction. *J. Phys. Chem.* **1993**, *97*, 1884–1890. https://doi.org/10.1021/j100111a028.
14. Pagnacco, M.C.; Mojović, M.D.; Popović-Bijelić, A.D.; Horváth, A.K. Investigation of the halogenate–hydrogen peroxide reactions using the electron paramagnetic resonance spin trapping technique. *J. Phys. Chem. A* **2017**, *121*, 3207–3212. https://doi.org/10.1021/acs.jpca.7b02035.

15. Li, Z.; Yuan, L.; Liu, M.; Cheng, Z.; Zheng, J.; Epstein, I.R.; Gao, Q. The briggs–rauscher reaction: A demonstration of sequential spatiotemporal patterns. *J. Chem. Educ.* **2021**, *98*, 665–668.

16. Pagnacco, M.C.; Maksimović, J.P.; Potkonjak, N.I.; Božić, B..; Horváth, A.K. The transition from low to high iodide and iodine concentration state in the briggs rauscher reaction‐evidence on crazy clock behavior. *J. Phys. Chem. A* **2018**, *122*, 482–491. https://doi.org/10.1021/acs.jpca.7b11774.

17. Furrow, S.D.; Cervellati, R.; Greco, E. Study of the transition to higher iodide in the malonic acid Briggs–Rauscher oscillator. *React. Kinet. Mech. Catal.* **2015**, *118*, 59–71. https://doi.org/10.1007/s11144-015-0967-4.

18. Epstein, I.R. The consequences of imperfect mixing in autocatalytic chemical and biological systems. *Nature* **1995**, *374*, 321–327. https://doi.org/10.1038/374321a0.

19. Valkai, L.; Cseko, G.; Horvath, A.K. Initial Inhomogeneity-induced crazy-clock behavior in the iodate-arsenous acid reaction in a buffered medium under stirred batch conditions. *Phys. Chem. Chem. Phys.* **2015**, *17*, 22187–22194.

20. Andersen, A.; Madsen, J.; Reichelt, C.; Ahl, S.R.; Lautrup, B.; Ellegaard, C.; Levinsen, M.T.; Bohr, T. Double-slit experiment with single wave-driven particles and its relation to quantum mechanics. *Phys. Rev. E* **2015**, *92*, 013006.

21. Ellegaard, C.; Levinsen, M.T. Interaction of wave-driven particles with slit structures. *Phys. Rev. E* **2020**, *102*, 023115.

22. Murtagh, F. *Multidimensional Clustering Algorithms in COMPSTAT Lectures 4*; Physica-Verlag: Wuerzburg, Germany, 1985.

23. R Core Team. *R: A Language and Environment for Statistical Computing*; R Foundation for Statistical Computing: Vienna, Austria, 2018. Available online: https://www.R-project.org/ (accessed on 20 November 2021).

24. Horváth, A.K.; Nagypál, I. Classification of Clock Reactions. *ChemPhysChem* **2014**, *16*, 588–594. https://doi.org/10.1002/cphc.201402806.

25. Kaufman, L.; Rousseeuw, P.J. *Finding Groups in Data: An Introduction to Cluster Analysis*; John Wiley & Sons: New York, NY, USA, 2009.

26. Available online: https://cran.r-project.org/web/packages/factoextra/factoextra.pdf (accessed on 20 November 2021).

27. Tibshirani, R.; Walther, G.; Hastiee, T. Estimating the number of clusters in a data set via the gap statistic. *J. R. Stat. Soc. Ser. B (Stat. Methodol.)* **2001**, *63*, 411–423.

28. Pagnacco, M.C.; Maksimovic, J.P.; Jankovic, B.Z. Analysis of transition from low to high iodide and iodine state in the briggs–rauscher oscillatory reaction containing malonic acid using kolmogorov–johnson–mehl–avrami (kjma) theory. *React. Kinet. Mech. Catal.* **2018**, *123*, 61–80.

29. Genz, H. Symmetry and symmetry breaking in nature. *Interdiscip. Sci. Rev.* **1999**, *24*, 129–138. https://doi.org/10.1179/030801899678731.

30. Ruoff, P. Excitability in a closed stirred Belousov—Zhabotinskii system. *Chem. Phys. Lett.* **1982**, *90*, 76–80. https://doi.org/10.1016/0009-2614(82)83328-9.

31. Rouff, P. Excitability created by oxygen inhibition in the stirred malonic acid belousov-zabotinskii system. *Chem. Phys. Lett.* **1982**, *92*, 239–244.

32. Vukojevic, V.; Anic, S.; Kolar-Anic, L. Investigation of dynamic behavior of the bray–liebhafsky reaction in the CSTR. Properties of the system examined by pulsed perturbations with I^-. *Phys. Chem. Chem. Phys.* **2002**, *4*, 1276–1283.

33. Muntean, N.; Szabo, G.; Wittmann, M.; Lawson, T.; Fulop, J.; Noszticzius, Z.; Onel, L. Reaction routes leading to CO_2 and CO in the briggs−rauscher oscillator: Analogies between the oscillatory br and bz reactions. *J. Phys. Chem. A* **2009**, *113*, 9102–9108.

34. Bowers, P.G.; Noyes, R.M. Chemical oscillations and instabilities. 51. Gas evolution oscillators. 1. Some new experimental examples. *J. Am. Chem. Soc.* **1983**, *105*, 2572–2574. https://doi.org/10.1021/ja00347a010.

35. Sevcik, P.; Kissimonova, K.; Adamcikova, L. Oxygen Production in the oscillatory bray−liebhafsky reaction. *J. Phys. Chem. A* **2000**, *104*, 3958–3963.

36. Stevanovic, K.Z.; Bubanja, I.N.M.; Stanisavljev, D.R. is iodine oxidation with hydrogen peroxide coupled with nucleation processes? *J. Phys. Chem. C* **2019**, *123*, 16671–16680.

37. Turing, A.M. The chemical basis of morphogenesis. *Philos. Trans. R. Soc. B Biol. Sci.* **1952**, *237*, 37–72.

38. Prigogine, I.; Nicolis, G. On symmetry-breaking instabilities in dissipative systems. *J. Chem. Phys.* **1967**, *46*, 3542–3550.

PROCEEDINGS OF SPIE

Preservation of spatial entanglement in surface plasmon polaritons

Eckmann, Bruno, Stefanov, André, Gasparini, Leonardo, Perenzoni, Matteo, Kolaric, Branko

SPIE.

Preservation of Spatial Entanglement in Surface Plasmon Polaritons

Bruno Eckmann[a], André Stefanov[a], Leonardo Gasparini[b], Matteo Perenzoni[b], and Branko Kolaric[c,d]

[a]University of Bern, Switzerland
[b]Fondazione Bruno Kessler, Trento, Italy
[c]University of Mons, Belgium
[d]University of Belgrade, Serbia

ABSTRACT

We report on the characterization of spatial entanglement of photon pairs after their interaction with nanopillar arrays. We don't observe any significant change in spatial entanglement, thus concluding that spatial entanglement is preserved in the interaction.

Keywords: Spatial entanglement, SPAD array, Surface Plasmon Polaritons

1. INTRODUCTION

Spontaneous parametric downconversion (SPDC) is a common method to generate entangled light. When pumping a non-linear crystal with laser light, photon pairs are created that can be entangled in polarization, energy-time and/or space-momentum, depending on the phase matching conditions and on the pump energy and momentum bandwidths. Photonic entanglement is preserved in a similar way as light properties are preserved in linear coherent processes, such as reflection or refraction. Extraordinary transmission through sub-wavelength hole arrays[1] is explained by the excitation of surface plasmon polaritons, where the incoming photons are converted into surface plasmons which tunnel through the structure and finally re-radiate as photons. The questions then arises if photonic entanglement is preserved in such a process. In 2002, Altewischer et al.[2] studied this plasmon-assisted transmission for polarization-entangled photons. They discovered that the re-radiated photons are still entangled, leading to the conclusion that also the surface plasmon itself is. The fact that surface plasmons are collective charge density waves, consisting of billions of electrons makes this observation remarkable. The question of how far the features of quantum mechanics can be transferred into the mesoscopic (or even macroscopic) world arises. Other authors observed the survival of entanglement within this photon-plasmon-photon conversion for time-energy entanglement,[3,4] orbital angular momentum.[5] or photon number interferences.[6] However, the survival of space-momentum entangled photons in plasmonic interaction has not been demonstrated up to now. Here we report on the characterization of spatial entanglement of photon pairs after their interaction with nanopillar arrays.

In order to investigate spatial entanglement from a continuous entangled photon source at 810 nm, we make use of recently developed CMOS SPAD arrays with up to 224x272 pixels and 200 ps temporal resolution. Thanks to their high temporal resolution and high repetition rate, those sensors allow us to measure the full correlation map between each pixel pairs within a short time window and the acquisition time is competitive with commercial single photon sensitive CCD cameras. We further quantify the strength of the correlations in the near-field of the SPDC emission and of the anti-correlations in the far-field. The product of those quantities violates a classical inequality, proving the quantum nature of the correlations. We then measure the effect on this violation of placing gold nanopillar arrays either in the near- or in the far-field of the entangled source. We don't observe any significant change the correlation strength after interaction. As classical characterization and numerical simulation show that light at 810 nm interacts with the nanopillars, we can conclude that the light-pillar interaction still preserves spatial entanglement. Those results support previous demonstration of entanglement preservation and show the capability of SPAD array to be used in quantum optical experiments.

Send correspondence to A.S.
A.S.: E-mail: andre.stefanov@unibe.ch

2. EXPERIMENTAL SETUP

The experimental setup is shown in Fig. 1. In the following we list the components used in the experimental setup and discuss their properties and influencing factors on the experiment.

Pump Laser A continuous wave (cw) laser with a maximal power output of $80\,\mathrm{mW}$ at a wavelength of $405\,\mathrm{nm}$ serves as the pump. The laser is quasi-monochromatic with a spectral bandwidth of $80\,\mathrm{MHz}$.

Polarization The pump emits elliptically polarized light. To maximize the down-conversion rate, a $\lambda/4$- and a $\lambda/2$-plate are used to achieve the desired horizontal polarization.

Telescope A two lens system ($f_1 = f_2 = 200\,\mathrm{mm}$, $f_2 = 200\,\mathrm{mm}$) slightly focuses onto the crystal's center plane Σ_0. The beam waist of the pump at this plane is $w_{0x} = 250\,\mathrm{\mu m}$ and $w_{0y} = 300\,\mathrm{\mu m}$.

PPKTP Crystal A $1\,\mathrm{mm}^3 \times 2\,\mathrm{mm}^3 \times 12\,\mathrm{mm}^3$ periodically poled KTiOPO$_4$ (PPKTP) non-linear crystal $G_0 = 3.510\,43\,\mathrm{\mu m}$ embedded into a temperature controlled oven provides the source for the down-converted photons. The oven is maintained at a temperature of $26.0\,^\circ\mathrm{C}$ to maximize the photon flux onto the SuperEllen sensor in the far field. The phase mismatch Δk_{inf} is very sensitive to the poling period $G(T)$, which can be varied due to thermal expansion.

Bandpass Filter The down-converted photons are separated from the pump by the bandpass filter (BP) ($810\,\mathrm{nm}$, FWHM $10\,\mathrm{nm}$).

4f Imaging System Two lenses ($f_3 = f_4 = 50\,\mathrm{mm}$) form a $4f$ imaging system and provide near-field and far-field planes (Σ_{NF} and Σ_{FF}) where nanostructures can be placed. The electric field at the plane Σ_{NF} is an exact replica of the field at Σ_0.

Near-Field Imaging A lens $f_{NF} = 25.4\,\mathrm{mm}$ images the near-field plane Σ_{NF} onto the SuperEllen sensor with a magnification factor $M = 9$.

Far-Field Imaging A lense $f_{FF} = 150\,\mathrm{mm}$ images the far-field onto SuperEllen. The area covered by the sensor corresponds in k-space to $\pm 36.2\,\mathrm{mm}^{-1}$, as $q = x\frac{k}{f_{FF}}$.
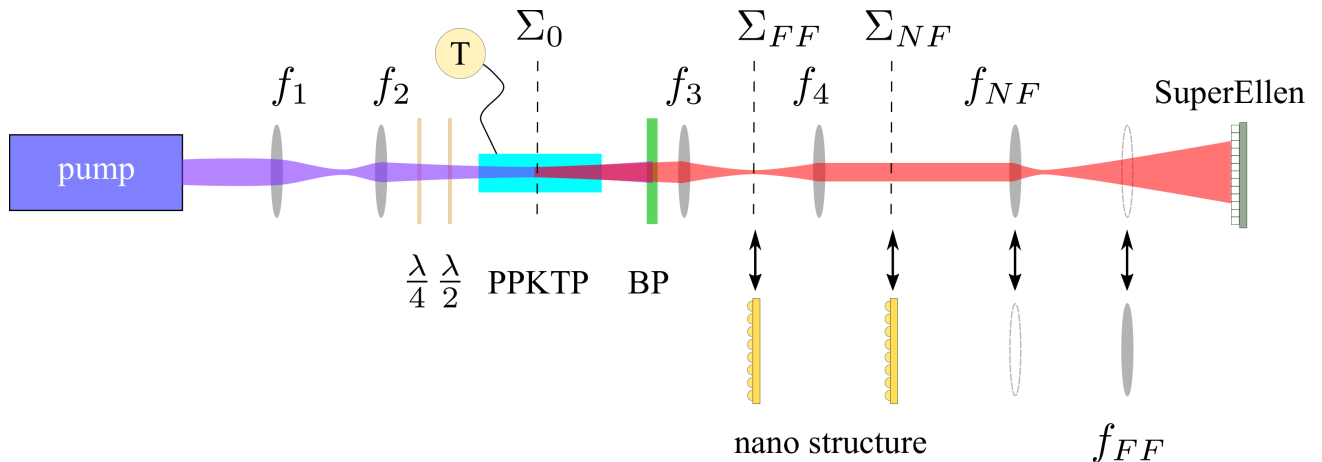
Figure 1: Experimental setup for the SPDC using a PPKTP nonlinear crystal. A cw laser at $405\,\mathrm{nm}$ is slightly focused by a telescope (f_1 and f_2) and pumps the crystal. The bandpass filter (BP) only transmits the down-converted photons at a central frequency of $810\,\mathrm{nm}$. The 4-f lens configuration (f_2 and f_3) create the fourier plane Σ_{FF} and near field plane Σ_{NF}. At these planes, a nanostrucure can be placed into the beam. Imaging onto the detector array SuperEllen occurs by either a 1 lens configuration f_{NF} for the near field or a fourier lens f_{FF} for the far field.

SuperEllen The single photon avalanche detector (SPAD) array SuperEllen[7] is kept fixed in place and the lenses f_{NF} and f_{FF} can be slided laterally into the beam path. SuperEllen is connected to a PC on which a LabView routine allows real-time observation and data acquisition. During the measurements, frames with less than 2 detection events are skipped in the acquisition, as we are only interested in correlated photon pairs. The exposure time is set to 30 ns and a coincidence window is defined to be 10 TDC units (~ 2 ns).

Nanostructures Are either placed in the far-field plane Σ_{FF} or near-field plane Σ_{NF}. The same nano structure samples were used to observe the survival and propagation of frequency-bin entangled photons.[4] The structure consists of hollow gold nano-pillar arrays (NPAs) and was fabricated using nanocoating lithography.[?] A transparent 100 µm polymer film (Zeon Corporation, ZF-14) serves as substrate. On the substrate, NPAs in a hexagonal pattern are arranged, where the width and height of the pillars are 200 nm, the thickness is 50 nm and the pillar-pitch is 460 nm, see Fig. 2 (a).
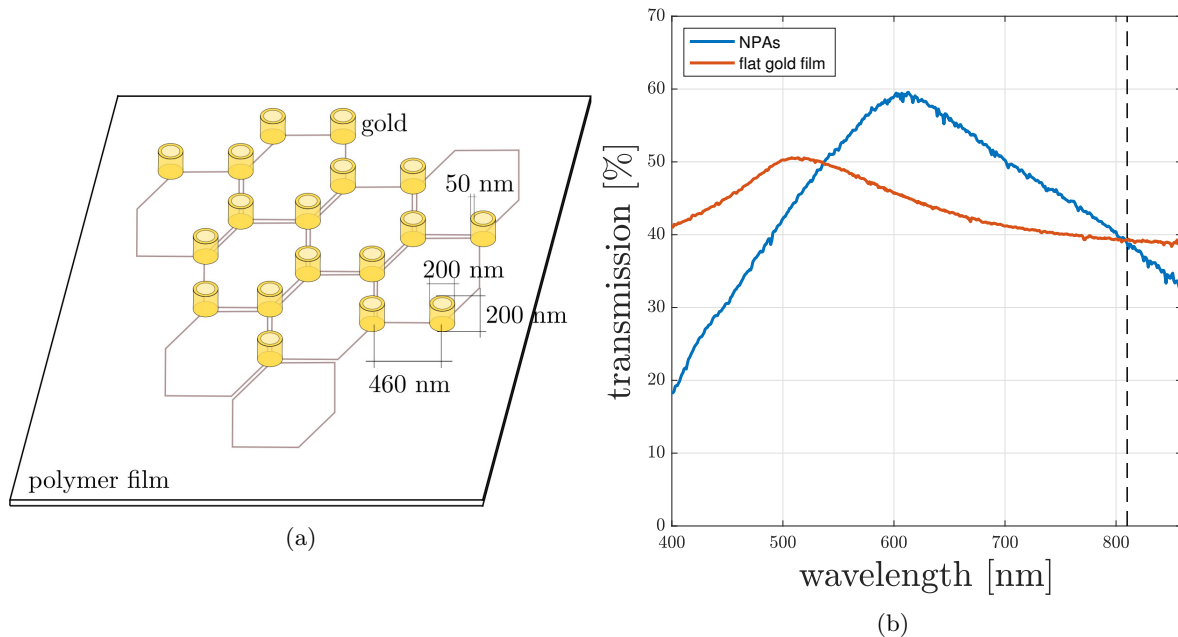

(a)

(b)

Figure 2: (a) Schematic of the nano pillar arrays (NPAs) used in the experiment. A polymere film (Zeon Corporation, ZF-14) serves as substrate and hollow nano pillars in a hexagonal pattern were fabricated by nanocoating lithography. (b) Transmission spectra of the NPAs and flat gold film. Both reach a transmission of 40% at 810 nm.

Entanglement has been characterized without and with the nano structure was placed either into the near-field plane Σ_{NF} or into the far-field plane Σ_{FF} (see Fig. 1) of the setup.

In order to prove entanglement, the following inequality has been tested, that relates the product of minimum inferred variances in the far- (momentum space q_x) and near-field (position space x) of a light source of two photons labeled 1 and 2. Its violation indicates EPR-type correlations, or entanglement

$$V_{min}^{(x)} \equiv \Delta^2_{min}(x_1|x_2)\Delta^2_{min}(q_{x_1}|q_{x_2}) > \frac{1}{4}. \tag{1}$$

The inequality can be rewritten in terms of the width of correlation and anti-correlation peaks, when fitted by Gaussian functions.

$$V_{min}^{(x)} \equiv \sigma^2_{x-}\sigma^2_{qx+} > 1. \tag{2}$$

3. RESULTS

The coincidence detection acquired with the SPAD array are processed (see[8] for the details) and the correlation and anti-correlation peaks are extracted for both the x and y directions (Fig. 3). From the width of the peaks, the value for the inequality are extracted and are $V_{min}^{(x)} = 1.7 \times 10^{-2}$ and $V_{min}^{(y)} = 1.4 \times 10^{-2}$ without nanostructure, $V_{min}^{(x)} = 3.5 \times 10^{-2}$ and $V_{min}^{(y)} = 2.2 \times 10^{-2}$ with the nanostructure in the near-field and $V_{min}^{(x)} = 4.3 \times 10^{-2}$ and $V_{min}^{(y)} = 2.5 \times 10^{-2}$ when placed in the far-field. When no nano-structure is present, all methods show that the biphoton state is indeed of EPR-type and thus the photons are entangled. When NPAs are placed at Σ_{NF} or Σ_{FF} the intensity of the measured signal is reduced and the signal-to-noise ratio drops dramatically. While the anti-correlation peak stays almost identical, we observe a slight broadening of the correlation peak. Crosstalk is an effect of the sensor that triggers nearby pixels after a pixel was triggered by an actual detection. This leads to a rate of false coincidence detection, that are spatially correlated. From an estimation of the crosstalk probability, this effect can be corrected for.[8] However, as the signal is lower, the corrected signal is more prone to bias. This could explain the larger correlation peak. Measurements with a higher density resolution sensor would allow for a better suppression of the crosstalk effects.

4. CONCLUSION

The survival of spatial entanglement in the interaction of light with nano pillar arrays has been demonstrated by a simple estimate using the correlation and anti-correlation peak of the near- and far-field, respectively, instead of analyzing the full second order correlations. When placed in the near-field, the plasmonic excitations due to the two photons are located within the entanglement area of the SPDC (few micrometers), while in the far-field, the two entangled plasmons are separated at the millimetre scale. As the process is coherent, entanglement was expected to be preserved but the experiment nevertheless demonstrates the persistence of photonic entanglement, not only in polarization and energy degrees of freedom but also for momentum and transverse position. Hence, applications of spatial entanglement, such as quantum imaging, could be implemented in nanophotonics structure.

ACKNOWLEDGMENTS

REFERENCES

[1] Ebbesen, T. W., Lezec, H. J., Ghaemi, H. F., Thio, T., and Wolff, P. A., "Extraordinary optical transmission through sub-wavelenght hole arrays," *Nature* **391**(6668), 667–669 (1998).

[2] Altewischer, E., van Exter, M. P., and Woerdman, J. P., "Plasmon-assisted transmission of entangled photons," *Nature* **418**, 304–306 (jul 2002).

[3] Fasel, S., Robin, F., Moreno, E., Erni, D., Gisin, N., and Zbinden, H., "Energy-time entanglement preservation in plasmon-assisted light transmission," *Physical Review Letters* **94**(11), 1–4 (2005).

[4] Olislager, L., Kubo, W., Tanaka, T., Ungureanu, S., Vallée, R. A., Kolaric, B., Emplit, P., and Massar, S., "Propagation and survival of frequency-bin entangled photons in metallic nanostructures," *Nanophotonics* **4**(1), 324–331 (2015).

[5] Ren, X. F., Guo, G. P., Huang, Y. F., Li, C. F., and Guo, G. C., "Plasmon-assisted transmission of high-dimensional orbital angular- Momentum entangled state," *Europhysics Letters* **76**(5), 753–759 (2006).

[6] Heeres, R. W., Kouwenhoven, L. P., and Zwiller, V., "Quantum interference in plasmonic circuits," *Nature Nanotechnology* **8**(10), 719–722 (2013).

[7] Zarghami, M., Gasparini, L., Parmesan, L., Moreno-Garcia, M., Stefanov, A., Bessire, B., Unternahrer, M., and Perenzoni, M., "A 32 × 32-Pixel CMOS Imager for Quantum Optics With Per-SPAD TDC, 19.4844.64-μm Pitch Reaching 1-MHz Observation Rate," *IEEE Journal of Solid-State Circuits* **55**, 2819–2830 (oct 2020).

[8] Eckmann, B., Bessire, B., Unternährer, M., Gasparini, L., Perenzoni, M., and Stefanov, A., "Characterization of space-momentum entangled photons with a time resolving CMOS SPAD array," *Optics Express* **28**, 31553 (oct 2020).

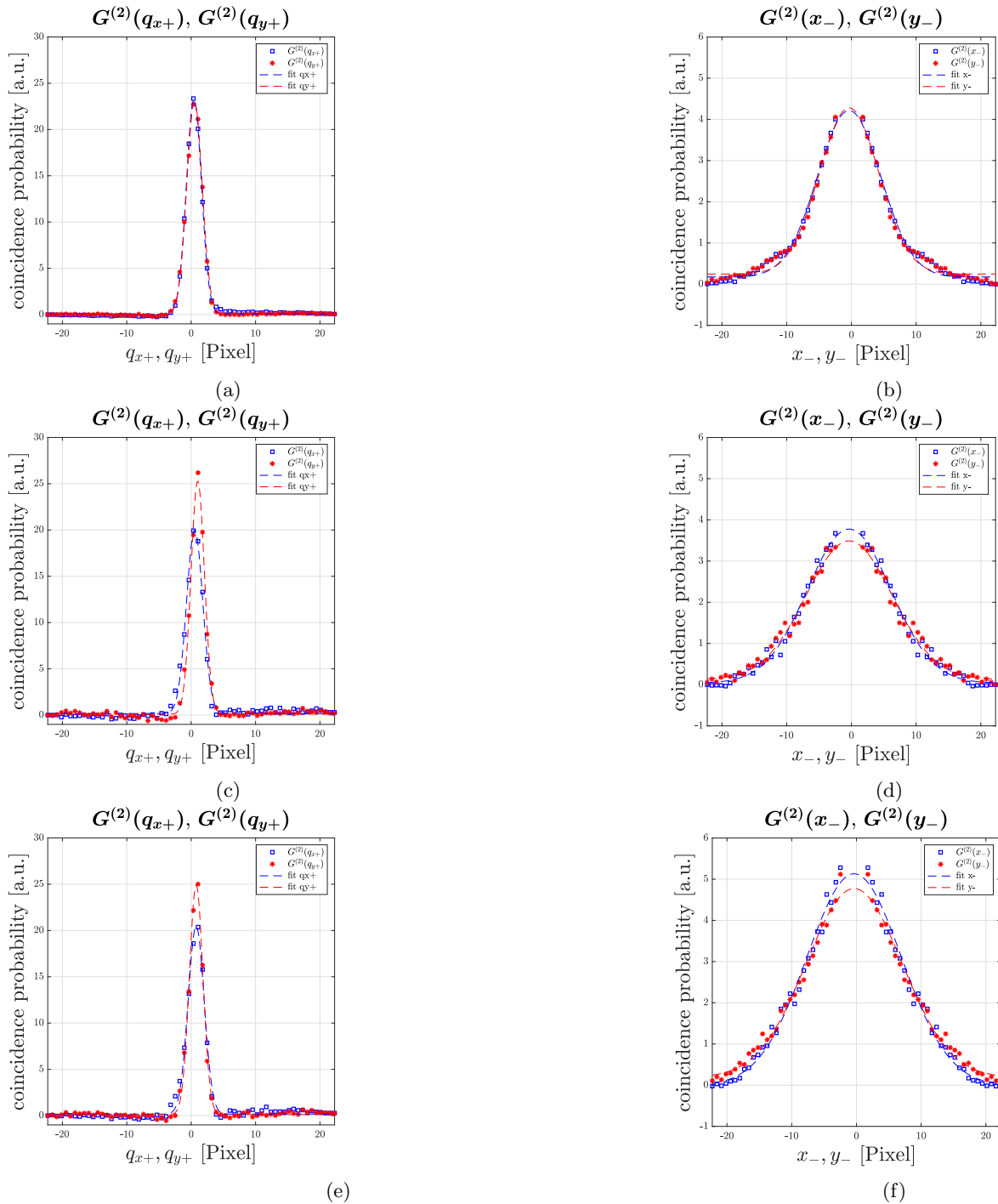Figure 3: Anti-correlations peaks (a, c, e) of the second order correlations in the far-field and correlation peaks (b,d,f) from near-field measurements. In (a,b) no structure is present, in (c,d) the NPAs are placed in the near-field plane, in (e,f) the NPAs are placed in the far-field plane. The width of the peak only increases slightly when a nanostructure is present, which indicates that the entanglement is mostly preserved.

Molecular dysprosium complexes for white-light and near-infrared emission controlled by the coordination environment

Dimitrije Mara [a,*], Flavia Artizzu [b,c], Joydeb Goura [b], Manjari Jayendran [b], Bojana Bokić [d], Branko Kolaric [d,e], Thierry Verbiest [a], Rik Van Deun [b,**]

[a] *Molecular Imaging and Photonics, Department of Chemistry, KU Leuven, Celestijnenlaan 200 D, box 2425, B-3001, Leuven, Belgium*
[b] *L³ – Luminescent Lanthanide Lab, Department of Chemistry, Ghent University, Krijgslaan 281 – S3, B-9000, Ghent, Belgium*
[c] *Department of Sciences and Technological Innovation, University of Eastern Piedmont "Amedeo Avogadro", Viale Teresa Michel 11, 15112, Alessandria, Italy*
[d] *Photonics Center, Institute of Physics, University of Belgrade, Pregrevica 118, 11080, Belgrade, Serbia*
[e] *Micro- and Nano-photonics Materials Group, University of Mons, Avenue Maistriau 19, B-7000, Mons, Belgium*

ARTICLE INFO

ABSTRACT

A series of single-molecule dysprosium (Dy^{3+}) complexes consisting of β-diketonate ligands, L_1 = 4,4,4-trifluoro-1-phenyl-1,3-butadionate and L_2 = 4,4,4-trifluoro-1-(4-chlorophenyl)-1,3-butadionate, as water-containing complexes, and the auxiliary triphenylphosphine oxide (tppo) ligand as water-free complexes were investigated as potential white-light emitters. The coordination environment and choice of the ligands play an important role in the behavior of the yellow/blue emission of the Dy^{3+} complexes (Y: $^4F_{9/2} \rightarrow {}^6H_{13/2}$ – yellow, and B: $^4F_{9/2} \rightarrow {}^6H_{15/2}$ and ligand phosphorescence – blue) based on the sensitization efficiency of the Dy^{3+} ion by the ligands. By introducing the auxiliary tppo ligand in the complex, the relative intensity of the Dy^{3+} emission increases due to a more efficient sensitization of the Dy^{3+} ion. The CIE (Commission International d'Eclairage) coordination at room temperature for water-containing, **DyL₁H₂O** (0.340, 0.333), and **DyL₂H₂O** (0.270, 0.249), and for water-free complexes, **DyL₁tppo** (0.364,0.391) and **DyL₂tppo** (0.316, 0.331), are close to the co-ordinates of 'ideal' white light (0.333, 0.333). The CCT (Correlated Color Temperature) values at room temperature for **DyL₁H₂O** (5129 K), **DyL₂H₂O** (18,173 K), and **DyL₂tppo** (6319 K) correspond to 'cold-white-light' emitters, while the **DyL₁tppo** (4537 K) matches a 'warm-white-light' emitter. Beside emitting in the visible (Vis) region, the Dy^{3+} complexes also show emission in the near-infrared (NIR) part of spectrum, which has been studied in detail.

1. Introduction

The growth of the global energy consumption has accelerated development and usage of energy-saving smart devices and energy-efficient solid-state lighting (SSL). Solid-state white-light-emitting materials posses exceptional properties such as energy saving and long operational lifetime, which has already led to their widespread application covering large-panel displays to ambient lighting [1–3]. First, the SSL sources can be subdivided based on the materials, from which they are made of, either inorganic phosphors (LED) or organic molecule semiconductors (OLDE). From another perspective, the SSLs are subdivided in two categories based on the way they are stimulated to emit light, that is, by UV excitation (LEDs) or by electrical excitation (OLEDs).

SSLs are much more efficient compared to the classical incandescent lamps, or environmentally friendly as compared to fluorescent and mercury lamps [4–6].

In general, there are two different approaches to obtain white-light emission (WLE): using dichromatic emitters (blue and yellow (B/Y) or blue and red (B/R)), or by using trichromatic emitters which combine the three primary colors (red, green, and blue (RGB)) [1,7–19]. White light is obtained by using separate dopants or multiple phase matrices such as organic compounds, metal complexes, nanomaterials, hybrid organic-inorganic materials or inorganic phosphors. All these types of materials have some unique characteristics to exploit their advantages in obtaining white light, but sometimes it is necessary to mix different types of materials to achieve the intended goal. On the other hand,

---

white-light emission (WLE) from single molecules can also be achieved, spanning the whole visible (Vis) spectrum [20–25]. The advantage of such systems is that they consist of a single phase single emitter, and this simplifies the production of lighter and thinner materials, which is highly favorable for the implementation of optical devices [26].

Additionally, because of the unique properties of the lanthanide (Ln^{3+}) ions, lanthanide complexes, are interesting platforms for applications in lighting technologies. The Ln^{3+} luminescence arises from 4f – 4f transitions, which correspond to characteristic colors (wavelengths) from the ultra-violet (UV) across the Vis to the near-infrared (NIR) spectral region. Unfortunately, the 4f – 4f transitions are difficult to excite directly according to Laporte's rule and a way to overcome this disadvantage is by using organic chromophores which act as antenna to sensitize the Ln^{3+} ions [27]. β-Diketonate complexes are well known in lanthanide coordination chemistry and have been studied in extent [28, 29]. Their ability to excite virtually every spectroscopically active Ln^{3+} ion to obtain the pure Ln^{3+} luminescence colors, as well as their processability into more complex matrices creates the opportunity for a wide range of applications, such as lighting, ion sensing, temperature sensing, telecommunications, etc. [30–33] The organic chromophores in this case should be designed or chosen to act as antennas for the Ln^{3+}, but at the same time they should be able to emit by themselves to yield the blue component necessary to obtain white light. The design of such WLE Ln^{3+} complexes is in fact typically based on the combination of an organic chromophore which emits in the blue region, with a Ln^{3+} ion that emits in the yellow (Dy^{3+}) or in the red (Eu^{3+}) region [34–50].

Here, we present a series of single-molecule WLE tris Dy^{3+} β-diketonate complexes of two different β-diketonate ligands (4,4,4-trifluoro-1-phenyl-1,3-butadionate and 4,4,4-trifluoro-1-(4-chlorophenyl)-1,3-butadionate), with either coordinated water molecules or triphenylphosphine oxide (tppo) as co-ligand, which can be excited at 365 nm [50,51]. Simultaneous emission from the ligand and Dy^{3+} has been observed, giving rise to WLE, which by modifying the coordination environment, could be altered from deep cold (blue) to warm (yellow) white light. In addition to white emission in the Vis region, the series of Dy^{3+} complexes also showed emission in the NIR spectral region.

2. Experimental Section

2.1. Materials

$DyCl_3 \cdot 6H_2O$ (99.9%), 4,4,4-trifluoro-1-phenyl-1,3-butadione (Hbfa) 99% and triphenylphosphine oxide 98% were purchased from Sigma Aldrich. The 4,4,4-trifluoro-1-(4-chlorophenyl)-1,3-butadione 98% was purchased from TCI Europe. Methanol (laboratory grade, 100%) and NaOH were purchased from Fisher Scientific. All chemicals were used without further purification. All reaction were carried out under atmospheric conditions.

2.2. Synthesis of [Dy($L_{1(2)}$)₃(H_2O)₂] and [Dy($L_{1(2)}$)₃(tppo)₂] complexes

The synthesis procedure has been previously reported in detailed and will be only discussed in short [51]. The synthesis of [Dy($L_{1(2)}$)₃(H_2O)₂] was done in methanol by first dissolving an appropriate amount of ligand L_1 and L_2 (0.9 mmol), which were then deprotonated with an equimolar amount of NaOH prior to the addition of methanol solution of $DyCl_3 \cdot 6H_2O$ (0.3 mmol). The obtained crystals were recrystallized from methanol solution and used for further analysis. The synthesis of [Dy($L_{1(2)}$)₃(tppo)₂] was done in methanol, by addition of a methanol solution of [Dy($L_{1(2)}$)₃(H_2O)₂] (0.1 mmol) to dissolve triphenylphosphine oxide (tppo) (0.2 mmol) and the complexes were used without any additional purification. No crystals suitable for single crystal X-ray diffraction could be obtained due to the formation of twinned crystals during crystallization.

[Dy(L_1)₃(H_2O)₂] **DyL₁H₂O**: Elemental analysis (%) calculated for $C_{30}H_{22}F_9O_8Dy$ (847.00): C 42.54, H 2.98, found: C 42.45, H 2.93. FT-IR

(KBr) ν_{max} (cm^{-1})): 3657 (s; ν_{st} O–H, free), 3449 (w; ν_{st} O–H, H-bonded), 3083, 2774, 2601, 2525 (w; ν_{st} C–H and Fermi resonance), 2482, 2381, 2321, 2273, 2229, 2137 (w; aromatic overtone), 2085 2044, 1985, 1908, 1863, 1820, 1775 (w; comb, aromatic), 1667 (w; ν_{st} C=O, keto form), 1628, 1571, 1532, 1493, 1467 (w; ν_{st} ar C–C), 1379, 1288 (w; ν_{st} C–F, CF3), 1249, 1197, 1144 (w; ν_{st} C–F, CF3 and δip ar C–H), 1096 (w), 1027 (s; δip ar C–H), 996 (s; δoop C–H), 817 (w; γ ar C–C and ν_{st} C–Cl), 773, 721 (w; δ C–F, CF3, δoop C–H and γ ar C–C and ν_{st} C–Cl). ESI-MS (negative mod, -), *m/z*: 868.00 [M + Na–2H]⁻, 1023.97 [M+2Br + H]⁻ Isotope used for calculation is ^{164}Dy.

[Dy(L_2)₃(H_2O)₂] **DyL₂H₂O**: Elemental analysis (%) calculated for $C_{30}H_{19}Cl_3F_9O_8Dy$ (950.33): C 37.92, H 2.33; found: C 37.88, H 2.25. FT-IR (KBr) ν_{max} (cm^{-1}): 3657 (s; ν_{st} O–H, free), 3434 (s; ν_{st} O–H, H-bonded), 3072, 2779, 2677, 2591 (w; ν_{st} C–H and Fermi resonance), 2508, 2434, 2389, 2327, 2286, 2232 (w; aromatic overtone), 2096, 2051, 1911, 1796 (w; comb, aromatic), 1681 (w; ν_{st} C=O, keto form), 1627, 1574, 1536, 1487, 1463 (w; ν_{st} ar C–C), 1401, 1359, 1294 (w; ν_{st} C–F, CF3), 1248, 1191, 1146 (w; ν_{st} C–F, CF3 and δip ar C–H), 1096 (w), 1014 (s; δip ar C–H), 944 (s; δoop C–H), 849 (w; γ ar C–C and ν_{st} C–Cl), 799, 738, 705, 664 (w; δ C–F, CF3, δoop C–H and γ ar C–C and ν_{st} C–Cl). ESI-MS (negative mod, -), *m/z*: 972.00 [M + Na–2H]⁻, 1159.00 [M+2Br + H]⁻. Isotope used for calculation is ^{164}Dy.

[Dy(L_1)₃(tppo)₂] **DyL₁tppo**: Elemental analysis (%) calculated for $C_{66}H_{48}F_9O_8P_2Dy$ (1367.54): C 57.97, H 3.76; found: C 57.88, H 3.70. FT-IR (KBr) ν_{max} (cm^{-1}): 3267, 3147 (w; ν_{st} C–O, enol beyond the range), 3061 (s; ν_{st} ar C–H), 2965, 2913, 2771, 2710, 2599 (w; ν_{st} C–H and Fermi resonance), 2520, 2471, 2434, 2381, 2323, 2278, 2129 (w; aromatic overtone), 2088, 2030, 1969, 1895, 1820 (w; comb, aromatic), 1776, 1713 (w; ν_{st} C=O, keto form), 1656, 1577, 1535, 1491, 1442 (w; ν_{st} ar C–C), 1376, 1323 (w; ν_{st} C–F, CF3), 1290 (w; ν_{st} P=O), 1244, 1199, 1146 (w; ν_{st} C–F, CF3, δip ar C–H and ν_{st} R3P=O), 1094, 1075, 1026 (s; δip ar C–H and ν_{st} R3P=O), 997, 972 (w; ν_{st} R3P=O), 943 (s; δoop C–H and ν_{st} R3P=O), 848, 807, 795 (w; γ ar C–C and ν_{st} P–C), 758, 725, 635 (w; δ C–F, CF3, δoop C–H and γ ar C–C). ESI-MS (positive mode +), *m/z*: 1428.00 [M + Na + ACN]⁺, 1150.00 [M-tppo + Na + ACN]⁺, 870.00 [M-2tppo + Na]⁺. Isotope used for calculation is ^{164}Dy.

[Dy(L_2)₃(tppo)₂] **DyL₂tppo**: Elemental analysis (%) calculated for $C_{66}H_{45}Cl_3F_9O_8P_2Dy$ (1470.87): C 53.89, H 3.29; found: C 53.80, H 3.25. FT-IR (KBr) ν_{max} (cm^{-1}): 3265, 3146 (w; ν_{st} C–O, enol beyond the range), 3060 (s; ν_{st} ar C–H), 2961, 2920, 2829, 2768, 2714, 2586 (w; ν_{st} C–H and Fermi resonance), 2467, 2380, 2327, 2286, 2249, 2129 (w; aromatic overtone), 2088, 2039, 1964, 1898, 1820 (w; comb, aromatic), 1776 (w; ν_{st} C=O, keto form), 1627, 1594, 1533, 1483, 1438 (w; ν_{st} ar C–C), 1380, 1318 (w; ν_{st} C–F, CF3), 1288 (w; ν_{st} P=O), 1240, 1187, 1141 (w; ν_{st} C–F, CF3, δip ar C–H and ν_{st} R3P=O), 1088, 1067, 1030 (s; δip ar C–H and ν_{st} R3P=O), 1014, 972 (w; ν_{st} R3P=O), 930 (s; δoop C–H and ν_{st} R3P=O), 849, 783 (w; γ ar C–C and ν_{st} P–C), 725, 693, 660 (w; δ C–F, CF3, δoop C–H and γ ar C–C). ESI-MS (positive mode +), *m/z*: 1497.87 [M + Na + ACN]⁺, 1218.87 [M-tppo + Na + ACN]⁺, 980.00 [M-2tppo + Na]⁺. Isotope used for calculation is ^{164}Dy.

2.3. Characterization

Luminescence measurements were performed on an Edinburgh Instruments FLSP920 UV–Vis–NIR spectrometer setup. A 450 W Xe lamp was used as steady-state excitation source. Time-resolved measurements were recorded using a 60 W Xe lamp operating at frequency of 100 Hz. A Hamamatsu R928P photomultiplier tube was used to detect emission signal in the visible region. A Hamamatsu R5509-72 multiplier tube was used to detect emission in the NIR region. The absolute quantum yield (QY) of the complex was determined using an integrating sphere coated with BENFLEC (provided by Edinburgh Instruments) and calculated using Equation (1):

$$\eta = \frac{\int L_{emission} d\lambda}{\int E_{blank} d\lambda - \int E_{sample} d\lambda} \tag{1}$$

Where $L_{emission}$ is the integrated area under the emission spectrum (dλ = 400–700 nm), E_{blank} is the integrated area under the "excitation" band of the blank, and E_{sample} is the integrated area under the excitation band of the sample (as the samples absorbs part of the light, this area will be smaller than E_{blank}). All luminescent measurements were recorded at room temperature. Crystals were put between quartz plates (Starna cuvettes for powder samples, type 20/C/Q/0.2). The time-resolved data were fitted with a biexponential function where the short component (in the range from 1.4 to 1.9 µs) is attributed to the Xe lamp signal, while the longer component is associated to the emission signal of the Dy^{3+} complexes and are presented in Tables 1 and 2. Only for the samples DyL$_1$tppo and DyL$_2$tppo the emission signal at ~995 nm, with a significantly longer decay time, was fitted with a monoexponential function.

Fourier Transform Infrared (FTIR) spectra were acquired in the region of 400–4000 cm^{-1} with a Thermo Scientific Nicolet 6700 FT-IR spectrometer equipped with a nitrogen-cooled Mercury Cadmium Telluride (MCT) detector and KBr beam splitter; samples were measured in KBr pellets. Elemental analysis (C, H, N) was performed on a Thermo Fisher 2000 elemental analyzer, using V_2O_5 as catalyst. ESI-MS was performed on an Agilent 6230 time-of-flight mass spectrometer (TOF-MS) equipped with Jetstream ESI source and positive and negative ionization modes were used.

3. Results and discussion

3.1. Synthesis and characterization of Dy^{3+} complexes

The complexes were synthesized using mild reaction conditions, where the β-diketonate ligand was deprotonated with an equimolar amount of sodium hydroxide and reacted with the Dy^{3+} ion in a stoichiometric ratio in methanol. The high reactivity of the β-diketonate ligand toward coordination to Dy^{3+} ions prevents the formation of highly insoluble lanthanide hydroxides, which could be formed under basic conditions. The complexes with formula $[Dy(L_1)_3(H_2O)_2]$ (L_1 = 4,4,4-trifluoro-1-phenyl-1,3-butadionate) and $[Dy(L_2)_3(H_2O)_2]$ (L_2 = 4,4,4-trifluoro-1-(4-chlorophenyl)-1,3-butadionate) were isolated. The synthesis of water-free complexes was performed by introducing tppo in methanol solution in a stochiometric ratio to the $[Dy(L_{1(2)})_3(H_2O)_2]$ complex to form and isolate the water-free complexes with formula $[Dy(L_1)_3(tppo)_2]$ and $[Dy(L_2)_3(tppo)_2]$. These complexes have been characterized by FT-IR, ESI-MS (see SI Figs. S1-S8) and elemental analysis which confirmed that all the complexes have the same composition as the previously reported analogs [51,52].

3.2. Steady-state and time-resolved photoluminescence (PL) studies

3.2.1. Steady-state and time-resolved PL of Dy^{3+} complexes in the visible region

Upon excitation into the β-diketonate ligand absorption band (see SI Figs. S9-S12) with UV light all studied Dy^{3+} complexes showed emission in the Vis and NIR spectral range displaying the characteristic Dy^{3+} peaks. In Fig. 1, the PL emission spectra of **DyL$_1$H$_2$O**, **DyL$_1$tppo** (a), **DyL$_2$H$_2$O** and **DyL$_2$tppo** (c) are presented. The Dy^{3+} $^4F_{9/2} \rightarrow {}^6H_{15/2}$ transition appearing at 480 nm, the $^4F_{9/2} \rightarrow {}^6H_{13/2}$ transition at 575 nm and the $^4F_{9/2} \rightarrow {}^6H_{11/2}$ transition at 660 nm are clearly observed. Besides the emission peaks of the Dy^{3+} ion, a broad band (400–450 nm) with a peak maximum at ~ 430 nm is observed, which is assigned to ligand-centered emission. In water-free complexes the relative intensity of this broad band is lower as compared to its intensity in water-containing complexes. The advantage of the introduction of the tppo ligand into the water-containing complexes brings two benefits: first, the exclusion of water molecules from the first coordination sphere around the Dy^{3+} ion
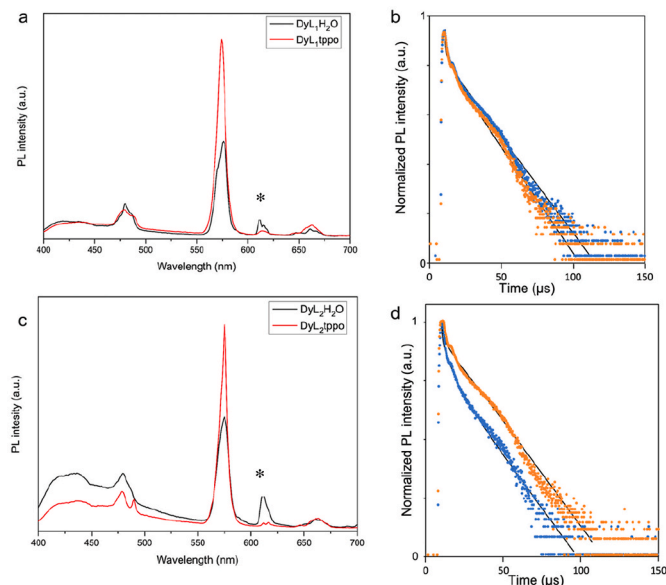

Fig. 1. (a) PL emission spectra of DyL$_1$H$_2$O and DyL$_1$tppo, excited at 365 nm and measured at RT; (b) decay profile of DyL$_1$H$_2$O (blue) and DyL$_1$tppo (orange) observed at 575 nm; (c) PL emission spectra of DyL$_2$H$_2$O and DyL$_2$tppo, excited at 365 nm and measured at RT; (d) decay profile of DyL$_2$H$_2$O (blue) and DyL$_2$tppo (orange) observed at 575 nm * Contamination of the DyCl$_3$•6H$_2$O salt with europium salts not influencing the photophysics of Dy^{3+}. (For interpretation of the references to color in this figure legend, the reader is referred to the Web version of this article.)

(reducing quenching) and second, a more efficient energy transfer from the tppo ligand to Dy^{3+}, increasing the relative intensity of the metal peaks in the emission spectra in comparison to the ligand band (Fig. 1 a and c).

Time-resolved measurements (Fig. 1 and Table 1) show that the decay dynamics of the Dy^{3+} $^4F_{9/2}$ level is monoexponential and that the water-free complexes have slightly longer luminescent lifetimes compared to the water-containing complexes, likely because of the reduced quenching efficiency by high-energy oscillators related to the water molecules in the first coordination sphere. The sensitization efficiency of the Dy^{3+} ion in the water-free complexes is estimated to be slightly higher as well, because of the possible contribution of the tppo co-ligand to the process. In fact, to realize an efficient energy transfer (ET), the difference between the energy donor, being the triplet state (T_1) of the ligand, and the acceptor, being the emitting level of the Ln^{3+} ion, should be ideally between 2500 and 3500 cm^{-1}. While an energy match between the donor and acceptor states is key to an efficient ET, a small energy gap, which could easily be overcome in molecular complexes by a vibrationally assisted ET, is also desirable to prevent collateral back energy transfer (BET) which could reduce the efficiency of the metal-to-ligand sensitization process (Fig. 2) [53]. This issue is

Table 1
Luminescence lifetimes and absolute quantum yields in the visible range for the Dy^{3+} complexes.

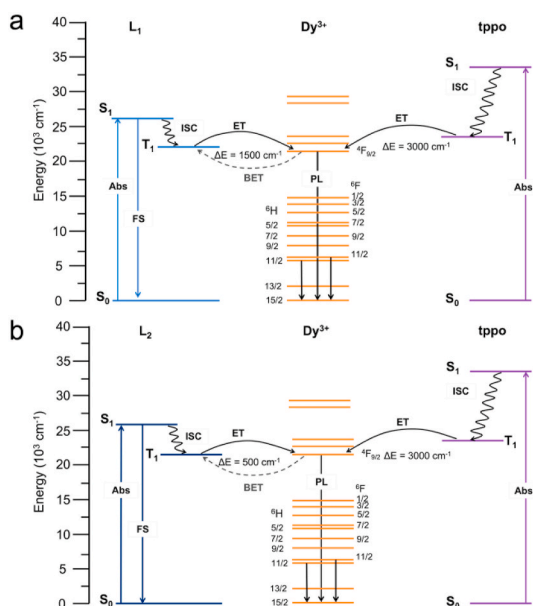| Compound	τ (µs)	R^2	QY [%]
DyL$_1$H$_2$O	9.85	0.996	4.94
DyL$_1$tppo	11.41	0.996	5.32
DyL$_2$H$_2$O	9.38	0.995	3.00
DyL$_2$tppo	10.49	0.996	3.58

Fig. 2. Jablonski diagram for the Dy^{3+} complexes with the ligand L_1 (a) and with the ligand L_2 (b). S_0 – singlet ground state, S_1 – singlet excited state, T_1 – triplet state, ISC – inter system crossing, ET – energy transfer, BET – back energy transfer, Abs – absorbance, FS – fluorescence, PL – photoluminescence.

particularly relevant in Dy^{3+} compounds where the long-lived main emitting $^4F_{9/2}$ level is placed at ~21,000 cm^{-1}, an energy that is relatively high with respect to the triplet energy level of most organic ligands. In the water-free compounds, the tppo co-ligand has a higher triplet state ($T_1 = 23,800$ cm^{-1}) compared to the triplet states of ligands L_1 ($T_1 = 22,500$ cm^{-1}) and L_2 ($T_1 = 21,500$ cm^{-1}) and is expected to be a more effective antenna towards Dy^{3+} [54,55]. These observations explain the increased relative intensity of the ligand-centered emission in the derivatives with ligand L_2, particularly with coordinated water, indicating a less effective ligand-to metal sensitization (Fig. 1).

3.2.2. Steady-state and time-resolved PL of Dy^{3+} complexes in the NIR region

When exciting into the absorption bands of the ligands, the investigated complexes, **DyL$_1$H$_2$O** and **DyL$_1$tppo** (Fig. 3a and b), **DyL$_2$H$_2$O** and **DyL$_2$tppo** (Fig. S13a and 13b in SI), show NIR luminescence. The PL spectrum in the range 800–1650 nm is dominated by the characteristic emission peaks of Dy^{3+} corresponding to the following transitions: $^4F_{9/2} \rightarrow {}^6H_{7/2} + {}^6F_{9/2}$ (846 nm), $^6H_{5/2} + {}^6F_{7/2} \rightarrow {}^6H_{15/2}$ (~ 994 nm), $^6F_{3/2} \rightarrow {}^6H_{13/2}$ (1066 nm), $^4F_{9/2} \rightarrow {}^6F_{5/2}$ (~ 1170 nm), $^6F_{11/2} \rightarrow {}^6H_{15/2}$ and $^6H_{9/2} \rightarrow {}^6H_{15/2}$ (~ 1320 nm), $^4F_{9/2} \rightarrow {}^6F_{1/2}$ (1404 nm) and $^6F_{5/2} \rightarrow {}^6H_{11/2}$ (~ 1500 nm) [56]. However, the **DyL$_2$H$_2$O** complex (Fig. S13a) only shows a clear emission peak at 1317 nm while the other peaks in this region are not visible. This is likely ascribable to a significant quenching effect on the Ln^{3+} ion to NIR-emission by high-strength oscillators such as C–H (ν C–H at 1650 nm and 3ν C–H 1130 nm) and O–H (2ν O–H at 1400 nm), especially for water molecules directly bonded to the emitter [50].

The luminescence decay traces of the Dy^{3+} complexes in the NIR have been recorded at 994 nm and ~ 1320 nm corresponding to the $^6H_{5/2} + {}^6F_{7/2}$ and $^6H_{9/2} + {}^6F_{11/2}$ levels, respectively. All decay traces are well fitted with a monoexponential function (see Experimental Section for details), pointing to the existence of one population of emitters and confirming the purity of the samples.

As expectable, for both series of complexes with ligands L_1 and L_2, the emission signal can be only barely detected in water-containing complexes (Fig. 3c and S13c). This effect can be attributed to vibrational quenching through the third harmonic of the OH stretching, as was previously observed in analogous Yb^{3+} complexes [51].
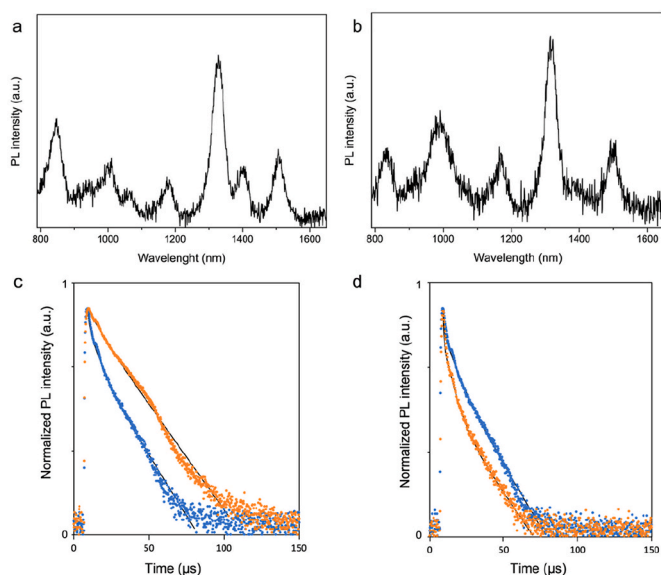

Fig. 3. NIR PL emission spectra of DyL$_1$H$_2$O (a) and DyL$_1$tppo (b), excited at 365 nm and measured at RT; (c) decay profile of DyL$_1$H$_2$O (blue) observed at 846 nm, DyL$_1$tppo (orange) observed at 994 nm; (d) decay profile of DyL$_1$H$_2$O (blue) and DyL$_1$tppo (orange) observed at 1320 nm. (For interpretation of the references to color in this figure legend, the reader is referred to the Web version of this article.)

Table 2
Observed luminescence decay time constants and corresponding Dy^{3+} transitions.

Compound	λ (nm)	Transition	τ (µs)	R^2
DyL$_1$H$_2$O	846	$^4F_{9/2} \rightarrow {}^6H_{7/2} + {}^6F_{9/2}$	10.82	0.998
	1320	$^6F_{11/2} \rightarrow {}^6H_{15/2}$ $^6H_{9/2} \rightarrow {}^6H_{15/2}$	10.34	0.997
DyL$_1$tppo	994	$^6F_{7/2} \rightarrow {}^6H_{15/2}$ $^6H_{5/2} \rightarrow {}^6H_{15/2}$	15.07	0.997
	1320	$^6F_{11/2} \rightarrow {}^6H_{15/2}$ $^6H_{9/2} \rightarrow {}^6H_{15/2}$	10.71	0.998
DyL$_2$H$_2$O	1320	$^6F_{11/2} \rightarrow {}^6H_{15/2}$ $^6H_{9/2} \rightarrow {}^6H_{15/2}$	10.73	0.996
DyL$_2$tppo	994	$^4F_{9/2} \rightarrow {}^6F_{7/2}$	16.33	0.998
	1320	$^6F_{11/2} \rightarrow {}^6H_{15/2}$ $^6H_{9/2} \rightarrow {}^6H_{15/2}$	10.34	0.997

Interestingly, the decay dynamics of the $^6F_{11/2} + {}^6H_{9/2} \rightarrow {}^6H_{15/2}$ transition at 1320 nm is very similar for the water-containing complexes and the tppo derivates of the same ligands. This finding seems apparently in contrast with the expected shortening of the lifetimes in the presence of bound water molecules and with observation made for the relaxation of the $^4F_{9/2}$ level. However, the change of the coordination environment, following the replacement of water molecules by tppo ligands, is likely to induce a significant variation of the oscillator strength of the transition, possibly leading to a decrease of the radiative lifetime in the water-free compounds [51,57]. This could therefore explain the similar observed lifetimes despite the envisaged quenching effect by water molecules. It should be also noted that the discrepancy of the observed lifetime values between the complexes with ligands L_1 and L_2 (Table 2), despite the similar amount of quenching sites, is attributed to a difference in the radiative lifetime dynamics induced by the subtle differences in the ligand structure, further highlighting the relevant role of the coordination environment of the emission properties of these compounds.

3.3. White-light emission (WLE) of Dy^{3+} complexes

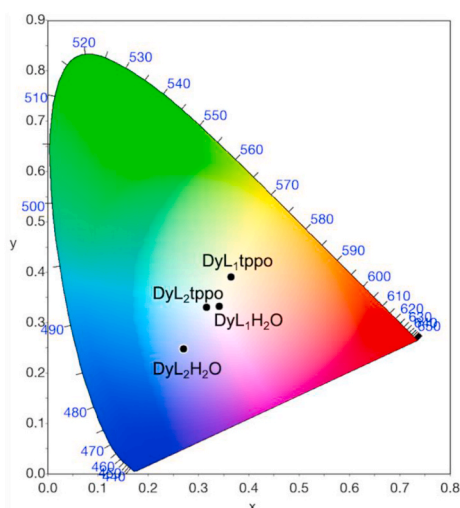The CIE chromaticity diagram (Fig. 4) shows that the Dy^{3+}

Fig. 4. The CIE chromaticity diagram with the color coordinates of the Dy^{3+} complexes excited at 365 nm. (For interpretation of the references to color in this figure legend, the reader is referred to the Web version of this article.)

Table 3
CIE color coordinates (x,y) and CCT for the Dy^{3+} complexes in the solid state.

Compound	x	y	CCT (K)
DyL_1H_2O	0.340	0.333	5129
DyL_1tppo	0.364	0.391	4537
DyL_2H_2O	0.270	0.249	18,173
DyL_2tppo	0.316	0.331	6319

complexes with both ligands, L_1 and L_2, are emitting in the region from cold to warm white light upon excitation with UV light (365 nm). Exciting by different wavelengths in the ligand absorption bands did not result in significant emission differences. According to the CIE coordinates (Table 3) obtained for the **DyL₁H₂O** and **DyL₂tppo** complexes, the emitted white light is close to the pure white light (CIE 1931 chromaticity x = 0.333, y = 0.333) with Correlated Color Temperatures (CCT) of 5470 K. Instead, the CIE coordinates for the **DyL₁tppo** complex are more situated toward the warm white light region leaning toward yellow-white light and the **DyL₂H₂O** complex shows emission in the cold-white light region, corresponding to blueish-white light. As it can be seen in the CIE diagram, color tunability was achieved by changing the coordination environment by introducing the auxiliary tppo ligand. This resulted in tuning the color for the complexes with ligand L_2 from blue to white light, while for the complexes with ligand L_1 the color was tuned from white to yellow-white light. The observed tunability is in accordance with the decrease of the intensity of the residual blue emission from the β-diketonate ligand upon introduction of the tppo co-ligand, as previously discussed.

4. Conclusions

A series of water-containing and water-free Dy^{3+} β-diketonate complexes were prepared with two ligands, L_1 and L_2, with similar chemical properties but with a slight structural difference. In the ligand L_2 the H-atom of the phenyl ring in *para*-position to the β-diketonate group was substituted with a Cl-atom. The water-free complexes have been prepared with a neutral tppo co-ligand that excludes water molecules from the first coordination sphere of the Dy^{3+} ion and acts as an additional sensitizer for energy transfer to the nearby Dy^{3+} ion. All the complexes showed emission with characteristic transitions in both Vis and NIR region. The proximity of the energies of the triplet (T_1) states of ligands L_1 and L_2 to the emitting level of Dy^{3+} ($^4F_{9/2}$) led to a partial depopulation of the ligand excites states and resulted in the observation

of ligand emission in the visible blue in addition to the emission of the Dy^{3+} ion in the yellow-green region. This was exploited to obtain white-light emission. The observed WLE of **DyL₁H₂O** (x = 0.340, y = 0.333) and **DyL₂tppo** (0.316, 0.331) is close to ideal white light with CCT in the cold white-light region. Interestingly, the complexes also yield the rarely observed Dy^{3+} - centered NIR emission with a peak at 1320 nm falling in the O-band region of interest in optical telecommunications. The careful design of a ligand that would promote the emission in the NIR region, without enhancing the quenching of Dy^{3+} emission in this region, could introduce Dy^{3+} as an alternative to the commonly used NIR-emitting lanthanide ions, such as Er^{3+} and Nd^{3+}, that are currently exploited for optical telecommunications. Also the possibility of wider use such as multifunctional molecular materials such as optical applications (lighting) and molecular magnets can be interesting for further design.

Author statement

Dimitrije Mara: Conceptualization, Methodology, Formal analysis, Investigation, Data curation, Writing – original draft. Flavia Artizzu: Formal analysis, Validation, Writing – review & editing. Joydeb Goura: Validation, Writing – review & editing. Manjari Jayerdran: Writing – review & editing. Bojana Bokic: Formal analysis, Writing – review & editing. Brako Kolaric: Formal analysis, Validation, Writing – review & editing. Thierry Verbiest: Supervision, Writing – review & editing. Rik Van Deun: Supervision, Resources, Writing – review & editing.

Declaration of competing interest

There are no conflicts to declare.

Acknowledgments

Appendix A. Supplementary data

Supplementary data to this article can be found online at https://doi.org/10.1016/j.jlumin.2021.118646.

References

[1] E.F. Schobert, J.K. Kim, Sciences 308 (2005) 1274–1278.
[2] C. Feldmann, T. Jüstel, C.R. Ronda, P.J. Schmidt, Adv. Funct. Mater. 13 (2003) 511–516.
[3] T. Jüstel, H. Nikol, C. Ronda, Angew. Chem. Int. Ed. 37 (1998) 3084–3103.
[4] A. De Almeida, B. Santos, B. Paolo, M. Quicheron, Renew. Sustain. Energy Rev. 34 (2014) 30–48.
[5] H.A. Höppe, Angew. Chem. Int. Ed. 48 (2009) 3572–3582.
[6] N.T. Kalyani, S.J. Dhoble, Renew. Sustain. Energy Rev. 16 (2016) 2696–2723.
[7] J. Leng, H. Li, P. Chen, W. Sun, T. Gao, P. Yan, Dalton Trnas 43 (2014) 12228–12235.
[8] E. Ravindra, S.J. Anathakrisahnan, E. Varanthan, V. Subramanian, N. Somanathan, J. Mater. Chem. C 3 (2015) 4359–4371.
[9] A.H. Shelton, I.V. Sazanovich, J.A. Weinstein, M.D. Ward, Chem. Commun. 48 (2012) 2749–2751.
[10] S. Kamal, K.P. Bera, M. Usman, B. Sainbileg, S. Mendiratta, A. Pathak, A. I. Inamdar, C.-H. Hung, M. Hayashi, Y.-F. Chen, K.-L. Lu, ACS Appl. Nano Mater. 4 (2021) 2395–2403.
[11] J. Qui, C. Yu, X. Wang, Y. Xie, A.M. Kirillov, W. Huang, J. Li, P. Gao, T. Wu, Q. Nie, D. Wu, Inorg. Chem. 58 (2019) 4524–4533.
[12] T.S. Mahapatra, H. Singh, A. Maity, A. Dey, S.K. Prananik, E. Suresh, A. Das, J. Mater. Chem. C 6 (2018) 9756–9766.
[13] Z. Zhang, Y. Chen, H. Chang, Y. Wang, X. Li, X. Zhu, J. Mater. Chem. C 8 (2020) 2205–2210.
[14] Y. Yang, L. Chen, F. Jiang, M. Yu, X. Wan, B. Zhang, M. Hong, J. Mater. Chem. C 5 (2017) 1981–1989.
[15] S. Reineke, F. Lindner, G. Schwartz, N. Seidler, K. Walzer, B. Lüssem, K. Leo, Nature 459 (2009) 234–238.

[16] J. Xue, X. Xu, Y. Zhu, D. Yang, J. Mater. Chem. C 8 (2020) 3380–3385.
[17] Q. Zhu, L. Zhang, K. Van Vilet, A. Miserez, N., ACS Appl. Mater. Interfaces 10 (2018) 10409–10418.
[18] L. Xu, Y. Li, Q. Pan, D. Wang, S. Li, G. Wang, Y. Chen, P. Zhu, W. Qin, ACS Appl. Mater. Interfaces 12 (2020) 18934–18943.
[19] M. Zhang, J. Xue, Y. Zhu, C. Yao, D. Yang, ACS Appl. Mater. Interfaces 12 (2020) 22191–22199.
[20] Z. Chen, C.-L. Ho, L. Wang, W.Y. Wong, Adv. Funct. Mater. 32 (2020) 1903269.
[21] Z. Xie, Q. Huang, T. Yu, L. Wang, Z. Mao, W. Li, Z. Yang, Y. Zhang, S. Liu, J. Xu, Z. Chi, M.P. Aldred, Adv. Funct. Mater. 27 (2017) 1703918.
[22] J. Chen, J. Wang, X. Xu, J. Li, J. Song, S. Lan, S. Liu, B. Cai, B. Han, J.T. Precht, D. Ginger, H. Zeng, Nat. Photonics 15 (2021) 238–244.
[23] M. Chen, Y. Zhao, L. Yan, S. Yang, Y. Zhu, I. Murtaza, G. He, H. Meng, W. Huang, Angew. Chem. Int. Ed. 56 (2017) 722–727.
[24] J. Manzur, R.C. De Santana, L.J.Q. Maia, A. Vega, E. Spodine, Inorg. Chem. 58 (2019) 10012–10018.
[25] R. Bouddula, K. Singh, S. Giri, S. Vaidyanathan, Inorg. Chem. 56 (2017) 10127–10130.
[26] G.-L. Law, K.-L. Wong, H.-L. Tam, K.-W. Cheah, W.-T. Wong, Inorg. Chem. 48 (2009) 10492–10494.
[27] S.I. Weissman, J. Chem. Phys. 10 (1942) 214–217.
[28] K. Binnemans, in: A.K. Gschneider Jr., J.-C.G. Bünzli, K.V. Pecharsky (Eds.), Handbook on Physics and Chemistry of Rare Earths, vol. 35, Elsevier B. V., Amsterdam, 2005, pp. 107–272.
[29] D.J. Bray, J.K. Cleeg, L.F. Lindoy, D. Schilter, Adv. Inorg. Chem. 59 (2006) 1–37.
[30] S.V. Eliseeva, J.-C.G. Bünzli, New J. Chem. 35 (2011) 1165–1176.
[31] K. Binnemans, Chem. Rev. 109 (2009) 4283–4374.
[32] D. Mara, F. Artizzu, B. Laforce, L. Vincze, K. Van Hecke, R. Van Deun, A. M. Kaczmarek, J. Lumin. 213 (2019) 343–355.
[33] Y. Yang, P. Wang, L. Lu, Y. Fan, C. Sun, L. Fan, C. Xu, A.M. El-Toni, M. Alhoshan, F. Zhang, Anal. Chem. 40 (2018) 7946–7952.
[34] S.V. Eliseeva, E.V. Salerno, B.A. Lopez Bermudez, S. Petoud, V.L. Pecoraro, J. Am. Chem. Soc. 142 (2020) 16173–16176.
[35] R. Devi, K. Singh, S. Vaidyanathan, J. Mater. Chem. C 8 (2020) 8643–8653.
[36] L. Zhong, W.-B. Chen, Z.-J. OuYang, M. Yang, Y.-Q. Zhang, S. Gao, M. Schulze, W. Wernsdofer, W. Dong, Chem. Commun. 56 (2020) 2590–2593.
[37] W.A. Dar, Z. Ahmed, K. Iftikhar, J. Photochem. Photobiol. Chem. 356 (2018) 502–511.

[38] J. Wang, S. Chorazy, K. Nakabayashi, B. Sieklucka, S.-i. Ohkosi, J. Mater. Chem. C 6 (2018) 473–481.
[39] Q.-Y. Yang, K. Wu, J.-J. Jiang, C.-W. Hsu, M. Pan, J.-M. Lehn, C.-Y. Su, Chem. Commun. 50 (2014) 7702–7704.
[40] Z.-F. Li, L. Zhou, J.-B. Yu, H.-J. Zhang, R.-P. Deng, Z.-P. Peng, Z.-Y. Guo, J. Phys. Chem. C 111 (2007) 2295–2300.
[41] P.-H. Guo, J.-L. Liu, J.-H. Jia, J. Wang, F.-S. Guo, Y.-C. Chen, W.-Q. Lin, J.-D. Leng, D.-H. Bao, Z.-D. Zhang, J.-H. Luo, M.-L. Tong, Chem. Eur J. 19 (2013) 8769–8773.
[42] L. Zhong, W.-B. Chen, X.-H. Li, Z.-J. OuYang, M. Yang, Y.-Q. Zhang, S. Gao, W. Dong, Inorg. Chem. 59 (2020) 4414–4423.
[43] J. Chen, Z. Xie, L. Meng, Z. Hu, X. Kuang, Y. Xie, C.-Z. Lu, Inorg. Chem. 59 (2020) 6963–6977.
[44] Z. Wang, H. Yang, P. He, Y. He, J. Zhao, H. Tang, Dalton Trans. 45 (2016) 2839–2844.
[45] Y. Wei, Q. Li, R. Sa, K. Wu, Chem. Commun. 50 (2014) 1820–1823.
[46] Y.-H. Zhang, X. Li, S. Song, Chem. Commun. 49 (2013) 10397–10399.
[47] Y.S.L.V. Narayana, S. Basak, M. Baumgarten, K. Müllen, R. Chandrasekar, Adv. Funct. Mater. 23 (2013) 5875–5880.
[48] D. Sykes, I.S. Tidmarsh, A. Barbieri, I.V. Sanzanovich, J.A. Weinstein, M.D. Ward, Inorg. Chem. 50 (2011) 11323–11339.
[49] P. Coppo, M. Duati, V.N. Kozhevnikov, J.W. Hofstraat, L. De Cola, Angew. Chem. Int. Ed. 44 (2005) 1806–1810.
[50] D. Mara, L. Pilia, M. Van de Steen, I. Miletto, M. Zeng, K. Van Hecke, A. Serpe, P. Deplano, R. Van Deun, F. Artizzu, J. Mater. Chem. C. 9 (2021) 15641–15648.
[51] D. Mara, F. Artizzu, P.F. Smet, A.M. Kaczmarek, K. Van Hecke, R. Van Deun, Chem. Eur J. 25 (2019) 15944–15956.
[52] D. Mara, A.M. Kaczmarek, F. Artizzu, A. Abalymov, A.G. Skirtach, K. Van Hecke, R. Van Deun, Chem. Eur J. 27 (2021) 6479–6488.
[53] M. Latva, H. Takalo, V.-M. Mukkala, C. Matachescu, J.C. Rodrígez-Ubis, J. Kankare, J. Lumin. 75 (1997) 149–169.
[54] M. Pietraszkiewicz, O. Pietraszkiewicz, J. Karpiuk, A. Majka, G. Kutkiewicz, T. Borowiak, A.M. Kaczmarek, R. Van Deun, J. Lumin. 170 (2016) 411–419.
[55] A. Zhang, J. Zhang, Q. Pan, S. Wang, H. Jia, B. Xu, J. Lumin. 132 (2012) 965–971.
[56] W.T. Carnall, P.R. Fields, K. Rajnak, J. Chem. Phys. 49 (1968) 4424–4442.
[57] J. Liu, P. Geiregat, L. Pilia, R. Van Deun, F. Artizzu, Adv. Optical Mater. 9 (2021) 2001678.

ROYAL SOCIETY OF CHEMISTRY

COMMUNICATION

Thermo-osmotic metamaterials with large negative thermal expansion

Svetlana Savić-Šević, [ID] *[a] Dejan Pantelić,[a] Branka Murić,[a] Dušan Grujić,[a] Darko Vasiljević, [ID] [a] Branko Kolaric [ID] [ab] and Branislav Jelenković[a]

Negative thermal expansion (NTE) is important for compensation of thermal dilatation effects and has significant applications in high-precision devices and instruments. Several materials with intrinsic negative expansion exist but are chemically complex, difficult to manufacture and their thermal expansion coefficients (TECs) are small, typically in the order of 10^{-5}/K–10^{-6}/K. Here we present a metamaterial with a large NTE, with TEC in the order of 10^{-3}/K, enabled by thermo-osmosis of entrapped air molecules through a multitude of nanometer-thin layers. We have generated this material by holographically patterning a biopolymer (dichromated pullulan). The presented manufacturing process is quite simple and capable of generating large-area NTE materials. The concept of achieving (NTE) through thermo-osmosis is universal and can be extended to many other polymers. Our research, for the first time, introduces a relation between NTE and thermo-osmosis.

Introduction

All materials change their dimensions with temperature due to thermally dependent interatomic distances.[1] This behavior is quantified by linear (α_l) or volumetric (α_v) thermal expansion coefficients (TEC):

$$\alpha_l = \frac{1}{l}\frac{dl}{dT} \quad \text{and} \quad \alpha_V = \frac{1}{V}\frac{dV}{dT} \tag{1}$$

where dl and dV are length l and volume V changes induced by temperature difference dT, respectively.[2] Almost all materials expand upon heating and the thermal expansion coefficient is thus positive (PTEC). Organic materials and polymers usually have a larger coefficient of thermal expansion (PTEC greater than 10^{-4}/K) than inorganic materials (such as metals and ceramics with PTEC of about 10^{-6}/K).[3]

Materials with negative thermal expansion coefficients (NTECs) are expensive, rare (except water between 273 K–277 K) and their chemical composition is very specific.[4,5] One of the main goals of NTE research is finding materials with large NTECs to compensate PTECs. In materials associated with a magnetic, ferroelectric or charge-transfer phase transition a large NTE has been discovered and such materials are used as thermal-expansion compensators.[6]

The development of a material with a large NTEC is possible by designing special structures made of several constituents.[7,8] For example, origami structures, consisting of a bi-material's 2D or 3D lattices, enable tailoring metamaterials with novel mechanical properties, including a wide range of PTECs and NTECs.[9] Such NTE materials have important applications for the control of the thermal expansion of materials. They allow adjustment of the thermal expansion of composites and can be used in microchip devices,[10] as dental fillings,[11] in optical and electronic devices,[12] for fasteners[13] and as coating materials.[14] However, such materials have a complex geometry difficult to manufacture.

Many methods have been used to fabricate metamaterials: laser interference lithography,[15] electron-beam lithography,[16] direct laser writing,[17] and focused-ion beam (FIB),[18] to mention just a few. Metamaterials can be fabricated from different substances including photoresists,[19] semiconductors,[20] and metals.[21] Holographic methods stand out as being capable of producing one-, two- and three–dimensional periodic metamaterials. Large areas can be fabricated simply and cheaply in a matter of minutes.

Here we describe a holographic method for generation of mechanical metamaterials with simple architecture and high NTECs, much higher than those of the other materials we found in the available literature. Pullulan, a biological polysaccharide, is used as a base material, which is further sensitized and holographically patterned at the nanoscale. Structural, optical and mechanical properties of the resulting metamaterial are studied, its NTEC measured and a thermo–mechanical model, explaining NTE behavior, presented. We also disclose a new physical mechanism behind such unusual behavior.

[a] *Institute of Physics, University of Belgrade, Pregrevica 118, Zemun 11080, Serbia. E-mail: savic@ipb.ac.rs*

[b] *MNM Group, Department of Physics, UMONS, Mons, Belgium*

This journal is © The Royal Society of Chemistry 2021

J. Mater. Chem. C, 2021, **9**, 8163–8168 | **8163**

Holographic generation of mechanical metamaterial

Doped pullulan is a home-made holographic photosensitive material used throughout this research to manufacture layered metamaterial and analyze its thermo-mechanical behavior. Pullulan is a linear polysaccharide produced from the yeast-like fungus *Aureobasidium pullulans*. The material is composed of maltotriose units connected by α-D-1,6-glycoside linkages[22] and can be photosensitized with chromium ions to produce dichromated pullulan (DCP)[23] as a transparent, thermo-stable film. Properties of DCP films as holographic material–surface gratings, its diffraction efficiency, copying and environmental stability–were previously investigated.[24,25]

DCP film was prepared by mixing an 8% aqueous solution of pullulan and 30% ammonium dichromate, which was poured on a flat glass plate. After drying, a thin film was placed in the holographic setup to produce a volume Bragg grating.[26] To do that, the laser beam from a single-frequency, a diode pumped Nd-YAG laser, at 532 nm, was expanded to expose the pullulan film at normal incidence. A mirror was set behind the film and a volume Bragg grating was recorded inside the DCP film by interference of two counter propagating beams. The interference pattern is responsible for generation of a large number of alternating DCP and air layers, parallel to the substrate. After exposure, the pullulan film was chemically processed by washing the plate in a mixture of water and isopropanol, followed by drying in pure isopropanol. Finally, the grating is slowly and fully dried in a closed vessel.

The resulting hologram is about 10 μm thick and has a complex structure, as shown in Fig. 1. On the nanoscopic level, the structure is characterized by approximately fifty Bragg layers. They are mutually separated and supported by nano-pillars with a diameter of up to 50 nm, enabling the mechanical stability of the whole structure.
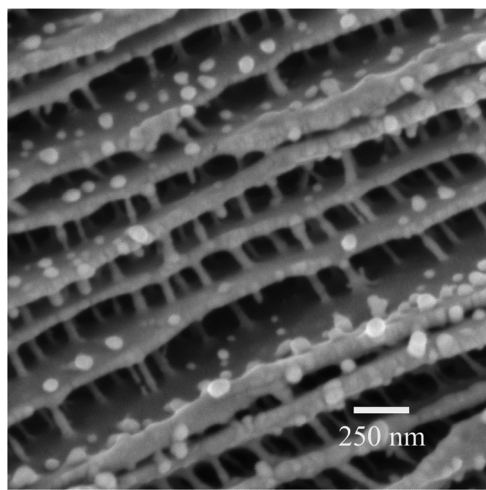

Fig. 1 A cross-section of pullulan metamaterial (recorded using a scanning electron microscope) showing pullulan layers separated by nanopillars.

The metamaterial acts as a selective reflector in the specific band of wavelengths in accordance with the Bragg's law:

$$\lambda = 2(n_a l_a + n_p l_p) \qquad (2)$$

where l_a and l_p are the thicknesses of the air and pullulan layers (both about 100 nm), and refractive indices $n_a = 1$ and $n_p = 1.45$, respectively. A Bragg maximum (as defined in eqn (2)) depends on thermal variation of refractive indices and layer thicknesses. Thus, the spectral shift as a function of temperature can be found by taking the first derivative of eqn (2):

$$\frac{\mathrm{d}\lambda}{\mathrm{d}T} = 2\left(l_a\frac{\mathrm{d}n_a}{\mathrm{d}T} + n_a\frac{\mathrm{d}l_a}{\mathrm{d}T} + l_p\frac{\mathrm{d}n_p}{\mathrm{d}T} + n_p\frac{\mathrm{d}l_p}{\mathrm{d}T}\right) \qquad (3)$$

This optical property of the DCP metamaterial was measured in a heating/cooling cycle. The sample was heated and cooled using a Peltier element (controlling temperature between 295 K and 323 K) and the reflection spectra of the white light from the halogen lamp were recorded using a fiber type spectrometer. A thermocouple was embedded within the sample to obtain accurate measurement of the temperature. As can be seen in Fig. 2a, the reflectance peaks are blue-shifted from 580 nm to 535 nm during heating, exhibiting a negative spectral shift of 45 nm for a positive temperature difference of +25 K (equivalent to 1.8 nm K^{-1}). Upon temperature decrease, a spectral maximum returns close to its initial position. Spectral shift *vs.* temperature, for the whole heating–cooling cycle, shows characteristic hysteresis, as in Fig. 2b. The hysteresis effects are inherent to many natural phenomena. In our case, we assume that hysteresis is a consequence of the nonlinear viscoelastic behaviour of the polymer,[27] *i.e.* pullulan nano-pillars, with temperature. Upon heating, air diffuses through membranes and escapes into the surrounding environment, lowering the pressure inside the multilayer. Outside pressure then compresses the layers until a new mechanical equilibrium is achieved. Due to the compression of the layers, the pullulan nano-pillars are bent. It is assumed that at higher temperatures the viscoelasticity of the pillars slightly decreases. Thanks to the capability to creep,[27] after strain due to pressure, the pillars return to their initial state, with a slightly lower temperature than the initial one.

Thermal behavior of optical systems is typically explained by thermal expansion and thermal variation of the refractive indices (as in eqn (3)). In the following, we will show that these mechanisms cannot account for the large and negative spectral shift.

First, we experimentally determined the linear TEC of a pure, unstructured DCP film. A circular, freestanding DCP membrane was produced, clamped at its perimeter, and its central zone was heated with the laser beam. The temperature of the film was measured using a thermal camera, while the resulting thermal bending was measured using digital holographic interferometry. The linear expansion coefficient was calculated from the recorded interferogram, Fig. 3, and found to be $\alpha_{\mathrm{DCP}} = 8.8 \times 10^{-5}$/K, which is in agreement with the values obtained for other polysaccharides.[28,29]

Now we can calculate spectral shift of the Bragg maximum using eqn (3). The thermo-optic coefficient of air $(\mathrm{d}n_a/\mathrm{d}T)$[30] is
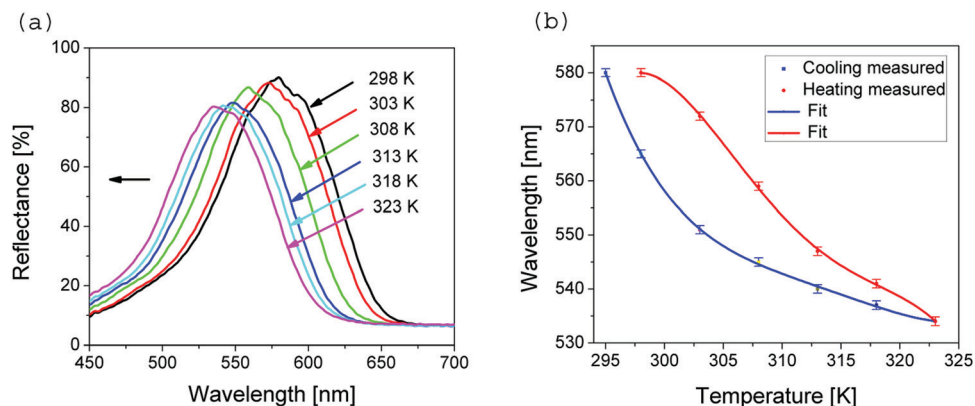
Fig. 2 (a) Reflectance spectra of DCP metamaterial during heating and (b) spectral peak shift during a heating and cooling cycle.
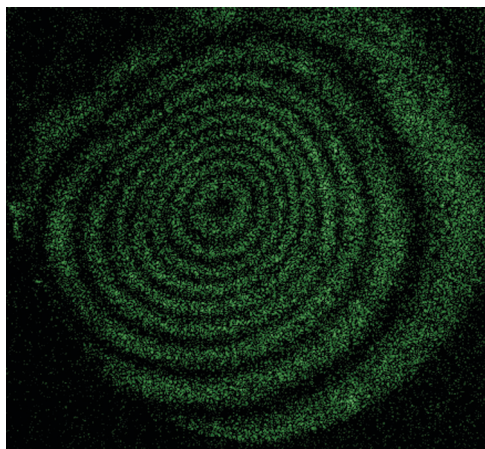

Fig. 3 Interferogram of the thermal bending of the DCP film.

very small and the first term in eqn (3) can be neglected. Additionally, thicknesses of air and pullulan layers are almost the same $l_a = l_p = l$ and eqn (3) can be simplified:

$$\frac{d\lambda}{dT} = 2\left(n_a\frac{dl}{dT} + l\frac{dn_p}{dT} + n_p\frac{dl}{dT}\right) \qquad (4)$$

In a linear approximation dilatation $dl = \alpha lT$ (see eqn (1)) and finally:

$$\frac{d\lambda}{dT} = 2l\left(\frac{dn_p}{dT} + \alpha(n_p + n_a)\right) \qquad (5)$$

We were not able to measure the thermo-optic coefficient of DCP, and we assumed the largest thermo-optical coefficient recorded up to now, $dn/dT = -5 \times 10^{-4}/K$.[31]

By including these values of thermal constants dn/dT and α_{DCP} into eqn (5), together with the value of the layer thickness $l = 118$ nm and refractive indices of air and pullulan, we have found that the expected temperature shift of the Bragg peak is $d\lambda/dT = -0.07$ nm K^{-1}. This value is much lower than the one recorded experimentally, $d\lambda/dT = -1.8$ nm K^{-1}, and classical thermal effects fail to explain the very large NTEC.

As shown above, while the change in the DCP film thermal expansion is small, the thickness variation of air layers must be the main contributor to the overall metamaterial contraction. From the experimentally observed spectral shift and a temperature change of +25 K, the calculated change in air layer thickness (using eqn (2)) is −22 nm. Knowing that there are fifty Bragg layers, the total thickness change is $dl = -1.1$ μm. Knowing that the initial thickness of the material is $l = 10$ μm, we estimate (using eqn (1)) that the linear thermal expansion coefficient of DCP metamaterial is $\alpha_{DCPm} = -4.4 \times 10^{-3}/K$. This value is quite large, compared to values of NTEC, available in the literature. The results presented here have been verified in a series of experiments on many different samples. We have found that the behaviour of pullulan metamaterial is the same, confirming a negative thermal expansion with NTEC of the order $10^{-3}/K$.

Thermo-osmotic mechanism of negative thermal expansion

As explained above, negative and large TEC cannot be explained by usual and simple thermal effects (thermal dilatation and refractive-index variation). In this section, the peculiar behavior of DCP metamaterial is explained through thermo-osmosis,[32] a process defined as fluid or gas diffusion through a membrane due to a temperature gradient.[32,33] This phenomenon was found in many areas from biology[34] to energy harvesting.[35]

We should note that the pullulan layers are very thin (about 100 nm) and their mutual separation is of the same order of magnitude. In such a small volume, only a small number of air molecules are entrapped between the pullulan layers (the mean path length of air molecules is 67 nm under normal conditions)[36] and molecules diffuse through the layers, depending on the temperature difference between the layer and their environment. In a thermal equilibrium, a net flow of molecules between the layer and the environment is zero. If the temperature of the layer rises, more molecules escape the layer, lowering the pressure inside the layer. The resulting pressure difference compresses the layers, supported only by tiny nanopillars (Fig. 1).

This journal is © The Royal Society of Chemistry 2021

J. Mater. Chem. C, 2021, **9**, 8163–8168 | **8165**

Diffusion through permeable membranes is described by Fick's law,[37] which determines the diffusive flux per unit area $\varnothing$ as a function of pressure p_0 and membrane thickness l:

$$\varnothing = \frac{Pp_0}{l} \qquad (6)$$

where P is membrane permeability, which is an intrinsic property of the material.

Effects of temperature on gas permeability were previously analyzed.[38,39] For gases, the temperature-dependence of permeability is defined according to the Arrhenius relationship:

$$P = P_0 \exp^{\frac{-E_p}{RT}} \qquad (7)$$

where P_0 is a constant (a kinetic frequency factor), R is the gas constant, and E_P is the activation energy for permeation. According to the above equation the gas permeability increases with temperature.

For simplicity of the further analysis, we will explore a single membrane separating a closed compartment from the surrounding air environment; see Fig. 4.

We suppose that the environment is a thermal reservoir with infinite capacity at constant temperature T_0 and pressure p_0. If a compartment with a membrane is at temperature T_1 and pressure p_1, we have a flux Φ_1 of molecules diffusing out of the compartment into the environment and flux Φ_0 of particles flowing from the environment into the compartment, i.e. by combining eqn (6) and (7):

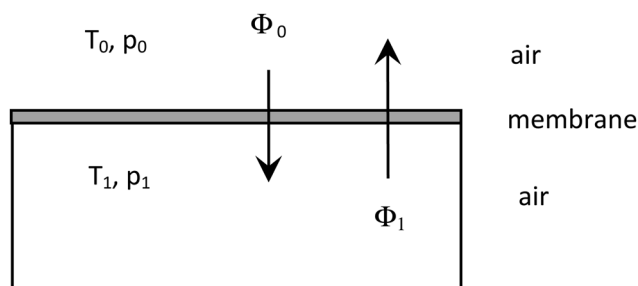$$\varnothing_0 = \frac{p_0}{l} P_0 \exp^{-\frac{E_p}{RT_0}} \qquad (8)$$

Fig. 4 Compartment with a single membrane, where T and p are temperatures and pressures, while Φ are fluxes.

$$\varnothing_1 = \frac{p_1}{l} P_0 \exp^{-\frac{E_p}{RT_1}} \qquad (9)$$

Due to the temperature difference between the compartment and its external environment, ingoing and outgoing fluxes are not equal any more, and there is a net molecular flow. Suppose that the temperature inside the compartment is larger than that of the surrounding air, molecules will leak out and reduce the pressure p_1 inside the compartment. The resulting pressure difference will exert a mechanical force on the membrane and compress it until a new equilibrium is reached, i.e. when $\Phi_1 = \Phi_0$. From eqn (8) and (9) we can easily find that this will happen when:

$$p_1 = p_0 \exp^{-\frac{E_p}{R\left(\frac{1}{T_0} - \frac{1}{T_1}\right)}} \qquad (10)$$

As stated before, this pressure difference is compensated by the mechanical resistance of nanopillars to compression.

In the case of DCP metamaterial, we have a number of pullulan membranes stacked one above the other and separated by tiny nanopillars. Air is gradually leaking from one layer to another until it goes out to the atmosphere. Air leakage is a process that takes some time, before thermo-mechanical equilibrium is reached.

Dependence of pressure p_1 on temperature was calculated from eqn (10) and is shown in Fig. 5(a). The activation energy of air permeation through the polysaccharide membrane is about 40 kJ mol^{-1}.[40] The graph shows that p_1 decreases with increasing temperature of the pullulan layers. Based on this dependence, Fig. 5(b) and (c) show the dependence of pressure p_1 on the measured time to achieve a new equilibrium state and the dependence of pressure p_1 on the air layer thickness, respectively.

Discussion and conclusions

We have shown that the proposed thermo-osmotic mechanism explains well all the experimentally recorded properties of the pullulan NTE metamaterial. However, there are other, less obvious mechanisms that could contribute to the negative thermal expansion, most notably the effect of air humidity.
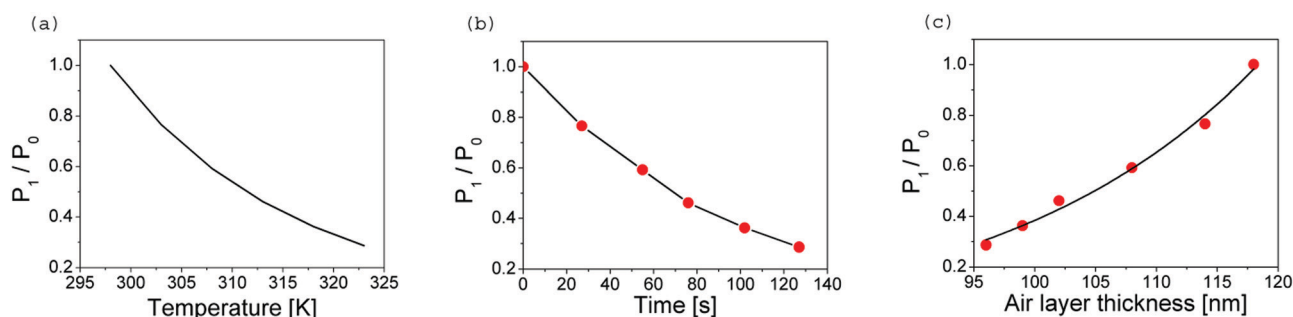

Fig. 5 Ratio of the pressure inside and outside of the compartment as a function of (a) DCP temperature, (b) time needed to reach a new equilibrium state, and (c) air layer thickness. The points on graphs (b and c) correspond to experimentally measured values.
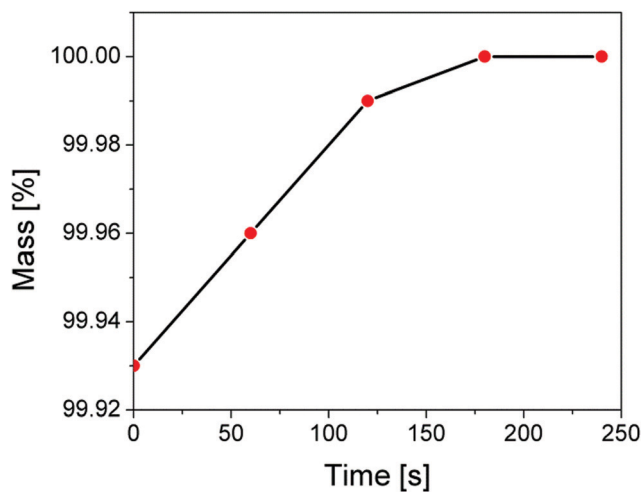
8166 | J. Mater. Chem. C, 2021, **9**, 8163–8168

This journal is © The Royal Society of Chemistry 2021

Fig. 6 The change of mass of DCP metamaterial in time due to humidity.

Fig. 7 Reflectance before and after vacuuming and exposing to air.

To test if pullulan absorbs water from the air we performed a simple gravimetric experiment with an analytical balance. First, the DCP metamaterial was measured under normal laboratory conditions, it was then heated to 373 K for 45 min, to eliminate moisture, and measured again. After that, the sample was kept under normal laboratory conditions and the mass was measured every hour until it reached its original value, see Fig. 6. It can be seen that the change of mass, caused by moisture, is only 0.07%. Bearing in mind that pullulan does not form the gel, and does not swell significantly, we conclude that the influence of moisture on the pullulan structure is negligible.

As a final proof of diffusion of air through pululan layers and the corresponding thermo-osmosis, as a dominant mechanism, we placed the pullulan metamaterial in a vacuum chamber, at the pressure of 4×10^{-2} Pa, for 45 minutes. During that time, entrapped air diffused out of the pullulan layers. The reflection spectra measured immediately after the sample was removed from the vacuum and placed back to the normal atmospheric conditions, were shifted towards lower wavelengths. This shift was caused by the air pressure compressing the layers due to the large pressure difference between the inside ($p \sim 0$ Pa) and outside of the metamaterial ($p_{\text{atm}} \sim 100\,000$ Pa). Following the prolonged stay in the atmosphere the air diffuses into the layers, equilibrating pressures and expanding the material as evidenced by the spectral shift, see Fig. 7.

It is also important to note that when the temperature excised a certain maximum value (higher than 383 K) the DCP metamaterial loses its NTE properties. We believe that in this case there are no more air molecules entrapped within the pullulan layers, and the pressure difference is large enough to break the pullulan nanopillars, which otherwise will sustain the mechanical integrity of the whole structure. Bear in mind that all the mentioned effects (dilatation, thermo-optical, and humidity) are simultaneously present, but nevertheless our experiments show that the thermo-osmosis is a dominant one, which converts an ordinary PTE into an NTE material. Without diffusion, a pressure of entrapped air between the pullulan
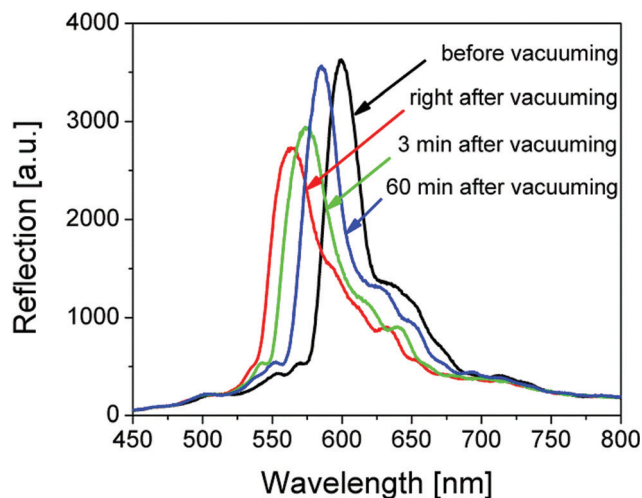
multilayers will follow the temperature variation–increasing upon heating, and decreasing upon cooling. This will turn the pullulan multilayer into a positive thermal expansion material, in contrast to what we observed experimentally.

Regarding the thermo-osmotic process, we emphasize the simplicity of the presented model, which very well describes the complex phenomenon responsible for NTE. First of all, the pullulan layers have a stochastic distribution of thicknesses, size and position of nanopillars, which is difficult to take into account in the model. Also, the mechanical properties of materials at the nanoscale level can be quite different, compared to those of the bulk. Additionally, for such thin layers, air cannot be treated as continuum and more complex effects come into play, such as thermophoresis and thermoconvection. In our case, the situation is further complicated by extremely small (100 nm) separation between the layers when the number of entrapped molecules is correspondingly small. This means that losing a single molecule from the layer significantly reduces the pressure. In spite of this, the proposed model is able to explain the most distinctive properties of the system: negative thermal expansion and the corresponding optical properties.

In conclusion, we have found that holographically patterned dichromated pullulan is a new mechanical metamaterial with a large NTE of $\alpha_{\text{DCPm}} = -4.4 \times 10^{-3}$/K in a temperature range between 295 K and 323 K. Our investigations are in this temperature range because most of the practical interests and potential applications of organic devices are around room temperature. We show that it is simple to fabricate a stable and durable material using the holographic technique. Our explanation of the mechanism that converts an ordinary positive thermal expansion material into an NTE material is based on thermo-osmosis of the air molecules through the pullulan nanolayers. Dependence of the optical response on temperature of the pullulan metamaterials was investigated. The reflection spectra show a blue shift with increasing temperature, which originates from the contraction of air nanolayers due to the thermo-osmosis of the air molecules through the pullulan nanolayers.

This journal is © The Royal Society of Chemistry 2021

J. Mater. Chem. C, 2021, **9**, 8163–8168 | **8167**

The proposed mechanism can be applied to various holographic structures and materials, as well as to different gases and temperature ranges. We have performed the same measurements using holographically patterned dextran (another polysaccharide) and found NTE, too. While pullulan is linear, dextran has a branching structure but shows the same behavior as pullulan, and the reflectance peaks are blue-shifted during heating. Our multilayer design is simple and the proposed mechanism is useful for surfaces of arbitrary size. We have shown that experimental results can be explained by simple relationships, in the nanoscale, linking the structures, mechanical and optical properties, and temperature-response. The disclosed mechanism is universal and opens a range of possibilities to construct engineered materials with tailored negative thermal expansion.

Conflicts of interest

There are no conflicts to declare.

Acknowledgements

Notes and references

1 K. Takenaka, *Front. Chem.*, 2018, **6**, 267.
2 J. P. Attfield, *Front. Chem.*, 2018, **6**, 371.
3 R. Lakes, *J. Mater. Sci. Lett.*, 1996, **15**, 475–477.
4 M. Szafránski, *J. Mater. Chem. C*, 2013, **1**, 7904–7913.
5 H. Liu, J. Chen, X. Jiang, Z. Pan, L. Zhang, Y. Rong, Z. Lin and X. Xing, *J. Mater. Chem. C*, 2017, **5**, 931–936.
6 K. Takenaka, Y. Okamoto, T. Shinoda, N. Katayam and Y. Sakai, *Nat. Commun.*, 2017, **8**, 14102.
7 L. Cabras, M. Brun and D. Misseroni, *Proc. Natl. Acad. Sci. U. S. A.*, 2019, **475**, 20190468.
8 J. Qu, M. Kadic, A. Naber and M. Wegener, *Sci. Rep.*, 2017, **7**, 40643.
9 E. Boatti, N. Vasios and K. Bertoldi, *Adv. Mater.*, 2017, **29**, 1700360.
10 J. Chen, L. Hu, J. Deng and X. Xing, *Chem. Soc. Rev.*, 2015, **44**, 3522–3567.
11 A. Versluisl, W. Douglasl and R. Sakaguchi, *Dent. Mater.*, 1996, **12**, 290–294.
12 R. Bastaits, G. Rodrigues, P. Jetteur, P. Hagedorn and A. Preumont, *Smart Mater. Struct.*, 2012, **21**, 064004.
13 O. Sigmund and S. Torquato, *J. Mech. Phys. Solids*, 1997, **45**, 1037–1067.
14 A. Sanson and J. Chen, *Front. Chem.*, 2019, **7**, 284.
15 Y. Zhou, X. Y. Chen, Y. H. Fu, G. Vienne, A. I. Kuznetsov and B. Luk'yanchuk, *Appl. Phys. Lett.*, 2013, **103**, 123116.
16 E. Almeida, O. Bitton and Y. Prior, *Nat. Commun.*, 2016, **7**, 12533.
17 M. S. Rill, C. Plet, M. Thiel, I. Staude, G. von Freymann, S. Linden and M. Wegener, *Nat. Mater.*, 2008, **7**, 543–546.
18 C. Enkrich, F. Pérez-Willard, D. Gerthsen, J. Zhou, T. Koschny, C. M. Soukoulis, M. Wegener and S. Linden, *Adv. Mater.*, 2005, **17**, 2547–2549.
19 D.-Y. Kang, W. Lee, D. Kim and J. H. Moon, *Langmuir*, 2016, **32**, 8436–8441.
20 T. K. Kormilina, E. A. Stepanidenko, S. A. Cherevkov, A. Dubavik, M. A. Baranov, A. V. Fedorov, A. V. Baranov, Y. K. Gun'ko and E. V. Ushakova, *J. Mater. Chem. C*, 2018, **6**, 5278–5285.
21 X. Zheng, W. Smith, J. Jackson, B. Moran, H. Cui, D. Chen, J. Ye, N. Fang, N. Rodriguez, T. Weisgraber and C. M. Spadaccini, *Nat. Mater.*, 2016, **15**, 1100–1107.
22 Y. Enomoto-Rogers, N. Lio, A. Takemura and T. Iwata, *Eur. Polym. J.*, 2015, **66**, 470–477.
23 D. Pantelic, S. Savic and D. Jakovljevic, *Opt. Lett.*, 1998, **15**, 807–809.
24 S. Savic-Sevic and D. Pantelic, *Appl. Opt.*, 2007, **46**, 287–291.
25 S. Savic-Sevic and D. Pantelic, *Opt. Express*, 2005, **13**, 2747–2754.
26 S. Savic-Sevic, D. Pantelic, B. Jelenkovic, B. Salatic and D. V. Stojanovic, *Soft Matter*, 2018, **14**, 5595–5603.
27 G. Strobl, *The Physics of Polymers*, Springer-Verlag, Berlin Heidelberg, 2007.
28 M. Wada and Y. Saito, *J. Polym. Sci., Part B: Polym. Phys.*, 2001, **39**, 168–174.
29 V. Ramiah and D. A. I. Goring, *J. Polym. Sci., Part C: Polym. Symp.*, 1965, **11**, 27–48.
30 B. Edlen, *Metrologia*, 1966, **2**, 71–80.
31 T. Handa, H. Tahara, T. Aharen and Y. Kanemitsu, *Sci. Adv.*, 2019, **5**, eaax0786.
32 K. G. Denbigh and G. Raumann, *Proc. R. Soc. London, Ser. A*, 1952, **210**, 377–387.
33 K. G. Denbigh, *Nature*, 1949, **163**, 60.
34 W. Große, *Aquat. Bot.*, 1996, **54**, 101–110.
35 A. P. Straub, N. Y. Yip, S. Lin, J. Lee and M. Elimelech, *Nat. Energy*, 2016, **1**, 1–6.
36 S. G. Jennings, *J. Aerosol Sci.*, 1988, **19**, 159–166.
37 N. Gontard, R. Thibault, B. Cuq and S. Guilbert, *J. Agric. Food Chem.*, 1996, **44**, 1064–1069.
38 C. G. Biliaderis, A. Lazaridou and I. Arvanitoyannis, *Carbohydr. Polym.*, 1999, **40**, 29–47.
39 N. Acharya, P. Yadav and Y. Vijay, *Indian J. Pure Appl. Phys.*, 2004, **42**, 179–181.
40 L. A. El-Azzami and E. A. Grulke, *J. Polym. Sci., Part B: Polym. Phys.*, 2007, **45**, 2620–2631.

Thermal radiation management by natural photonic structures: *Morimus asper funereus* case

Darko Vasiljević [a], Danica Pavlović [a,*], Vladimir Lazović [a], Branko Kolarić [a,c], Branislav Salatić [a], Wang Zhang [b], Di Zhang [b], Dejan Pantelić [a]

[a] *Institute of Physics, University of Belgrade, Pregrevica 118, 11080, Belgrade, Zemun, Serbia*
[b] *State Key Lab of Metal Matrix Composite, Shanghai Jiao Tong University, 800 Dongchuan Road, Shanghai, 200240, China*
[c] *Micro- and Nanophotonic Materials Group, University of Mons, Place du Parc 20, 7000, Mons, Belgium*

ARTICLE INFO

ABSTRACT

Convective, conductive and radiative mechanisms of thermal management are extremely important for life. Photonic structures, used to detect infrared radiation (IR) and enhance radiative energy exchange, were observed in a number of organisms. Here we report on sophisticated radiative mechanisms used by *Morimus asper funereus*, a longicorn beetle whose elytra possess a suitably aligned array of lenslets and blackbodies. Additionally, a dense array of microtrichia hyperuniformly covers blackbodies and operates as a stochastic, full-bandgap, IR-photonic structure. All these features, whose characteristic dimensions cover a range from several hundred down to a few micrometres, operate synergistically to improve the absorption, emission and, possibly, detection of IR radiation. We present a morphological characterization of the elytron, thermal imaging measurements and a theoretical IR model of insect elytron, uncovering a synergistic operation of all structures.

1. Introduction

Colouration in the living world serves multiple purposes, such as: camouflage, mimicry, warning or attraction (Doucet and Meadows, 2009; Kemp, 2007; Sweeney et al., 2003; Verstraete et al., 2019), and it sometimes affects the very existence of animals. Radiative heat exchange with the environment can also be influenced by colours, through absorption or reflection of the visible light. There is a delicate balance between colouration and other mechanisms of thermal regulation: convection, conduction, radiation emission and absorption, evaporation, perspiration, internal heat generation, behaviour (Bosi et al., 2008; Cossins, 2012).

Such mechanisms have also been observed in insects. Their exoskeleton (cuticle) serves many functions, such as: locomotion, providing a defence barrier (against mechanical stress, cold, hot or wet environment), a reservoir for the storage of metabolic waste products, mechano- and chemoreception, balancing radiant energy absorption in the visible and dissipation in the infrared (IR) part of the spectrum (Capinera, 2008; Gillott, 2005; Gullan and Cranston, 2004; Shi et al., 2015). The cuticle is usually patterned on micro- and nano-scale and produces striking optical effects. Such photonic structures (Vukusic and

Sambles, 2003) create structural colouration (Vukusic et al., 2001) in the visible, but can have an important role in the infrared part of the spectrum, participating in thermoregulation (Scoble, 1992; Shi et al., 2015).

Most insects are primarily ectothermic and rely on external heat sources, such as solar radiation (Nijhout, 1991). It is proven that butterflies use physiological mechanisms to regulate the heat gain by orientation and posture relative to the sun (Kingsolver, 1985). On the other hand, structures are developed during evolution to efficiently reflect the visible light, simultaneously dissipating infrared radiation directly into the atmospheric window at mid-infrared, as in the Saharan silver ant, *Cataglyphis bombycina* (Roger, 1859) (Shi et al., 2015). This clever mechanism enables an insect to efficiently regulate its body temperature in a hostile desert environment.

In addition, the insect cuticle can be a place where so-called extraocular photoreception occurs. Also known as "dermal light sense" and defined as a "widespread photic sense that is not mediated by eyes or eyespots and in which light does not act directly on an effector" (Millott, 1968), it has been reported in several orders of insects. Some butterflies have such photoreceptors located at the end of their abdomens to control copulation in males and oviposition in females (Arikawa and Takagi,

---

2001). In some cases, dermal light sensitivity has been confirmed from behavioural responses, mediated by light intensity and wavelength (Desmond Ramirez et al., 2011). For example the larvae of *Tenebrio molitor* avoid light even after decapitation (Tucolesco, 1933). Light sensitivity of the *Aphis fabae* antennae is responsible for the insect's photokinetic activity (Booth, 1963).

Here we highlight the specific architecture of *Morimus asper funereus* (Mulsant, 1863) (Insecta: Coleoptera: Cerambycidae) elytra, which implicates dermal detection of IR radiation, a feature not previously observed in any other species. We also study the radiative properties of the elytra. Electron and optical microscopy were used to reveal the external and internal morphology of elytra, and thermal imaging to establish its radiative properties in the thermal IR (7.5–13 μm) part of the spectrum. Theoretical analysis and 3D modelling were used to reveal the role of microstructures.

2. Materials and methods

2.1. Insect

Morimus asper funereus (Fig. 1) (family Cerambycidae, subfamily Lamiinae) is a large longicorn beetle inhabiting central and southern Europe. The species is characterized by grey elytra with four black patches and a body length of 15–40 mm (Parisi and Busetto, 1992). The colouration and velvety appearance of the elytra comes from the dense tomentum of the setae, grey hairs and black scales, embedded in the elytral surface, which is black and shiny. The hind wings (alae) of *M. asper funereus* are reduced and the species is flightless (Solano et al., 2013).

M. asper funereus is a saproxylic species (Carpaneto et al., 2015; Hardersen et al., 2017) and depends on decaying wood during larval development. This process takes place in tree trunks and stumps and lasts approximately three or four years (Stanić et al., 1985). We noticed that the insects evade direct sunlight. We never found them on trunks that were directly exposed to solar radiation: when we subjected an insect to sunlight, it hid in the shadow. This was confirmed by other research, which found that this species is active during the evening and at night (Polak and Maja, 2012; Romero-Samper and Bahülo, 1993). Hardersen et al. (2017) determined that the highest activity of the species was between 20:00 and 24:00. However, the authors stated that *M. asper funereus* individuals were seen during the day, but that the number was only 30% of the maximum recorded in the evening and at night.

The species is strictly protected in Europe (and Serbia) by Annex II of the Habitat Directive 92/43/CEE. In the IUCN Red List of Threatened Species, it is designated as vulnerable (A1c) (IUCN Red List of Threatened Species, 2018). We had ten, conserved and pinned, specimens at our disposal, collected during the summer of 2018 on Mt. Avala, near the city of Belgrade, with the permission of the Serbian Ministry of Environmental Protection (N°:353-01 –1310/2018-04).

2.2. Microanalysis

A stereomicroscope (STEBA600, Colo Lab Experts, Slovenia) with maximum magnification up to 180X, eyepiece 20X, auxiliary objective 2X, working distance 100 mm, reflection and transmission mode, and equipped with a digital camera (Canon EOS 50D, Tokyo, Japan) was used to examine the anatomy of the whole insect.

The optical characteristics of the elytra and setae were analysed on a trinocular microscope (MET104, Colo Lab Experts, Slovenia) (maximum magnification 400X, polarization set, objectives Plan Achromatic POL Polarizing 10X/20X/40X).

Micro-computed tomography (micro-CT) was employed to view the overall anatomy of the beetle and measure the thickness of the elytra. We had at our disposal the Skyscan 1172 system (Bruker, USA). To ensure the optimum signal/noise ratio during micro-CT imaging, the specimens were scanned without filter, with scanning parameters set as follows: 40 kV, 244 μA, 530 ms, rotation step 0.2° (pixel size 13.5 μm). For the purpose of this experiment, CT scanning was performed without any special preparation of a specimen.

A field emission gun scanning electron microscope (FEGSEM) (MiraSystem, TESCAN, Czech Republic) was used for ultrastructural analysis. Prior to analysis, insect elytra were removed and placed on an aluminium mount and coated with a thin layer (5–10 nm) of gold palladium (AuPd), using a SC7620 Mini Sputter Coater (Quorum Technologies Ltd., UK).

2.3. Thermal infrared (IR) analysis

Assessment of the thermal properties of insects is normally done by some kind of thermometry (Heinrich, 2013). With the advent of IR cameras, thermal imaging (TI) becomes a method of choice. It is a non-invasive and non-contact technique with applications in numerous fields (Vollmer and Möllmann, 2010). Recently, TI become an important sensing technology in biological investigations (Kastberger and Stachl, 2003). TI cameras are a relatively new tool in studying nocturnal flying animals: birds, bats and insects (Horton et al., 2015). So far, most TI studies of insects have focused on the thermoregulation of Hymenoptera species (Stabentheiner and Schmaranzer, 1987; Stabentheiner et al., 2012).

In this research, the emission of thermal radiation was analysed by an IR thermal camera corresponding to an atmospheric window at 7.5–13 μm (FLIR A65, USA, 640 x 512 pixels, thermal resolution/NETD 50 mK). Thermal measurements were corrected for surface emissivity, and reflected temperature, while images were acquired without binning. Due to the smallness of the insect, we positioned the camera as close as possible (at a distance between 10 and 20 cm), and sometimes used an additional lens to further magnify the thermal image. Under these conditions, the Narcissus effect (radiation emitted by the camera itself) was pronounced. For this reason, we positioned the elytra outside the thermal beam emanating from the camera objective. The rest of the camera body was shielded by aluminium foil.

We manufactured an aluminium cavity and coated it with an absorbing, velvety material whose absorbance was measured at 0.996, in agreement with the calculated value (Prokhorov, 2012). It was used as a reference to measure elytra emissivities, as shown in Fig. 2.

Fig. 1. *Morismus asper funereus*: a longicorn beetle whose most prominent features are black body and greyish elytra with four prominent black patches.

Fig. 2. A simple experimental setup for thermal measurements.

3. Results

3.1. Morphological and optical characterization of photonic structures of M. asper funereus

The macroscopic anatomy of a dried specimen, visualized using micro-CT (Fig. 3), showed that the elytra of *M. asper funereus* are ellipsoidal, sclerotized and thick (between 200 and 350 μm). The hind wings of *M. asper funereus* are highly reduced and there is a large, air-filled space between the elytra and the insect body.

The elytra of *M. asper funereus* (Fig. 1) possess a hierarchical structure with a number of features ranging from macroscopic to micron and submicron levels.

The inner surface (facing the insect body) looks spongy (Fig. 4(a)), with an array of oval zones (approx. 0.2–0.4 mm in size – see Fig. 4(b)), surrounded by yellowish walls. If observed in transmission, it can be seen that the walls are actually a complex, connected network of channels that transport hemolymph (Fig. 4(c)) (Unruh and Chauvin, 1993; van de Kamp and Greven, 2010). Within each zone, there is a spherical-looking object with a circular opening at its centre that looks like a standard blackbody (BB) model found in textbooks. In transmission (Fig. 4(c)), BBs are deep red, doughnut-shaped features in the middle of each oval zone. It should be noted that the red colour is due to melanin, characterized by strong absorption in the blue-green part of the spectrum and good transmission in the red. By bleaching elytra using hydrogen peroxide (H_2O_2) we were able to reveal a network of smaller channels, connecting the BB to the main microfluidic channels. (Fig. 4 (d)).

All the structures described above are protected by an optically transparent layer. This layer is electron-dense (Fig. 5) and hides all the structures observed optically. Microtrichia (thorn-like structures, approx. 5 μm in height – inset in Fig. 5) are a dominant feature of the internal surface. As can be seen, the microtrichia are arranged in an ordered but not completely regular pattern (average mutual distance is 11 μm). In many other insects, such structures are used to lock the hind wings to the elytra, as in the Asian ladybeetle (Sun et al., 2018).

Outer surface of elytra is black and covered with two different types of microtrichiae (Fig. 6(a) and (b)). One type is transparent and covers most of the body, which looks greyish (grey zone) due to the scattered radiation. The other type is pigmented and densely covers four distinct areas producing characteristic black patches. However, in thermal infrared, the whole body looks quite uniform.

On grey elytral zone there is also an array of shiny black, quite smooth, microlens-like protrusions, surrounded with hairs (compare optical and SEM images in Fig. 6(c), respectively). The microlenses and BBs have a well-defined mutual orientation, which was observed by simultaneously illuminating the elytron in transmission and reflection (Fig. 7). As observed before (Fig. 4), the BB occupies the centre of an oval zone, while the microlens is at its rim, directly facing a hemolymph-filled channel.

The elytron directly beneath the surface (procuticle 200-μm thick) is well organized, as in all coleopteran (van de Kamp and Greven, 2010; van de Kamp et al., 2016). It is layered and possesses a number of laminae that envelope the BBs and microchannels (Fig. 8(a)). It is interesting to note a number of tiny hairs covering the internal surface of the blackbody (Fig. 8(b)). At the moment, we can only speculate about their biological function, because this can be revealed only by physiological investigation of live specimens, which we didn't have at our disposal. However, from purely physical point of view, we note that hairs increase the absorbance of the black body wall due to enhanced scattering and trapping of radiation.

3.2. Radiative properties of M. asper funereus

We used thermal imaging to evaluate radiative properties of elytra. An elytron was placed in front of the reference cavity (with absorbance higher than 99% (Prokhorov, 2012)) and observed with a thermal camera (operating within the 8–14 μm wavelength range). In thermal equilibrium (room temperature), the elytron completely disappears from thermal image (Fig. 9(a)) and becomes visible only when heated by the laser beam (Fig. 9(b)). The same is true for both the outer and inner sides, along the entire, highly curved, elytral surface. Thus, we may conclude that the high directional emissivity (higher than 99%) is constant along the surface and has the characteristics of a Lambertian source.

It is interesting to note that the emissivity of both black and grey areas of elytra is the same. This is because the wavelength of thermal radiation is close to characteristic dimensions of hairs covering the

Fig. 3. (a)3D reconstruction of *M. asper funereus* from a stack of MictoCT images. (b) frontal, (c)axial and (d) longitudinal cross sections of insect showing air filled space between elytra and the rest of the body.
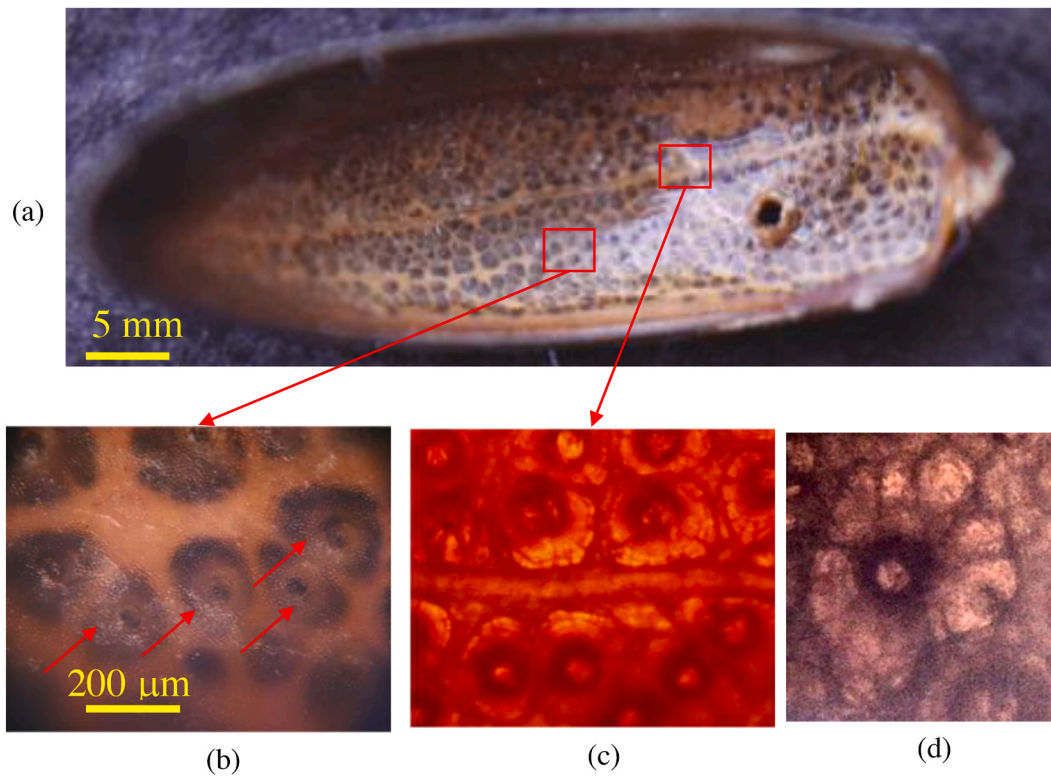
Fig. 4. (a) Optical image of inner elytral surface of *M. asper funereus* in its natural state, exhibiting its original pigmentation. Enlarged portion in (b) shows blackbody-like (BB) structures (spherical-looking, with a black spot in the centre – red arrows). (c) Transmission optical image of elytron reveals a system of channels, branching from the central channel and surrounding each BB. (d) Elytron bleached in peroxide reveals a network of smaller channels, connecting the BB to the main microfluidic channels.
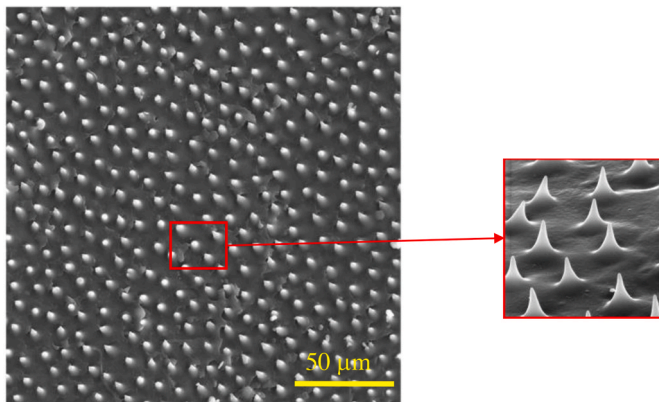
Fig. 5. SEM image of inner elytral surface of *M. asper funereus* with an array of microtrichia, enlarged in the inset.

elytra. That is why both types of hairs efficiently scatter the radiation and enhance the probability of radiation being absorbed.

3.3. Modelling of M. asper funereus elytron

3.3.1. Blackbody array

Based on the anatomical features described in section 3.1, we were able to design a model of *M. asper funereus*. We took the oval zone of Fig. 4 as an elementary unit, composed of a layered blackbody surrounded by walls with microchannels. Blackbody is enclosed between two layers, one containing microlenses and the other covered by microtrichia.

We used 3D, open-source, computer graphics software (Blender, free

under GPL) to visualize the elementary unit of *M. asper funereus* elytra. Fig. 10(a) and (b) show two aspects of an elementary cell, so that the spatial relations between the microlenses, walls with microchannels and blackbody are clearly seen. Microlenses focus radiation directly into the elytron and microchannel filled with hemolymph (primarily water), as confirmed by ray tracing (Fig. 11) within a quite large angular range ($-20°$ to $+20°$).

We made a more exact finite element modelling of IR wave propagation in the cuticle. To do that, we needed complex refractive indices of chemolimph and insect cuticle at thermal infrared wavelengths. Chemolimph is mostly composed of water and we used the data from Hale and Querry (1973) – complex refractive index was averaged to *n = 1.2 + i · 0.0343,* within 3–5 μm, and *n = 1.35 + i · 0.13,* within 8–12 μm. Optical constants of insect cuticle at thermal infrared are not very well known and we used data extracted from Shi (2018) – within 3–5 μm complex refractive index was *n = 1.57 + i · 0.005* and within 8–12 μm, *n = 1.57 + i · 0.1.* The absorption of melanin was not taken into account because it is found only in a thin superficial layer of elytra, its concentration is low, compared to that of chitin, and its absorption maximum is at UV.

Within the 8–12 μm window, radiation is efficiently absorbed in the superficial layers of the cuticle due to the very high absorption coefficient of chitin (see Fig. 12(b)). The situation is more interesting within the 3–5 μm window, where the absorption as an order of magnitude lower (Shi, 2018). There, the radiation is indeed focused onto the microchannels (Fig. 12(c)), while the multilayer structure of the BB efficiently reflects and expels the radiation from the central cavity. Within this spectral range, radiation penetrates deep and heats the internal structures of cuticle (Fig. 12 (c)). If there is a constant flow of hemolyph through the cuticle (Unruh and Chauvin, 1993) heat will be convectively transferred to the central cavity of the blackbody. That is why we propose that tiny hairs lining the cavity might function as
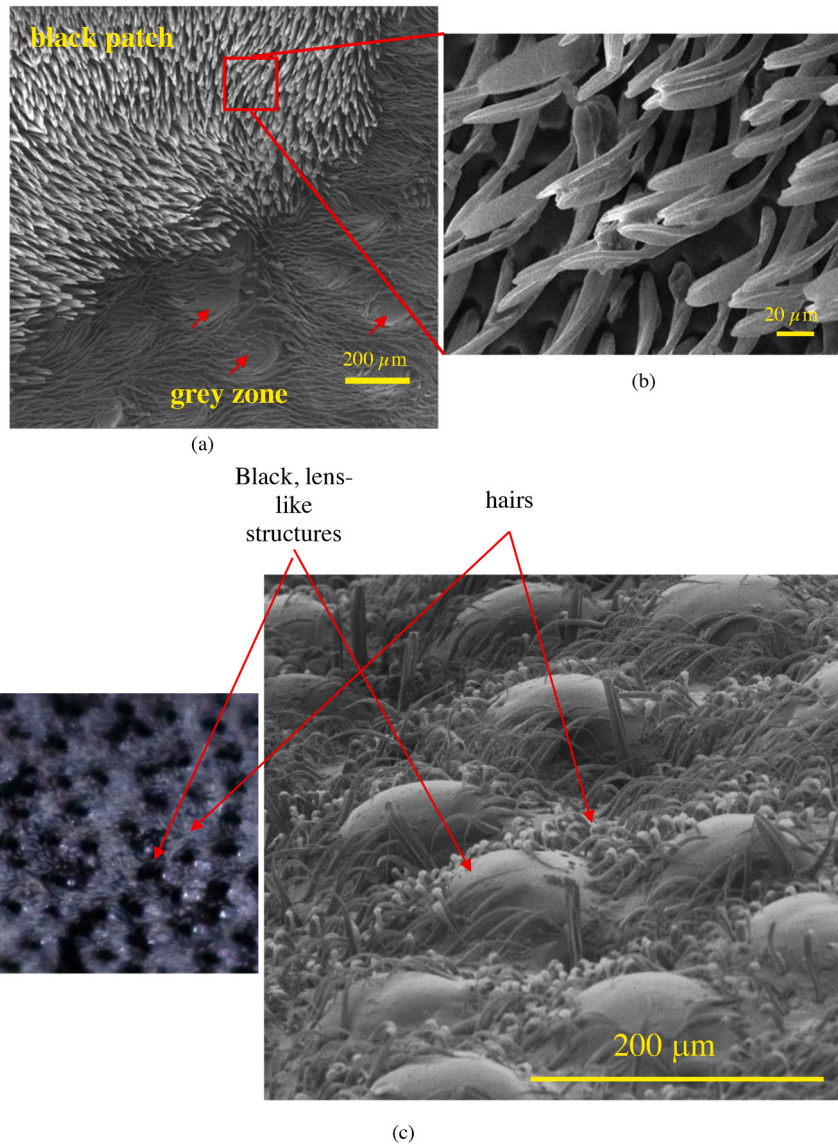
(a)

(b)

(c)

Fig. 6. SEM of the outer surface of the *M. asper funereus* elytra: (a) an edge between grey and black areas (red arrows indicate microlens-like protrusions); (b) enlarged SEM image of black scales. (c) Lens-like structures and hairs on the outer surface of *M. asper funereus*. Optical image is on the left and SEM image on the right. The captured area with lens-like structures is from the grey zone of the elytra.
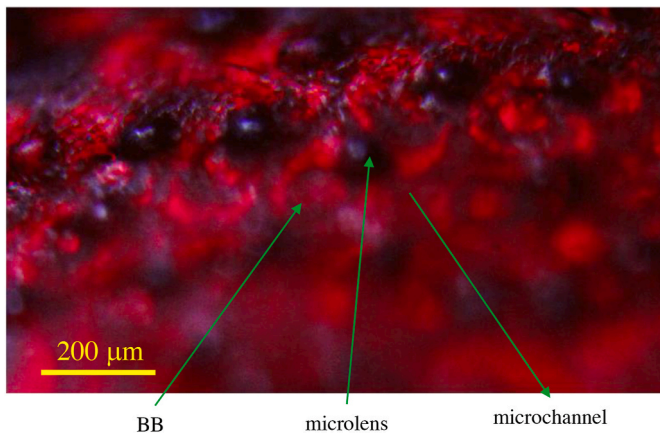

Fig. 7. Optical microscope image of elytron, simultaneously illuminated in reflection and transmission. Microlenses can be seen as black circular areas, blackbodies are doughnut-shaped zones within the network of channels.

sensilla, signalling the insect to search for a cooler place - which is a behavioural characteristic of this particular insect.

It seems that cuticular microlenses function like the cornea of an ommatidium, i.e. they focus radiation onto the sensitive layer. The architecture of *M. asper funereus* is well organized for the purpose.

3.3.2. Array of microtrichia

As can be seen from micro-CT images (Fig. 3), there is a thin (less than a millimetre) air-filled gap between the elytra and the insect body (see scheme at Fig. 13). Thermal energy is radiatively exchanged between those layers, thus filling the gap with infrared radiation. For the part of radiative energy propagating at grazing incidence, gap behaves as a hollow waveguide (such as those used for 10.6 μm CO_2 lasers – (Komachi et al., 2000)) with microtrichie as subwavelength scattering (diffractive) structures. In such waveguides, radiation propagates in a whispering-gallery manner.

In the following we will analyze their possible role in thermal radiation exchange of *M. asper funereus*. For the purpose of better understanding, we will treat microtrichie as a forest-like structure of almost conical protuberances on an otherwise flat surface. Each cone is 4.4 μm
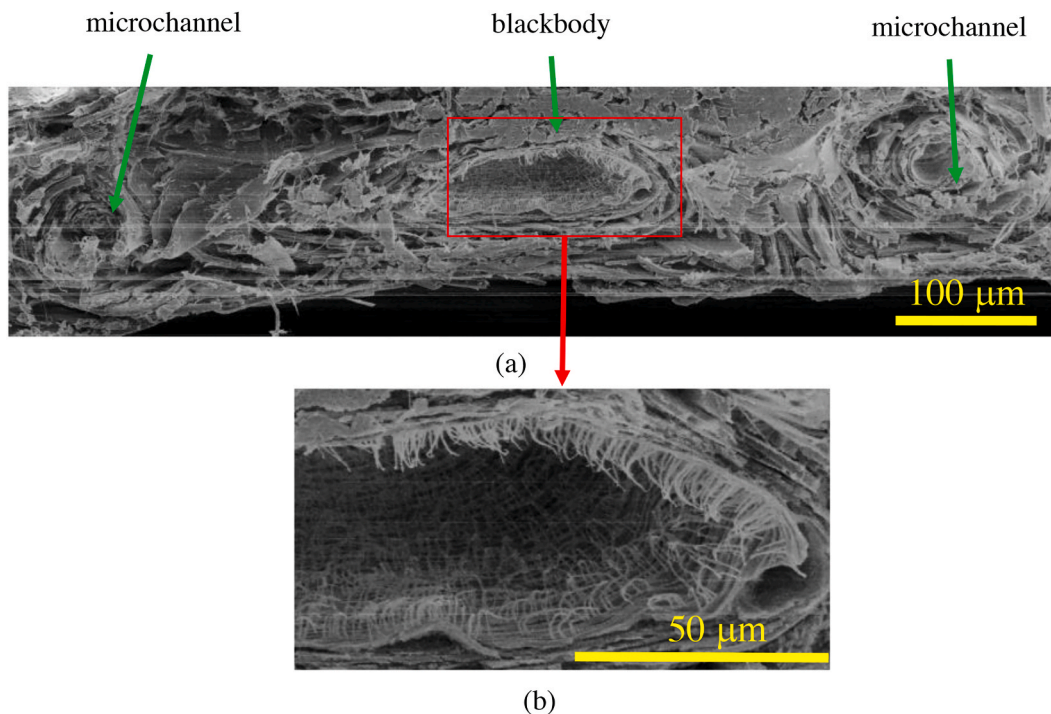
5

Fig. 8. (a) Cross section of *M. asper funereus* elytron with clearly visible blackbody with microchannels on both sides. (b) Enlarged image reveals the hair-like protrusions lining the internal surface of the blackbody.
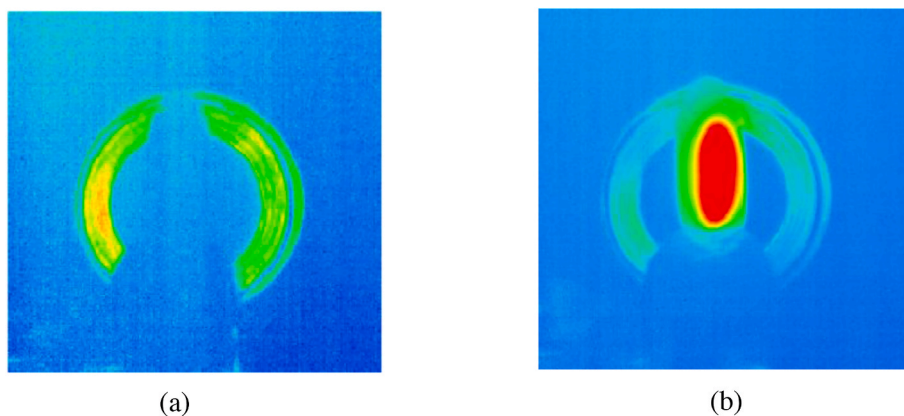

Fig. 9. (a) Thermal image of *M. asper funereus* elytra positioned in front of a blackbody. Emissivity is the same and they cannot be discerned. (b) When heated, the elytron becomes visible.

in diameter at its base and 3.8 μm in height. An observer looking from above will see an arrangement like that in Fig. 14, schematically drawn using the section of Fig. 5 as a template. Looking from the side, as if sitting on the substrate, densely overlapping cone projections, even for a small number of microtrichia surrounding the central one, are observed. Thus, for the large number of microtrichia on the elytron, the radiation propagating close to the surface has a high chance of hitting a cone and being absorbed. This is a purely geometric optic analysis – in the following we will present a wave optics perspective.

Upon closer inspection of the spatial distribution of microtrichia (Fig. 5), we can see that it is neither regular nor completely random (rods in the chicken retina are arranged in a similar fashion (Jiao et al., 2014)). It is characterized by a ring-like Fourier transform, as in Fig. 15 (a). The spatial frequency of the prominent ring-like structure is 0.1/μm, corresponding to the average 10-μm distance between microtrichia (Fig. 15(b)). The amplitude of the Fourier transform goes to zero as the spatial frequencies approach the central Fourier peak. This is a

characteristic of hyperuniform point distributions, which were shown to behave as a complete photonic bandgap structure (Florescu et al., 2009). The slight ellipticity of the Fourier transform observed here is possibly a consequence of the ellipsoidal profile of the elytron.

For thermal radiation entrapped between the elytra and the body, A 2-dimensional hyperuniform system behaves as a random full-bandgap photonic crystal. This can be inferred from the ring-like Fourier transform (Fig. 15(a)), which can be understood as a superposition of sinusoidal gratings with a 10-μm period oriented in all directions along the plane substrate. Under grazing incidence, gratings behave as Bragg reflectors, blocking the propagation of radiation with the wavelength:

$$\lambda = 2d/N$$

where *d* is a grating period, *N* is an integer, assuming the normal angle of incidence. For the 10 μm average period of microtrichia and *N* = 2, the Bragg wavelength is 10 μm, right in the middle of an 8–12 μm atmospheric window. Additionally, for N = 4, the Bragg wavelength
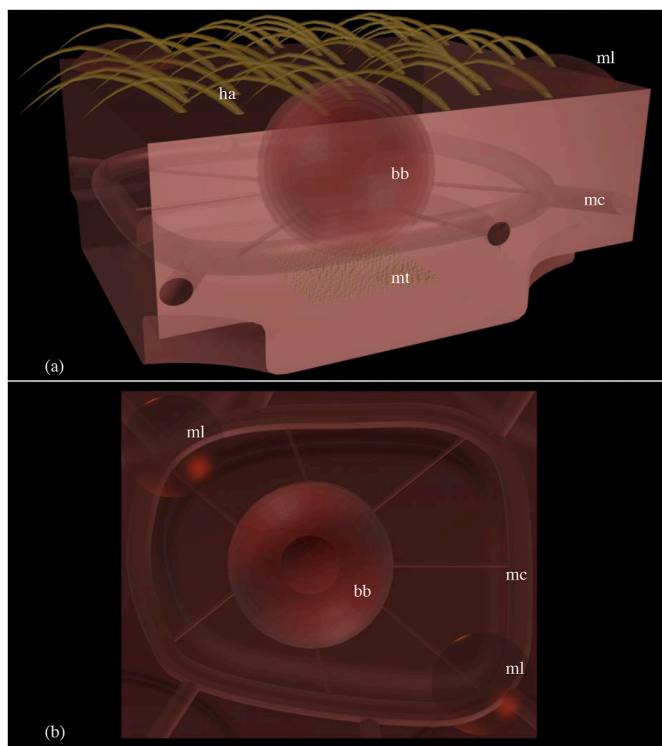
Fig. 10. (a) A semi-transparent 3D model of *M. asper funereus* elytron presenting internal structures hidden within the elytron (mt – microtrichia, mc – microchannels, ml – microlens, bb – black body, ha – hairs) (a) with microlenses and hairs clearly seen; (b) top view displaying alignment of microlenses and microchannels. The microchannel completely surrounds the blackbody and is connected to it via even smaller channels.
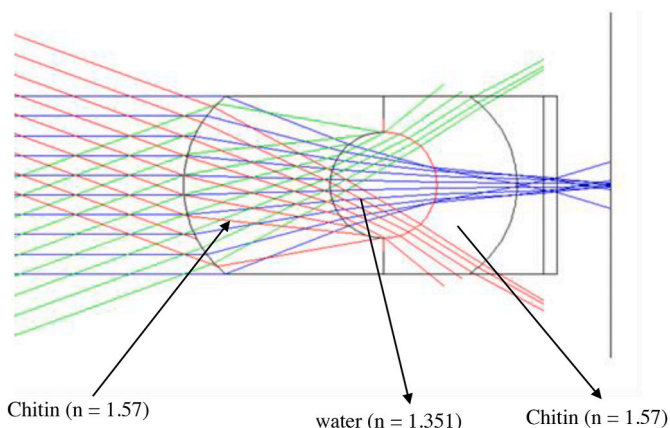

Fig. 11. Ray tracing through a microlens and microchannel (blue rays are incoming at normal incidence, while red and green rays obliquely, at $+20^0$ and -20^0, illuminate the elytron). Calculations were done at 3 μm, where refractive indices are as indicated in figure.

corresponds to another window at 3–5 μm, but we were not able to check this experimentally.

4. Discussion and conclusions

The search for highly absorbing structures is a long-standing one and many structured materials have been engineered so far (Mizuno et al., 2009), but only the vertically aligned nanotube array (VANTA black) (De Nicola et al., 2017) approaches the emissivity of a blackbody. In line with the research on silicon photonics for NIR silicon devices (Milošević
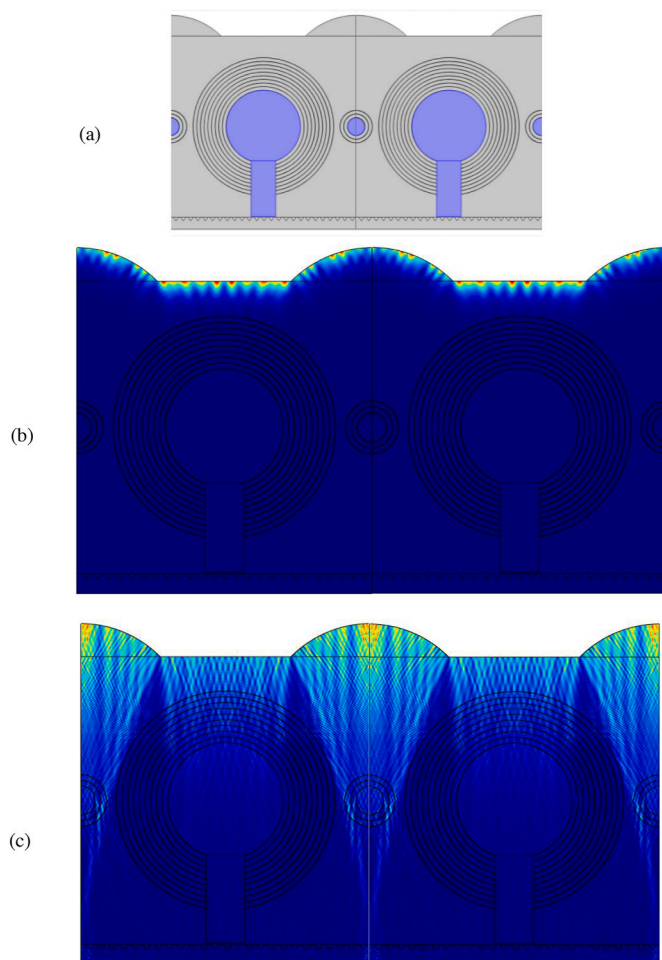

Fig. 12. (a) A model of *M. asper funereus* elytron used in FEM analysis (grey colour corresponds to chitin and purple to water). Distribution of thermal IR radiation inside *M. asper funereus* blackbody-like cuticular structure calculated by FEM. Two spectral windows were analysed: (b) 8–12 μm (image at 10 μm is shown) and (c) 3–5 μm (image at 4 μm is shown).
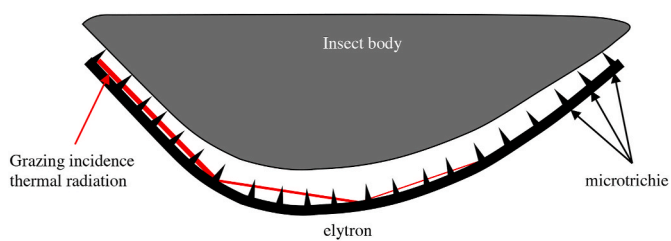

Fig. 13. M. funereus elytron and body with air filled gap acting as a hollow waveguide for grazing incidence thermal radiation.

et al., 2019), here we show that natural, less complex structures can achieve similar results owing to their forest-like structure and intrinsic curvature (Leonhardt and Tyc, 2009). A clever arrangement of hyperuniform disordered structures efficiently competes with highly advanced nanotube structures. In contrast to artificial VANTA black material, which is fragile and complex to manufacture, the natural solution is robust and simple.

At this point, we are not able to estimate how important the role of microtrichie is. We must stress, however, that the amount of the radiation entrapped between elytra and the body is non-negligible due to Fresnel reflections and waveguiding. Simple calculation shows that, for the refractive index used in this study (n = 1.57) and normal incidence,
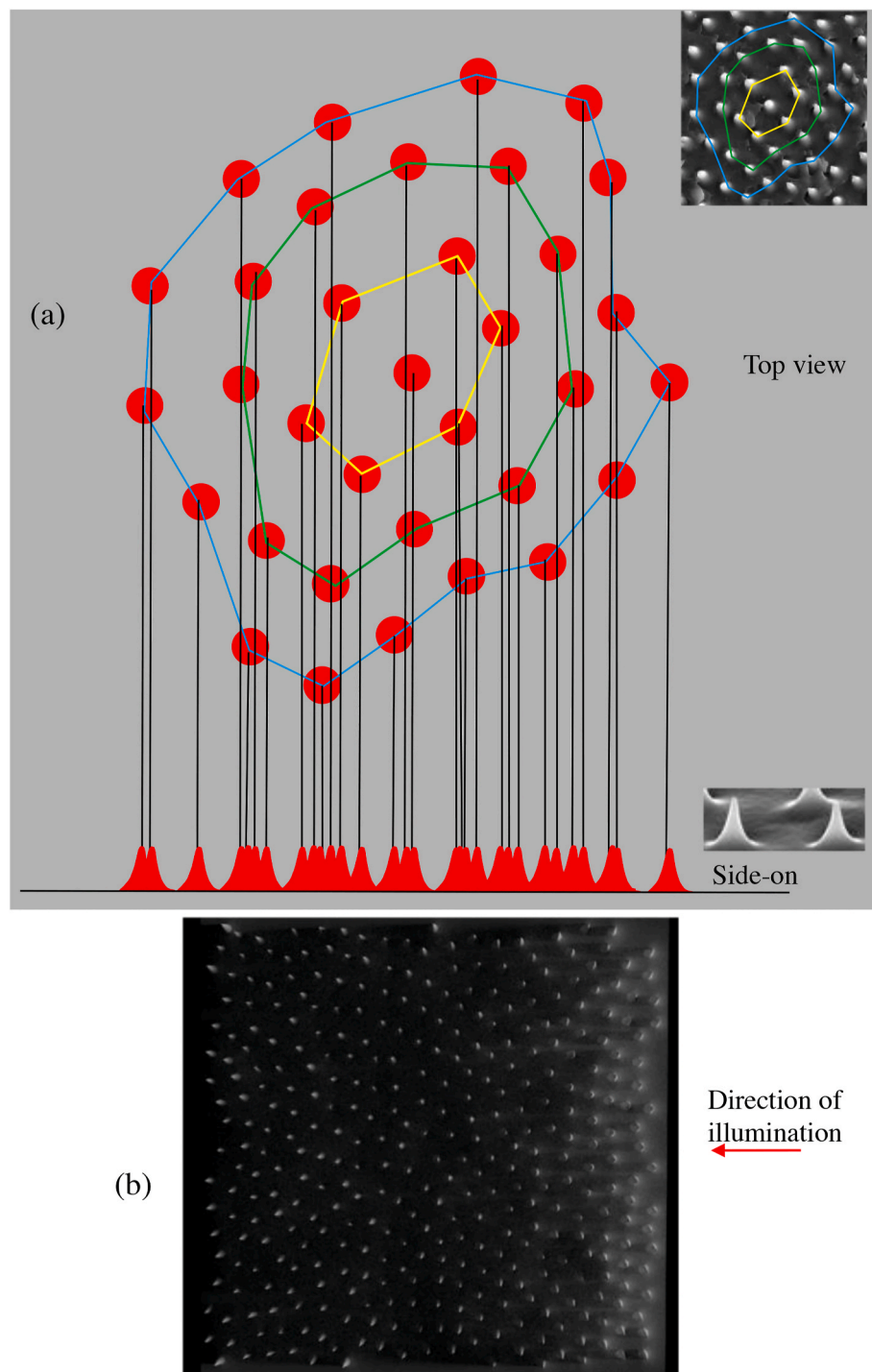
Fig. 14. (a) An arrangement of conical structures seen from above and drawn using Fig. 2 as a template. Inset in the upper right corner shows part of the SEM image used as a template. Side-on view is shown at the bottom of this figure. (b) Top view of a microtrichia 3D model illuminated obliquely from the right (red arrow) shows that microtrichia preclude the propagation of light.

4.99% of radiation is reflected, while for grazing incidence almost all radiation is reflected. Between those two extremes, due to uniform angular distribution of thermal radiation, it is clear that more than 4.99% of thermal radiation is entrapped and waveguided between body and elytra. More detailed answer to this question will be given in further studies.

In the interests of brevity and focus, several other elytral features that might be effective in thermal IR had to be left out of the scope of this paper. First of all, the chitinous lamellae of *M. asper funereus* have a characteristic dimension of 4–5 μm with the corresponding Bragg wavelength of 8–10 μm. Each layer contains well-oriented microfibrils that certainly introduce birefringence, and the orientation of microfibrils is different in each layer (Supplement file). The exact value of the refractive index of chitinous structures is not very well known, in particular in the thermal infrared, and it is therefore difficult to make the correct theoretical calculations and numerical simulations. Thirdly, interfaces between each layer are rough and scatter radiation, so that the layers may act as planar waveguides to additionally absorb the
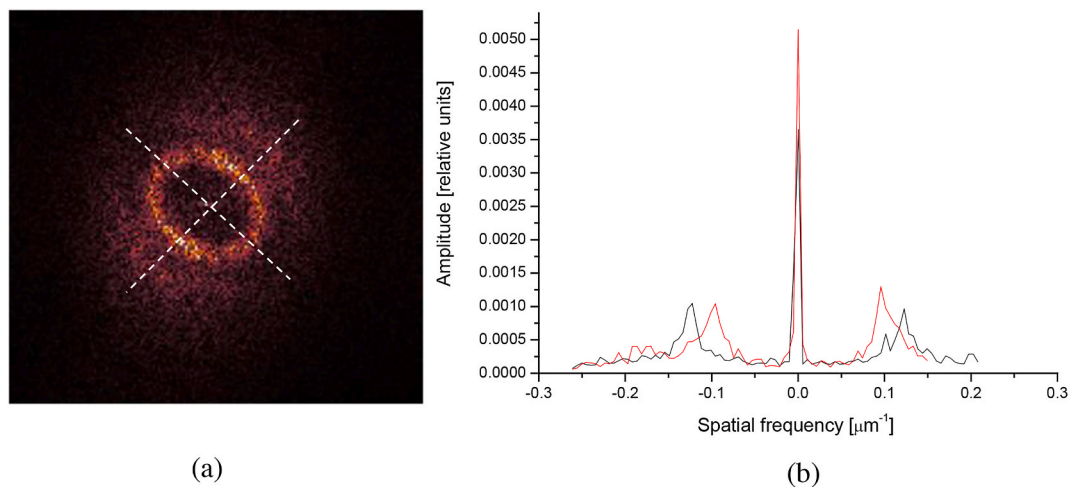
Fig. 15. (a) A Fourier transform of the image in Fig. 2 depicting the arrangement of microtrichia. Note the ring-like pattern with slight ellipticity. (b) Scanning along two orthogonal directions (see dotted lines in (a)) shows a pronounced peak at spatial frequency close to 0.1/μm, corresponding to the average 10-μm distance between microtrichia.

radiation. Finally, microtrichia can act as transmission gratings for non-obliquely impinging radiation and diffraction orders can be coupled into layers as planar waveguides.

From a theoretical point of view, it is quite difficult to treat inherently random structures (such as those of *M. asper funereus*) using exact methods like FEM, RCWA or FDTD. For large structures, periodic boundary conditions have to be introduced, thereby violating inherent randomness. If a random structure is to be simulated, computer memory requirements become extremely large and computational time intolerably long.

We performed other measurements that have revealed the excellent thermal insulation properties of this particular insect. By laser-heating one side of an elytron we observed that, in thermal equilibrium, the other side was approximately 20 °C lower in temperature. It is difficult to discern the contribution of radiative dissipation, with respect to other processes (convection and conduction) (Supplement file). However, the *M. asper funereus* elytron could be an excellent model to design similar thermally insulating materials.

Furthermore, taking into account that *M. asper funereus* lays its eggs in and emerging larvae feed on decaying wood (a saproxylic way of life), similarly to pyrophilous insects (Klocke et al., 2011), it is important for an insect to detect dead trees. Thermal fingerprint of a decaying wood is different, compared to healthy specimens, primarily due to the reduced amount of water. (Pitarma et al., 2019). Based on the structures and properties we have observed, we postulate that a number of infrared detectors on the elytron is used to detect the infrared fingerprint of wood and discriminate between healthy and decaying tree trunks. Even though the number of elytral IR detectors (approx. 400) is small, it is still a useable one, if compared to that of FLIR ONE Gen3 smart-phone, clip-on thermal cameras (60 x 80 IR pixels). By making this comparison we emphasize the "ingenuity" of evolution, in no way endorsing any particular IR camera.

It is well known that Coleoptera elytron has a complex layered structure with number of cavities, trabeculae, channels and pores (Sun and Bhushan, 2012). Research mostly dealt with mechanical significance of internal architecture of elytron (Du and Hao, 2018), and to a lesser degree with thermal effects (Le et al., 2019). By studying available literature we may say that many of structures might serve similar role in thermal radiation management, due to their characteristic dimensions being close to the wavelength of thermal radiation.

In conclusion, we have shown that a combination of micron-sized blackbodies and uniformly random microstructures possesses excellent properties to manage thermal radiation. The range of potential applications is enormous and even might even extend from NIR to terahertz technology.

Ethical approval

All necessary permissions to collect the samples of *M. asper funereus* were obtained from the Ministry of Environmental Protection of the Republic of Serbia and the Institute for Nature Conservation of Serbia. The research did not include live insects.

Author statement

Darko Vasiljević : Formal analysis, Data Curation, Visualization.
Danica Pavlović: Conceptualization, Formal analysis, Investigation, Resources, Writing-Original Draft Preparation.
Vladimir Lazović: Formal analysis.
Branko Kolarić: Project Administration, Writing Review and Editing.
Branislav Salatić: Softwer, Formal analysis.
Wang Zhang: Supervision, Validation.
Di Zhang: Supervision, Validation.
Dejan Pantelić: Conceptualization, Methodology, Investigation, Formal analysis, Writing-Original Draft Preparation.

Declaration of competing interest

The authors declare no conflict of interest.
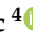
Appendix A. Supplementary data

Supplementary data to this article can be found online at https://doi.org/10.1016/j.jtherbio.2021.102932.

References

Arikawa, K., Takagi, N., 2001. Genital photoreceptors have crucial role in oviposition in Japanese yellow swallowtail butterfly, Papilio xuthus. Zool. Sci. 18 (2), 175–179. https://doi.org/10.2108/zsj.18.175.

Booth, C.O., 1963. Photocinetic function of aphid antennae. Nature 197, 265–266.

Bosi, S.G., Hayes, J., Large, M.C.J., Poladian, L., 2008. Color, iridescence, and thermoregulation in Lepidoptera. Appl. Opt. 47, 5235–5241. https://doi.org/10.1364/AO.47.005235.

Capinera, J.L., 2008. Encyclopedia of Entomology. Springer, New York.

Carpaneto, G.M., Baviera, C., Biscaccianti, A.B., Brandmayr, P., Mazzei, A., Mason, F., Battistoni, A., Teofili, C., Rondinini, C., Fattorini, S., Audisio, P., 2015. A Red List of Italian Saproxylic Beetles: taxonomic overview, ecological features and conservation issues (Coleoptera). Fragm. Entomol. 47, 53. https://doi.org/10.4081/fe.2015.138.

Cossins, A., 2012. Temperature Biology of Animals. Springer Science & Business Media.

De Nicola, F., Hines, P., De Crescenzi, M., Motta, N., 2017. Thin randomly aligned hierarchical carbon nanotube arrays as ultrablack metamaterials. Phys. Rev. B 96 (4), 045409. https://doi.org/10.1103/PhysRevB.96.045409.

Desmond Ramirez, M., Speiser, D.I., Sabrina Pankey, M., Oakley, T.H., 2011. Understanding the dermal light sense in the context of integrative photoreceptor cell biology. Vis. Neurosci. 28, 265–279. https://doi.org/10.1017/S0952523811000150.

Doucet, S.M., Meadows, M.G., 2009. Iridescence: a functional perspective. J. R. Soc. Interface 6 (Suppl. l_2), S115–S132. https://doi.org/10.1098/rsif.2008.0395.focus.

Du, J., Hao, P., 2018. Investigation on microstructure of beetle elytra and energy absorption properties of bio-inspired honeycomb thin-walled structure under axial dynamic crushing. Nanomaterials 8 (9), 667. https://doi.org/10.3390/nano8090667.

Florescu, M., Torquato, S., Steinhardt, P.J., 2009. Designer disordered materials with large, complete photonic band gaps. Proc. Natl. Acad. Sci. Unit. States Am. 106 (49), 20658–20663. https://doi.org/10.1073/pnas.0907744106.

Gillott, C., 2005. Food uptake and utilization. Entomology (Tokyo) 487–513. https://doi.org/10.1007/1-4020-3183-1_16.

Gullan, P.J., Cranston, P.S., 2004. The Insects: an Outline of Entomology. John Wiley & Sons.

Hale, G.M., Querry, M.R., 1973. Optical constants of water in the 200-nm to 200-μm wavelength region. Appl. Opt. 12 (3), 555–563. https://doi.org/10.1364/ao.12.000555.

Hardersen, S., Bardiani, M., Chiari, S., Maura, M., Maurizi, E., Roversi, P.F., Mason, F., Bologna, M.A., 2017. Guidelines for the monitoring of Morimus asper funereus and Morimus asper asper. Nat. Conserv. 20, 205–236. https://doi.org/10.3897/natureconservation.20.12676.

Heinrich, B., 2013. The Hot-Blooded Insects: Strategies and Mechanisms of Thermoregulation. Springer Science & Business Media, New York.

Horton, K.G., Shriver, W.G., Buler, J.J., 2015. A comparison of traffic estimates of nocturnal flying animals using radar, thermal imaging, and acoustic recording. Ecol. Appl. 25 (2), 390–401. https://doi.org/10.1890/14-0279.1.sm.

Jiao, Y., Lau, T., Hatzikirou, H., Corbo, J.C., Torquato, S., Mathematics, A., 2014. Avian photoreceptor patterns represent a disordered hyperuniform solution to a multiscale packing. Phys. Rev. 89 (2), 022721 https://doi.org/10.1103/PhysRevE.89.022721.Avian.

Kastberger, G., Stachl, R., 2003. Infrared imaging technologies. Behav. Res. Methods Instrum. Comput. 35 (3), 429–439.

Kemp, D.J., 2007. Female butterflies prefer males bearing bright iridescent ornamentation. Proc. Biol. Sci. 274 (1613), 1043–1047. https://doi.org/10.1098/rspb.2006.0043.

Kingsolver, J.G., 1985. Butterfly thermoregulation: organismic. J. Res. Lepid. 24 (1), 1–20.

Klocke, D., Schmitz, A., Soltner, H., Bousack, H., Schmitz, H., 2011. Infrared receptors in pyrophilous ("fire loving") insects as model for new un-cooled infrared sensors. Beilstein J. Nanotechnol. 2 (1), 186–197. https://doi.org/10.3762/bjnano.2.22.

Komachi, Y., Wakaki, M., Kanai, G., 2000. Fabrication of hollow waveguides for CO_2 lasers. Appl. Opt. 39 (10), 1555–1560. https://doi.org/10.1364/ao.39.001555.

Le, V.T., Ha, N.S., Goo, N.S., 2019. Thermal protective properties of the allomyrina dichotoma beetle forewing for thermal protection systems. Heat Tran. Eng. 40, 1539–1549. https://doi.org/10.1080/01457632.2018.1474603.

Leonhardt, U., Tyc, T., 2009. Broadband invisibility by non-Euclidean cloaking. Science 323 (5910), 110–112. https://doi.org/10.1126/science.1166332.

Millott, N., 1968. The dermal light sense. In: Symp. Zool.Soc. London, pp. 1–36.

Milošević, M.M., Man, W., Nahal, G., Steinhardt, P.J., Torquato, S., Chaikin, P.M., Amoah, T., Yu, B., Mullen, R.A., Florescu, M., 2019. Hyperuniform disordered waveguides and devices for near infrared silicon photonics. Sci. Rep. 9 (1), 1–11. https://doi.org/10.1038/s41598-019-56692-5.

Mizuno, K., Ishii, J., Kishida, H., Hayamizu, Y., Yasuda, S., Futaba, D.N., Yumura, M., Hata, K., 2009. A black body absorber from vertically aligned single-walled carbon nanotubes. Proc. Natl. Acad. Sci. Unit. States Am. 106 (15), 6044–6047. https://doi.org/10.1073/pnas.0900155106.

Nijhout, H.F., 1991. The Development and Evolution of Butterfly Wing Patterns, vol. 293. Smithson. Inst. Sch. Press.

Parisi, V., Busetto, A., 1992. Revisione dei Coleotteri presenti nella collezione "A. Leosini". Parte 2a. Scarabaeidae, Lucanidae, Cerambycidae. Pubblicazioni del Museo di Storia naturale dell'Università di Parma 5 (1), 1–93.

Pitarma, R., Crisóstomo, J., Ferreira, M.E., 2019. Contribution to trees health assessment using infrared thermography. Agriculture 9 (8), 171. https://doi.org/10.3390/agriculture9080171.

Polak, S., Maja, J., 2012. Phenology and mating behaviour of Morimus funereus (Coleoptera, Cerambycidae). Saproxylic beetles in Europe: monitoring, biology and conservation. Studia Forestalia Slovenica 137, 43–52.

Prokhorov, A., 2012. Effective emissivities of isothermal blackbody cavities calculated by the Monte Carlo method using the three-component bidirectional reflectance distribution function model. Appl. Opt. 51, 2322–2332. https://doi.org/10.1364/AO.51.002322.

Romero-Samper, J., Bahülo, J., 1993. Algunas observaciones sobre la distribución y biología de Morimus asper Cerambicidae en la Península Ibérica. Bol. Asoc. Esp. Entomol. 17, 103–122.

Scoble, M.J., 1992. The Lepidoptera. Form, Function and Diversity. Oxford University Press.

Shi, N.N., 2018. Biological and Bioinspired Photonic Materials for Passive Radiative Cooling and Waveguiding. Doctoral dissertation. Columbia University.

Shi, N.N., Tsai, C.C., Camino, F., Bernard, G.D., Yu, N., Wehner, R., 2015. Keeping cool: enhanced optical reflection and radiative heat dissipation in Saharan silver ants. Science 349 (6245), 298–301. https://doi.org/10.1126/science.aab3564.

Solano, E., Mancini, E., Ciucci, P., Mason, F., Audisio, P., Antonini, G., 2013. The EU protected taxon Morimus funereus Mulsant, 1862 (Coleoptera: Cerambycidae) and its western Palaearctic allies: systematics and conservation outcomes. Conserv. Genet. 14 (3), 683–694. https://doi.org/10.1007/s10592-013-0461-3.

Stabentheiner, S., Schmaranzer, A., 1987. Thermographic determination of body temperatures in honey bees and hornets: calibration and applications. Thermology 2, 563–572.

Stabentheiner, A., Kovac, H., Hetz, S.K., Käfer, H., Stabentheiner, G., 2012. Assessing honeybee and wasp thermoregulation and energetics - new insights by combination of flow-through respirometry with infrared thermography. Thermochim. Acta 534, 77–86. https://doi.org/10.1016/j.tca.2012.02.006.

Stanić, V., Ivanović, J., Janković-Hladni, M., Nenadović, V., Marović, R., 1985. Feeding habits, behavior, oviposition and longevity of the adult cerambycid beetle Morimus asper funereus Muls.(Col., Cerambycidae) under laboratory condition. Acta Entomol. Jugosl. 21, 87–94.

Sun, J., Bhushan, B., 2012. Structure and mechanical properties of beetle wings: a review. RSC Adv. 2 (33), 12606–12623. https://doi.org/10.1039/c2ra21276e.

Sun, J., Liu, C., Bhushan, B., Wu, W., Tong, J., 2018. Effect of microtrichia on the interlocking mechanism in the Asian ladybeetle, Harmonia axyridis (Coleoptera: Coccinellidae). Beilstein J. Nanotechnol. 9 (1), 812–823. https://doi.org/10.3762/bjnano.9.75.

Sweeney, A., Jiggins, C., Johnsen, S., 2003. Polarized light as a butterfly mating signal. Nature 423, 31–32. https://doi.org/10.1038/423031a.

Tucolesco, J., 1933. La dynamique de la larve de Tenebrio molitor et la théorie des tropismes. Bull. Biol. 4, 1–35.

Unruh, T.R., Chauvin, R., 1993. Elytral punctures: a rapid, reliable method for marking Colorado potato beetle. Can. Entomol. 125 (1), 55–63.

van de Kamp, T., Greven, H., 2010. On the architecture of beetel elytra. Entomol. Heute 22, 191–204.

van de Kamp, T., Riedel, A., Greven, H., 2016. Micromorphology of the elytral cuticle of beetles, with an emphasis on weevils (Coleoptera: Curculionoidea). Arthropod Struct. Dev. 45 (1), 14–22. https://doi.org/10.1016/j.asd.2015.10.002.

Verstraete, C., Mouchet, S.R., Verbiest, T., Kolaric, B., 2019. Linear and nonlinear optical effects in biophotonic structures using classical and nonclassical light. J. Biophot. 12, 1–13. https://doi.org/10.1002/jbio.201800262.

Vollmer, M., Möllmann, K.P., 2010. Infrared Thermal Imaging: Fundamentals, Research and Applications. John Wiley & Sons.

Vukusic, P., Sambles, J.R., 2003. Photonic structures in biology. Nature 424 (6950), 852–855. https://doi.org/10.1038/nature01941.

Vukusic, P., Sambles, J.R., Lawrence, C.R., Wootton, R.J., 2001. Now you see it - now you don't. Nature 410 (6824). https://doi.org/10.1038/35065161, 36-36.

Fluorimetry in the Strong-Coupling Regime: From a Fundamental Perspective to Engineering New Tools for Tracing and Marking Materials and Objects

Mohamed Hatifi [1,2,*], Dimitrije Mara [3], Bojana Bokic [4], Rik Van Deun [5], Brian Stout [1], Emmanuel Lassalle [1,6], Branko Kolaric [4,7] and Thomas Durt [1]

1 Aix Marseille Univ, CNRS, Centrale Marseille, Institut Fresnel, UMR 7249, 13013 Marseille, France
2 Quantum Dynamics Unit, Okinawa Institute of Science and Technology Graduate University, Onna, Okinawa 904-0495, Japan
3 Institute of General and Physical Chemistry, Studentski trg 12/V, 11158 Belgrade, Serbia
4 Center for Photonics, Institute of Physics, University of Belgrade, Pregrevica 118, 11080 Belgrade, Serbia
5 L^3—Luminescent Lanthanide Lab, Department of Chemistry, Ghent University, Krijgslaan 281-S3, 9000 Ghent, Belgium
6 Institute of Materials Research and Engineering, A*STAR (Agency for Science, Technology and Research), Singapore 138634, Singapore
7 Micro- and Nanophotonic Materials Group, University of Mons, Place du Parc 20, 7000 Mons, Belgium
* Correspondence: hatifi.mohamed@gmail.com

Abstract: Under exceptional circumstances, light and molecules bond together, creating new hybrid light–matter states with far-reaching consequences for these strongly coupled entities. The present article describes the quantum-mechanical foundation of strong-coupling and experimental evidence for molding the radiation properties of nanoprobes by strong-coupling. When applied to tracing and marking, the new fluorometry technique proposed here, which harnesses strong-coupling, has a triple advantage compared to its classical counterparts such as DNA tracing. It is fast, and its signal-to-noise ratio can be improved by spectral filtering; moreover, it reveals a specific quantum signature of the strong-coupling, which is extremely difficult to reproduce classically, thereby opening the door to new anti-counterfeiting strategies.

Keywords: strong-coupling; light-matter interaction; steady-state and time-resolved fluorescence spectroscopy; metallic cavities

1. Introduction

Fluorophores possess numerous biomedical applications where they are used as tracers and markers. For instance, they can be linked to DNA branes in devices aimed at detecting the presence of viruses in blood samples. Lab-on-a-chip applications of such techniques present promising applications [1], especially in the times of pandemic, where it offers possibilities for the fast detection of viruses in airports or other public places. They could also be used as markers for authenticating the origin of certain manufactured products and avoiding copies and counterfeits as we propose here. The most significant advantages of fluorimetry are its extremely fast response time, the sensitivity of the excited states to the local environment, and the possibility of incorporating fluorophore in a chip/device and simultaneously measuring many samples for a short time [2].

This article proposes a new fluorescence technique that exploits the strong light–matter interaction of an embedded nanoprobe within a plasmonic cavity. The signature of strong light–matter interactions between nanoprobes and cavity modes is typically detected through changes in the excitation spectrum (electronic or vibrational) of the coupled system [3–8].

When strong-coupling occurs, the isolated excited emitter is no longer an eigenstate of the system but corresponds to a superposition of the higher and lower polaritons, which evolve at different frequencies, leading to coherent oscillations of the excitation between the emitter and the cavity mode. On account of these vacuum Rabi oscillations, the emitter cycles through absorption and emission instead of exhibiting the more familiar exponential decay process. Amplification of the signal in a resonant cavity therefore plays an essential role and is accompanied by a specific quantum effect (frequency shift). It presents significant advantages regarding tracing and marking applications:

- Frequency shifts make it possible to improve the signal-to-noise ratio;
- Frequency splitting constitutes a signature of strong-coupling which is difficult to counterfeit.

The paper is structured as follows. In Section 2, we outline the basic principles of our proposal, aimed at applying the properties of strongly coupled emitters for authentication and tracing. In Section 3, we summarize the theory of strong-coupling, and we explain the transition from the weak to the strong-coupling regimes in terms of Poincaré recurrences. In Section 4, we describe our experimental set-up. In Section 5, we discuss its specific advantages regarding tracing and marking. The Supplementary Material contains details concerning the implementation of our experimental set-up and a theoretical derivation of the spectrum of emission of the cavity in the strong-coupling regime.

2. Concept of "Quantum Filigran" Based on Strong-Coupling

2.1. Physically Unclonable Functions

A physically unclonable function (PUF) is a physical structure that is widely used as a unique identifier for various objects. PUFs depend on the uniqueness of their physical microstructure [9]. Generally, PUF microstructures depend on random physical factors introduced during manufacturing to create a unique response, or on biologically induced randomness (cellular noise) during the morphogenesis of natural photonic structures [9,10]. These factors are unpredictable and uncontrollable, which makes it virtually impossible to duplicate or clone the structure. However, the dependence of PUF on modern colloidal or biological self-assembly processes makes this approach, in many cases, complicated and limited. In this article, we offer an entirely different approach that can be used for authentication and marking based on quantum filigran where uniqueness is achieved by controlling the light–matter interaction in the strong-coupling regime. The advantage of the present method, besides its uniqueness, is that it also offers a fast and unique read-out that could be exploited for different sensing and marking applications at large scale. The first example of quantum PUF can be traced back to Wiesner quantum money protocol [11] which is based on the quantum no cloning theorem. Here, we propose a semi-classical protocol in which quantized light–matter interaction plays a prominent role, the "quantum filigran".

2.2. Quantum Filigran

The principle of the filigran used for authenticating banknotes is common knowledge. In summary, when we submit the banknote to a specific optical excitation (illumination at normal incidence), a specific response is induced at the level of the filigran (the image of the filigran becomes visible if we observe it in transparency along the axis joining it to the source). It is not easy to counterfeit such filigrans, which differ from usual 2D images by the fact that they are not visible under grazing illumination. Ultimately, it is this specific response of the filigran that explains why it is a useful tool for authentication. Our goal, roughly expressed, is to conceive quantum filigrans based on the specific optical response of well-chosen fluorophores, in the quantum strong-coupling regime. The scheme of principle of our idea is depicted in Figure 1: a solution containing fluorophores is placed inside a tunable Fabry–Pérot cavity; a fluorophore is resonantly excited by a laser source and absorbs a photon at a wavelength of 440 nm. A part of the energy is lost in

an initial non-radiative process, followed by a radiative quantum jump at wavelengths of 530 ± 25 nm.
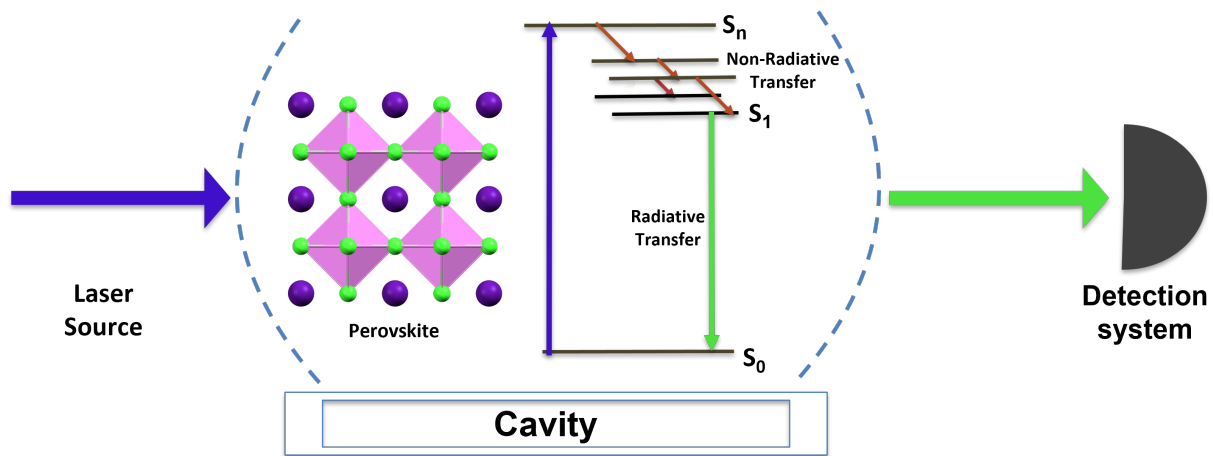

Figure 1. Scheme of *Quantum Filigran* experiment. The blue arrow represents the light emitted by the laser, resonant with the peak of absorption of the fluorophore (440 nm). The green arrow represents the emitted photon. Note that in the strong coupling regime, photons are emitted at two possible wavelengths (530 ± 25 nm), a manifestation of frequency splitting.

This frequency splitting is the signature of quantum strong coupling which is ensured by placing the fluorophore in a cavity resonant at 530 nm (for more details, see Section 4). The single photons emitted one at a time by the fluorophores are filtered in frequency around one of the two emission peaks and collected in a typical fluorescence device consisting of a single photon detector coupled to an acquisition table. The statistical distribution of the arrival times of the photons emitted by the fluorophore is well-approximated by a double exponential distribution. As a last resort, this distribution is, as explained in Section 4), the signature of the presence, at the level of the fluorophore, of two competing non-radiative processes, a short one and a long one. This specific response of the fluorophore (single photon emission, plus frequency splitting and frequency shift, plus specific temporal statistics) is extremely difficult to clone by classical methods; it will play the role of a quantum filigran in our proposal.

3. Fluorophore Coupled to a Resonant Cavity in the Strong-Coupling Regime

3.1. Strong-Coupling with a Perfect Lossless Cavity

Strong-coupling naturally appears if we consider a two-level system (atom, fluorophore) resonantly coupled to an ideal, lossless and isolated, cavity mode. The Hamiltonian describing such a system is well-known. It is the so-called Jaynes–Cumming (J–C) Hamiltonian. It is obtained after performing various approximations (such as dipolar coupling and rotating wave approximation). In an empty cavity, for an atom dipole moment $\mathbf{d} = d\vec{u}_d$ and a perfect polarization and position matching with the mode, the dipolar interaction is equal to the product $-dE_0$ between the dipole moment and the effective cavity electric field (in the absence of photon). The electric field of the empty cavity is $E_0 = \sqrt{\hbar\omega_c/(2\epsilon_0 V_c)}$, where V_c is the cavity volume and ω_c is the cavity mode frequency. The coupling strength is characterized by $g = dE_0/\hbar = \Omega_0/2$.

$$\hbar g = d\sqrt{\frac{\hbar\omega_c}{2\epsilon_0 V_c}} \tag{1}$$

The J–C Hamiltonian [12] then reads

$$\hat{H}_{\text{JC}} = \hbar\omega_0\hat{\sigma}^\dagger\hat{\sigma} + \hbar\omega_c\hat{a}^\dagger\hat{a} + \hbar g\left(\hat{\sigma}\hat{a}^\dagger + \hat{\sigma}^\dagger\hat{a}\right) \tag{2}$$

The parameters of this Hamiltonian are the atomic transition frequency ω_0, the cavity mode frequency ω_c, and the coupling constant g. When a single dipole (atom/fluorophore) is considered, the state of the system is

$$|\psi(t)\rangle = \alpha(t)|e, 0_c\rangle + \beta(t)|g, 1_c\rangle \tag{3}$$

where the state $|e, 0_c\rangle$ stands for dipole in the excited state and no photon in the cavity and $|g, 1_c\rangle$ stands for dipole in the ground state and one photon in the cavity. The J–C Hamiltonian then reduces to a 2×2 matrix

$$\hat{H}_{\text{J-C}} = \hbar \begin{bmatrix} \omega_0 & g \\ g & \omega_c \end{bmatrix} \tag{4}$$

It is worth noting that $\hat{H}_{\text{JC}}$ is Hermitian. In what follows, we shall consider a nearly resonant cavity ($\omega_c \approx \omega_0$ so that the detuning $\delta = \omega_c - \omega_0$ is small).

The new eigenenergies of the coupled system are [13]

$$E_\pm = \hbar\omega_c \pm \frac{1}{2}\hbar\sqrt{\delta^2 + \Omega_0^2} \tag{5}$$

where we defined the so-called vacuum Rabi frequency:

$$\Omega_0 \equiv \sqrt{4g^2} \tag{6}$$

At resonance ($\delta = 0$), the energy difference between the two modes is minimal and equal to $\hbar\Omega_0$. The energy eigenstates are given by

$$\begin{aligned} |+\rangle &= \sin\theta\,|e, 0_c\rangle + \cos\theta\,|g, 1_c\rangle \\ |-\rangle &= \cos\theta\,|e, 0_c\rangle - \sin\theta\,|g, 1_c\rangle \end{aligned} \tag{7}$$

The parameter θ defines the entanglement strength [3] between the dipole and the cavity mode ($\tan 2\theta = \Omega_0/\delta$). At resonance, entanglement is maximal ($\theta = \pi/4$) and the dressed states have matter and field components of equal weight. The separation between two distinct matter–radiation subsystems is then impossible. Far from resonance ($\theta \approx 0$ and $\theta \approx \pi/2$), these states exhibit dominant matter or electromagnetic components. These polaritonic states inherit dispersion relations from their electromagnetic component. Let us note that the pair of eigenenergies $E_\pm$ and eigenstates $|\pm\rangle$ are only the lowest of an infinite ladder of pairs. Similar pairs exist for the quantum superposition of states $|n_c, e\rangle$ and $|n_c + 1, g\rangle$ involving the presence of n_c or $n_c + 1$ photons in the cavity, respectively. Their energy gap at resonance is given by $\hbar\Omega_0\sqrt{n_c + 1}$.

In practice, perfectly lossless cavities do not exist and the criterium to enter the strong-coupling regime is that the Rabi frequency Ω_0 must be significantly larger than the widths γ_c and γ related to the cavity mode and matter excitation lifetimes, respectively. In other words, coupling must dominate over dissipative processes. This condition is required to preserve quantum coherence, as the Rabi frequency describes the rate of coherent energy conversions between matter and the radiation field in the dressed states. In general, to increase the coupling g, one needs to select quantum emitters with a strong transition dipole and to confine the electromagnetic field in a small volume. To decrease γ_c, high-finesse cavities are required. The team of S. Haroche (Nobel prize 2012), which is at the same time a pioneering and a leading team in the domain of strong coupling, developed high-finesse superconducting cavities cooled down to a few millikelvins, and reached huge values for the coupling factors g by using, as two-level systems, Rydberg atoms resonant with the cavity [14]. In our approach, it is rather the Purcell effect [15] that plays a prior role in increasing the value of g. This explains why we realize strong coupling even at room temperatures, as explained in Section 4.

3.2. Strong-Coupling with a Lossy Cavity

In order to phenomenologically describe losses [16] let us now consider the pure state (3) dynamics described by a *non-Hermitian* "effective" Hamiltonian $\hat{H} = \hat{H}_{\text{J-C}} + \hat{H}_{\text{loss}}$ where $\hat{H}_{\text{loss}}$ is introduced phenomenologically and, in the basis $\{|e, 0_c\rangle, |g, 1_c\rangle\}$, reads:

$$\hat{H}_{\text{loss}} = \hbar \begin{bmatrix} 0 & 0 \\ 0 & -i\frac{\gamma_c}{2} \end{bmatrix} \tag{8}$$

where the parameter γ_c is called the cavity decay rate.

The coefficients $\alpha(t)$ and $\beta(t)$ are obtained by solving the Schrödinger equation with the non-Hermitian Hamiltonian $\hat{H} = \hat{H}_{\text{J-C}} + \hat{H}_{\text{loss}}$:

$$i\hbar \frac{\partial}{\partial t} \begin{bmatrix} \alpha(t) \\ \beta(t) \end{bmatrix} = \hbar \begin{bmatrix} \omega_0 & g \\ g & \omega_c - i\frac{\gamma_c}{2} \end{bmatrix} \begin{bmatrix} \alpha(t) \\ \beta(t) \end{bmatrix} \tag{9}$$

In order to solve the dynamics of such a system, let us diagonalize the above matrix. Upon diagonalization, one finds the following eigenvalues:

$$\omega_\pm = \frac{\omega_0 + \omega_c}{2} - i\frac{\gamma_c}{4} \pm \frac{\Omega}{2} \tag{10}$$

where we defined the quantity:

$$\Omega \equiv \sqrt{4g^2 + \left(\delta + i\frac{\gamma_c}{2}\right)^2} \tag{11}$$

(where $\delta \equiv \omega_0 - \omega_c$ represents the detuning). We are first of all interested in the probability of finding the atom in the excited state, the *survival probability* defined as $P_{\text{surv}}(t) \equiv |\alpha(t)|^2$, so we want to find the expression of $\alpha(t)$. Its general expression reads:

$$\alpha(t) = A_+ e^{-i\omega_+ t} + A_- e^{-i\omega_- t} \tag{12}$$

where the constants A_+ and A_- are determined by the initial conditions $\alpha(0) = 1$ and $\dot{\alpha}(0) = -i\omega_0$ (coming from the fact that $\beta(0) = 0$ in Equation (9)):

$$A_\pm = \frac{1}{2} \pm \frac{\delta + i\gamma_c/2}{2\Omega} \tag{13}$$

It is worth noting that for one excitation (photon), the phenomenological approach is equivalent to a rigorous dissipative approach using a master equation (see, e.g., Ref. [17] Chapter 6, especially Section 6.2, entitled "Spontaneous emission: From irreversible decay to Rabi oscillations").

3.3. Weak and Strong-Coupling Regime in the Resonant Case $\omega_0 = \omega_c$

In the *resonant case*, $\omega_0 = \omega_c$, the eigen-frequencies in Equation (10) become:

$$\omega_\pm = \omega_c - i\frac{\gamma_c}{4} \pm \frac{\Omega}{2} \tag{14}$$

where Ω now reads:

$$\Omega = \sqrt{4g^2 - \left(\frac{\gamma_c}{2}\right)^2} \tag{15}$$

One can clearly see that two different regimes in the time-domain are possible depending on the values of g and γ_c:

(i) For a small coupling constant, $g < \frac{1}{4}\gamma_c$, Ω becomes purely imaginary, and the eigen-frequencies $\omega_\pm$ (Equation (14)) are now complex, leading to a monotonic decay of the amplitude $\alpha(t)$ in time (Equation (12)), known as the **weak-coupling regime.**

(ii) For a large coupling constant, $g > \frac{1}{4}\gamma_c$, Ω is real, and the eigen-frequencies $\omega_\pm$ (Equation (14)) show a different real part, leading to *oscillations* of the amplitude $\alpha(t)$ in the time-domain, known as the **strong-coupling regime**.

The general solution will not be considered in detail here but we shall focus on the (very) strong-coupling regime, i.e., when $g \gg \gamma_c$. A very good approximation of the solution may be derived in this case by means of power series expansion:

$$\Omega \simeq 2g - \frac{\gamma_c^2}{16g} \tag{16}$$

$$\omega_\pm \simeq -i\frac{\gamma_c}{4} \pm g \tag{17}$$

$$A_\pm \simeq \frac{1}{2} \pm i\frac{\gamma_c}{8g}\left(1 + \frac{\gamma_c^2}{32g^2}\right)$$
$$\simeq \frac{1}{2} \tag{18}$$

Then, $\alpha(t)$ becomes

$$\alpha(t) \simeq e^{-\frac{\gamma_c}{2}\frac{t}{2}}\cos(gt) \tag{19}$$

which gives a survival probability $P_{\text{surv}}(t) = |\alpha(t)|^2$

$$P_{\text{surv}}(t) = e^{-\frac{\gamma_c}{2}t}\cos^2(gt) = \frac{1}{2}e^{-\frac{\gamma_c}{2}t}[1 + \cos(2gt)] \tag{20}$$

One can see in this equation that $P_{\text{surv}}(t) = |\alpha(t)|^2$ oscillates at the frequency $\Omega = 2g$. These oscillations, also called "vacuum Rabi oscillations", are characteristic of the strong-coupling [17].

3.4. Emission Spectrum in the Strong-Coupling Regime

There exists an alternative way to describe the coupling of a dipole to a lossy cavity, which is conceptually quite different from the ones presented in the previous sections. This model ([18], Chapter 1, Complement 1A) treats the spontaneous emission of an atom coupled to a bounded continuum of electromagnetic modes, with a bandwidth γ_c. As previously, the atom is modeled as a two-level system with transition frequency ω_0, and the continuum is assumed to have a "Lorentzian" density of states (modes) centered on a frequency ω_c and with a bandwidth expressed through the Full Width Half Maximum (FWHM) and from now on taken to be equal to γ_c. In particular, while conceptually very different, this model predicts the same temporal behavior as the previous ones. Its interest is that it predicts the distribution in energy of the emitted photons in the continuum which is an observable that one can measure in practice: the so-called vacuum Rabi splitting.

This model is developed in appendix (Supplementary Material), where we show that, in the highly strong-coupling regime, the probability of emitting a photon in mode j, denoted $P_{\text{emit,j}}(t \to +\infty) \equiv |\beta_j(t \to +\infty)|^2$ obeys

$$P_{\text{emit,j}}(t \to +\infty) = \frac{1}{4}\frac{|g_j|^2}{[(\omega_j - \omega_0) + g]^2 + \left(\frac{\gamma_c}{4}\right)^2} + \frac{1}{4}\frac{|g_j|^2}{[(\omega_j - \omega_0) - g]^2 + \left(\frac{\gamma_c}{4}\right)^2} + \text{C.T.} \tag{21}$$

where the cross-term C.T. is given by:

$$\text{C.T.} = \frac{|g_{\text{j}}|^2}{2} \frac{(\omega_{\text{j}} - \omega_0)^2 - g^2 + \left(\frac{\gamma_c}{4}\right)^2}{\left[(\omega_{\text{j}} - \omega_0)^2 - g^2 + \left(\frac{\gamma_c}{4}\right)^2\right]^2 + 4\left(\frac{\gamma_c}{4}\right)^2 g^2} \tag{22}$$

As seen from Equation (21), in the strong-coupling regime $g > \gamma_c$, the distribution of emitted photons features two peaks separated by $2g$, and of FWHM= $2 \times \gamma_c/4 = \gamma_c/2$. Therefore, an "order of magnitude" condition to be able to distinguish the two peaks is:

$$2g > \frac{\gamma_c}{2} \quad \Rightarrow \quad \boxed{g > \frac{\gamma_c}{4}} \tag{23}$$

When this condition is fulfilled, strong-coupling is achieved and the emission spectrum consists of two non-overlapping Lorentzian distributions respectively centered around $\omega_0 - g$ and $\omega_0 + g$, which is the Rabi splitting previously described in Equations (5) and (6).

3.5. Studying Poincaré Recurrences with a Discrete Model of Evolution

As we show now, the weak- to strong-coupling transition can also be interpreted in terms of Poincaré recurrences, in the framework of a discrete model which can be tackled numerically. We have already considered this model in the past, in Refs. [3,19] where we focused on energy conservation, and also showed its good agreement with the Wigner-Weiskopff model [20]. In this model, one considers a single atom coupled to N states j with a "door" distribution centered on the atomic frequency ω_0 and of variable bandwidth γ_c. They represent the distribution of the e-m modes in the cavity. One can then express the evolution equation in a matrix form:

$$i\hbar \frac{\partial}{\partial t} \begin{pmatrix} \alpha(t) \\ \beta_1(t) \\ \vdots \\ \beta_N(t) \end{pmatrix} = \hbar \underbrace{\begin{pmatrix} \omega_0 & g_1^*(\mathbf{r_0}) & \cdots & g_N^*(\mathbf{r_0}) \\ g_1(\mathbf{r_0}) & \omega_1 & & \\ \vdots & & \ddots & \mathbf{0} \\ g_N(\mathbf{r_0}) & \mathbf{0} & & \omega_N \end{pmatrix}}_{M} \cdot \begin{pmatrix} \alpha(t) \\ \beta_1(t) \\ \vdots \\ \beta_N(t) \end{pmatrix}, \tag{24}$$

Moreover, one assumes equal and real coupling constants: $g_j(\mathbf{r_0}) \equiv \mathbf{g}$ for all modes j.

The square matrix M can be numerically diagonalised. The program gives back the eigenvalues κ_n and eigenvectors $|\kappa_n\rangle$ of M, which can be used to solve $\alpha(t)$ and $\beta_j(t)$, using the general expression of their solution

$$\begin{pmatrix} \alpha(t) \\ \beta_1(t) \\ \vdots \\ \beta_N(t) \end{pmatrix} = \sum_{n=1}^{N+1} c_n |\kappa_n\rangle e^{-i\kappa_n t}. \tag{25}$$

where the c_n are given by the initial conditions:

$$\alpha(t = 0) = 1 \tag{26}$$
$$\beta_j(t = 0) = 0 \tag{27}$$

In order to better understand the implications of our toy model, we plotted the survival probability of the initially excited atom/fluorophore in function of the coupling to the cavity, varying the parameters of the model. These parameters are: $\rho = 1/\delta\omega$ which is the density of states in the comb (with $\delta\omega$ equal to the difference $\omega_i - \omega_{i-1}$ for $i \geq 1$); N is the number of modes and λ the coupling between the "atom" and the "cavity". $N \cdot \delta\omega$ is thus equal to

the "continuum" bandwidth γ_c, while the theoretical value of the gamma factor obtained by applying the Fermi golden rule is denoted γ. It is equal to $2\pi\lambda^2\rho$.

In Figure 2, we plot the survival probability $P_{\text{surv}}(t) = |\alpha(t)|^2$ obtained with this numerical method in the weak coupling regime, for two values of the density of modes, adjusting, however, the coupling constant in order to keep constant the theoretical value of the gamma factor obtained by applying the Fermi golden rule. Exponential decay is well observed, in agreement with the Fermi golden rule, but for very long times there appear large "revival" peaks which are an artefact peculiar to the discretization [3]. It is a manifestation of partial Poincaré recurrence due to the fact that when the Hilbert space of the quantum system is of finite dimension, the Poincaré recurrence time is finite (and its value is the smallest common multiple of all the eigenfrequencies of the Hamiltonian in Equation (24)). The Poincaré recurrence time increases when the density of modes increases as we can check comparing the red and blue recurrences, illustrating that, at least in the weak-coupling regime, the Poincaré recurrence goes to infinity in the continuum's limit.
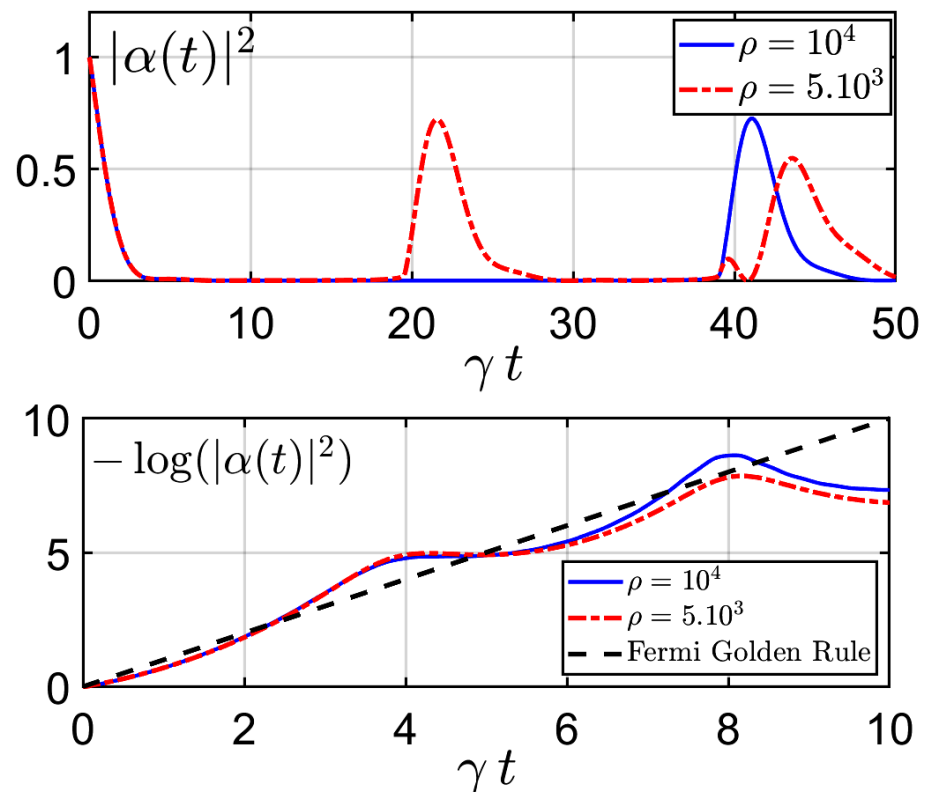

Figure 2. Survival probability in function of time in the weak coupling regime: linear–linear plot (above) and log–linear plot (below) for two values of the mode density ρ, respecting the scaling constraint $2\pi\rho \cdot \lambda^2 = \gamma =$ constant (where γ is the decay factor obtained from the Fermi golden rule and γt the rescaled time).

As can be seen in Figure 3, when we vary the bandwidth, keeping constant the spacing between the states in the comb, as well as the gamma factor obtained by applying the Fermi golden rule, the Poincaré recurrence time is constant. This effect is easy to explain in the weak-coupling regime because "active" resonant modes are then confined in an interval of width Γ around the resonant frequency in agreement with time-energy uncertainties; therefore, in the broad spectrum regime ($N \cdot \delta\omega >> 2\pi\gamma$), the physics of the system is unchanged when we vary the bandwidth.
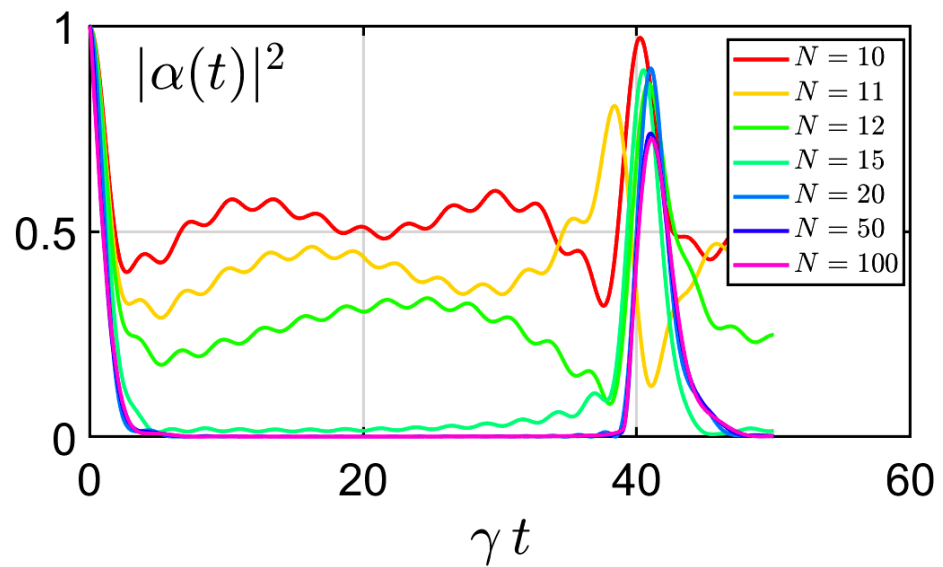
Figure 3. Survival probability in function of time respecting the scaling constraint $\rho \cdot \lambda^2 = \gamma_F =$ constant but varying the number of modes N.

This is no longer true however if we keep the number of modes constant, even when we vary the bandwidth (respecting the scaling constraint $\rho \cdot \lambda^2 = $ constant), as already seen in Figure 2.

When the number of modes is small enough, new fractional Poincaré recurrences appear, announcing the Rabi oscillations of Figure 4, typical of the strong coupling regime.

As can be seen from Figure 4, fractional Poincaré recurrences appear at the weak–strong transition ($N \cdot \delta\omega/\gamma = \gamma_c/\gamma > 2\pi$). In the strong-coupling regimes the revivals become indistinguishable from Rabi oscillations. The nature of Poincaré recurrences is clearly different in the weak- and strong-coupling regimes: in the weak-coupling regime they are an artefact of the discretization; in the strong-coupling regime, (fractional) Poincaré recurrences correspond to Rabi oscillations.
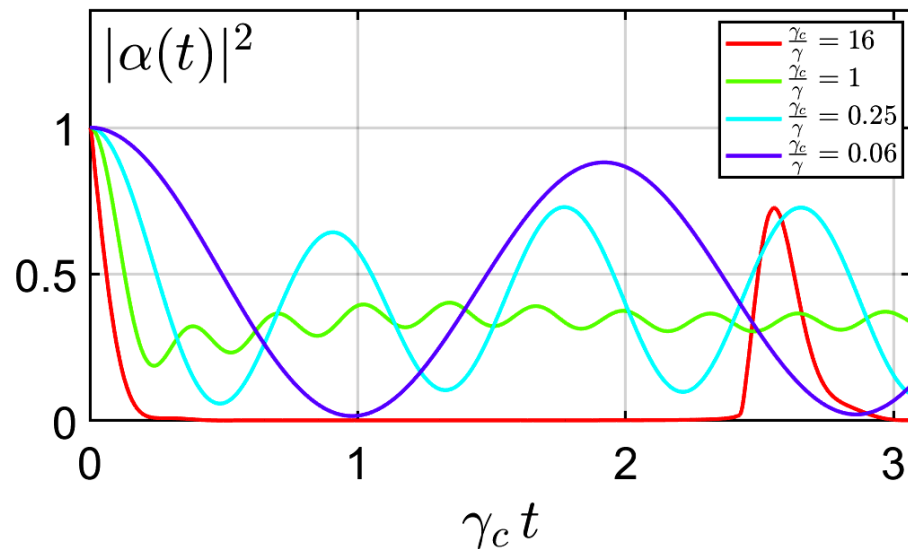

Figure 4. Survival probability in function of time for various values of γ_c/γ. In the weak-coupling regime, the Poincaré recurrence is an artefact of discretization, whereas in the strong-coupling regime Poincaré recurrences become indistinguishable from Rabi oscillations, typical of a system consisting of two coupled modes.

4. Experimental Study

4.1. Experimental Protocol

In order to perform the strong-coupling between nanoprobe and the cavity, we fabricated the plasmonic cavity by combining thermal-sputtering (for metal/Al deposition), and spin coating (for controlling the thickness of the cavity and for embedding nanoprobes into the cavity). The obtained cavity has a quality factor of around 70. Later we dissolved perovskite fluorophores (commercially available), at the concentration of 0.1 nM. The schematic structure of perovskite is presented in Figure 5.

Subsequently, 10 microliters of the perovskite solution (dissolved in toluen) were transferred into polymer solution (polystyrene(PS), volume 2 mL) used for spin coating in order to place the nanoprobe inside a cavity. The thickness of the cavity was adjusted to achieve resonance ($\delta = \omega_c - \omega_0$ close to zero, where ω_0 represents the Bohr frequency of the fluorophores in free space).

The details concerning cavity design, sample preparation, and quality factor estimation are described in Supplementary Materials.
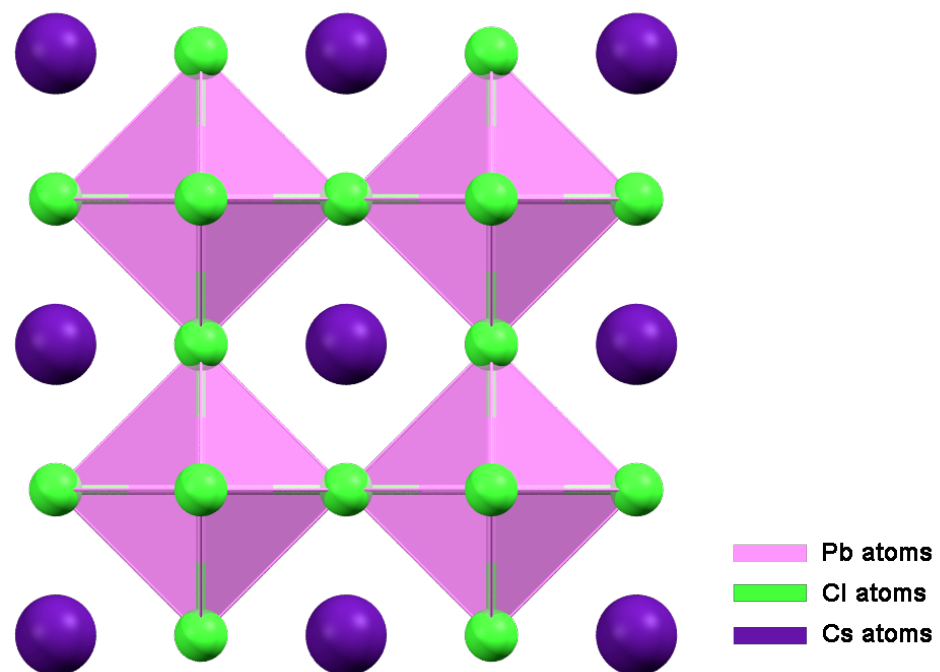

Figure 5. Structure of CsPbCl$_3$ perovskite is based on crystal structure from ICSD database 201250 [21].

4.2. Results

First, we investigate the fluorescence response of the perovskite outside the cavity. Figure 6 shows the fluorescence response of the perovskite probes in solution. The excitation wavelength used for fluorescence measurement was 440 nm. The observed emission spectrum is relatively narrow (for organic and metalorganic compounds), with the maximum around 530 nm and full width half maximum (FWHM) approximately 25 nm.
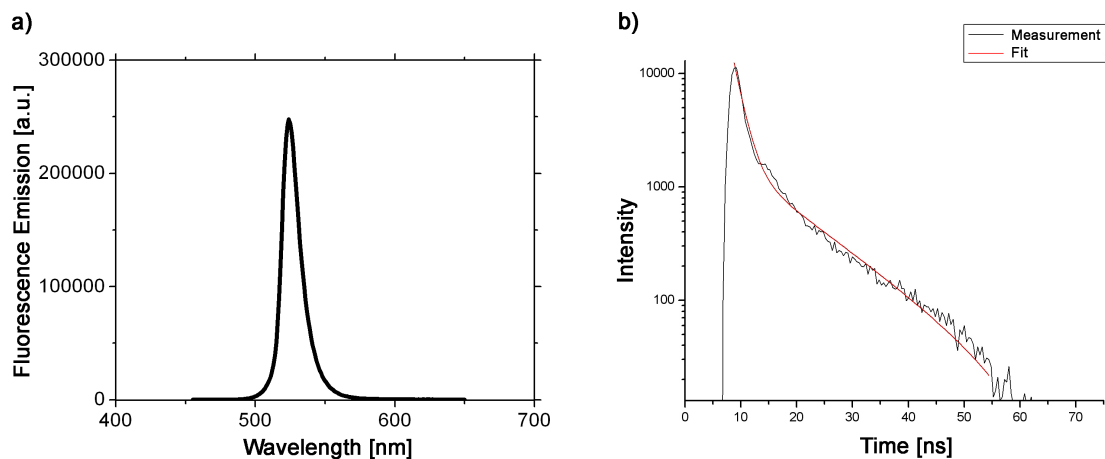
Figure 6. (**a**) Fluorescence steady state spectrum of perovskite in solution; (**b**) Fluorescence decay time response of the perovskite in solution fitted with a double exponential function.

In order to understand better the radiative response, we performed time-resolved measurements of the emitted fluorescence intensity (Figure 6b). The best fits of experimental results are obtained with a double exponential function that gave rise to a long decay time (of ca. 12.2 ns) that is related to the actual lifetime of the probe in this particular environment, and a short decay time (of ca. 1.6 ns), is associated with different nonradiative processes that affect the radiative dynamics of the dye. After that, we perform the steady-state investigation of the perovskite embedded into the plasmonic cavity at two different temperatures (room temperature 298 K and 10K). The sample was excited from outside the cavity; the excess energy $\delta\omega$ is necessary for creating a complex metastable excited state that will firstly follow a complicated non-radiative decay process before arriving at the radiative excited dipole state $|e, 0_c\rangle$ considered in Section 3. The steady-state response of the perovskite within the cavity is presented in Figure 7 and shows the signature of Rabi splitting that confirms that strong coupling between cavity and probe is achieved. As can be seen from Figure 7b, the splitting remains observable at room temperature, even though the height of the peaks diminished by then due to various sources of decoherence that increase with increasing temperature of the sample. Figure 7a exhibits the typical response of a Fabry–Pérot cavity.
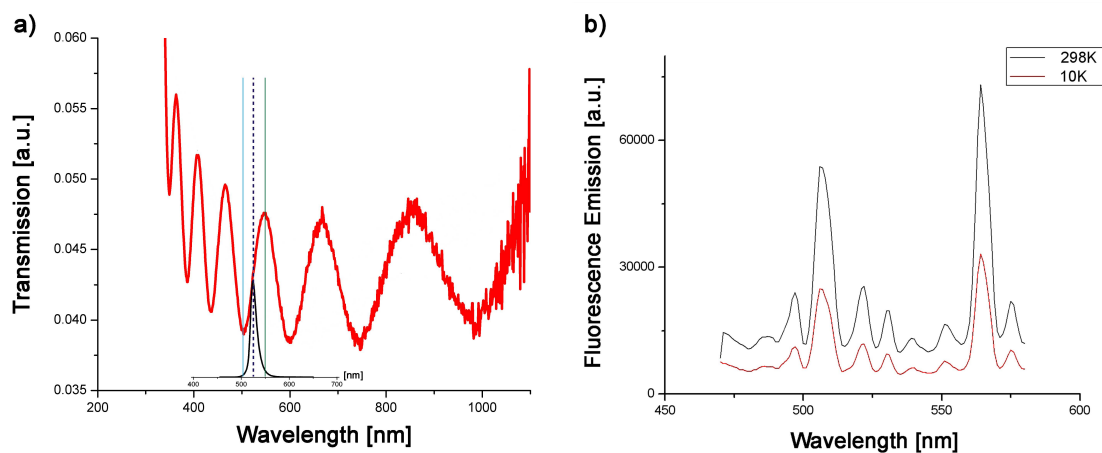

Figure 7. (**a**) Optical response of the cavity with emission spectrum from perovskite fluorophores in solution (inset); (**b**) emission spectrum from perovskite fluorophores in cavity—signature of Rabi splitting.

After a steady-state fluorescence study that shows the signature of the strong-coupling through Rabi splitting, the fluorescence time-resolved study reveals the effect of the strong coupling on the dynamics of the excited state. The theoretical decay time of the cavity is comparable, in the strong-coupling regime, to the survival time of the excited state $|e, 0_c\rangle$. It can be estimated by measuring the width of one of the Lorentzian peaks of Figure 7. By so doing, we estimate the lifetime of the cavity to be in the picosecond range. The distance between the two peaks makes it possible to estimate the value of the coupling constant g from which the ratio g/γ_c is thus predicted to be equal to 5.9, which confirms once more that we are well in the strong-coupling regime. Results of the measurement show that, as in the case of the probe in solution, the perovskite radiation dynamics within the cavity are best fitted with the double exponential functions. Like the energy splitting, the two decay signatures survive at room temperature (as can be seen from Figure 8. At room temperature (298 K), the perovskite within the cavity gave rise to a long decay time (of ca. 7.7 ns) that is related to the actual lifetime of the probe within the cavity and a short decay time (of ca. 0.87 ns) that is associated with different nonradiative processes that affect the radiative dynamics of the dye. The probe's lifetime within the cavity is significantly shorter (37%) compared to the lifetime in solution (decay rate increases). Decreasing temperature causes the increase of the lifetime of the probe to the value of 8.1 ns (5%), while the short decay stays unchanged, indicating that non-radiative processes within the cavity are not so strongly affected by the decrease in temperature.
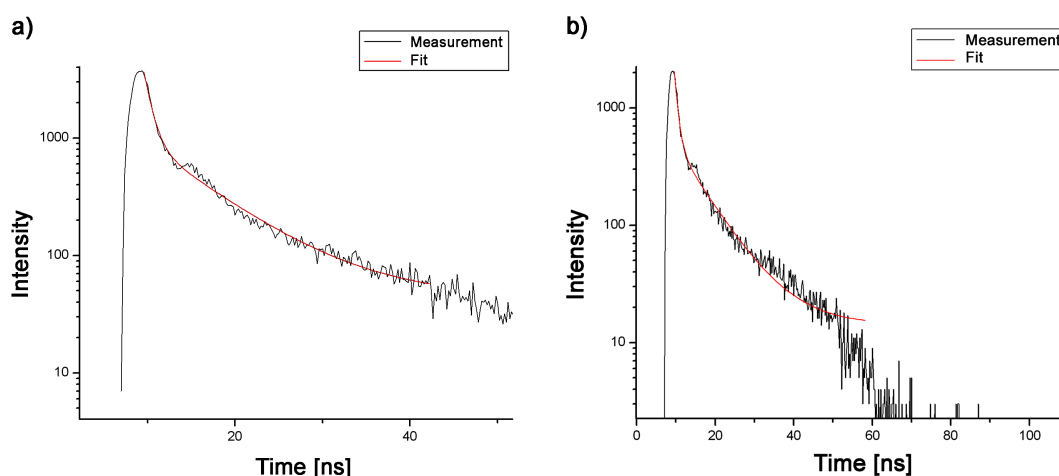

Figure 8. Fluorescence time-resolved measurements of the perovoskite within plasmonic cavity at two temperatures: (**a**) 298 K, and (**b**) 10 K.

The duration of the radiative process, estimated by measuring the width of the Lorentzian emission curve, is quite smaller than the duration of the non-radiative part of the decay process. Among other consequences, the probability that two photons will be emitted at the same time goes to zero, and we are thus always operating in the single photon regime. Due to the coexistence of the (long) fluorescence timescale and of the (short) timescale of the photon emission process, it is impossible for us to put into evidence specific signatures of the strong-coupling such as Rabi oscillations, without speaking about the entanglement between the dipole and the field inside the cavity. However, frequency splitting is directly observable with our device. It constitutes an authentic signature of the quantum strong-coupling, which offers promising perspectives regarding tracing and marking as we shall explain now.

5. Tracing and Marking in the Strong-Coupling Regime

Fluorophores are widely used for tracing and marking [2,22–24], but it is uncommon to let them operate in the strong-coupling regime. Recently, strong-coupling has been exploited for potential quantum chip applications using fluorophores attached to oligonu-

cleotide strands and embedded into the cavity [25]. These DNA or RNA oligonucleotide strands offer the possibility of putting the probe in a particular position within the cavity, and/or to link it with a plasmonic nanoobject (for instance a golden nanosphere) playing the same role as an external cavity [26–28], but this advantage comes with the relatively high cost of design and purification of oligonucleotides associated with the aging problem (stability of oligonucleotide probes within the cavity). In our approach, combining cavity design, spin coating, and specifically chosen fluorophores, we reach the strong-coupling regime without resorting to DNA strands. Another advantage of this regime is that it increases the signal-to-noise ratio, due to the fact that the frequency of the emitted photons differs from the resonance frequency of the cavity, and from the excitation frequency of the laser as well, which makes it easy to filter out the noise at those frequencies, by using well-chosen frequency filters (as we described in the previous section). The use of a resonant cavity also grandly amplifies the signal, which is a well-known manifestation of the Purcell effect [15]. In summary, our approach reduces noise and increases the signal, directly benefiting the signal-to-noise ratio.

6. Conclusions

In order to prevent counterfeiting, and to be able to authenticate their own manufactured goods, certain brands hide specific DNA branes in their products (clothes for instance), since they are difficult to imitate and can be revealed through DNA sequencing. We propose to use fluorophores in the strong-coupling regime described in the previous sections to realize the same goal. The present manuscript describes the quantum foundation of the strong-coupling and the experimental study of radiation dynamics in the strong-coupling regime. It also highlights how these dynamics can be harnessed in tracing and authentication, due to their unique response and simple detection requirements. The specific signature of strong-coupling is difficult to counterfeit (it also requires good overlap between the cavity resonance and absorption/emission spectrum of the probe), and it is easy to reveal because it needs a basic fluorescence device, is widely commercialized, and is versatile and fast to operate compared to DNA sequencing, for instance. It should be emphasized that instead of using expensive lithography techniques or time-consuming self-assembly processes, the new PUF that we propose here is solely based on the light–matter interaction. It constitutes a compromise between quantum encryption, *à la* Wiesner [11], and classical encryption. This approach opens a large field of potential applications.

Conflicts of Interest: The authors declare no conflict of interest.

References

1. Sengupta, P.; Khanra, K.; Chowdhury, A.R.; Datta, P. Lab-on-a-chip sensing devices for biomedical applications. In *Bioelectronics and Medical Devices from Materials to Devices—Fabrication, Applications and Reliability*, 1st ed.; Pal, K., Kraatz, H.-B., Khasnobish, A., Bag, S., Banerjee, I., Kuruganti, U., Eds.; Woodhead Publishing: Sawston, UK, 2019; pp. 47–95.
2. Lakowicz, J.R. *Principles of Fluorescence Spectroscopy*, 3rd ed.; Springer: New York, NY, USA, 2006; pp. 623–740.
3. Kolaric, B.; Maes, B.; Clays, K.; Durt, T.; Caudano, Y. Strong Light-Matter Coupling as a New Tool for Molecular and Material Engineering: Quantum Approach. *Adv. Quantum Technol.* **2018**, *1*, 1800001. [CrossRef]
4. Shalabney, A.; George, J.; Hiura, H.; Hutchison, J.A.; Genet, C.; Hellwig, P.; Ebbesen, T.W. Enhanced Raman Scattering from Vibro-Polariton Hybrid States. *Angew. Chem. Int. Ed.* **2015**, *54*, 7971–7975. [CrossRef]
5. Orgiu, E.; George, J.; Hutchison, J.A.; Devaux, E.; Dayen, J.F.; Doudin, B.; Stellacci, F.; Genet, C.; Schachenmayer, J.; Genes, C.; et al. Conductivity in organic semiconductors hybridized with the vacuum field. *Nat. Mater.* **2015**, *14*, 1123–1129. [CrossRef] [PubMed]
6. Vergauwe, R.M.A.; George, J.; Chervy, T.; Hutchison, J.A.; Shalabney, A.; Torbeev, V.Y.; Ebbesen, T.W. Quantum Strong Coupling with Protein Vibrational Modes. *J. Phys. Chem. Lett.* **2016**, *7*, 4159. [CrossRef]
7. Ramezani, M.; Berghuis, M.; Gómez Rivas, J. Strong light–matter coupling and exciton-polariton condensation in lattices of plasmonic nanoparticles (Review). *J. Opt. Soc. Am. B Opt. Phys.* **2019**, *36*, E88–E103. [CrossRef]
8. Pelton, M.; Storm, S.D.; Leng, H. Strong coupling of emitters to single plasmonic nanoparticles: Exciton-induced transparency and Rabi splitting. *Nanoscale* **2019**, *11*, 14540–14552. [CrossRef]
9. Pappu, R.; Recht, B.; Taylor, R.; Gershenfeld, N. Physical One-Way Functions. *Science* **2002**, *297*, 2026–2030. [CrossRef] [PubMed]
10. Pavlović, D.; Rabasović, M.D.; Krmpot, A.J.; Lazović, V.; Ćurčić, S.; Stojanović, D.V.; Jelenković, B.; Zhang, W.; Zhang, D.; Vukmirović, N.; et al. Naturally safe: Cellular noise for document security. *J. Biophotonics* **2019**, *12*, e201900218. [CrossRef]
11. Wiesner Quantum Money. Available online: https://wiki.veriqloud.fr/index.php?title=WiesnerQuantumMoney,seealsohttp://users.cms.caltech.edu/~vidick/teaching/120qcrypto/wiesner.pdf (accessed on 1 September 2022).
12. Jaynes, E.T.; Cummings, F.W. Comparison of Quantum and Semiclassical Radiation Theories with Application to the Beam Maser. *Proc. IEEE* **1963**, *51*, 89–109. [CrossRef]
13. Bina, M. The coherent interaction between matter and radiation. *Eur. Phys. J. Spec. Top.* **2012**, *203*, 163–183. [CrossRef]
14. Haroche, S.; Raimond, J.M. *Exploring the Quantum—Atoms, Cavities and Photons*; Oxford University Press: Oxford, UK, 2007.
15. Carminati, R.; Greffet, J.J.; Henkel, C.; Vigoureux, J. Radiative and non-radiative decay of a single molecule close to a metallic nanoparticle. *Opt. Commun.* **2006**, *261*, 368–375. [CrossRef]
16. Lassalle, E. Environment Induced Modifications of Spontaneous Quantum Emissions. Ph.D. Thesis, University of Marseille, Marseille, France, 2019.
17. Dutra, S.M. *Cavity Quantum Electrodynamics: The Strange Theory of Light in a Box*, 1st ed.; John Wiley & Sons: Hoboken, NJ, USA, 2005.
18. Grynberg, G.; Aspect, A.; Fabre, C. *Introduction to Quantum Optics: From the Semi-Classical Approach to Quantized Light*, 1st ed.; Cambridge University Press: Cambridge, UK, 2010.
19. Debierre, V.; Goessens, I.; Brainis, E.; Durt, T. Fermi's golden rule beyond the zeno regime. *Phys. Rev. A* **2015**, *92*, 023825. [CrossRef]
20. Weisskopf, V.; Wigner, E. Berechnung der natürlichen linienbreite auf grund der diracschen lichttheorie. *Z. Für Phys.* **1930**, *63*, 54–73. [CrossRef]
21. Hunton, J.; Nelmes, R.J.; Moyer, G.M.; Eriksson, V.R. High resolution study of cubic perovskites by elastic neutron diffraction: $CsPbCl_3$. *J. Phys. C Solid State Phys.* **1979**, *12*, 5393.
22. Cowen, E.A.; Ward, K.B. Chemical Plume Tracing. *Environ. Fluid Mech.* **2002**, *2*, 1–7. [CrossRef]
23. *Anti-Counterfeiting Technology Guide*; European Union Intellectual Property Office: Alicante, Spain, 2021.
24. *Trace Chemical Sensing of Explosives*, 1st ed.; Woodfin, R.L., Ed.; Wiley: Hoboken, NJ, USA, 2006.
25. Chan, W.P.; Chen, J.H.; Chou, W.L.; Chen, W.Y.; Liu, H.Y.; Hu, H.C.; Jeng, C.C.; Li, J.R.; Chen, C.; Chen, S.Y. Efficient DNA-Driven Nanocavities for Approaching Quasi-Deterministic Strong Coupling to a Few Fluorophores. *ACS Nano* **2021** , *15*, 13085–13093. [CrossRef] [PubMed]
26. Punj, D.; Regmi, R.; Devilez, A.; Plauchu, R.; Moparthi, S.B.; Stout, B.; Bonod, N.; Rigneault, H.; Wenger, J. Self-Assembled Nanoparticle Dimer Antennas for Plasmonic-Enhanced Single-Molecule Fluorescence Detection at Micromolar Concentrations. *ACS Photonics* **2025**, *2*, 1099–1107. [CrossRef]

27. Busson, M.; Rolly, B.; Stout, B.; Bonod, N.; Bidault, S. Accelerated single photon emission from dye molecule-driven nanoantennas assembled on DNA. *Nat. Commun.* **2012**, *3*, 962. [CrossRef] [PubMed]
28. Busson, M.P.; Rolly, B.; Stout, B.; Bonod, N.; Wenger, J.; Bidault, S. Photonic Engineering of Hybrid Metal—Organic Chromophores. *Angew. Chem. Int. Ed.* **2012**, *51*, 44, 11083–11087. [CrossRef] [PubMed]

Perspective

Revealing the Wonder of Natural Photonics by Nonlinear Optics

Dimitrije Mara [1] **, Bojana Bokic** [2] **, Thierry Verbiest** [3] **, Sébastien R. Mouchet** [4,5,*] **and Branko Kolaric** [2,6,*]

1 Institute of General and Physical Chemistry, Studentski trg 12/V, 11158 Belgrade, Serbia
2 Center for Photonics, Institute of Physics, University of Belgrade, Pregrevica 118, 11080 Belgrade, Serbia
3 Molecular Imaging and Photonics, Department of Chemistry, KU Leuven, Celestijnenlaan 200D, 3001 Heverlee, Belgium
4 Department of Physics and Astronomy, University of Exeter, Stocker Road, Exeter EX4 4QL, UK
5 Department of Physics & Namur Institute of Structured Matter (NISM), University of Namur, Rue de Bruxelles 61, 5000 Namur, Belgium
6 Micro- and Nanophotonic Materials Group, University of Mons, Place du Parc 20, 7000 Mons, Belgium
* Correspondence: sebastien.mouchet@unamur.be (S.R.M.); branko.kolaric@umons.ac.be (B.K.)

Abstract: Nano-optics explores linear and nonlinear phenomena at the nanoscale to advance fundamental knowledge about materials and their interaction with light in the classical and quantum domains in order to develop new photonics-based technologies. In this perspective article, we review recent progress regarding the application of nonlinear optical methods to reveal the links between photonic structures and functions of natural photonic geometries. Furthermore, nonlinear optics offers a way to unveil and exploit the complexity of the natural world for developing new materials and technologies for the generation, detection, manipulation, and storage of light at the nanoscale, as well as sensing, metrology, and communication.

Keywords: natural photonics; photonics; linear and nonlinearspectroscopy; fluorescence; fluorescence spectroscopy; two-photon fluorescence; second-harmonic generation; third-harmonic generation

1. Introduction

It has been known for a long time that colors in nature are not designed for beauty but are of the utmost importance for communication. Structural colors belong to a special class of colors that have no chemical origin, but they arise from the interaction of light with structures, such as periodically arranged materials [1,2]. Structural colors are ubiquitous colors among insects, fish, and birds. In addition, they are a main topic of research in fields such as biophotonics and biomimetics. In this perspective article, we demonstrate the interest and impact of nonlinear optical studies of photonic structures. We highlight the benefit of nonlinear optical techniques for revealing the details of structured matter at the nanoscale and its interaction with light. We also emphasize that the control of structural colors is essential for various applications in materials science. After introducing the readers to basic concepts of nonlinear optics and natural photonics, we present different cases of natural photonic structures (sometimes combined with artificial materials) investigated by nonlinear optical techniques.

2. Basics of Nonlinear Optics

Nonlinear optics is a part of optics that studies light propagation in nonlinear media. In such media, the polarization P has a nonlinear response to the electric field E. Such optical behavior usually occurs at a high intensity of light, such as the one generated by a laser.

In the linear regime, when an electromagnetic wave interacts with some materials, e.g., a medium containing electric charges, a dipolar type of interaction appears between the

dipoles in the medium and the incident electromagnetic fields at a frequency ω [3]. This interaction can be described by an induced polarization P_{ind} that is linear with the electric field E of the incident light and acts as the source of radiation:

$$P_{\text{ind}} = \chi^{(1)} E, \tag{1}$$

with $\chi^{(1)}$, the linear susceptibility that is related to the refractive index. The response can be modelled by a classical harmonic oscillator, yielding a linear complex refractive index of the medium that scales with ω [3].

However, in the case of high-intensity incident electromagnetic fields, such as laser light (Figure 1), the harmonic oscillator response is not sufficient anymore to describe the observed phenomena [4–7]. The oscillations become anharmonic, i.e., they do not respond linearly to the incident electromagnetic wave. In the nonlinear regime, the induced polarization P_{ind} is expanded in a Taylor series as a function of the total applied electric field. The induced polarization is then written as [7]:

$$P_{\text{ind}} = P^{(1)} + P^{(2)} + P^{(3)} + \cdots = \chi^{(1)} E + \chi^{(2)} EE + \chi^{(3)} EEE + \cdots \tag{2}$$

with $P^{(1)}$, the linear part of the induced polarization; $P^{(2)}$, the second-order nonlinear response; and $P^{(3)}$, the third order nonlinear response. $\chi^{(1)}$, $\chi^{(2)}$, and $\chi^{(3)}$ are the linear, the first nonlinear, and the second nonlinear susceptibilities, respectively. The latter two quantify the second-order and third-order nonlinear optical response. Since all susceptibilities are related to the refractive index, a nonlinear complex refractive index is obtained.
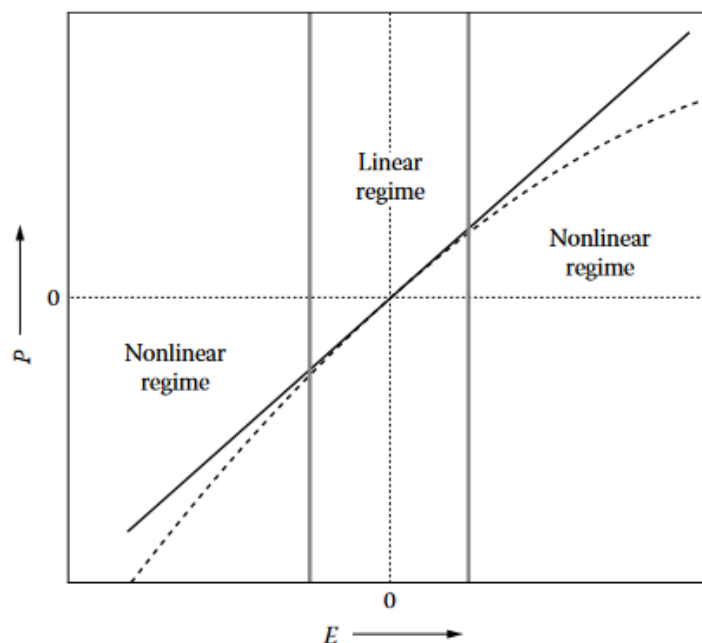
Figure 1. Depending on the intensity of the incident electric field (E), the electric polarization (P) will respond linearly or nonlinearly. As long as the intensity of the electric field is small, the electric polarization is linear to the electric field intensity. This case corresponds to the linear regime. When the intensity of the electric field is high, P is not proportional to E and the regime is nonlinear. Reproduced from Verbiest, T., Clays, K., and Rodriguez, V., 2009. Second-order Nonlinear Optical Characterization Techniques: An Introduction, with permission from Taylor and Francis Group, LLC, a division of Informa plc.

One of the advantages of nonlinear optical techniques is due to the nature of the non-linear susceptibilities, which are tensors of third and fourth rank, respectively. Especially, second-order nonlinear optical effects, which are described by the third-rank tensor $\chi^{(2)}$, have extremely interesting symmetry properties. In general, $\chi^{(2)}$ is a third-rank tensor

with 27 components, but the number of independent and nonvanishing components is dependent on the symmetry of the medium. All of the components of $\chi^{(2)}$ will vanish in a medium with inversion symmetry. On the other hand, any surface where the symmetry is necessarily broken will typically yield four independent susceptibility components [7]. Since the nonlinear susceptibility directly determines the magnitude and phase of the nonlinear response, the measured response can serve as a means to evaluate the symmetry of the sample.

In addition to the optical properties of matter that can be probed by linear techniques, much more information is available by exploiting the interaction of matter with higher-intensity laser beams. Multiphoton (including two-photon) excitation fluorescence is certainly the most used nonlinear optical technique. In the case of two-photon excitation fluorescence (TPEF), high-intensity photons illuminate a sample [7]. Because of this high intensity, two photons simultaneously interact with the sample, following different selection rules from the photons in the linear light–matter interaction regime. Since two photons are absorbed initially and give rise to only one emitted photon, the resulting photon has a higher energy than each of the two absorbed photons. Multiphoton absorption and fluorescence originate from a third-order nonlinear optical response [7].

In second harmonic generation (SHG), the material also interacts with two photons [7]. Unlike two-photon excitation fluorescence, a third photon is instantaneously emitted (within ca 10^{-15} s) with exactly twice the energy (and, thus, half the wavelength) of the two initial photons. Since SHG is a second-order nonlinear optical process, selection rules that are different from TPEF apply: symmetry requirements such as non-centrosymmetric samples are essential to observe SHG [4–7]. Similarly, third harmonic generation (THG) corresponds to the instantaneous emission of a single photon following the interaction of three incident photons [7]. The generated photon has three times the energy and a third of the wavelength of the three initial photons.

There are multiple advantages to nonlinear techniques with respect to linear optical techniques [8,9]. An important feature is the increase in imaging depth, which can be attributed to multiple factors: first, there is a low probability of multiple photons interacting simultaneously, resulting in a minimal imaging volume at the femtoliter scale by reducing out-of-focus fluorescence. It is therefore possible to image accurately at different depths, similarly to confocal microscopes, and to create 3D reconstructions of the investigated material without the use of a pinhole. Due to the absence of a pinhole, more light can be collected and thus a clearer image can be formed. This also results in an increase in the practical resolution as the pinhole of confocal microscopes is often opened to increase the amount of incoming light to image fluorescing samples. This results in a lower resolution. Practically, the resolution of a multiphoton microscope was shown to approach 250 nm, which equals the best possible resolution of the confocal fluorescence microscopy. Another significant advantage of nonlinear optical techniques is the use of near-infrared excitation light with wavelengths corresponding to the transparency window of biological tissue. This leads to an increase in penetration depth, and it is therefore possible to image sensitive samples without damaging the structure or with minimal damage. Furthermore, most multi-photon microscopes use femtosecond-lasers as an excitation source, which further reduces the risk of photodamage. In addition, no sample preparation is necessary. This constitutes the main advantage over more complicated microscopy techniques such as scanning electron microscopy (SEM) or transmission electron microscopy (TEM) [10,11]. Finally, another interesting application of multiphoton microscopy is the imaging of the local polarization anisotropy via SHG, enabling the user to seperately determine the orientation and degree of organization of each non-centrosymmetric component within a sample .

3. Introduction to Natural Photonics

Colours in nature originate from chemical or physical properties of matter, light sources, or combinations of them [1,2]. Chemical colours are caused by pigments. These

molecules selectively absorb incident light within a given wavelength band. Examples are eumelanins and pheomelanins, which give rise to brown/black and yellow/red human skins, respectively [12,13]. Light that is not absorbed by pigments is scattered, giving rise to colours that an observer may perceive. Physical colours are due to interference between incident light and a physical structure. Hence, they are often called structural colours, as a synonym. Structures giving rise to such colours have geometrical dimensions at the micro- or nanoscale. They encompass optical thin films [14–17], diffraction gratings [18–20], Bragg mirrors [21–26], chirped multilayer reflectors [27,28], and photonic crystals [29–34], as well as quasi-ordered [35–40] and randomly disordered [41–44] photonic structures.

Natural photonics is the field of research that studies the interaction between light and such physical structures in nature. Natural structural colours occur in organisms ranging from mammals such as primates (including human blue eyes) and marsupials, fish, or birds such as hummingbirds and pigeons to insects such as butterflies and beetles (Figure 2) [1,2,45].

This section introduces key concepts and presents some selected case studies from natural photonics, in the linear regime.
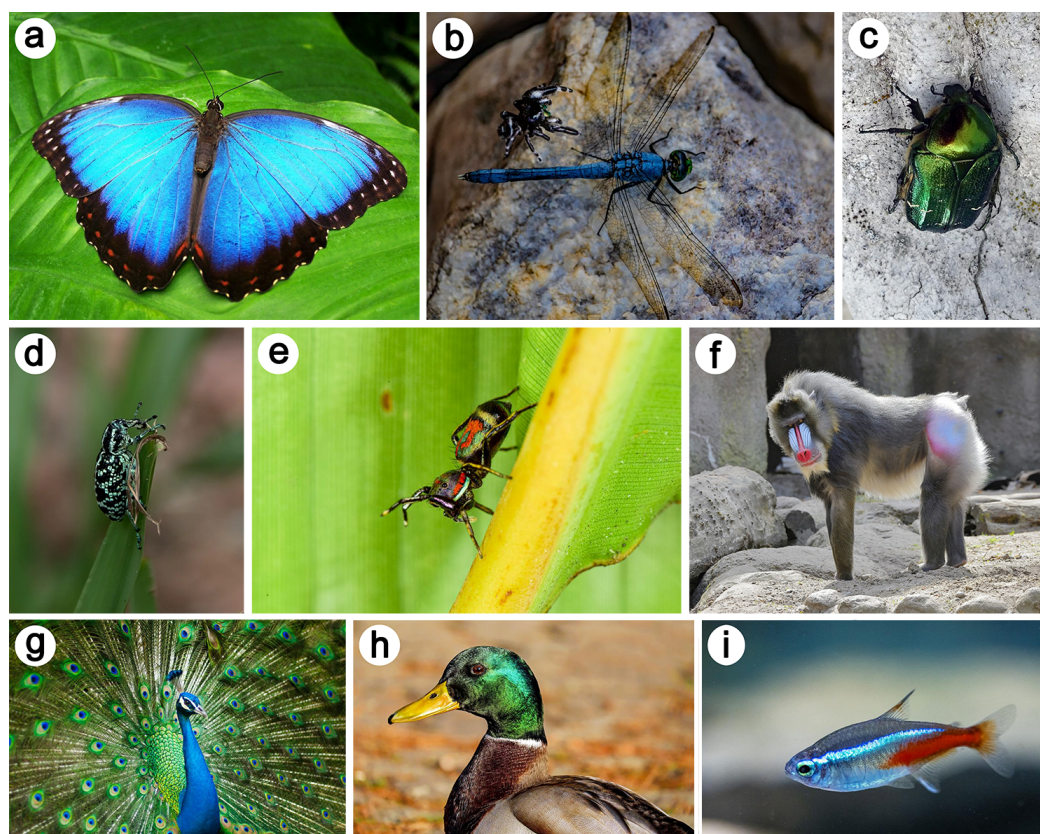

Figure 2. Many examples of structural colours are found in the integuments of natural organisms. They include the wings of the common morpho *Morpho peleides* (**a**), the body of some dragonfly species (**b**), the thorax and elytra of the green rose chafer *Cetonia aurata* (**c**), the body of the Botany Bay diamond weevil *Chrysolopus spectabilis* (**d**), the integuments of some jumping spider species (**e**), the skin of the mandrill *Mandrillus sphinx* (**f**), the feathers of the Indian peafowl *Pavo cristatus* (**g**), the head of the mallard *Anas platyrhynchos* (**h**), and the body of the neon tetra fish *Paracheirodon innesi* (**i**). Reproduced from from pixabay.com.

One striking example is the case of the male beetle *Hoplia coerulea* (Figure 3). The blue-violet iridescent colour of its elytra and body observed in reflection with incident visible light arises from a photonic structure, namely, a porous periodic multilayer, within the round scales occurring on its body [46,47].
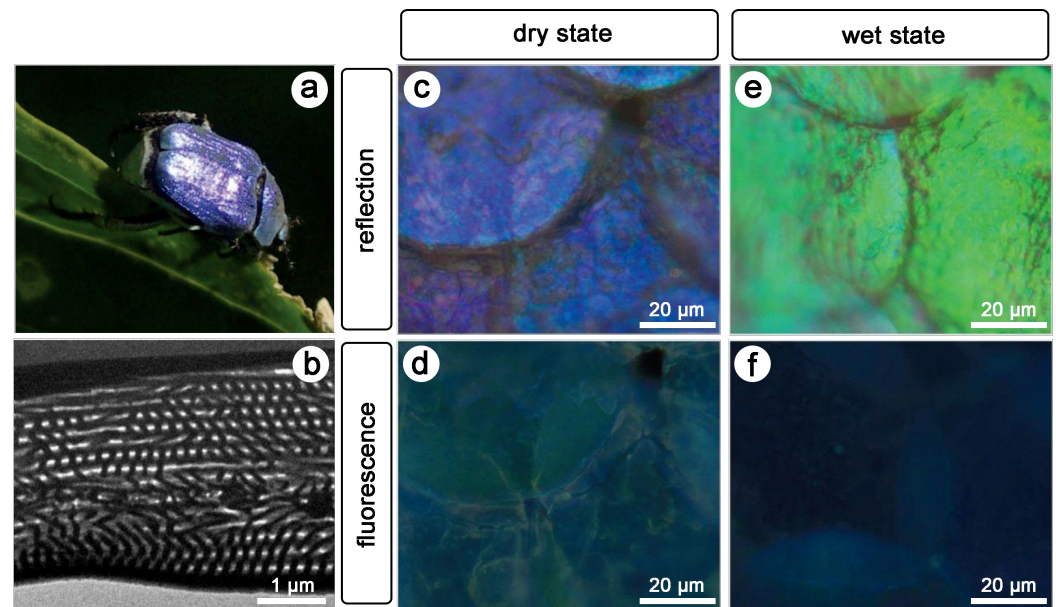
Figure 3. The blue-violet colour of the male beetle *Hoplia coerulea* (**a**) originates from a multilayer photonic structure. This porous periodic multilayer (**b**) occurs in the scales covering the elytra (**c**) and body of the insect. Upon UV light illumination, the scales display a turquoise colour through fluorescence (**d**). When in contact with water, the scales turn to green (**e**) and navy blue (**f**) under visible and UV lightillumination, respectively. Reproduced from Mouchet, S.R., Lobet, M., Kolaric, B., Kaczmarek, A.M., Van Deun, R., Vukusic, P., Deparis, O., and Van Hooijdonk, E., 2016. Controlled fluorescence in a beetle's photonic structure and its sensitivity to environmentally induced changes. Proc. R. Soc. B 283, 20162334, with permission from The Royal Society.

This multilayer is mainly composed of chitin, the building material of insects [1,2]. Upon contact with liquids and vapour, these scales change their colour to green [48–52]: the spectral reflectance peak red-shifts. This colour change arises from the penetration of some liquid into the pores of the scales, filling the pores and changing the refractive index.

Furthermore, one-photon excitation fluorescence (OPEF) emission was observed when the beetle was illuminated with UV light (Figure 3d) [53,54]. The colour of the scales covering the elytra and body of this insect is turquoise. This phenomenon arises in biological organisms, the integuments of which contain so-called fluorophores [55,56]. Examples include birds [44,57–59], insects [60–71], arachnids [72,73], mammals [74], amphibians [75,76], reptiles [77], marine animals [78,79], and plants [80,81] (Figure 2). These molecules emit longer-wavelength light (typically, visible photons) following the absorption of incident shorter-wavelength light (typically, UV, violet or blue photons).

Fluorescence emission results from transition between two real electron states with the same multiplicity of spin. The role, if any, of fluorescence (Figure 4) in visual communication is unclear [55,56]. Biopterin, the green fluorescent protein (GFP), papiliochrom II, psittacofulvin, and resilin are examples of fluorophores.

When light emission takes place in photonic structures, the structure may modify the directionality, the decay time, and the spectral intensity of the emitted light [82,83]. Light emission can be reduced or even inhibited if the emission wavelength is in the range of the photonic bandgap of the structure. The decay time of the excited is then increased and can, theoretically, be infinite. When such light emitted in a photonic structure originates from fluorescence, this phenomenon is often referred to as controlled fluorescence. The confinement of fluorophores in natural photonic structures was found in several species [84–88], including the male beetle *H. coerulea* [53,54]. Upon contact with water, the peak in the fluorescence emission spectrum from the scales of this beetle blue-shifts, giving rise to a navy blue colour (Figure 3d,f). Following the penetration of the porous structure by water, the local density of optical states (LDOS) is modified, leading to the observed colour change.
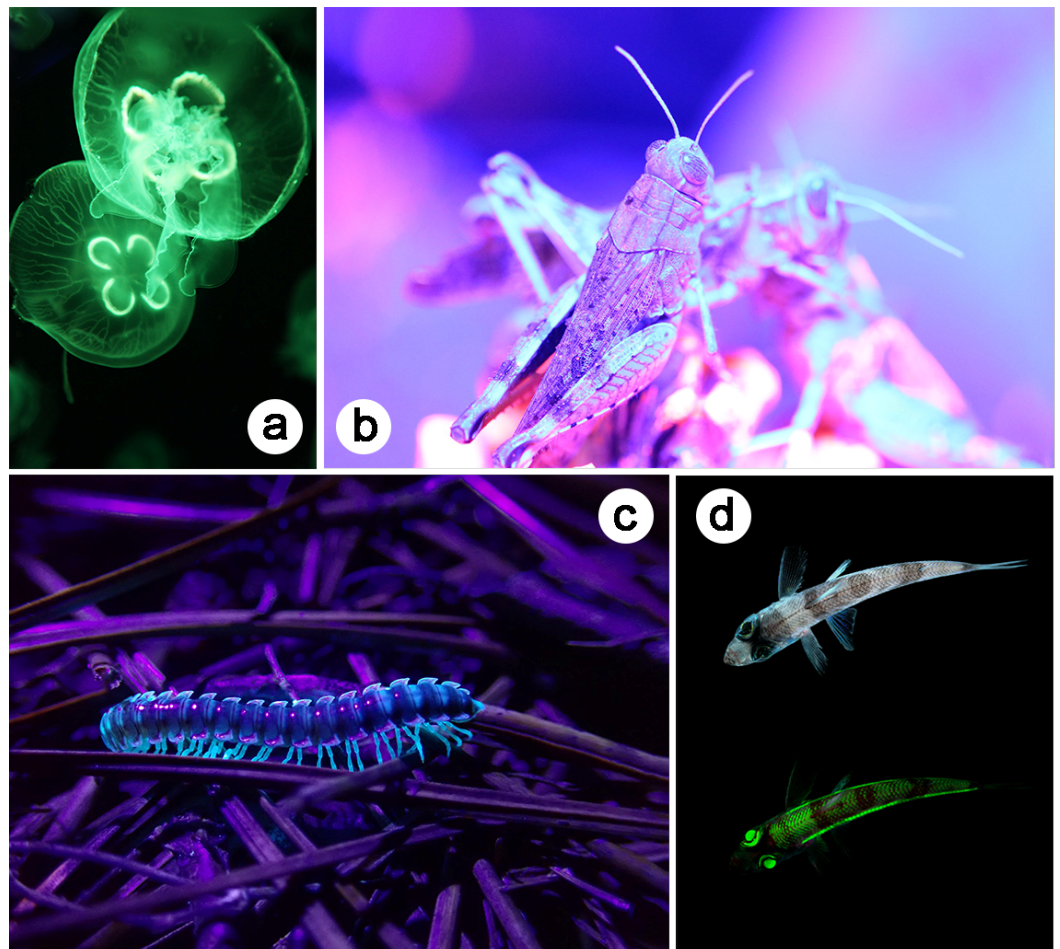
Figure 4. Fluorescence is ubiquitous in the integuments of natural organisms. The integuments of some jellyfish species (**a**), some grasshopper species (**b**), some millipede species (**c**), and some greeneye fish species (**d**) are known for their fluorescent properties. (**d**) Top (bottom): greeneye fish under visible (UV) light. Reproduced from from pixabay.com.

The interaction between fluorescent light and photonic structures was also highlighted in the scales covering the elytra of longhorn beetles *Celosterna pollinosa sulfurea* and *Phosphorus virescens* [68]. These scales exhibit yellow and turquoise colours under visible and UV incident light, respectively, with an underlying basal brown membrane (Figure 5a–d), akin to the beetles *Euchroea auripigmenta* and *Trictenotoma childreni* [69,70]. Through scatterograms and detailed series of simulations, it was demonstrated that the scales play the role of waveguides for light emitted by the embedded fluorophores (Figure 5e,f).
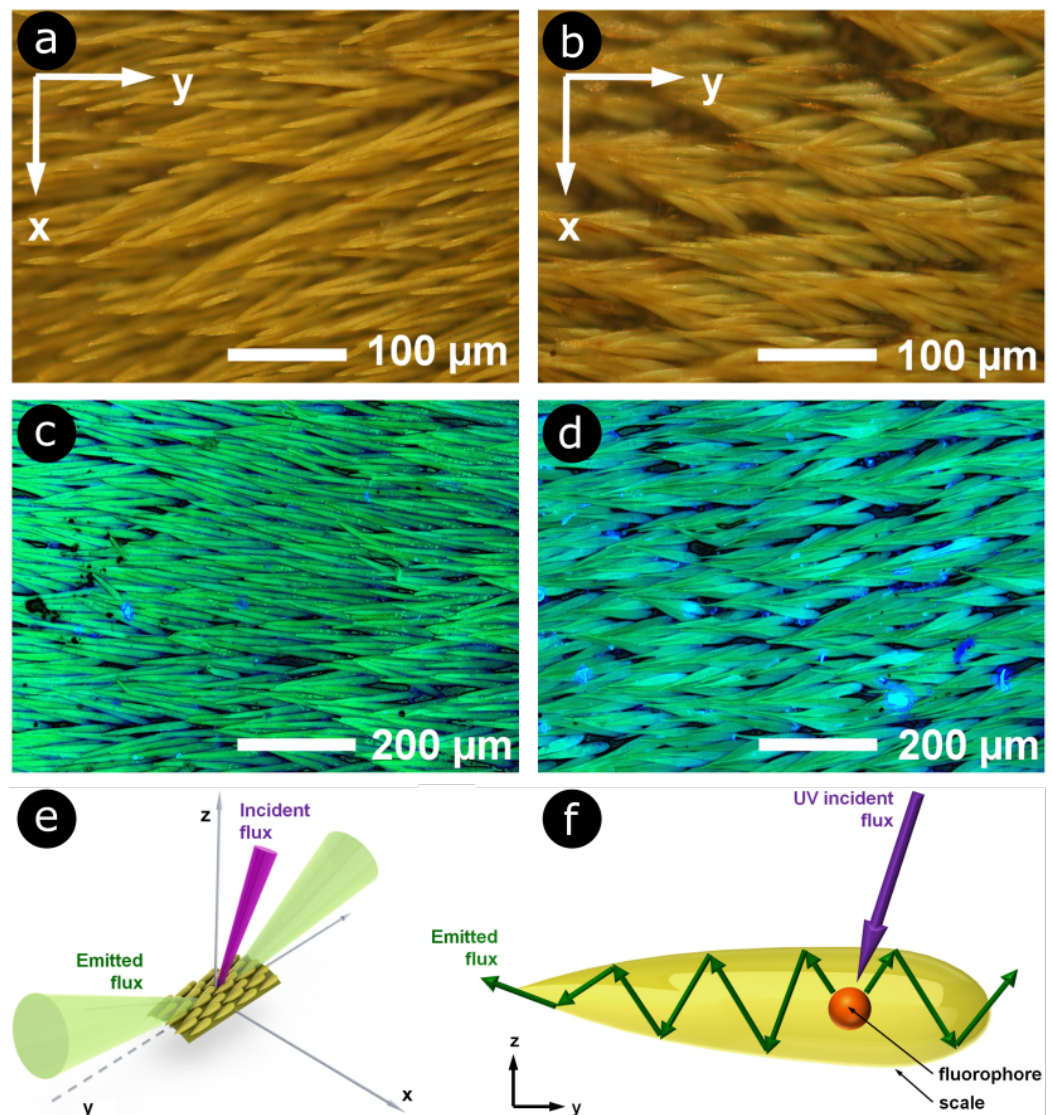
Figure 5. The elytra of longhorn beetles *Celosterna pollinosa sulfurea* and *Phosphorus virescens* are covered by elongated scales, in which fluorophores are embedded. These scales act as waveguides for the light emitted by the fluorophores. They display a yellow colour under visible light for *C. pollinosa sulfurea* (**a**) and *P. virescens* (**b**) (here, observation by optical microscopy). Under UV light, the observed colour is turquoise in both respective cases (**c**,**d**). Upon illumination with UV light (represented in magenta), embedded fluorophores mostly emitted within two emission cones (in green) (**e**) due to a waveguide effect taking place within the scales (**f**). Reproduced from Van Hooijdonk, E., Barthou, C., Vigneron, J.-P., and Berthier, S., 2013. Yellow structurally modified fluorescence in the longhorn beetles *Celosterna pollinosa sulfurea* and *Phosphorus virescens* (Cerambycidae). J. Lumin. 136, 313–321, with permission from Elsevier.

4. Nonlinear Optical Study of Natural Photonic Structures

Harnessing light–matter interaction in a nonlinear regime, researchers and engineers developed various tools for imaging and spectroscopy analyses of biological samples [8,62,89–105]. Nonlinear optical imaging and spectroscopy have proved to be versatile and efficient techniques in biomedical and biological research, with many benefits, including an increase in analytic depth and a reduction in photodamage, with respect to classical linear optical techniques [8]. In general, nonlinear optical studies led to a better understanding of the link between the optical response and geometries of natural photonic structures that are essential for potential applications of these structures in biomimetics and quantum technology [9].

For instance, the multi-excited states character of the fluorophores embedded in the integuments of *H. coerulea* were revealed by comparing OPEF spectra with TPEF measurements [106] (Figure 6a–d).
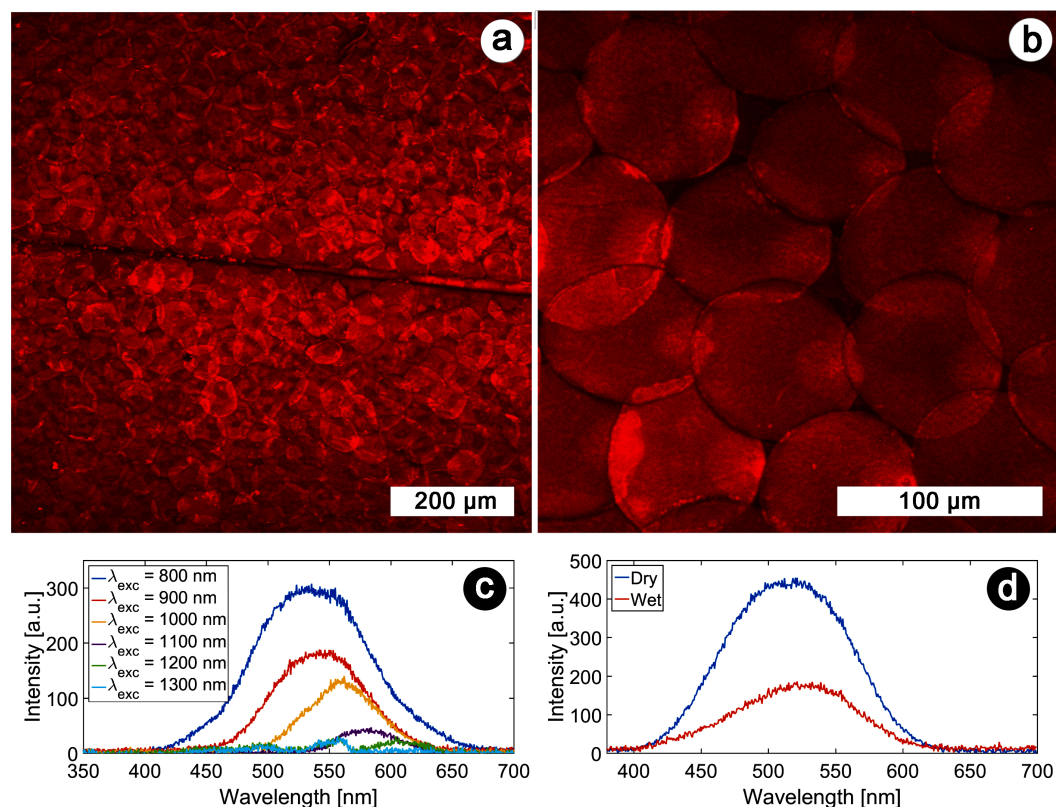

Figure 6. TPEF microscopy and spectroscopy of the scales covering *H. coerulea*'s elytra. An intense TPEF response was detected from the elytra of the male beetle *H. coerulea* with an excitation wavelength equal to 900 nm (**a**) and 800 nm (**b**). TPEF excitation spectra were measured with various excitation wavelengths (**c**). Upon contact with water, the emitted intensity decreases and the peak wavelength red-shifts slightly (the excitation wavelength equals 800 nm). Scale bars: (**a**) 200 μm and (**b**) 100 μm. Reproduced from Mouchet, S. R., Verstraete, C., Mara, D., Van Cleuvenbergen, S., Finlayson, E. D., Van Deun, R., Deparis, O., Verbiest, T., Maes, B., Vukusic, P., and Kolaric, B., 2019 Nonlinear optical spectroscopy and two-photon excited fluorescence spectroscopy reveal the excited states of fluorophores embedded in a beetle's elytra, Interface Focus 9(1), 20180052, with permission from The Royal Society.

This provided insight into the electron structure of the embedded fluorophores.

Furthermore, local-form anisotropy arising from local-direction-dependent subwavelength morphology was shown to influence both linear and nonlinear optical responses (in reflection and emission) thanks to THG spectroscopy [106] . The anisotropy is caused due to the subwavelength spacers located in the mixed air-chitin layers (Figure 3b). These spacers are locally parallel.

This finding highlighted the need to take a more accurate model into account for predicting some of the optical properties of the elytra of this beetle.

Similarly, the yellow and fluorescent elongated scales covering the elytra of the logboring beetle *Trictenotoma childreni* were investigated by nonlinear optical methods, including OPEF, TPEF, and SHG microscopy and spectroscopy (Figure 7) [70]. These scales appear similar to the ones of the longhorn beetles *Celosterna pollinosa sulfurea* and *Phosphorus virescens* (Figure 5) [68]. They contain fluorophores that give rise to a yellow visual appearance upon UV illumination. These observations allowed one to highlight the noncentrosymmetric nature of the fluorophores embedded within these scales [70].
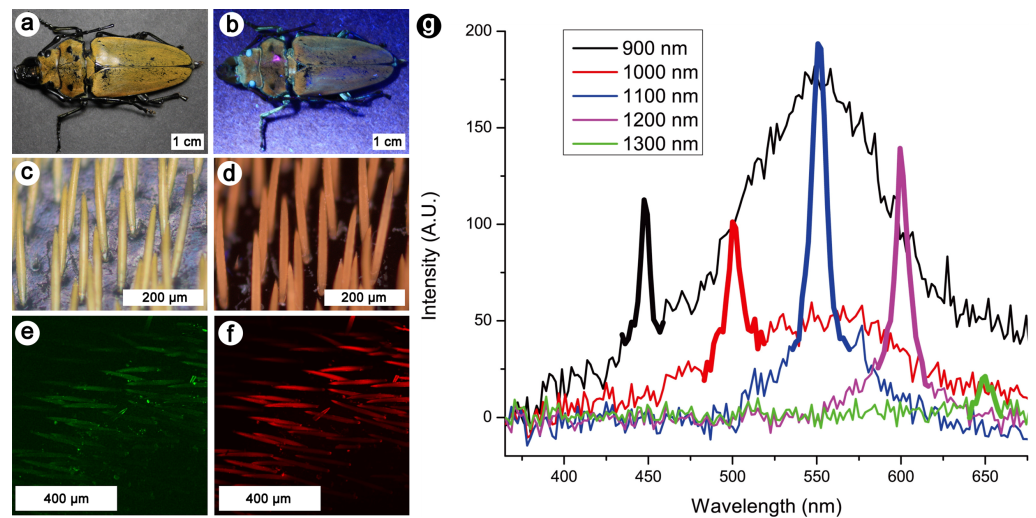
Figure 7. The yellow and fluorescent scales occurring on the elytra of the log-boring beetle *T. childreni* were investigated by nonlinear optical techniques, including OPEF, TPEF, and SHG microscopy and spectroscopy. The elytra exhibit a yellow colour under both incident visible white (**a**) and UV (**b**) light. This colour is due to the presence of elongated scales covering the elytra (**c,d**). Under visible (**c**) or UV light (**d**), they appear in shades of yellow. Upon excitation with a fundamental wavelength of 1000 nm, a SHG (**e**) and a TPEF (**f**) signal can be detected from the scales (here observed by microscopy in false colours). Multiphoton emission spectra of the log-boring beetle's scales measured with various excitation wavelengths exhibit SHG peaks at half the excitation wavelengths (thick lines). TPEF peaks were observed around 550 nm at most excitation wavelengths. Reproduced from Mouchet, S. R., Verstraete, C., Kaczmarek, A. M., Mara, D., van Cleuvenbergen, S., Van Deun, R., Verbiest, T., Maes, B., Vukusic, P., and Kolaric, B., 2019, Unveiling the nonlinear optical response of *Trictenotoma childreni* longhorn beetle, J. Biophot. 12(9), 12:e201800470, with permission from John Wiley and Sons.

So far, various natural photonic structures from different insects, including butterflies and cicadas, have been investigated for sensing and materials-oriented applications. For example, corrugated natural photonic structures offer a unique possibility to develop new sensing platforms by combing corrugation at different scales, plasmonic properties, and surface-enhanced Raman spectroscopy (SERS) [107–111]. The work of Garrett and coworkers clearly shows the benefit of natural and bioinspired structuring, which can be used for different sensing applications (Figure 8) [108–110]. The development of such novel platforms relying on SERS will lead to the fast and accurate screening of chemical, biochemical, and pharmaceutical compounds, which is crucial for the growing fields of proteomics, genomics, molecular medicine, and biophysics, as well as for the development of assays for the detection of diseases [107,112].
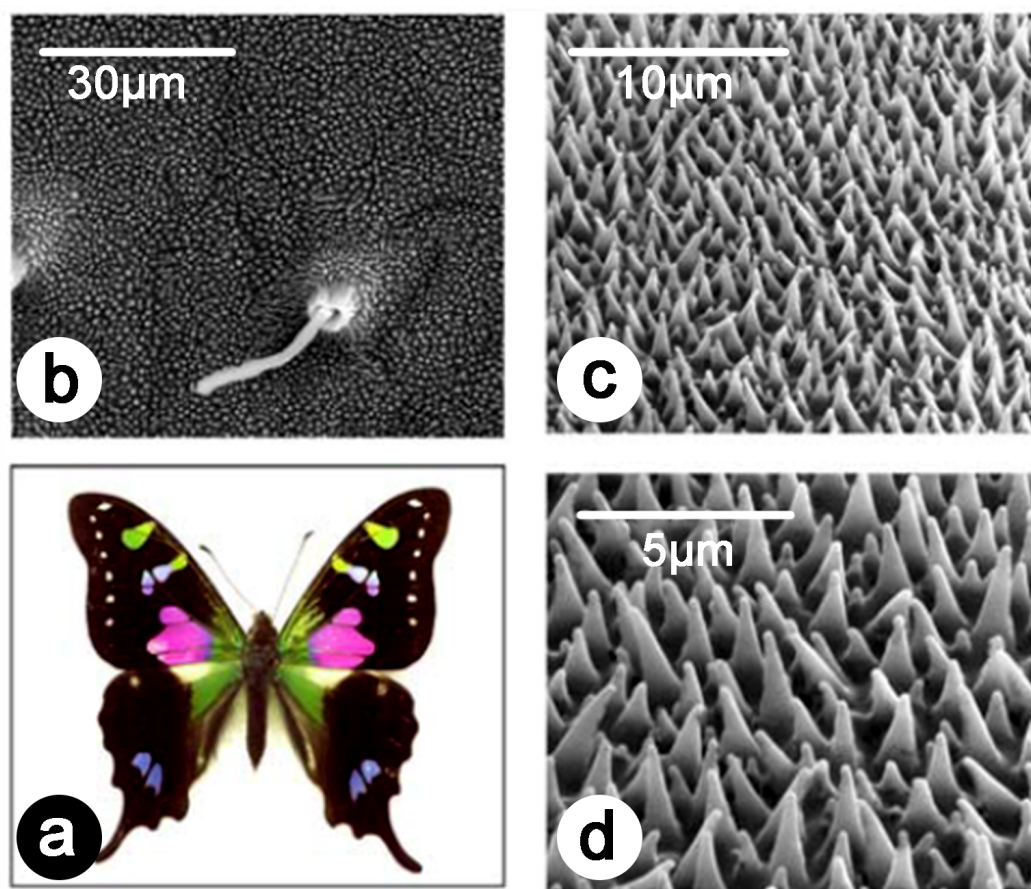
Figure 8. The structures occurring on the wings of the purple spotted swallowtail butterfly (*Graphium weiskei*) coated with a metal thin film were found to be an excellent substrate for SERS, in terms of biocompatibility and sensitivity [108–110]. *G. weiskei* (**a**) exhibit conical microstructures on its wings (**b**–**d**) as observed here by SEM. After coating by gold or silver, these structures can be used to detect protein binding from direct observation of the modifications in the SERS response. Reproduced from Garrett, N. L., Vukusic, P., Ogrin, F., Sirotkin, E., Winlove, C. P., and Moger, J., 2009, Spectroscopy on the wing: Naturally inspired SERS substrates for biochemical analysis, J. Biophot. 2(3), 157–166.

The work of Stoddart and coworkers highlighted that practical applications of SERS for sensing depend on the development of manufacturing methods that will be used to mimic the complex morphology of insect integuments [107]. It pointed out the importance of biomimetics for the advancement of materials science [107]. In addition, it was shown that the enhancement of SERS also depends on the aspect ratio of metallic nanoparticles. The presence of different multiscale groove-like structures presented the possibility of developing smart surfaces for controlling optical response and wetting properties [113]. Structuring materials have a significant effect on the latter, as was demonstrated both theoretically and experimentally, specifically at different length scales [114–116] .

Furthermore, the natural photonic structures occurring in the wings of the butterfly *Cymothoe sangaris* were used for tuning the upconversion luminescence of nanoparticles doped with lanthanide ($NaYF_4 : Yb^{3+}, Er^{3+}$) [117]. Upon illumination with a light at 980 nm, both red and green emission bands of $NaYF_4 : Yb^{3+}, Er^{3+}$ could be controlled, producing different luminescent colours Figure 9. Doping natural photonic structures with materials including metals and oxides also presents the possibility of using these structures as templates to design nanocorrugated materials (with complex shapes and geometries) on demand for various material applications [118].
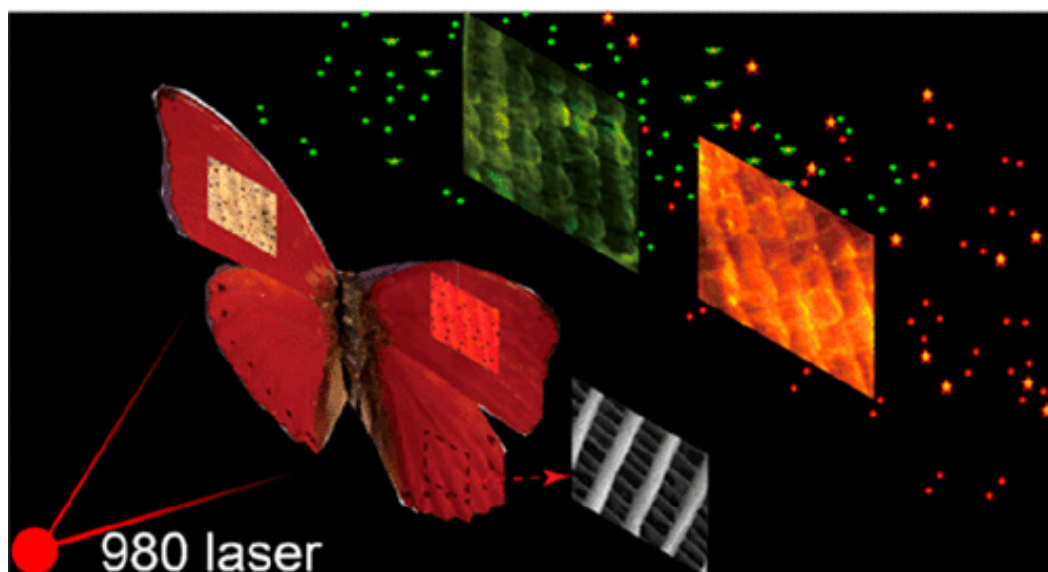
Figure 9. The upconversion luminescence of nanoparticles doped with lanthanide ($NaYF_4 : Yb^{3+}, Er^{3+}$) was controlled thanks to the natural photonic crystals occurring in the wings of the butterfly *Cymothoe sangaris*. With a 980 nm incident light, various luminescent colours were generated. Reproduced from Gao, T., Zhu, X., Wu, X. J., Zhang, B., and Liu, H. L., 2021, Selectively Manipulating Upconversion Emission Channels with Tunable Biological Photonic Crystals, J. Phys. Chem. C, 125(1), 732–739, with permission from ACS Publications.

5. Conclusions

In this perspective article, we presented theoretical key concepts of nonlinear optics and discussed the results of nonlinear optical studies in the field of natural photonics. Because nonlinear optical techniques are inherently sensitive to symmetry; the presence of interfaces; and chirality, they offer a more detailed insight into the molecular properties of biomaterials . This is crucial for applications in different areas of material science. Even though, at the moment, nonlinear optical investigations of natural photonics are still at their infant stage of development, the primary aim of this article is to draw the attention of the broad material, photonic, and biological scientific communities to the capability of nonlinear optics, which could be used to forge new horizons in physical, biological and material research.

References

1. Kinoshita, S. *Structural Colors in the Realm of Nature*; World Scientific Publishing Co: Singapore, 2008.
2. Mouchet, S.R.; Deparis, O. *Natural Photonics and Bioinspiration*; Artech House: Boston, MA, USA, 2021.
3. Hecht, E. *Optics*; Addison-Wesley Publishing Company: Reading, MA, USA, 2001.
4. Stratton, J. *Electromagnetic Theory*; McGraw-Hill: New York, NY, USA, 1941.
5. Böttcher, C. *Theory of Electric Polarization*, 2nd ed.; Elsevier: Amsterdam, The Netherlands, 1973.
6. Zernike, F.; Midwinter, J. *Applied Nonlinear Optics*; Wiley: New York, NY, USA, 1973.
7. Verbiest, T.; Clays, K.; Rodriguez, V. *Second-Order Nonlinear Optical Characterization Techniques: An Introduction*; CRC Press Taylor & Francis Group: Boca Raton, FL, USA, 2009.
8. Zipfel, W.R.; Williams, R.M.; Webb, W.W. Nonlinear magic: Multiphoton microscopy in the biosciences. *Nat. Biotechnol.* **2003**, *21*, 1369.
9. Verstraete, C.; Mouchet, S.R.; Verbiest, T.; Kolaric, B. Linear and nonlinear optical effects in biophotonic structures using classical and nonclassical light. *J. Biophotonics* **2019**, *12*, e201800262.
10. Pathan, A.; Bond, J.; Gaskin, R. Sample preparation for scanning electron microscopy of plant surfaces—Horses for courses. *Micron* **2008**, *39*, 1049–1061. https://doi.org/10.1016/j.micron.2008.05.006.
11. Ayache, J.; Beaunier, L.; Boumendil, J.; Ehret, G.; Laub, D. *Sample Preparation Handbook for Transmission Electron Microscopy*; Springer: New York, NY, USA, 2010.
12. Slominski, A.; Tobin, D.J.; Shibahara, S.; Wortsman, J. Melanin Pigmentation in Mammalian Skin and Its Hormonal Regulation. *Physiol. Rev.* **2004**, *84*, 1155–1228. https://doi.org/10.1152/physrev.00044.2003.
13. Ito, S.; Wakamatsu, K. Diversity of human hair pigmentation as studied by chemical analysis of eumelanin and pheomelanin. *J. Eur. Acad. Dermatol. Venereol.* **2011**, *25*, 1369–1380, https://doi.org/10.1111/j.1468-3083.2011.04278.x.
14. Stavenga, D.G.; Giraldo, M.A.; Leertouwer, H.L. Butterfly wing colors: Glass scales of Graphium sarpedon cause polarized iridescence and enhance blue/green pigment coloration of the wing membrane. *J. Exp. Biol.* **2010**, *213*, 1731–1739. https://doi.org/10.1242/jeb.041434.
15. Stavenga, D.G.; Matsushita, A.; Arikawa, K.; Leertouwer, H.L.; Wilts, B.D. Glass scales on the wing of the swordtail butterfly Graphium sarpedon act as thin film polarizing reflectors. *J. Exp. Biol.* **2012**, *215*, 657–662. https://doi.org/10.1242/jeb.066902.
16. Stavenga, D. Thin film and multilayer optics cause structural colors of many insects and birds. *Materials Today: Proceedings* **2014**, *1S*, 109–121.
17. Siddique, R.; Vignolini, S.; Bartels, C.; Wacker, I.; Hölscher, H. Colour formation on the wings of the butterfly *Hypolimnas Salmacis* Scale Stacking. *Sci. Rep.* **2016**, *6*, 36204. https://doi.org/10.1038/srep36204.
18. Vukusic, P.; Sambles, J.R.; Lawrence, C.R.; Wootton, R.J. Limited-view iridescence in the butterfly *Ancyluris Meliboeus*. *Proc. R. Soc. London. Ser. B: Biol. Sci.* **2002**, *269*, 7–14. https://doi.org/10.1098/rspb.2001.1836.
19. Vukusic, P.; Kelly, R.; Hooper, I. A biological sub-micron thickness optical broadband reflector characterized using both light and microwaves. *J. R. Soc. Interface* **2009**, *6*, S193–S201. https://doi.org/10.1098/rsif.2008.0345.focus.
20. Vigneron, J.P.; Simonis, P.; Aiello, A.; Bay, A.; Windsor, D.M.; Colomer, J.F.; Rassart, M. Reverse color sequence in the diffraction of white light by the wing of the male butterfly *Pierella Luna* (Nymphalidae: Satyrinae). *Phys. Rev. E* **2010**, *82*, 021903. https://doi.org/10.1103/PhysRevE.82.021903.
21. Biró, L.P.; Bálint, Z.; Kertész, K.; Vértesy, Z.; Márk, G.I.; Horváth, Z.E.; Balázs, J.; Méhn, D.; Kiricsi, I.; Lousse, V.; et al. Role of photonic-crystal-type structures in the thermal regulation of a Lycaenid butterfly sister species pair. *Phys. Rev. E* **2003**, *67*, 021907. https://doi.org/10.1103/PhysRevE.67.021907.
22. Yoshioka, S.; Kinoshita, S. Single-scale spectroscopy of structurally colored butterflies: measurements of quantified reflectance and transmittance. *J. Opt. Soc. Am. A* **2006**, *23*, 134–141. https://doi.org/10.1364/JOSAA.23.000134.
23. Noyes, J.A.; Vukusic, P.; Hooper, I.R. Experimental method for reliably establishing the refractive index of buprestid beetle exocuticle. *Opt. Express* **2007**, *15*, 4351–4358. https://doi.org/10.1364/OE.15.004351.
24. Kertész, K.; Molnár, G.; Vértesy, Z.; Koós, A.; Horváth, Z.; Márk, G.; Tapasztó, L.; Bálint, Z.; Tamáska, I.; Deparis, O.; et al. Photonic band gap materials in butterfly scales: A possible source of "blueprints". E-MRS 2007 Spring Conference Symposium A: Sub-wavelength photonics throughout the spectrum: Materials and Techniques. *Mater. Sci. Eng. B* **2008**, *149*, 259–265. https://doi.org/10.1016/j.mseb.2007.10.013.
25. Wilts, B.D.; Leertouwer, H.L.; Stavenga, D.G. Imaging scatterometry and microspectrophotometry of lycaenid butterfly wing scales with perforated multilayers. *J. R. Soc. Interface* **2009**, *6*, S185–S192. https://doi.org/10.1098/rsif.2008.0299.focus.
26. Stavenga, D.G.; Wilts, B.D.; Leertouwer, H.L.; Hariyama, T. Polarized iridescence of the multilayered elytra of the Japanese jewel beetle, *Chrysochroa Fulgidissima*. *Philos. Trans. R. Soc. B: Biol. Sci.* **2011**, *366*, 709–723. https://doi.org/10.1098/rstb.2010.0197.
27. Vigneron, J.P.; Pasteels, J.M.; Windsor, D.M.; Vértesy, Z.; Rassart, M.; Seldrum, T.; Dumont, J.; Deparis, O.; Lousse, V.; Biró, L.P.; et al. Switchable reflector in the Panamanian tortoise beetle *Charidotella Egregia* (Chrysomelidae: Cassidinae). *Phys. Rev. E* **2007**, *76*, 031907. https://doi.org/10.1103/PhysRevE.76.031907.
28. Pasteels, J.M.; Deparis, O.; Mouchet, S.R.; Windsor, D.M.; Billen, J. Structural and physical evidence for an endocuticular gold reflector in the tortoise beetle, *Charidotella Ambita*. *Arthropod Struct. Dev.* **2016**, *45*, 509–518. https://doi.org/10.1016/j.asd.2016.10.008.

29. Kertész, K.; Bálint, Z.; Vértesy, Z.; Márk, G.I.; Lousse, V.; Vigneron, J.P.; Rassart, M.; Biró, L.P. Gleaming and dull surface textures from photonic-crystal-type nanostructures in the butterfly Cyanophrys remus. *Phys. Rev. E* **2006**, *74*, 021922. https://doi.org/10.1103/PhysRevE.74.021922.

30. Michielsen, K.; Stavenga, D. Gyroid cuticular structures in butterfly wing scales: Biological photonic crystals. *J. R. Soc. Interface* **2008**, *5*, 85–94. https://doi.org/10.1098/rsif.2007.1065.

31. Saranathan, V.; Osuji, C.O.; Mochrie, S.G.J.; Noh, H.; Narayanan, S.; Sandy, A.; Dufresne, E.R.; Prum, R.O. Structure, function, and self-assembly of single network gyroid ($I4_132$) Photonic Cryst. Butterfly Wing Scales. *Proc. Natl. Acad. Sci. USA* **2010**, *107*, 11676–11681. https://doi.org/10.1073/pnas.0909616107.

32. Pouya, C.; Vukusic, P. Electromagnetic characterization of millimetre-scale replicas of the gyroid photonic crystal found in the butterfly *Parides Sesostris*. *Interface Focus* **2012**, *2*, 645–650. https://doi.org/10.1098/rsfs.2011.0091.

33. Mouchet, S.R.; Vigneron, J.P.; Colomer, J.F.; Vandenbem, C.; Deparis, O. Additive photonic colors in the Brazilian diamond weevil: *Entimus imperialis*. *Proc. SPIE 8480* **2012**. *8480*, 848003. https://doi.org/10.1117/12.928352.

34. Mouchet, S.; Colomer, J.F.; Vandenbem, C.; Deparis, O.; Vigneron, J.P. Method for modeling additive color effect in photonic polycrystals with form anisotropic elements: The case of *Entimus Imp. Weevil*. *Opt. Express* **2013**, *21*, 13228–13240. https://doi.org/10.1364/OE.21.013228.

35. R. O. Prum, R. H. Torres, S.W.; Dyck, J. Coherent light scattering by blue feather barbs. *Nature* **1998**, *396*, 28–29. https://doi.org/10.1038/23838.

36. Prum, R.O.; Torres, R.H. A Fourier Tool for the Analysis of Coherent Light Scattering by Bio-Optical Nanostructures1. *Integr. Comp. Biol.* **2003**, *43*, 591–602. https://doi.org/10.1093/icb/43.4.591.

37. Prum, R.O.; Torres, R. Structural colouration of avian skin: Convergent evolution of coherently scattering dermal collagen arrays. *J. Exp. Biol.* **2003**, *206*, 2409–2429. https://doi.org/10.1242/jeb.00431.

38. Prum, R.O.; Torres, R.H. Structural colouration of mammalian skin: Convergent evolution of coherently scattering dermal collagen arrays. *J. Exp. Biol.* **2004**, *207*, 2157–2172. https://doi.org/10.1242/jeb.00989.

39. Henze, M.J.; Lind, O.; Wilts, B.D.; Kelber, A. Pterin-pigmented nanospheres create the colours of the polymorphic damselfly *Ischnura Elegans*. *J. R. Soc. Interface* **2019**, *16*, 20180785. https://doi.org/10.1098/rsif.2018.0785.

40. Mouchet, S.R.; Luke, S.; McDonald, L.T.; Vukusic, P. Optical costs and benefits of disorder in biological photonic crystals. *Faraday Discuss.* **2020**, *223*, 9–48. https://doi.org/10.1039/D0FD00101E.

41. Morehouse, N.I.; Vukusic, P.; Rutowski, R. Pterin pigment granules are responsible for both broadband light scattering and wavelength selective absorption in the wing scales of pierid butterflies. *Proc. R. Soc. B Biol. Sci.* **2007**, *274*, 359–366. https://doi.org/10.1098/rspb.2006.3730.

42. Stavenga, D.G.; Stowe, S.; Siebke, K.; Zeil, J.; Arikawa, K. Butterfly wing colours: Scale beads make white pierid wings brighter. *Proc. R. Soc. Lond. Ser. B Biol. Sci.* **2004**, *271*, 1577–1584. https://doi.org/10.1098/rspb.2004.2781.

43. Stavenga, D.G.; Giraldo, M.A.; Hoenders, B.J. Reflectance and transmittance of light scattering scales stacked on the wings of pierid butterflies. *Opt. Express* **2006**, *14*, 4880–4890. https://doi.org/10.1364/OE.14.004880.

44. Ladouce, M.; Barakat, T.; Su, B.L.; Deparis, O.; Mouchet, S.R. Scattering of ultraviolet light by avian eggshells. *Faraday Discuss.* **2020**, *223*, 63–80. https://doi.org/10.1039/D0FD00034E.

45. Mouchet, S.R.; Vukusic, P. Structural Colours in Lepidopteran Scales. *Adv. Insect Physiol.* **2018**, *54*, 1–53. https://doi.org/10.1016/bs.aiip.2017.11.002.

46. Vigneron, J.P.; Colomer, J.F.m.; Vigneron, N.; Lousse, V. Natural layer-by-layer photonic structure in the squamae of *Hoplia Coerulea* (Coleoptera). *Phys. Rev. E* **2005**, *72*, 061904. https://doi.org/10.1103/PhysRevE.72.061904.

47. Mouchet, S.; Lobet, M.; Kolaric, B.; Kaczmarek, A.; Van Deun, R.; Vukusic, P.; Deparis, O.; Van Hooijdonk, E. Photonic scales of *Hoplia Coerulea* Beetle: Any Colour You Like. *Mater. Today Proc.* **2017**, *4*, 4979–4986. https://doi.org/10.1016/j.matpr.2017.04.104.

48. Rassart, M.; Simonis, P.; Bay, A.; Deparis, O.; Vigneron, J.P. Scale coloration change following water absorption in the beetle *Hoplia Coerulea* (Coleoptera). *Phys. Rev. E* **2009**, *80*, 031910. https://doi.org/10.1103/PhysRevE.80.031910.

49. Mouchet, S.R.; Su, B.L.; Tabarrant, T.; Lucas, S.; Deparis, O. *Hoplia Coerulea*, A Porous Nat. Photonic Struct. Template Opt. Vap. Sensor. *Proc. SPIE* **2014**, *9127*. https://doi.org/10.1117/12.2050409.

50. Mouchet, S.R.; Tabarrant, T.; Lucas, S.; Su, B.L.; Vukusic, P.; Deparis, O. Vapor sensing with a natural photonic cell. *Opt. Express* **2016**, *24*, 12267–12280. https://doi.org/10.1364/OE.24.012267.

51. Mouchet, S.; Van Hooijdonk, E.; Welch, V.; Louette, P.; Colomer, J.F.; Su, B.L.; Deparis, O. Liquid-induced colour change in a beetle: The concept of a photonic cell. *Sci. Rep.* **2016**, *6*, 19322. https://doi.org/10.1038/srep19322.

52. Mouchet, S.; Van Hooijdonk, E.; Welch, V.; Louette, P.; Tabarrant, T.; Vukusic, P.; Lucas, S.; Colomer, J.F.; Su, B.L.; Deparis, O. Assessment of environmental spectral ellipsometry for characterising fluid-induced colour changes in natural photonic structures. *Mater. Today Proc.* **2017**, *4*, 4987–4997. https://doi.org/10.1016/j.matpr.2017.04.105.

53. Van Hooijdonk, E.; Berthier, S.; Vigneron, J.P. Bio-inspired approach of the fluorescence emission properties in the scarabaeid beetle *Hoplia Coerulea* (Coleoptera): Model. Transf.-Matrix Opt. Simulations. *J. Appl. Phys.* **2012**, *112*, 114702. https://doi.org/10.1063/1.4768896.

54. Mouchet, S.R.; Lobet, M.; Kolaric, B.; Kaczmarek, A.M.; Van Deun, R.; Vukusic, P.; Deparis, O.; Van Hooijdonk, E. Controlled fluorescence in a beetle's photonic structure and its sensitivity to environmentally induced changes. *Proc. R. Soc. Lond. B Biol. Sci.* **2016**, *283*. https://doi.org/10.1098/rspb.2016.2334.

55. Lagorio, M.G.; Cordon, G.B.; Iriel, A. Reviewing the relevance of fluorescence in biological systems. *Photochem. Photobiol. Sci.* **2015**, *14*, 1538–1559. https://doi.org/10.1039/C5PP00122F.

56. Marshall, J.; Johnsen, S. Fluorescence as a means of colour signal enhancement. *Philos. Trans. R. Soc. Lond. B Biol. Sci.* **2017**, *372*. https://doi.org/10.1098/rstb.2016.0335.

57. Arnold, K.E.; Owens, I.P.F.; Marshall, N.J. Fluorescent Signaling in Parrots. *Science* **2002**, *295*, 92. https://doi.org/10.1126/science.295.5552.92.

58. McGraw, K.J.; Toomey, M.B.; Nolan, P.M.; Morehouse, N.I.; Massaro, M.; Jouventin, P. A description of unique fluorescent yellow pigments in penguin feathers. *Pigment Cell Res.* **2007**, *20*, 301–304. https://doi.org/10.1111/j.1600-0749.2007.00386.x.

59. Ladouce, M.; Barakat, T.; Su, B.L.; Deparis, O.; Mouchet, S.R. UV scattering by pores in avian eggshells. *Proc. SPIE* **2020**, *11481*, 101–109. https://doi.org/10.1117/12.2567915.

60. Cockayne, E. I. The Distribution of Fluorescent Pigments in Lepidoptera. *Trans. R. Entomol. Soc. Lond.* **1924**, *72*, 1–19. https://doi.org/10.1111/j.1365-2311.1924.tb03347.x.

61. Vukusic, P.; Hooper, I. Directionally Controlled Fluorescence Emission in Butterflies. *Science* **2005**, *310*, 1151. https://doi.org/10.1126/science.1116612).

62. Israelowitz, M.; Rizvi, S.H.; von Schroeder, H.P. Fluorescence of the "fire-chaser" beetle *Melanophila Acuminata*. *J. Lumin.* **2007**, *126*, 149–154.

63. Trzeciak, T.M.; Wilts, B.D.; Stavenga, D.G.; Vukusic, P. Variable multilayer reflection together with long-pass filtering pigment determines the wing coloration of papilionid butterflies of the *Nireus* Group. *Opt. Express* **2012**, *20*, 8877–8890. https://doi.org/10.1098/rsfs.2011.0082.

64. Hooijdonk, E.V.; Vandenbem, C.; Berthier, S.; Vigneron, J.P. Bi-functional photonic structure in the *Papilio Nireus* (Papilionidae): Model. Scatt.-Matrix Opt. Simulations. *Opt. Express* **2012**, *20*, 22001–22011. https://doi.org/10.1364/OE.20.022001.

65. Van Hooijdonk, E.; Berthier, S.; Vigneron, J.P. Contribution of both the upperside and the underside of the wing on the iridescence in the male butterfly *Troïdes Magellanus* (Papilionidae). *J. Appl. Phys.* **2012**, *112*, 074702. https://doi.org/10.1063/1.4755796.

66. Welch, V.L.; Van Hooijdonk, E.; Intrater, N.; Vigneron, J.P. Fluorescence in insects. *Proc. SPIE* **2012**, *8480*, 848004. https://doi.org/10.1117/12.929547.

67. Wilts, B.D.; Trzeciak, T.M.; Vukusic, P.; Stavenga, D.G. Papiliochrome II pigment reduces the angle dependency of structural wing colouration in *Nireus* Group Papilionids. *J. Exp. Biol.* **2012**, *215*, 796–805. https://doi.org/10.1242/jeb.060103.

68. Van Hooijdonk, E.; Barthou, C.; Vigneron, J.P.; Berthier, S. Yellow structurally modified fluorescence in the longhorn beetles Celosterna pollinosa sulfurea and Phosphorus virescens (Cerambycidae). *J. Lumin.* **2013**, *136*, 313–321. https://doi.org/10.1016/j.jlumin.2012.12.022.

69. Mouchet, S.R.; Kaczmarek, A.M.; Mara, D.; Deun, R.V.; Vukusic, P. Colour and fluorescence emission of *Euchroea Auripigmenta* Beetle. *Proc. SPIE* **2019**, *10965*, 72 – 82. https://doi.org/10.1117/12.2513660.

70. Mouchet, S.R.; Verstraete, C.; Kaczmarek, A.M.; Mara, D.; van Cleuvenbergen, S.; Van Deun, R.; Verbiest, T.; Maes, B.; Vukusic, P.; Kolaric, B. Unveiling the nonlinear optical response of *Trictenotoma Child. Longhorn Beetle*. *J. Biophotonics* **2019**, *12*, e201800470. https://doi.org/10.1002/jbio.201800470.

71. Mouchet, S.R.; Verstraete, C.; Bokic, B.; Mara, D.; Dellieu, L.; Orr, A.G.; Deparis, O.; Deun, R.V.; Verbiest, T.; Vukusic, P.; et al. Naturally occurring fluorescence in transparent insect wings. *arXiv* **2021**, arXiv:2110.06086.

72. Lawrence, R.F. Fluorescence in Arthropoda. *J. Entomol. Soc. South. Afr.* **1954**, *17*, 167–170.

73. Pavan, M.; Vachon, M. Sur l'existence d'une substance fluorescente dans les téguments des Scorpions (Arachnides). *Comptes Rendus De L'Académie Des Sci.* **1954**, *239*, 1700–1702.

74. Tani, K.; Watari, F.; Uo, M.; Morita, M. Fluorescent Properties of Porcelain-Restored Teeth and Their Discrimination. *Mater. Trans.* **2004**, *45*, 1010–1014. https://doi.org/10.2320/matertrans.45.1010).

75. Taboada, C.; Brunetti, A.E.; Pedron, F.N.; Carnevale Neto, F.; Estrin, D.A.; Bari, S.E.; Chemes, L.B.; Peporine Lopes, N.; Lagorio, M.G.; Faivovich, J. Naturally occurring fluorescence in frogs. *Proc. Natl. Acad. Sci. USA* **2017**, *114*, 3672–3677.

76. Deschepper, P.; Jonckheere, B.; Matthys, J. A Light in the Dark: The Discovery of Another Fluorescent Frog in the Costa Rican Rainforests. *Wilderness Environ. Med.* **2018**, *29*, 421–422.

77. Mohd Top, M.; Puan, C.L.; Chuang, M.F.; Othman, S.N.; Borzée, A. First record of ultraviolet fluorescence in the Bent-toed Gecko *Cyrtodactylus Quadrivirgatus* Taylor, 1962 (Gekkonidae: Sauria). *Herpetol. Notes* **2020**, *13*, 211–212.

78. Gruber, D.F.; Gaffney, J.P.; Mehr, S.; DeSalle, R.; Sparks, J.S.; Platisa, J.; Pieribone, V.A. Adaptive Evolution of Eel Fluorescent Proteins from Fatty Acid Binding Proteins Produces Bright Fluorescence in the Marine Environment. *PLoS ONE* **2015**, *10*, e0140972. https://doi.org/10.1371/journal.pone.0140972.

79. Gruber, D.F.; Loew, E.R.; Deheyn, D.D.; Akkaynak, D.; Gaffney, J.P.; Smith, W.L.; Davis, M.P.; Stern, J.H.; Pieribone, V.A.; Sparks, J.S. Biofluorescence in Catsharks (Scyliorhinidae): Fundamental Description and Relevance for Elasmobranch Visual Ecology. *Sci. Rep.* **2016**, *6*, 1–16. https://doi.org/10.1038/srep24751.

80. Iriel, A.; Lagorio, M.G. Is the flower fluorescence relevant in biocommunication? *Naturwissenschaften* **2010**, *97*, 915–924. https://doi.org/10.1007/s00114-010-0709-4.

81. Iriel, A.; Lagorio, M.G. Implications of reflectance and fluorescence of *Rhododendr. Indicum* Flowers Biosignaling. *Photochem. Photobiol. Sci.* **2010**, *9*, 342–348. https://doi.org/10.1039/B9PP00104B.

82. Purcell, E.M. Spontaneous emission probabilities at radio frequencies. *Phys. Rev.* **1946**, *69*, 681.

83. Yablonovitch, E. Inhibited Spontaneous Emission in Solid-State Physics and Electronics. *Phys. Rev. Lett.* **1987**, *58*, 2059–2062.

84. Kumazawa, K.; Tanaka, S.; Negita, K.; Tabata, H. Fluorescence from Wing of *Morpho Sulkowskyi* Butterfly. *Jpn. J. Appl. Phys.* **1994**, *33*, 2119–2122. https://doi.org/10.1143/jjap.33.2119.

85. Lawrence, C.R.; Vukusic, P.; Sambles, J.R. Grazing-incidence iridescence from a butterfly wing. *Appl. Opt.* **2002**, *41*, 437–441.

86. Vigneron, J.P.; Kertész, K.; Vértesy, Z.; Rassart, M.; Lousse, V.; Bálint, Z.; Biró, L.P. Correlated diffraction and fluorescence in the backscattering iridescence of the male butterfly *Troides Magellanus* (Papilionidae). *Phys. Rev. E* **2008**, *78*, 021903. https://doi.org/10.1103/PhysRevE.78.021903.

87. Van Hooijdonk, E.; Barthou, C.; Vigneron, J.P.; Berthier, S. Detailed experimental analysis of the structural fluorescence in the butterfly *Morpho Sulkowskyi* (Nymphalidae). *J. Nanophotonics* **2011**, *5*, 053525. https://doi.org/10.1117/1.3659147.

88. Hooijdonk, E.V.; Barthou, C.; Vigneron, J.P.; Berthier, S. Angular dependence of structural fluorescent emission from the scales of the male butterfly *Troïdes Magellanus* (Papilionidae). *J. Opt. Soc. Am. B* **2012**, *29*, 1104–1111. https://doi.org/10.1364/JOSAB.29.001104.

89. Verbiest, T.; Kauranen, M.; Persoons, A.; Ikonen, M.; Kurkela, J.; Lemmetyinen, H. Nonlinear Optical Activity and Biomolecular Chirality. *J. Am. Chem. Soc.* **1994**, *116*, 9203–9205. https://doi.org/10.1021/ja00099a040.

90. Campagnola, P.J.; Millard, A.C.; Terasaki, M.; Hoppe, P.E.; Malone, C.J.; Mohler, W.A. Three-dimensional high-resolution second-harmonic generation imaging of endogenous structural proteins in biological tissues. *Biophys. J.* **2002**, *82*, 493–508.

91. Friedl, P.; Wolf, K.; Harms, G.; Andrian, U.H. Biological Second and Third Harmonic Generation Microscopy. *Curr. Protoc. Cell Biol.* **2007**, *34*, 4.15.1–4.15.21. https://doi.org/10.1002/0471143030.cb0415s34.

92. Ries, R.S.; Choi, H.; Blunck, R.; Bezanilla, F.; Heath, J.R. Black Lipid Membranes: Visualizing the Structure, Dynamics, and Substrate Dependence of Membranes. *J. Phys. Chem. B* **2004**, *108*, 16040–16049. https://doi.org/10.1021/jp048098h.

93. Brown, D.J.; Morishige, N.; Neekhra, A.; Minckler, D.S.; Jester, J.V. Application of second harmonic imaging microscopy to assess structural changes in optic nerve head structure ex vivo. *J. Biomed. Opt.* **2007**, *12*, 5. https://doi.org/10.1117/1.2717540.

94. Lis, D.; Guthmuller, J.; Champagne, B.; Humbert, C.; Busson, B.; Tadjeddine, A.; Peremans, A.; Cecchet, F. Selective detection of the antigenic polar heads of model lipid membranes supported on metals from their vibrational nonlinear optical response. *Chem. Phys. Lett.* **2010**, *489*, 12–15. https://doi.org/10.1016/j.cplett.2010.02.061.

95. Nguyen, T.T.; Conboy, J.C. High-Throughput Screening of Drug-Lipid Membrane Interactions via Counter-Propagating Second Harmonic Generation Imaging. *Anal. Chem.* **2011**, *83*, 5979–5988. https://doi.org/10.1021/ac2009614.

96. Theer, P.; Denk, W.; Sheves, M.; Lewis, A.; Detwiler, P.B. Second-Harmonic Generation Imaging of Membrane Potential with Retinal Analogues. *Biophys. J.* **2011**, *100*, 232–242. https://doi.org/10.1016/j.bpj.2010.11.021.

97. Chen, X.; Nadiarynkh, O.; Plotnikov, S.; Campagnola, P.J. Second harmonic generation microscopy for quantitative analysis of collagen fibrillar structure. *Nat. Protoc.* **2012**, *7*, 654.

98. Akerboom, J.; Carreras Calderón, N.; Tian, L.; Wabnig, S.; Prigge, M.; Tolö, J.; Gordus, A.; Orger, M.B.; Severi, K.E.; Macklin, J.J.; et al. Genetically encoded calcium indicators for multi-color neural activity imaging and combination with optogenetics. *Front. Mol. Neurosci.* **2013**, *6*, 2.

99. Rabasović, M.D.; Pantelić, D.V.; Jelenković, B.M.; Ćurčić, S.B.; Rabasović, M.S.; Vrbica, M.D.; Lazović, V.M.; Ćurčić, B.P.; Krmpot, A.J. Nonlinear microscopy of chitin and chitinous structures: A case study of two cave-dwelling insects. *J. Biomed. Opt.* **2015**, *20*, 016010.

100. Chen, Y.C.; Lee, S.Y.; Wu, Y.; Brink, K.; Shieh, D.B.; Huang, T.D.; Reisz, R.R.; Sun, C.K. Third-harmonic generation microscopy reveals dental anatomy in ancient fossils. *Opt. Lett.* **2015**, *40*, 1354–1357.

101. Lis, D.; Cecchet, F. Unique Vibrational Features as a Direct Probe of Specific Antigen–Antibody Recognition at the Surface of a Solid-Supported Hybrid Lipid Bilayer. *ChemPhysChem* **2016**, *17*, 2645–2649. https://doi.org/10.1002/cphc.201600419.

102. Rowlands, C.J.; Park, D.; Bruns, O.T.; Piatkevich, K.D.; Fukumura, D.; Jain, R.K.; Bawendi, M.G.; Boyden, E.S.; So, P.T. Wide-field three-photon excitation in biological samples. *Light Sci Appl* **2017**, *6*, e16255. https://doi.org/10.1038/lsa.2016.255).

103. Reynaud, C.; Thoury, M.; Dazzi, A.; Latour, G.; Scheel, M.; Li, J.; Thomas, A.; Moulhérat, C.; Didier, A.; Bertrand, L. In-place molecular preservation of cellulose in 5,000-year-old archaeological textiles. *Proc. Natl. Acad. Sci. USA* **2020**, *117*, 19670–19676.

104. Raoux, C.; Schmeltz, M.; Bied, M.; Alnawaiseh, M.; Hansen, U.; Latour, G.; Schanne-Klein, M.C. Quantitative structural imaging of keratoconic corneas using polarization-resolved SHG microscopy. *Biomed. Opt. Express* **2021**, *12*, 4163–4178. https://doi.org/10.1364/BOE.426145.

105. Schmeltz, M.; Robinet, L.; Heu-Thao, S.; Sintès, J.M.; Teulon, C.; Ducourthial, G.; Mahou, P.; Schanne-Klein, M.C.; Latour, G. Noninvasive quantitative assessment of collagen degradation in parchments by polarization-resolved SHG microscopy. *Sci. Adv.* **2021**, *7*, eabg1090. https://doi.org/10.1126/sciadv.abg1090.

106. Mouchet, S.R.; Verstraete, C.; Mara, D.; Cleuvenbergen, S.V.; Finlayson, E.D.; Deun, R.V.; Deparis, O.; Verbiest, T.; Maes, B.; Vukusic, P.; et al. Nonlinear optical spectroscopy and two-photon excited fluorescence spectroscopy reveal the excited states of fluorophores embedded in a beetle's elytra. *Interface Focus* **2019**, *9*, 20180052. https://doi.org/10.1098/rsfs.2018.0052.

107. Stoddart, P.R.; Cadusch, P.J.; Boyce, T.M.; Erasmus, R.M.; Comins, J.D. Optical properties of chitin: Surface-enhanced Raman scattering substrates based on antireflection structures on cicada wings. *Nanotechnology* **2006**, *17*, 680.

108. Garrett, N.L.; Vukusic, P.; Ogrin, F.; Sirotkin, E.; Winlove, C.P.; Moger, J. Spectroscopy on the wing: Naturally inspired SERS substrates for biochemical analysis. *J. Biophotonics* **2009**, *2*, 157–166. https://doi.org/10.1002/jbio.200810057.

109. Garrett, N.L. *Naturally Inspired SERS Substrates: Datasheet from · Volume : "Raman Spectroscopy for Nanomaterials Characterization"*; SpringerMaterials: 2012. https://doi.org/10.1007/978-3-642-20620-7{_}4.

110. Garrett, N.L.; Sekine, R.; Dixon, M.W.A.; Tilley, L.; Bambery, K.R.; Wood, B.R. Bio-sensing with butterfly wings: Naturally occurring nano-structures for SERS-based malaria parasite detection. *Phys. Chem. Chem. Phys.* **2015**, *17*, 21164–21168. https://doi.org/10.1039/C4CP04930F.

111. Palmer, L.D.; Brooks, J.L.; Frontiera, R.R. Probing the coupling of butterfly wing photonic crystals to plasmon resonances with surface-enhanced Raman spectroscopy. *J. Mater. Chem. C* **2019**, *7*, 13887–13895. https://doi.org/10.1039/C9TC02629K.

112. Langer, J.; et al. Present and Future of Surface-Enhanced Raman Scattering. *ACS Nano* **2020**, *14*, 28–117. https://doi.org/10.1021/acsnano.9b04224.

113. Zhang, G.; Zhang, J.; Xie, G.; Liu, Z.; Shao, H. Cicada Wings: A Stamp from Nature for Nanoimprint Lithography. *Small* **2006**, *2*, 1440–1443. https://doi.org/10.1002/smll.200600255.

114. Dellieu, L.; Sarrazin, M.; Simonis, P.; Deparis, O.; Vigneron, J.P. A two-in-one superhydrophobic and anti-reflective nanodevice in the grey cicada *Cicada Orni* (Hemiptera). *J. Appl. Phys.* **2014**, *116*, 024701. https://doi.org/10.1063/1.4889849.

115. Deparis, O.; Mouchet, S.R.; Dellieu, L.; Colomer, J.F.; Sarrazin, M. Nanostructured Surfaces: Bioinspiration for Transparency, Coloration and Wettability. *Mater. Today Proc.* **2014**, *1S*, 122–129. https://doi.org/10.1016/j.matpr.2014.09.008.

116. Kovačević, A.; Petrović, S.; Mimidis, Alexandros.and Stratakis, E.; Pantelić, D.; Kolaric, B. Molding Wetting by Laser-Induced Nanostructures. *Appl. Sci.* **2020**, *10*, 6008–6018. https://doi.org/10.3390/app10176008.

117. Gao, T.; Zhu, X.; Wu, X.J.; Zhang, B.; Liu, H.L. Selectively Manipulating Upconversion Emission Channels with Tunable Biological Photonic Crystals. *J. Phys. Chem. C* **2021**, *125*, 732–739.

118. Zhang, D. *Morphology Genetic Materials Templated from Nature Species*; Springer: Berlin/Heidelberg, Germany, 2012.